

**Rapidity Dependence of Kaon Production
in Si+Au and Si+Al at 14.6 A·GeV/c**

by

David P. Morrison

A.B. Physics, University of California, Berkeley (1988)

Submitted to the Department of Physics
in partial fulfillment of the requirements for the degree of

Doctor of Philosophy

at the

MASSACHUSETTS INSTITUTE OF TECHNOLOGY

May 1994

© David P. Morrison, 1994. All rights reserved.

The author hereby grants to MIT permission to reproduce and
to distribute copies of this thesis document in whole or in part.

Author
Department of Physics
May 10, 1994

Certified by
George S. F. Stephans
Principal Research Scientist, Laboratory for Nuclear Science
Thesis Supervisor

Certified by
Wit Busza
Professor, Department of Physics
Thesis Co-supervisor

Accepted by
George Koster
Chairman, Physics Graduate Committee

**Rapidity Dependence of Kaon Production
in Si+Au and Si+Al at 14.6 A·GeV/c**

by

David P. Morrison

Submitted to the Department of Physics
on May 10, 1994, in partial fulfillment of the
requirements for the degree of
Doctor of Philosophy

Abstract

As part of BNL-AGS Experiment 859, transverse distributions, rapidity distributions and total yields have been measured for K^+ and K^- produced in collisions of a 14.6 A·GeV/c ^{28}Si beam incident on ^{27}Al and ^{197}Au targets. The experimental apparatus consists of a magnetic spectrometer and a spectrometer trigger with a second level veto capable of online particle identification. An array of streamer tubes surrounding the target are used to select classes of events based on charged particle multiplicity, and the energy measured in a zero-degree calorimeter is used to calculate the number of projectile participants. For kaons, the acceptance of the spectrometer covers the rapidity range of $0.5 < y < 2.1$ and a transverse momentum range of $0.1 < p_{\perp} < 2.5$. Minimum bias results are shown, as are results for events gated in 4 different multiplicity bins. It is found that the rapidity distributions for K^+ peak closer to the target rapidity than the K^- for all centralities, a trend consistent with the dominance of associated production for the K^+ . The K^+ m_{\perp} inverse slope parameters for all systems are consistently 10–20 MeV/c² higher than those for the K^- . The ratio of K^+ to K^- versus rapidity is shown to have very little dependence on target or centrality, an effect which may point to the importance of secondary production of K^- via meson-baryon collisions such as the strangeness exchange reaction $\pi\Lambda \rightarrow NK^-$. Comparisons with the microscopic model RQMD are made and it is found that the model produces m_{\perp} inverse slope parameters for the K^- that are significantly too high and generally under predicts the kaon production, but that it follows the systematic trends in the data very well. The rapidity distributions are shown and the effect of intermediate resonance production is discussed.

Thesis Supervisor: George S. F. Stephans

Title: Principal Research Scientist, Laboratory for Nuclear Science

Thesis Co-supervisor: Wit Busza

Title: Professor, Department of Physics

For Kunya, for my parents, and for Katie

Contents

1	Introduction	17
1.1	Kinematic Variables	20
1.2	General Features of Nuclear Collisions	22
1.3	BNL-AGS Experiment 859	23
1.3.1	A Second-Level Veto for Rare Events	25
1.4	Goals of this Thesis	26
2	Strangeness in Heavy Ion Collisions	29
2.1	Theoretical Background	29
2.1.1	Strangeness in the Quark-Gluon Plasma and Hadron Gas	30
2.1.2	Strangeness Production in Real Collisions	32
2.2	Experimental Background	35
2.2.1	Strange Particle Production in Proton-Proton Collisions	35
2.2.2	Interactions of Strange Particles with Nucleons	37
2.2.3	Strange Particle Production in Proton-Nucleus Collisions	40
2.2.4	Other Nucleus-Nucleus Results	40
3	Experimental Description	45
3.1	The Beam and Target	45
3.1.1	Beam Production and Acceleration	46
3.1.2	Beam Definition and Counting	49
3.1.3	The Target Assembly	51
3.2	Event Characterization	52

CONTENTS

3.2.1	The Target Multiplicity Array	53
3.2.2	The Zero Degree Calorimeter	55
3.3	The Spectrometer	57
3.3.1	The TPC and F0	57
3.3.2	The Drift Chambers	57
3.3.3	The Trigger Chambers	63
3.3.4	The Time of Flight Wall	66
3.3.5	The Gas Čerenkov and Back Counter	66
3.4	The Data Acquisition System	68
3.5	LVL2 Trigger	70
3.5.1	Hardware of the LVL2 Trigger	70
3.5.2	Operation of the LVL2 trigger	73
4	Data Analysis	77
4.1	Overview of Data and Analysis	77
4.2	Track Reconstruction	79
4.2.1	Overview of Algorithm	80
4.2.2	Momentum Determination	81
4.3	Particle Identification	83
4.3.1	Overview of Algorithm	83
4.3.2	Determination of Cuts	84
4.4	Reconstruction and PID Efficiency	88
4.5	Effect of the GASČ on Kaon Identification	92
4.5.1	Multiparticle GASČ Effects Leading to Kaon Loss	94
4.5.2	Pion Contamination of Kaons	94
4.5.3	Corrections Applied to Data	97
4.6	LVL2 Trigger Biases	100
4.7	Spectrometer Acceptance	105
4.8	Trigger Conditions	107
4.8.1	BEAM and INT Trigger	110

CONTENTS

4.8.2	SPEC Trigger and LVL2 Veto	116
4.9	Invariant Cross Sections and Yields	118
4.9.1	Matching Data for Different Target Thicknesses	121
4.10	TMA Data Analysis	124
4.10.1	General Features of TMA Distribution	125
4.10.2	Rate Dependence of TMA Signal	127
4.10.3	Determination of TMA Cuts	128
4.10.4	Consistency of TMA Cuts	133
4.11	ZCAL Analysis	135
4.11.1	Rate Dependence of ZCAL Signal	137
4.11.2	ZCAL Distributions for TMA Gated Events	137
5	Data Presentation and Discussion	143
5.1	Slopes and Invariant Yields	143
5.2	Average Transverse Momentum	148
5.3	Rapidity Distributions	150
5.4	Scaling of Kaon Yields	157
5.5	Particle Ratios	159
5.6	Estimates of Systematic Errors in the Kaon Analysis	163
5.6.1	Overall Normalization	163
5.6.2	Relative Normalization of Different Targets	165
5.6.3	Uncertainty in TMA Cuts and Event Selection	166
5.6.4	Uncertainties in Slope and dn/dy	166
5.6.5	Total Systematic Errors	167
5.7	Discussion of Data	167
6	Model Comparisons	173
6.1	Overview	173
6.2	Synopsis of RQMD Algorithm	174
6.3	Event Selection and Acceptance Issues	179
6.4	Kaon Yields and Slopes	182

6.5	Scaling of Kaon Yields in RQMD	186
6.6	K^+/K^- Ratio	189
6.7	Kaon Production Mechanisms	193
6.8	Summary of Model Comparison	197
7	Summary and Conclusions	201
A	Kaon m_\perp Distributions	207
B	E802 Si+A Reference	229
C	LVL2 Trigger Details	231
C.1	Calibrations	231
C.2	Taking Data Using the LVL2 Trigger	232
C.3	Software Control of the LVL2 Trigger	234
D	Spectrometer Acceptance Details	237
E	Time of Flight Wall Calibration	243
E.1	Calibration Procedure	243
E.2	TOF Wall Intrinsic Timing Resolution	244
E.3	Monitoring of Calibrations During PASS3	245
F	Cross Section Fitting Procedure	249
F.1	Log Likelihood Fits to Histograms	249
F.2	Log Likelihood Fits to Invariant Yields	251
G	TMA Groups	255
H	Preliminary ARC 1.9.5 Results	259
I	E859 Collaboration List	261

List of Tables

1.1	Particle abundances per TMA trigger	25
3.1	Targets used in E859	52
3.2	Tracking Chamber Wire Orientations	60
4.1	Summary of statistics for E859 single particle kaon runs.	78
4.2	Contributors to PID Inefficiency	92
4.3	LVL2 Mass and Momentum Cuts	117
4.4	E859 Rejection Factors	118
4.5	Interaction rate consistency check	124
4.6	Properties of ZCAL distributions for TMA gated events	142
5.1	Comparison of the χ^2/dof for different fits to the K^\pm transverse distributions	146
5.2	Parameters of kaon rapidity distributions	155
6.1	RQMD switches. Courtesy of R. Soltz	178
6.2	Systematic yield variation in peripheral RQMD event selection	179
6.3	Comparison of RQMD and data m_\perp inverse slope parameters	183
6.4	Comparison of RQMD dn/dy from fits and counts	186
6.5	Comparison of ZCAL for TMA cuts between RQMD and real data	189
C.1	LVL2 initialization procedures	232
G.1	Si+Al 3% TMA Groups	255
G.2	Si+Al 6% TMA Groups	256

LIST OF TABLES

G.3	Si+Au 1% TMA Groups	256
G.4	Si+Au 3% TMA Groups	257

List of Figures

1-1	Coordinate system definition	21
2-1	Rapidity density of a daughter in a two-body decay	34
2-2	Rapidity distribution of strange particles in pp collisions	36
2-3	Rapidity distribution of net strangeness in pp collisions	37
2-4	K^- p cross section	38
2-5	K^+ p cross section	39
2-6	E802 p+A dn/dy summary	41
2-7	Si+Al $\rightarrow\Lambda$ dn/dy from AGS experiment E810	42
2-8	Kaon m_\perp slopes from E814	43
3-1	Layout of the AGS facility	46
3-2	Diagram of beam transport and acceleration	47
3-3	Beam Counter Assembly	50
3-4	Detail of target assembly	51
3-5	Perspective View of the TMA	54
3-6	ZCAL energy distribution	56
3-7	Plan View of the Spectrometer	58
3-8	Drift cell	60
3-9	Schematic of Gas Supply	63
3-10	View of Detectors Behind Magnet	64
3-11	View of the Gas Čerenkov and Back Counter	67
3-12	Data Acquisition Hardware	68

LIST OF FIGURES

3-13	LVL2 trigger diagram	72
3-14	LVL2 Flowchart	73
4-1	Determination of momentum from bend angle	82
4-2	PICD Particle identification cuts	87
4-3	AUSCONand PICD efficiency summary	90
4-4	Fraction of TOF identified kaons firing the GASČ versus TOF panel number.	95
4-5	Fraction of tracks firing the GASČ	96
4-6	K/ π Ratio versus p for GASČ Correction	98
4-7	Online and offline masses for rejected kaon events	101
4-8	Possible decay masquerading as a kaon	103
4-9	Reconstructed target position creating kaon	104
4-10	Expected fraction of kaon events lost	106
4-11	TOF slat for tracks firing GASČ	108
4-12	Kaon $y - m_{\perp}$ Acceptance	109
4-13	Bull's-eye Charge Distribution	111
4-14	Bull's-eye charge distribution for empty target runs	113
4-15	Empty Target Interaction Rate	115
4-16	INT/BEAM rates	123
4-17	TMA distribution for INT events	126
4-18	Mar92 Instantaneous Beam Rate	129
4-19	Rate dependence of TMA for Feb91 data	130
4-20	TMA Distribution for Kaon Events	134
4-21	Spectrometer integrated K^+ counts for Si+Au TMA1 cut	136
4-22	Feb91 ZCAL rate dependent beam peak	138
4-23	Mar92 ZCAL rate dependent beam peak	139
4-24	Mar92 ZCAL rate dependent resolution	140
4-25	ZCAL distribution for Si+Al TMA1 events	141
5-1	Central Si+Au \rightarrow K $^-$ m_{\perp} distribution	144
5-2	m_{\perp} inverse slope parameter summary	147

LIST OF FIGURES

5-3	Average p_{\perp} versus rapidity for Si+Al and Si+Au	149
5-4	Si+Al \rightarrow K $^{+}$ dn/dy	151
5-5	Si+Al \rightarrow K $^{-}$ dn/dy	152
5-6	Si+Au \rightarrow K $^{+}$ dn/dy	153
5-7	Si+Au \rightarrow K $^{-}$ dn/dy	154
5-8	Widths of kaon rapidity distributions	156
5-9	N_{targ}^{proj} vs N_{proj}^{targ} within FRITIOF	158
5-10	Kaon yields versus total participants	160
5-11	Si+Al K $^{+}$ /K $^{-}$ ratio of dn/dy versus rapidity	161
5-12	Si+Au K $^{+}$ /K $^{-}$ ratio of dn/dy versus rapidity	162
5-13	Comparison of central and peripheral yields and slopes	164
6-1	ARC primary K $_s$ rapidity distribution	175
6-2	Compilation of strangeness production cross sections in p-p collisions	177
6-3	Simulated TMA versus impact parameter for RQMD events	180
6-4	RQMD Si+Au impact parameter for high multiplicity events	181
6-5	RQMD Si+Au K $^{+}$ dn/dy for different event selections	182
6-6	RQMD and E859 K $^{-}$ m_{\perp} distribution	184
6-7	RQMD Si+Au \rightarrow K $^{+}$ slope systematics	185
6-8	RQMD Si+Al \rightarrow K dn/dy versus rapidity	187
6-9	RQMD Si+Au \rightarrow K dn/dy versus rapidity	188
6-10	Scaling of RQMD kaon production	190
6-11	RQMD Si+Al K $^{+}$ /K $^{-}$ dn/dy ratio versus rapidity	191
6-12	RQMD Si+Au K $^{+}$ /K $^{-}$ dn/dy ratio versus rapidity	192
6-13	RQMD Si+Al \rightarrow K production mechanisms	193
6-14	RQMD Si+Au \rightarrow K production mechanisms	195
6-15	RQMD Si+Au \rightarrow K production mechanisms versus rapidity	196
A-1	Si+Al Inelastic K $^{+}$ m_{\perp} Distributions	208
A-2	Si+Al Inelastic K $^{-}$ m_{\perp} Distributions	209
A-3	Si+Al 0–7% TMA K $^{+}$ m_{\perp} Distributions	210

LIST OF FIGURES

A-4	Si+Al 0–7% TMA K^- m_{\perp} Distributions	211
A-5	Si+Al 7–20% TMA K^+ m_{\perp} Distributions	212
A-6	Si+Al 7–20% TMA K^- m_{\perp} Distributions	213
A-7	Si+Al 20–40% TMA K^+ m_{\perp} Distributions	214
A-8	Si+Al 20–40% TMA K^- m_{\perp} Distributions	215
A-9	Si+Al 40–100% TMA K^+ m_{\perp} Distributions	216
A-10	Si+Al 40–100% TMA K^- m_{\perp} Distributions	217
A-11	Si+Au Inelastic K^+ m_{\perp} Distributions	218
A-12	Si+Au Inelastic K^- m_{\perp} Distributions	219
A-13	Si+Au 0–7% TMA K^+ m_{\perp} Distributions	220
A-14	Si+Au 0–7% TMA K^- m_{\perp} Distributions	221
A-15	Si+Au 7–20% TMA K^+ m_{\perp} Distributions	222
A-16	Si+Au 7–20% TMA K^- m_{\perp} Distributions	223
A-17	Si+Au 20–40% TMA K^+ m_{\perp} Distributions	224
A-18	Si+Au 20–40% TMA K^- m_{\perp} Distributions	225
A-19	Si+Au 40–100% TMA K^+ m_{\perp} Distributions	226
A-20	Si+Au 40–100% TMA K^- m_{\perp} Distributions	227
B-1	E802 Peripheral Si+A dn/dy	229
B-2	E802 Central Si+A dn/dy	230
C-1	Flowchart of trigger initialization of LVL2 trigger for data taking	233
D-1	ϑ versus $qB dl/p$ for good tracks	238
D-2	Schematic of a track in the spectrometer.	240
E-1	Intrinsic TOF wall timing resolution	245
E-2	Comparison of TOF calibrations for different species	247
H-1	Comparison of central Si+Au ARC and E859 kaon dn/dy	260

Chapter 1

Introduction

The study of relativistic heavy-ion physics is a new area of research that brings together aspects of both nuclear and high energy physics. The basic aim of the field is to use very energetic collisions of nuclei to investigate the phenomenology of dense and hot hadronic matter with the consequent goal of probing the physics of quantum chromodynamics (QCD). There are several outstanding issues in QCD that may eventually be resolved by the data provided by these collisions, and preeminent among them is the issue of confinement, the mechanism that keeps QCD color charge inextricably bound into hadrons. By heating and compressing nuclear matter through collisions at high energies, there may be a chance of causing a phase transition from normal nuclear matter into the quark-gluon plasma (QGP). The exact nature of this state of matter is a subject of debate, but at the very least the quarks and gluons of which it is made are no longer confined, in the sense that they are able to roam over distances large compared to the 1 fm (10^{-15} m) size typical of hadrons. In fact, there is little doubt that such a state of matter exists, the real question is whether it can be created and detected in the laboratory.

Although the demonstration of a deconfined phase serves as a major goal for the field, it is hardly the only issue of interest along the way. In this thesis, collisions between whole nuclei at incident energies of 14.6 GeV will be studied. Whatever else may be happening, these high energy nucleus-nucleus (A-A) collisions certainly create systems of incredible energy and baryon number density, and there are intriguing physics issues related to the production of particles in such a system. There is an immense challenge in making a quantitative theoretical analysis of such collisions, however. At incident energies of several GeV per nucleon, the energy scale is far below

that for which perturbative techniques for treating QCD are applicable. On the other hand, the energy scale is high enough that it is unclear whether individual nucleons or subnucleonic degrees of freedom make a more appropriate basis for describing the collisions. Also, it is not clear that the collision of two nuclei forms a system large enough to be treated in a thermal or statistical manner. Nonetheless, many particles are involved in a collision, many of which are short-lived hadronic resonances and excited states. This means that unlike the case in more elementary proton-proton (p-p) collisions in which particles that are produced have little chance to reinteract, the particles in a heavy-ion collision find themselves surrounded by other particles. The interactions of the produced particles among themselves and with the surrounding medium make for a situation that is quite different from a series of simultaneous p-p collisions. The created resonances act as a reservoir of the initial energy of the collision, making possible physical processes that would ordinarily be energetically suppressed.

One of these processes, rare in p-p collisions at these energies, is the production of strangeness. Ordinary nuclei consist of protons and neutrons, which in turn contain only up (u) and down (d) valence quarks. When enough energy becomes available (in nuclear collisions above a few hundred MeV per nucleon incident energy) pions, which also contain anti-up (\bar{u}) and anti-down (\bar{d}) quarks begin to be produced. At energies above ~ 1 GeV per nucleon, mesons containing strange (s) and anti-strange (\bar{s}) quarks begin appearing. The lightest of these strange mesons are the kaons, with masses of $494 \text{ MeV}/c^2$. Strangeness is effectively a conserved quantum number in nuclear collisions. Weak interactions, which can violate strangeness conservation, occur on time scales of 10^{-18} sec, several orders of magnitude longer than the duration of a collision. Since the system begins with no net strangeness, the quantity $S = s - \bar{s} = 0$ remains constant during the collision. An even stronger condition arises because the density of strange quarks is always quite low, even in the most violent nuclear collisions. Therefore strangeness annihilation is rare, and a strange quark, once produced, should typically survive during the entire collision. In any physics problem, these types of conserved quantities are highly valued because of the constraints they impose on possible dynamical solutions. At the energies studied in this thesis, strangeness creation is above threshold, but not vastly so, making its production sensitive to the dynamics of the collision, which makes its study quite valuable in relativistic heavy-ion physics.

One of the first predictions of novel behavior in relativistic heavy ion collisions was made by

Rafelski [RM82], who hypothesized that if a quark-gluon plasma were produced, it would lead to the enhanced production of $s\bar{s}$ pairs, which in the final state appear mainly as Λ 's, Σ 's, and K and ϕ mesons. The enhanced production of strangeness, measured via the K/π ratio, was an early and exciting observation made by our own collaboration [A⁺90], raising some hopes that the QGP had been discovered. However, following the shouts of “Eureka!” were others of “Not so fast. . .”, as further work, both experimental and theoretical, has led to a deeper appreciation of the complexity of heavy ion collisions at these energies. It may be possible to account for the strangeness production seen in a scenario devoid of QGP, but with a large degree of reinteraction among the produced particles. Strangeness production can therefore serve as a probe of the complicated dynamics of a collision since cooperative processes among the particles may be able to affect the rate at which strangeness is produced and how that produced strangeness is reflected in the final particle abundances.

The issue of strangeness production has evolved into a detailed question of production rates and interaction cross sections. It is possible that the strangeness production that is measured is a naturally synergistic process due to the interaction of produced particles in the dense nuclear environment of a collision. It is also possible that the level of strangeness production that is seen suggests that the QGP is being formed. What is clear is that there is little hope of addressing these questions without solid, comprehensive data. Because the system of hot and dense matter created during a collision is so transient, the rates of many different particle production processes play an important role in determining the final outcome of the collision.

Sophisticated models that follow the trajectories of individual hadrons have been developed and used for simulating these collisions over the last ten years. These models are not rigorous implementations of QCD, but are “QCD-inspired”, attempting to embody some key features of the real theory, while properly conserving energy, momentum, charge and baryon number. Where possible, the experimentally measured cross sections and branching ratios are used to decide the outcome of hadron-hadron collisions. At higher energies, most models turn to some type of a string formalism, where q - q interactions form a color flux tube which subsequently fragments as q - \bar{q} pairs tunnel out of the vacuum. One such model, Relativistic Quantum Molecular Dynamics (RQMD), has been widely used to simulate nuclear collisions and to investigate the production of particles and the space-time development of the collision [SSG89].

This thesis will add considerable new data on strangeness production for heavy ion collisions at an energy of 14.6 GeV per nucleon. In particular, the yields of positive and negative kaons have been measured over a very broad range in kinematic variables. These yields have been determined in concert with several different measures of event topology, allowing one to study the variation of the yields for different event classes. In addition, the measurements of kaon production will be compared to RQMD, a widely-used model of relativistic heavy ion collisions, and the extent to which the model reproduces the data will be examined. The contributions of different processes to the production of kaons will then be investigated, and a physically reasonable picture of strangeness production will be developed. In the next few sections, a brief overview of the experiment and its immediate predecessor will be given, and the kinematic variables central to the analysis will be defined. These definitions will allow the description of the goals of this thesis in the final section of this chapter to be recast in an appropriately precise language.

1.1 Kinematic Variables

Because of the high energies involved in these collisions, it is convenient to use kinematic variables with simple Lorentz transformation properties. The quantities which will be important in this thesis are rapidity, momentum, transverse momentum and transverse mass, and a particularly clear presentation of these variables may be found in an article by Ole Hansen [Han90].

Figure 1-1 shows the coordinate system which will be used to describe the collisions. Conventionally, the z axis is parallel to the beam direction, the y axis points vertically, and the x axis is defined so that the coordinate system is right-handed, $\hat{x} = \hat{y} \times \hat{z}$. Now consider a particle of mass m and moving with total momentum p . Its momentum vector may be decomposed into components parallel and perpendicular to the beam direction, p_{\parallel} (or p_z) and p_{\perp} (often written p_t). In terms of the coordinate system in the figure these may be written as

$$p_{\parallel} = p \cos \theta \tag{1.1}$$

$$p_{\perp} = p \sin \theta = \sqrt{p_x^2 + p_y^2} \tag{1.2}$$

The transverse mass is often used to characterize the distribution of particles perpendicular to the

1.1. KINEMATIC VARIABLES

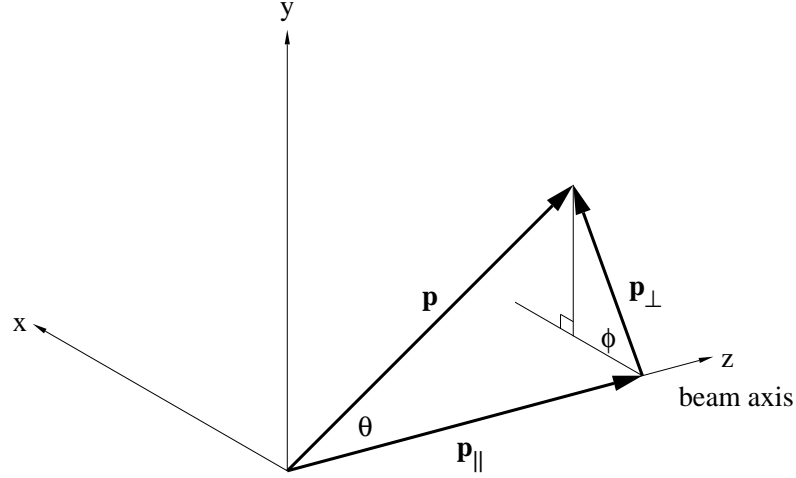


Figure 1-1: Coordinate system definition

beam direction, and it is defined as

$$m_{\perp} = \sqrt{p_{\perp}^2 + m_0^2} \quad (1.3)$$

where m_0 is the rest mass of the particle. Often, the rest mass is subtracted, and the quantity $m_{\perp} - m_0$ (sometimes called the transverse kinetic energy) is plotted.

Rapidity is the relativistic analog of longitudinal velocity, and is defined as¹

$$y = \frac{1}{2} \ln \frac{E + p_{\parallel}}{E - p_{\parallel}} = \tanh^{-1} \beta_{\parallel}, \quad (1.4)$$

where β_{\parallel} is the component of the velocity parallel to the beam direction. For boosts along the beam direction, rapidity undergoes Galilean transformations. If a particle has rapidity y_0 in a frame S , its rapidity measured in a frame S' moving with rapidity $y_{S'}$ with respect to frame S is just $y' = y_0 - y_{S'}$. This means that intervals in rapidity are invariant, and so any quantity histogrammed as a function of rapidity retains its shape under longitudinal boosts, only shifting the location of the

¹Unfortunately, y is used as the symbol of both rapidity and one of the coordinate axes. Context should make clear which is meant.

origin. Several relationships among energy, momentum and rapidity are quite useful

$$E = m_{\perp} \cosh y \quad (1.5)$$

$$p_{\parallel} = m_{\perp} \sinh y. \quad (1.6)$$

1.2 General Features of Nuclear Collisions

There are two ideas which form the basis for much of the discussion of heavy-ion collisions. The first is that nuclear cross sections are largely determined by the geometry of the collision. This is a point that is taken for granted among heavy-ion physicists, but is often not made explicit when addressing those outside the field. The second point is that there is assumed to be a rough mapping between the final rapidity of a particle and its production point in the collision.

At 14.6 A·GeV/c, the deBroglie wavelength of a nucleon is ~ 0.1 fm, and the deBroglie wavelength of a whole nucleus is correspondingly smaller. This scale is small compared to the typical internucleon separation of ~ 2 fm in a nucleus, and it is small compared to the range of the strong nuclear force. Because of this one can talk of a well defined impact parameter for a collision. The total cross section for the collision of two nuclei is very nearly given by the sum of their radii,

$$\sigma_{tot} \approx \pi(r_p + r_t)^2 \approx \pi(1.2A_p^{1/3} + 1.2A_t^{1/3})^2, \quad (1.7)$$

where r_p and A_p are the projectile radius and mass number; r_t and A_t are the identical quantities for the target. In a collision, the nucleons that are in a direct line to be struck by nucleons in the other nucleus are called *participants*. The remaining nucleons are *spectators*. In very peripheral collisions, most of the projectile nucleons continue travelling straight ahead, leading to a strong correlation between impact parameter and the forward going energy. In a more central collision, less energy continues forward and is instead converted into particle production and generating transverse momentum. Because of this, the multiplicity and forward energy (or impact parameter) are inversely correlated. This leads to terminology in which events with high multiplicity or small forward energy are central events and those with small multiplicity or large forward energy are peripheral events.

The correlation between rapidity and production point is a little less straightforward. At very

1.3. BNL-AGS EXPERIMENT 859

high energies, the rapidity distribution of produced particles in p-p collisions is known to divide into three regions: two fragmentation regions approximately 2 units of rapidity wide near the rapidities of the initial protons, and a broad plateau of particle production in the central rapidities between the fragmentation regions. One physical picture underlying this observation is that the collision of two nuclei results in a hot, elongated volume in which the rapidity, y , and the longitudinal position in the volume are directly correlated, $y \propto z$ [Bjo83]. In this picture, high rapidity particles in the forward fragmentation region are created surrounded by other projectile particles, but far away from the target particles. At lower energies, the separation into these three regions is not so clean, and there is a fair amount of mixing in rapidity. Nonetheless, one still talks of the *target region*, the *projectile region* and the *central region*. To set the scale, a resonance decay like $\Delta(1232) \rightarrow N\pi$ generates a rapidity difference of up to 1.5 units between the nucleon and the pion. Particles separated by much more than that are unlikely to be causally related.

1.3 BNL-AGS Experiment 859

The data for this thesis was collected by the E802 Collaboration (see Appendix I) as part of Experiment 859 (E859) at the Brookhaven National Laboratory Alternating Gradient Synchrotron (BNL-AGS). E802, the immediate ancestor of the current experiment, was one of the first round of experiments designed to take advantage of the coupling of the Tandem Van de Graaff heavy-ion facility with the AGS to look at the characteristics and properties of relativistic heavy-ion collisions. The apparatus of the original experiment, which has remained basically whole through E859, consists of a large acceptance (~ 25 msr) single-arm magnetic spectrometer containing several precision tracking chambers capable of $150\text{--}200\text{ }\mu\text{m}$ intrinsic position resolution, a time-of-flight wall (TOF) with ~ 100 ps timing resolution, and event characterization provided by a target multiplicity array (TMA), a zero-degree calorimeter (ZCAL) and a lead-glass array to measure transverse neutral energy. During E802, collisions of beams of ^{16}O and ^{28}Si accelerated to 14.6 GeV/c per nucleon ($\text{A}\cdot\text{GeV/c}$) and incident on targets of ^{27}Al , ^{63}Cu and ^{197}Au were studied.

As a first generation experiment, E802 was designed to provide a broad survey—it would have been difficult to plan for a precision experiment when few concrete facts about the environment of a relativistic heavy ion collision were known. Fundamental quantities such as particle multiplicity

distributions were unknown, and predictions seemed to vary considerably. The early design for the E802 track reconstruction program anticipated events commonly having 20 tracks in the spectrometer, though as it has turned out, this was perhaps a factor of ten more than was actually seen. In any case, a survey experiment was the appropriate thing to plan for in the early days of the field. The E802 spectrometer was designed with good momentum and timing resolution, and consequently, good particle identification capabilities. It was designed to map out the distributions of abundant hadrons over a large region of phase space. Global features of A-A collisions at these energies, such as charged particle multiplicity, transverse and forward energy distributions were measured. Inclusive and semi-inclusive spectra for π^\pm , K^\pm , and protons were measured, as were two-particle correlations for pions and protons.

One of the most startling observations seen during E802 was a significantly higher K^+/π^+ ratio in A-A collisions as compared to p-p collisions at similar energies [SSS87]. Over a rapidity interval of $1.2 < y < 1.4$, the K^+/π^+ in central Si+Au was found to be $(19.2 \pm 3)\%$; the K^-/π^- for the same system was found to be $(3.6 \pm 0.8)\%$. Both the formation of a quark-gluon plasma and hadronic rescattering were put forth as possible explanations. Though private analyses were somewhat more daring, the official publication reporting the results showed only three (3) dn/dy points for the kaons. The yields of K^+ appeared to increase toward the target rapidities, consistent with a scenario of K^+ production dominated by the processes $NN \rightarrow NYK^+$ and $\pi N \rightarrow YK^+$, where Y is one of the hyperons, Σ or Λ . No trend in the yields of K^- as a function of rapidity were discernible. At the 1σ level, the slope parameters of exponential fits to the transverse mass spectra for K^+ and K^- were consistent with one another. An aggressive analysis of the E802 data by Charles Parsons amplified on these collaboration-approved results [Par92]. Several more dn/dy points for both K^+ and K^- were reported and the transverse mass slope parameters of the K^+ seemed to be consistently higher than those for the K^- .

These, and other, experimental results seen by E802 led to the proposal of E859 whose goals included providing:

“a comprehensive body of data on inclusive (π , K, p, d) and two-particle correlations ($\pi\pi$, K^+K^+ and pp) from which may emerge systematic trends which will give insight into the formation of high density nuclear matter, its subsequent space-time evolution, source kinematics, and possible thermodynamic properties [A⁺89].”

1.3. BNL-AGS EXPERIMENT 859

The experimental apparatus for E859 consisted of the E802 spectrometer, augmented with two new wire trigger chambers and an online trigger based on particle identification to improve the selectivity of the experiment for rare events.

1.3.1 A Second-Level Veto for Rare Events

Given the limited beam time available for the experiment, one would like to increase the intensity of the beam to increase the collection rate of rare events. Several of the high intensity heavy ion experiments at BNL can use as much silicon beam as the AGS can deliver, about 10^9 particles/spill. However, there are limits in any experiment that keep one from increasing the beam rate indefinitely. In E802, the primary limitation was the data acquisition system, which was able to write about 100 events to tape per AGS beam pulse. During E802, a typical beam rate of 10^5 particles per spill incident on a 1% target would generate 10^3 interactions per spill. A high multiplicity trigger (TMA trigger) could reduce this rate to about 100 events/spill, the maximum allowable. Table 1.1 shows the abundances of some rare events per TMA trigger. Even with the TMA trigger, it would be difficult to collect the statistics needed for an adequate analysis of the kaons. Of course, using

Event Type	Abundance/TMA trigger
K^+	0.026
K^-	0.005
$\pi^+ \pi^+$	0.010
$\pi^- \pi^-$	0.017
$K^+ K^+$	2.5×10^{-4}

Table 1.1: Particle abundances per TMA trigger. Taken from E859 proposal [A⁺89].

the TMA as a trigger automatically biases the data sample toward high multiplicity events, which makes it difficult to study the variation in yields as a function of event multiplicity. To make such studies possible, E802 used a spectrometer trigger (SPEC trigger) made up of a coincidence of signals taken from scintillators near the front and near the rear of the spectrometer. Selecting events using the SPEC trigger improves the odds that the event actually contains a track. SPEC is far from perfect, however, and many SPEC-triggered events contain no tracks at all.

To improve the selectivity of the experiment for rare events, E859 has added a flexible, com-

puterized second-level (LVL2) veto to the SPEC trigger. In the $40\ \mu\text{s}$ between the generation of a SPEC trigger and the time when the data acquisition begins to read out the detectors, the LVL2 veto searches the event for straight-line coincidences of hits in two new wire trigger chambers and the segmented time-of-flight wall. This improves on the SPEC trigger by rejecting events that don't actually contain tracks. The veto hardware can also use a fast digitization of the time-of-flight and a calculation of the momentum to assign a rough mass to the track, allowing it to veto events based on the number and type of identified particles in the event. The construction and operation of the LVL2 veto will be described in more detail in Section 3.5.

1.4 Goals of this Thesis

The energy of the heavy ion beams used in the AGS program results in a system of very high baryon density. The rapidity of the beam is 3.4 units, so in the picture of a nuclear collision described in Section 1.2, the target and projectile fragmentation regions overlap with the central region. This means that the particles in collisions at the AGS are created in an environment crowded with other baryons and hadrons. In symmetric collisions, the baryon density is highest around mid-rapidity. In asymmetric collisions, with a large target and small projectile, the density peaks more toward the target rapidity. Because of the channel $\pi Y \rightarrow N K^-$, one would expect that the K^- production would be associated with regions of high baryon density. On the other hand, the large inelastic cross section of K^- in nuclei means that they will interact strongly in these same regions. The presence of the associated production channel $NN \rightarrow N \Lambda K^+$ means that the K^+ production should also be correlated with the baryon density.

To try and unravel these tightly correlated production mechanisms, the variation in the K^+ and K^- yields and slopes as a function of rapidity will be examined. Keeping in mind the variation of the baryon density as a function of rapidity, the possible contribution of different processes will be investigated. This will be carried further by comparing the output of the RQMD model with the data.

- The first task is to characterize kaon production, in particular K^- production, in Si+Al and Si+Au, as completely as possible, over as large a range in rapidity and transverse momentum as possible. The m_\perp slope parameter and the yield as a function of rapidity will be determined.

1.4. GOALS OF THIS THESIS

- Using the TMA, several multiplicity cuts on the data will be made and the systematic variation in the data as a function of these cuts will be examined.
- Using the ZCAL energy as a measure of the number of projectile participants, N_{part}^{proj} , the average and rms of N_{part}^{proj} for the different TMA cuts will be determined. This will allow a characterization of the kaon yields as a function of N_{part}^{proj} .
- A detailed examination of a widely used model of heavy-ion collisions (RQMD) will be made to see how well it is able to reproduce the features of the kaon data. The wide range of the present measurement will place severe constraints on any model which purports to reproduce strangeness production.
- Using RQMD, the sources of kaon production will be examined. The contribution of the different mechanisms contributing to kaon production will be examined as a function of rapidity, and the change in the relative importance of different mechanisms will be examined as the event selection is varied.

CHAPTER 1. INTRODUCTION

Chapter 2

Strangeness in Heavy Ion Collisions

This chapter discusses some of the experimental and theoretical results relevant to the present work. A discussion of strange particle production, in particular various mechanisms for the production of K^+ and K^- , are examined. An overview of some relevant experimental results is also shown. The reader interested in further details should consider consulting the Quark Matter and HIPAGS series of conference proceedings.¹

2.1 Theoretical Background

The orientation that will be taken in this section is to look at two extremes relevant to heavy-ion collisions, and argue that we are somewhere in the middle. The first part of this process is to examine strangeness production in an equilibrated system, made of either deconfined quarks and gluons or a hierarchy of hadrons and their excited states. It is not believed that such a large-scale equilibrated system is actually achieved in relativistic heavy-ion collisions at AGS energies, but it provides a limiting case against which we can compare the E859 results. The other part of the process is to examine strangeness production in heavy-ion collisions at much lower energies, where strangeness production is below threshold in individual nucleon-nucleon collisions. Seeing strangeness production under these conditions, one can be confident that some form of collective process is playing a role. In particular, models of strangeness production at 1–2 GeV per nucleon,

¹As the field is still quite volatile, G. Stephans has suggested that reverse chronological order may be the best plan for approaching the literature.

usually have to include the Δ resonance as a way of building up sufficient energy in subsequent collisions to produce enough strange particles to explain the data.

The extrapolation to the energy regime midway between the two extremes described above takes the form of arguing that even though we may not be in a situation where enough collisions take place to equilibrate the system, the consideration of particle reinteractions is important. At the same time, the energies involved at the AGS make it unlikely that the Δ is the only resonance of consequence in the collision. In particular, hadronic resonances may play a large role as facilitators of strangeness production and in redistributing the created strangeness among different particle species. For a detailed reference, a good review of the physics of strangeness production in heavy-ion collisions may be found in an article by Koch [Koc90].

2.1.1 Strangeness in the Quark-Gluon Plasma and Hadron Gas

Consider a large, long-lived volume of quark-gluon plasma with nonzero baryon number density, but zero net strangeness. As stated above, this is not expected to be created in Si+Al and Si+Au collisions at AGS energies, but it is a place to begin the discussion. In such a system, the number of strange and antistrange quarks present will be completely determined by thermodynamic considerations. Very few parameters are needed to describe the state of the equilibrated plasma—just the temperature, T , and light quark and strange quark chemical potentials, μ_q and μ_s . By assumption, there are already u and d quarks about, and it costs energy in addition to the mass of the $q\bar{q}$ pair to add any more to the system, since the new quark must be added at the top of the Fermi sea. In a system dense with light quarks, it becomes energetically favorable at some point to begin producing $s\bar{s}$ pairs. To add $s\bar{s}$ pairs, one must pay the larger energy cost of the strange quark mass, but there is no Fermi energy to overcome initially. Using a spin and color degeneracy $g_s = 6$, the mass of the strange quark m_s and the temperature T , the density of strange quarks can be derived in the grand canonical ensemble [Koc90]:

$$\rho_s = g_s \frac{T^3}{2\pi^2} \left(\frac{m_s}{T} \right)^2 K_2 \left(\frac{m_s}{T} \right) \quad (2.1)$$

The combination $x^2 K_2(x)$ varies fairly slowly, from 2.0 when $x = 0$ to 1.0 when $x = 2$, so the density is much more sensitive to the absolute temperature than to the combination m_s/T . Putting in $T = 160 \text{ MeV}$ and $m_s = 150 \text{ MeV}/c^2$ gives a density of about 0.5 strange quarks (and an equal

2.1. THEORETICAL BACKGROUND

number of strange antiquarks) per fm^{-3} .

Once these strange quarks are created, they manifest themselves in the final state particles when the QGP begins to hadronize. At this point, the difference in the abundance of K^+ and K^- may arise because of kaon distillation. The quark content of a K^+ is $u\bar{s}$, that of a K^- is $\bar{u}s$. In a QGP with large positive baryon number, the \bar{s} quark can readily find a u quark to form a K^+ . An s quark can also find u and d quarks to form a Λ . But, it is more difficult for the s quark to find a \bar{u} quark to form a K^- [Nag91]. Not only does this reduce the number of K^- 's produced, but on average it delays their production until later in the evolution of the plasma to a time when it will also have cooled somewhat. Therefore, one would expect a difference in the transverse slopes as well as the abundances.

In a hadron gas, the argument proceeds similarly, except there is an additional constraint on the production of strangeness, because no open color is allowed. Therefore, strangeness production must proceed through the creation of colorless hadronic states. The lightest strange hadrons are the kaons, and when the baryon number density becomes large enough to make the creation of strangeness energetically favorable, the kaons will be among the first particles created. Using Equation 2.1, but with the change $m_s \rightarrow m_K$ where m_K is the mass of a kaon, $494 \text{ MeV}/c^2$, one expects about 0.15 strange quark per fm^{-3} for a system with a temperature of 160 MeV.

In a thermally equilibrated system, there is no reason to expect any difference in the K^+ and K^- spectra. However, several authors have proposed that interactions of the kaons with pions and nucleons can result in an effective mass in dense hadronic matter that is different than the free space mass of the kaon [Gon92, KWXB91, FK BK93]. The change in the mass of the K^+ is usually given by

$$m_K = m_K \left(1 - \frac{\rho_B}{\rho_c} \right)^{1/2} \quad (2.2)$$

where ρ_B is the baryon density and ρ_c is a critical density which is estimated to have a value [FK BK93]

$$2.5\rho_0 < \rho_c < 5\rho_0. \quad (2.3)$$

The medium has the opposite effect on K^- raising its effective mass because of a net attractive force between the K^- and nucleons. The result of these changes in the kaon masses is to make the K^+ more abundant than the K^- and to give it a higher average transverse kinetic energy.

2.1.2 Strangeness Production in Real Collisions

In a system created through the collision of two nuclei, the limited lifetime of the hot and dense system that is formed adds another dimension to the problem. Even if one expects an appreciable amount of strangeness to be present in the equilibrated case, a real A-A collision may not result in a system that exists long enough to fully populate the available phase space. In 1982, Rafelski and Müller proposed that enhanced strangeness production might therefore be a signal of the creation of a quark-gluon plasma in a heavy-ion collision [RM82]. Their reasoning was that strangeness creation at the parton level, especially the process $gg \rightarrow s\bar{s}$, proceeds quite rapidly, and during the brief lifetime of the plasma state, these processes would be able to bring the strange quark population close to the asymptotic value expected from thermodynamic considerations.

If one avoids making the assumption that the QGP is formed and therefore hastens the approach to equilibrium, one is forced into a much more complex situation where the rate of strangeness production, not just its equilibrated value, plays a large role in determining what is seen in the final state. Handling the introduction of the dynamics into the problem makes this a complicated quantum many-body problem—in general, an intractable mess. This is where microscopic models play a role in understanding these collisions. At AGS energies and below, the most common type of microscopic model is a *hadronic cascade*. The ingredients in such a model are typically some subset of the known hadrons, and a table of interaction cross sections, σ . Each particle is propagated forward in time until it approaches within a distance $d = \sqrt{\sigma/\pi}$ of another particle. When this happens, a collision occurs, and the known branching ratios are consulted to decide the outcome of the collision. By explicitly following the particles created during a collision, the issue of the rate dependence of strangeness is built into the model.²

At energies of $\sim 1\text{--}2\text{ GeV}$, strangeness production is below threshold, and therefore requires collective interactions of several nucleons for significant production. In a paper by Koch [KD89], an estimate is made of the production of K^+ and K^- using a model in which nucleons and Δ 's are in thermal and chemical equilibrium. There are no pions in the model, as they are assumed to come from decay of the Δ 's at a very late stage in the collision. If Δ 's are eliminated from the model, it under-predicts the K^-/p ratio by nearly a factor of 10. The reason that the Δ helps in

²A list of some of the relevant strangeness creation processes will be presented in Section 2.2.3.

2.1. THEORETICAL BACKGROUND

the production of K^- is twofold: its mass brings more energy into collisions with other nucleons making the relatively expensive kaon pair production more likely, and its spin and isopin are greater than a nucleon which provides more equivalent channels for the production to proceed through. In a paper by Ko [Ko83], an explanation of the observed K^- yields is made in a model which does not include Δ 's but does include hyperons. These particles make strangeness exchange reactions like $\pi Y \rightarrow NK^-$ possible. This model claims to account for a large fraction of the K^- production.

For collisions at AGS energies an intermediate scenario is probably more relevant. The time scale of a real collision is short enough that complete equilibrium, chemical or thermal, is probably not reached. While effects such as chiral restoration, or effective kaon masses may play some role, it is almost certainly true that the effect of resonances is quite important in creating and redistributing strangeness. In π -nucleus interactions, for instance, it is essential to include the role of the Δ resonance to explain the data.

For the present study, it is important to know how far away in rapidity a source of kaons could be and still contribute to the kaon yields at a particular point in rapidity. In the decay of a hyperon resonance into a K^- and a nucleon, some mixing in rapidity is possible.³ For a two-body decay in the rest frame of the decaying particle, the energy of the daughter particles is divided according to [Gro90]:

$$E_1 = \frac{M^2 - m_2^2 + m_1^2}{2M}. \quad (2.4)$$

If we look at an ensemble of randomly oriented decays, the rapidity density of one of the daughters is given by

$$\frac{dn}{dy} = \frac{dn}{d(\cos \theta)} \left| \frac{d(\cos \theta)}{dy} \right|. \quad (2.5)$$

Using one of the many definitions of rapidity to calculate the Jacobian gives

$$y = \frac{1}{2} \ln \left(\frac{E + p \cos \theta}{E - p \cos \theta} \right) \quad (2.6)$$

$$\frac{dy}{d(\cos \theta)} = \frac{p/E}{(1 + \frac{p}{E} \cos \theta)(1 - \frac{p}{E} \cos \theta)} = \frac{p}{E} \cosh^2 y. \quad (2.7)$$

³This derivation of the rapidity spread of the daughter products of a decay borrows from a very similar calculation done by Charles Parsons in studying the rapidity mixing of pions from $\Delta(1232)$ decays.

CHAPTER 2. STRANGENESS IN HEAVY ION COLLISIONS

Substituting this expression into Equation 2.5, and normalizing properly, yields

$$\frac{dn}{dy} = \frac{1}{2 \tanh(\Delta y_{max}) \cosh^2 y} \quad (2.8)$$

where Δy_{max} is the maximum rapidity throw of the daughter particle being considered. This maximum is completely determined by the Q of the decay. The shape of the rapidity density is independent of the Q of the decay; only the kinematic limits depend on it. Taking $\Lambda(1520) \rightarrow N\bar{K}$ as an example, the maximum rapidity throw of the K^- is $y_{\bar{K}} = 0.43$, and the distribution in rapidity is shown in Figure 2-1.

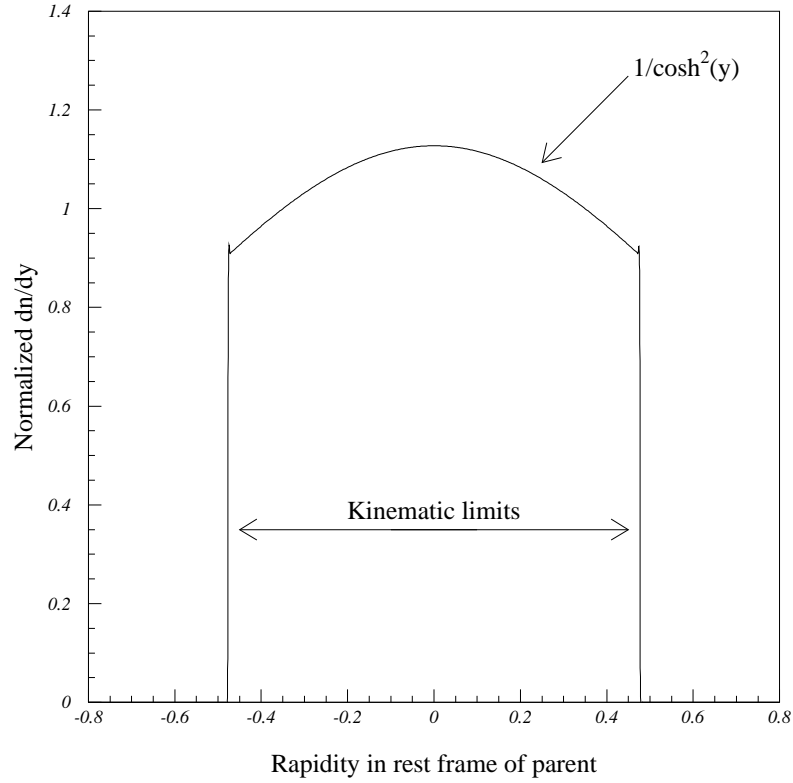


Figure 2-1: Rapidity density of a daughter in a two-body decay.

2.2. EXPERIMENTAL BACKGROUND

2.2 Experimental Background

If we imagine the development of a nucleus-nucleus collision as a hadronic cascade, there are two important ingredients. First, how and where is strangeness created? We can turn to p-p data for a partial answer to this. And then, how is strangeness redistributed and affected by subsequent collisions in the cascade. For this, we can get some idea by looking at the cross sections of strange particles with nucleons.

2.2.1 Strange Particle Production in Proton-Proton Collisions

There is some p-p data from experiments conducted around the AGS energy of 14.6 GeV, and we can turn to this data to find the kaon production cross sections and to see how these particles are distributed in rapidity. A useful overview of strangeness production in p-p collisions can be found in Brian Cole's thesis [Col92]. There are a few channels available for producing kaons in p-p collisions. Some of these are:

$$pp \rightarrow ppK^-K^+ \quad (2.9)$$

$$pp \rightarrow ppYK^+ \quad (2.10)$$

Here, Y indicates one of the hyperons, Λ ($m = 1116 \text{ MeV}/c^2$) or Σ ($m = 1189 \text{ MeV}/c^2$).

In an experiment by Fesefeldt *et al.*, strangeness production in p-p collisions at 12 and 24 GeV was measured, and Figure 2-2 shows $d\sigma/dy$ in the center of mass system normalized to the total two particle strangeness production cross section. At both 12 and 24 GeV, the process $pp \rightarrow KYX$ has a much larger cross section than the process $pp \rightarrow K\bar{K}X$. The K^- is only produced in the second of these processes, so there are many fewer K^- than K^+ at these energies. Taking the 12 GeV data, the ratio of the cross sections at mid-rapidity ($y^* = 0$) for the K^+ and the K^- is a factor of between 4 and 5 (note the breaks in the vertical scale in the figure). The large difference occurs primarily because of the difference in the thresholds of the two reactions.

Also note that at 12 GeV, the Λ rapidity distribution is roughly similar to the K^+ . Where the K^+ yield is peaked at mid-rapidity, the Λ distribution is more or less flat for a unit of rapidity about $y^* = 0$, but the differences between the two are typically no more than 15–20%. This is no longer true at 24 GeV, where the Λ peak has clearly moved away from mid-rapidity, while the K^+ still has

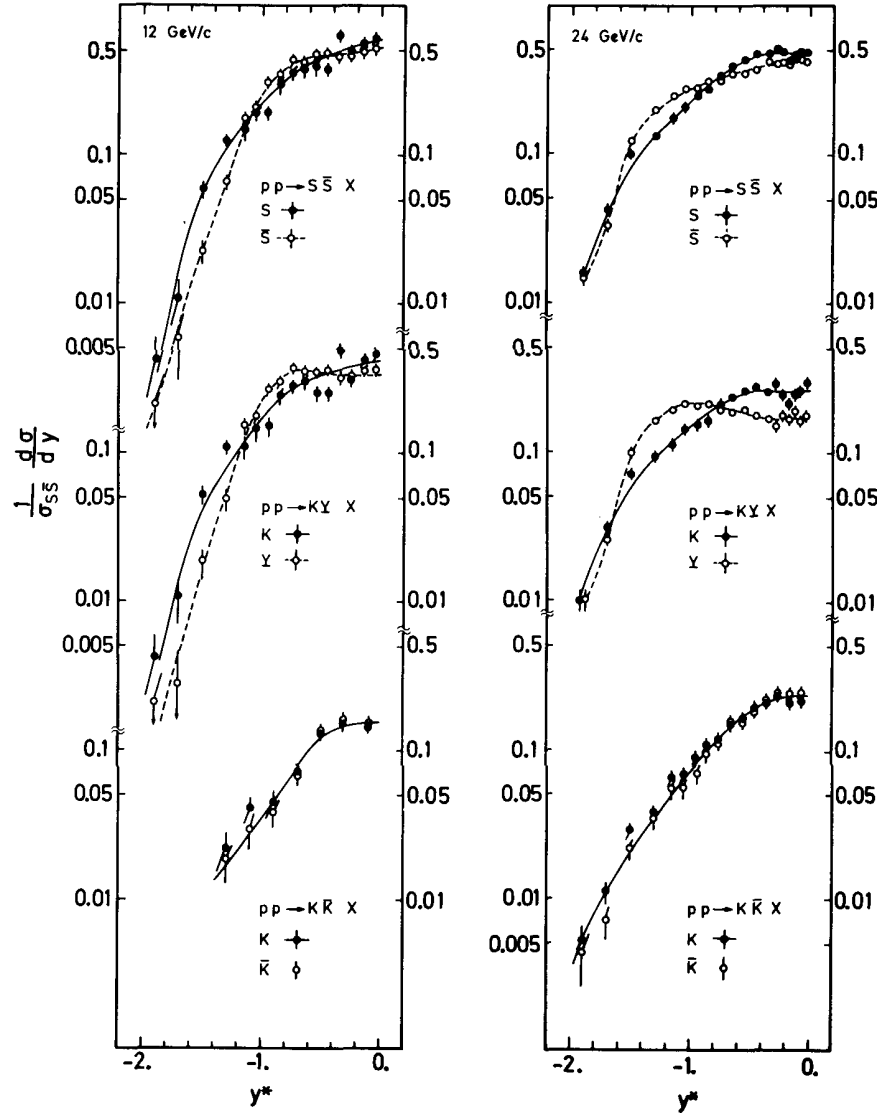


Figure 2-2: Rapidity distribution in the c.m.s. of strange particles in p-p collisions [F⁺79].

2.2. EXPERIMENTAL BACKGROUND

a maximum there. The degree of similarity between the Λ and K^+ rapidity distributions is shown in Figure 2-3, taken from the same paper. The upper right panel in the figure shows the normalized

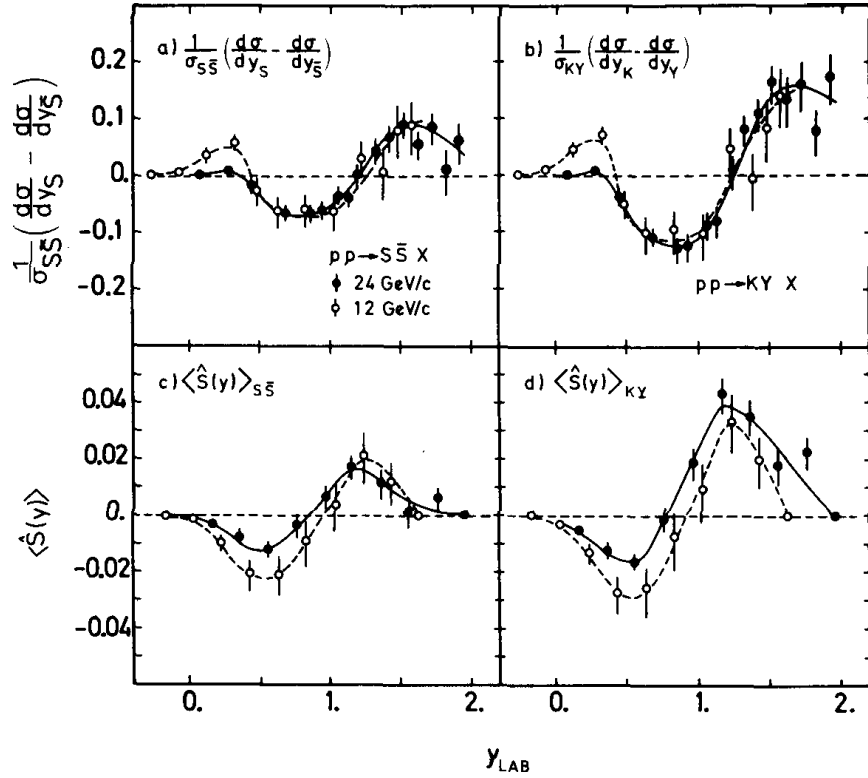


Figure 2-3: Laboratory rapidity distribution of net strangeness in p-p collisions [F⁺79].

difference between the kaons and hyperons from associated production. In this figure, the rapidity is measured in the laboratory system. The kaons are peaked at mid-rapidity, while the hyperons are fairly flat for about 0.5 unit of rapidity about mid-rapidity.

2.2.2 Interactions of Strange Particles with Nucleons

In moving from p-p to p-A and A-A collisions, it becomes important to know what happens to kaons and other strange particles in their interaction with nucleons. Figures 2-4 and 2-5 show the total and elastic cross sections for positive and negative kaons incident on protons. These are compilations of data taken from the particle data book [Gro90]. There are several features in each figure that are worth noting. First is the energy scale of the cross section. A nucleon-nucleon collision at a beam energy of 14.6 GeV corresponds to a \sqrt{s} of 5.4 GeV. Interactions among secondaries take place at

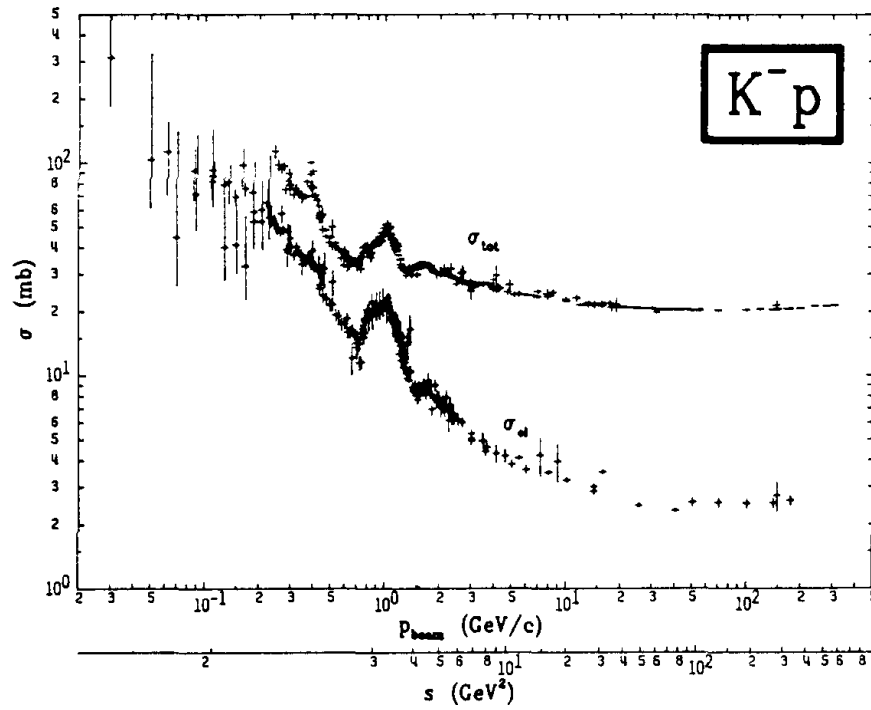


Figure 2-4: K⁻p cross section total and elastic cross section as a function of incident momentum and as a function of s [Gro90].

2.2. EXPERIMENTAL BACKGROUND

lower energies than this as the initial beam energy is dissipated in particle production and rapidity loss. The kaons detected in the spectrometer have a typical energy between 500 MeV and 1 GeV, putting them right in the range of some interesting features in the cross sections. For the K^+ , this energy is near a threshold below which nearly all of the inelastic cross section disappears. Below about $s = 3 \text{ GeV}^2$, the inelastic cross section falls to just a few mb, while the total cross section levels out at 10–20 mb. For the K^- , the inelastic cross section does not drop as the energy decreases, instead it rises to 30–40 mb for interactions with $s = 2 - 3 \text{ GeV}^2$. There is a resonant interaction in the $K^- p$ system between $s = 3 - 4 \text{ GeV}^2$. There are several hyperon resonances in this energy region, providing a large cross section for reactions such as $\pi Y \leftrightarrow Y^* \leftrightarrow NK^-$. The $K^+ p$ and the

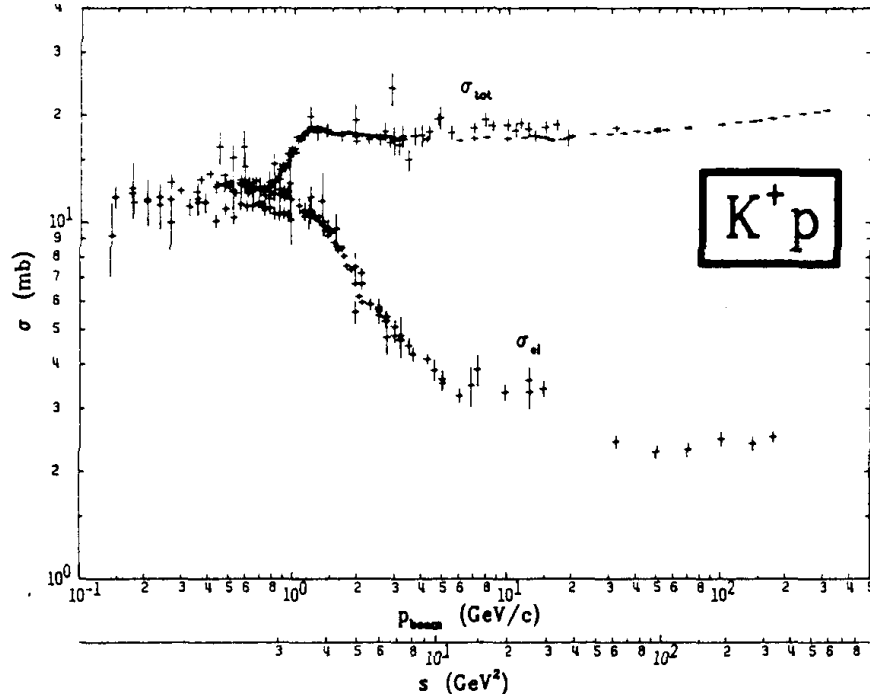


Figure 2-5: $K^+ p$ cross section total and elastic cross section as a function of incident momentum and as a function of s [Gro90].

$K^- p$ total cross sections differ by perhaps a factor of two. The mean free path of a K^+ in normal nuclear matter is about 4 fm; for a K^- it is closer to 2 fm. Therefore, for kaons emitted at the center of a gold nucleus 7 fm in radius, the outside world is 1–2 mean free paths away.

2.2.3 Strange Particle Production in Proton-Nucleus Collisions

Fortunately for the present work, there are now some very relevant proton-nucleus (p-A) results at AGS energies, taken by our own collaboration [A⁺92a]. A useful summary of hadron production in p-A collisions can be found in the review article by Ziping Chen [Che93]. It has been argued that in the sequence of p-p to p-A to A-A, the real difference comes in going from p-p to p-A collisions, since p-A collisions introduce the possibility of reinteraction for the first time. This means that in addition to the primary production mechanisms discussed in Section 2.2.1, new processes appear, including

$$N\Delta \rightarrow N\Lambda K^+ \quad (2.11a)$$

$$N\Delta \rightarrow NNK^+K^- \quad (2.11b)$$

$$NN^* \rightarrow N\Lambda K^+ \quad (2.11c)$$

$$NN^* \rightarrow NNK^+K^- \quad (2.11d)$$

and there are absorption effects to consider for the K^- 's through processes like $K^-N \rightarrow \pi Y$. Figure 2-6 shows the p-A dn/dy results for a series of systems increasing in size from p+Be to p+Au. It is apparent that the yield of K^+ increases as one goes to heavier systems, and there seems to be a similar trend in the K^- , though the statistics are limited.

2.2.4 Other Nucleus-Nucleus Results

This section will provide a look at strangeness production in other heavy-ion experiments. There are data available at lower energies from experiments at the Bevalac (2.1 A·GeV/c) and from the KAOS experiment at GSI (1.0 A·GeV/c). In addition to the E859 results, there are data on strangeness production at the AGS from E814 (now E877), and E810. At higher energies, there are results from several CERN experiments, NA35, NA36 and NA44.

Because it will be argued later that the reinteraction of Λ 's and Σ 's with pions and other baryons could be a source of K^- 's, it is also important to survey what is known about the properties of these particles in heavy-ion collisions. The production of Λ 's has actually been measured in E859, and results can be found in the thesis work of Ted Sung [Sun94]. For a rapidity slice $1.1 < y < 1.7$, the Λ

2.2. EXPERIMENTAL BACKGROUND

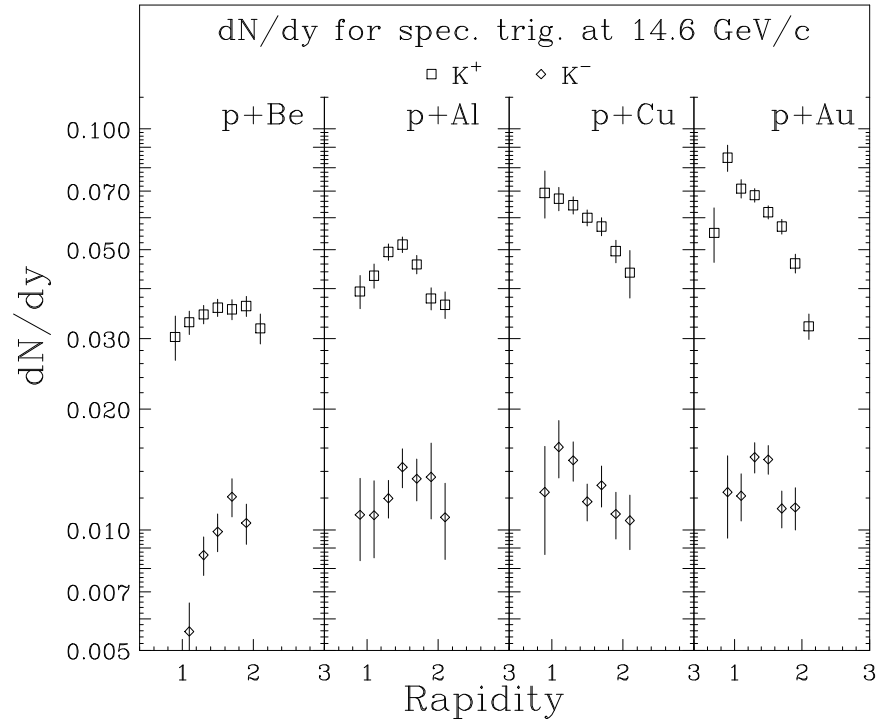


Figure 2-6: E802 p+A dn/dy summary

m_{\perp} distribution is found to be well fit with an exponential in m_{\perp} with a slope of $171 \pm 13 \pm 7$ MeV/c². The Λ dn/dy in this rapidity slice is reported to be $3.85 \pm 0.6 \pm 0.5$. AGS Experiment 810 has also measured Λ production and some of their recent results are shown in Figure 2-7 [SGOO93]. The

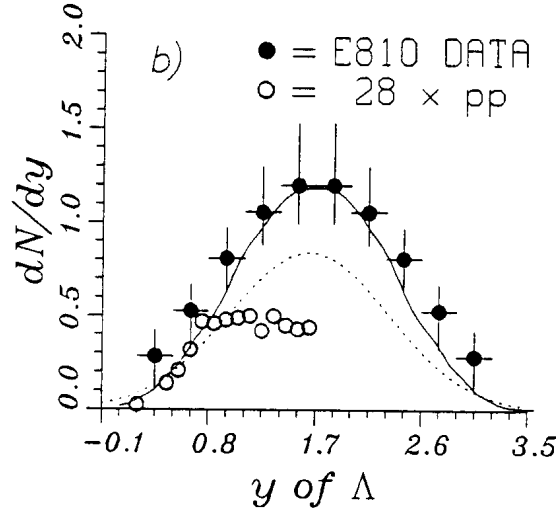


Figure 2-7: E810 Si+Al $\rightarrow\Lambda$ dn/dy . For comparison, a Gaussian fit to the Si+Al $\rightarrow K^+$ dn/dy in E859 has a peak value of 1.25 and a σ of 0.8, very similar to the E810 Λ 's shown here. The complete E859 kaon results are shown in Chapter 5.

most important aspect of the Λ measurements is that their abundance and rapidity distribution are similar to those for the K^+ . Therefore, any process such as $\Lambda\pi\rightarrow NK^-$ which produces a K^- from a Λ will tend to scale the K^- 's with the K^+ 's.

E814 is another heavy-ion experiment at the AGS that has measured charged kaon rapidity distributions. That experiment is designed to measure high rapidity spectra down to zero p_{\perp} . Unfortunately, this gives essentially no acceptance overlap with the E859 spectrometer, so their results are complementary rather than comparable. Figure 2-8 shows some recent results for kaon m_{\perp} distributions in the rapidity range $2.2 < y < 2.6$ presented at the Quark Matter '93 conference [SGOO93]. Intriguingly, the inverse slopes are extremely small, between 10–12 MeV/c². This is to be compared with the ~ 180 MeV/c² measured in central Si+Au in E859 (see Chapter 5). It will be interesting to see if this result holds after further analysis.

There are several heavy-ion experiments at CERN using beams at incident energies of 200 A·GeV/c. One of these experiments, NA44, a focussing spectrometer, has measured yields and slopes for K^+

2.2. EXPERIMENTAL BACKGROUND

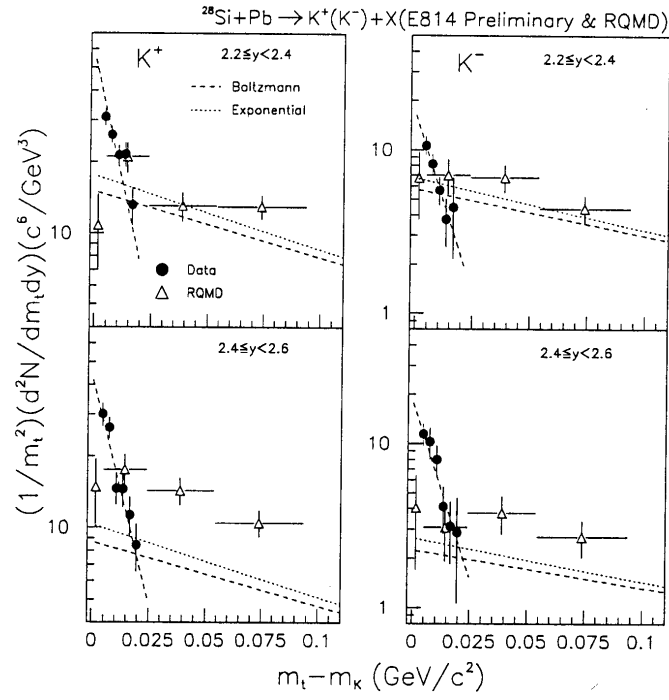


Figure 2-8: Kaon m_{\perp} slopes from E814 [SGOO93]

CHAPTER 2. STRANGENESS IN HEAVY ION COLLISIONS

and K^- in systems ranging from p+Be to S+Pb. At the higher CERN energies, the kaons are not produced in the same high baryon density environment as at the AGS. Also, the higher energy means that the lower threshold associated production of K^+ is not as heavily favored as at the lower AGS energies. In p+Be, the slopes measured for the K^+ and K^- are $165 \pm 10 \text{ MeV}/c^2$ and $145 \pm 10 \text{ MeV}/c^2$, respectively. These slopes rise monotonically with system size to $210 \pm 5 \text{ MeV}/c^2$ and $200 \pm 5 \text{ MeV}/c^2$ for K^+ and K^- in S+Pb, respectively [SGOO93].

Chapter 3

Experimental Description

In this chapter, the experimental apparatus used in this thesis is described. BNL-AGS experiment E859 is a fixed target, single-arm magnetic spectrometer with event characterization detectors and a particle identification trigger. The beam is provided by the Tandem-Booster-AGS complex, a recently upgraded version of the original heavy-ion acceleration system. I will describe these major components of the experiment; briefly where little has changed since E802, and in more detail for those components which are new or have changed significantly.

3.1 The Beam and Target

Before one can study heavy-ion collisions, one needs a beam of heavy ions. Not a particularly deep statement, but true, nonetheless. Although as mere users of the AGS facility we are not directly responsible for the operation of the accelerator, it is, in a very real sense, a part of the experiment: if the AGS still isn't delivering beam, we still aren't taking data¹. Even when the AGS is operating, the quality of the data taking is affected by such things as the time structure of the beam and how well it is steered on target.

The basic layout of the accelerator site is shown in Figure 3-1. The heavy ions are created and initially accelerated in the Tandem Van de Graaff facility and are transported to the main acceleration rings via the Heavy Ion Transfer line (HITL). The ions are next accelerated to 1 A·GeV/c in the Booster, injected into the AGS, accelerated to 14.6 A·GeV/c, and then extracted and sent to the

¹Apologies to Bill Zajc and Clint Black.

experimental areas. With the exception of the HITL and the Booster, the facilities used to generate

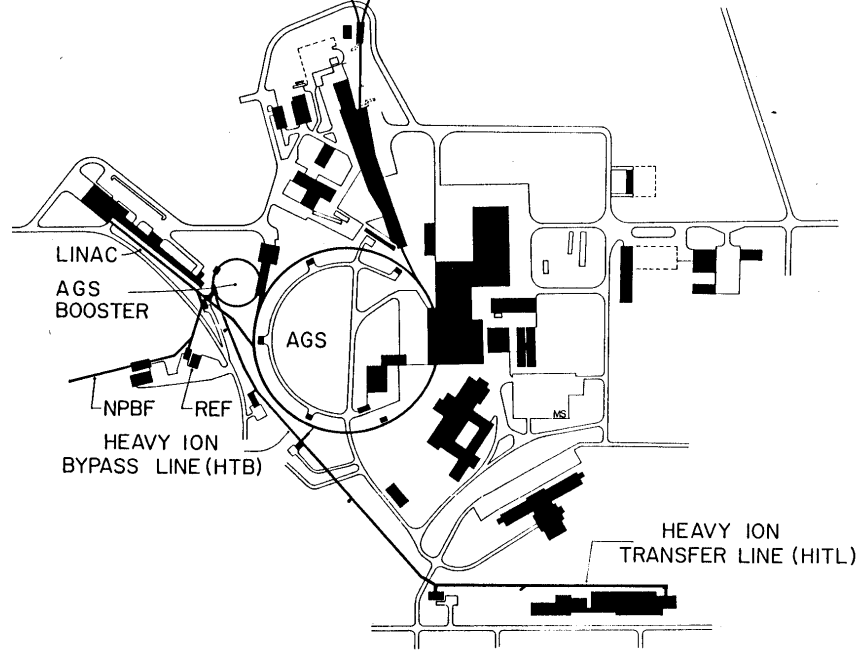


Figure 3-1: Layout of the AGS facility. The source of the heavy ion beam is in the Tandem Van de Graaff building at lower right. The Heavy Ion Transfer Line (HITL) crosses the figure from right to left. The Booster is the smaller ring; the AGS is the larger one. The experimental area is at middle center.

the beams of ions used in the BNL heavy ion experiments were previously existing pieces of equipment. The AGS has been used as a proton accelerator since the 1960s. The Tandem has been used since the 1970's to study several A·MeV heavy-ion reactions. The commissioning of the HITL in 1986 connected the two facilities and allowed the generation of truly relativistic heavy ion beams for the first time. The addition of the Booster is the most significant difference in the beam delivery system since the days of E802, and its impact will be discussed in more detail below.

3.1.1 Beam Production and Acceleration

The beam used in the collisions studied in this thesis consists of $14.6 \text{ A} \cdot \text{GeV}/c$ fully stripped ^{28}Si ions which are produced in a cesium ion sputter source [T⁺ 88]. The source works by heating a small reservoir of cesium, generating vapor which passes a hot tungsten filament and becomes ionized to

3.1. THE BEAM AND TARGET

Cs^+ . An electrostatic potential accelerates the cesium into a target of silicon. When this cesium ion hits the surface it loses an electron to a silicon atom, creating Cs^{++} and Si^- ions. A series of high voltage grids provides the initial acceleration of the silicon ions out of the source to 20 keV [Par88].

The source sits outside a Van de Graaff which is held at a positive potential of 10-15 MV. The negative ions accelerate into this potential well, and at the center is a stripping foil which removes a few of the electrons from the silicon ion, creating a positive ion which is now accelerated out of the Van de Graaff by the same positive potential. As the ion velocity increases, further stripping foils remove additional electrons, finally resulting in a Si^{+8} ion with a kinetic energy of 6-7 A·MeV.

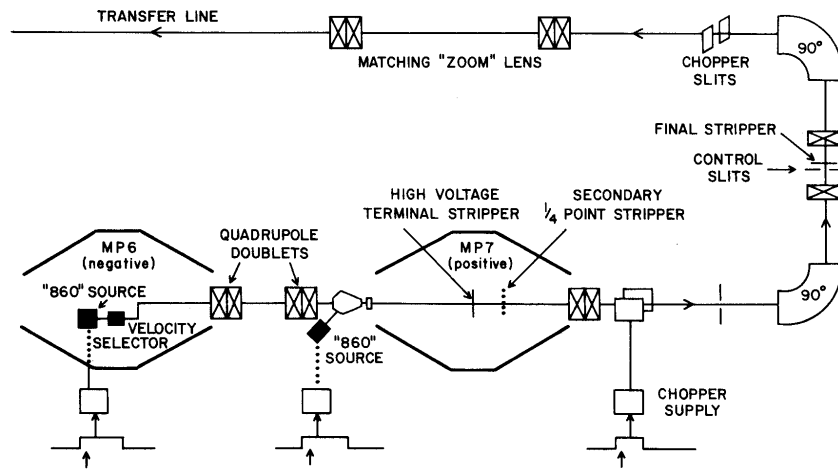


Figure 3-2: Diagram of the source, initial acceleration and transport of a beam of heavy ions in the Tandem Van de Graaff. During E859 running, only one of the Van de Graaff accelerators was used at any time.

In the past, the partially stripped silicon beam was passed through another Van de Graaff to give it a velocity high enough to allow it to be completely stripped. The main AGS ring requires a beam of fully stripped projectiles, because the vacuum in the main ring is poor enough that there is a significant probability of a collision between beam particles and gas molecules in the beam pipe. Collisions between beam ions and gas molecules will very likely remove electrons from the beam ions, and the change in the charge state will cause that ion to careen into the wall of the next dipole in the ring. Projectile-gas collisions rarely add electrons to the beam ions, so the same type of event is not a problem for a fully stripped beam. Since the advent of the Booster the partially stripped beam is sent directly into the Heavy-Ion Transfer Line (HITL). The Booster does not require a fully

CHAPTER 3. EXPERIMENTAL DESCRIPTION

stripped beam because it has a very high quality vacuum system which is able to maintain a pressure of less than 5×10^{-11} Torr [A⁺92b]. This reduces the probability of a stripping collision to a low enough level that Si⁺⁸ may be used directly. The ions are only fully stripped after being accelerated by the Booster.

The relaxation of the requirement that the Si ions be fully stripped has two advantages. One is that only one of the Van de Graaff accelerators needs to be run at a time, allowing the other to be used as a backup. It also means that a larger current of ions can be delivered to the Booster than would be possible otherwise. Each stripping foil produces a spectrum of different charge states and an analyzing magnet is used to select the desired charge state. The efficiency with which a foil produces a given charge depends on the incident velocity of the ion. Fully stripping the Si ions at the relatively low energies that the Tandem Van de Graaff could produce resulted in a current of 20 μ A, but the same facility can produce a current of 140 μ A of Si⁺⁸ [A⁺92b].

The Tandem produces the ions in a pulsed beam, synchronized with the injection requirements of the Booster. Once a full pulse of silicon ions has been transferred from the HITL and injected in the Booster, radio frequency (rf) cavities accelerate the ions to 1 A·GeV/c and then inject the ions into the AGS. A final stripping foil just before the AGS removes all of the remaining electrons from the silicon. The AGS is loaded with several pulses worth of ions and then its rf cavities complete the acceleration of the beam to 14.6 A·GeV/c after which the rf cavities are turned off, and the beam is allowed to coast around the ring. An electrostatic kicker begins peeling off ions into a system of magnets that directs the beam down the B2 beam line to our experiment. The whole process of beam generation, acceleration and delivery is repeated every 3.4 sec, and the heavy ion experiments receive beam for 1 sec out of this cycle.

Though the Booster is needed in order to provide the AGS with nearly fully stripped gold ions and held promise for improving the AGS uptime for the silicon beam, the addition of the Booster was not an unqualified improvement for the experiment. The main negative effect of the Booster was a serious degradation in the time profile of the beam, namely the introduction of a high frequency component that greatly increased the number of closely spaced beam particles. This limited the maximum beam intensity that E859 could profitably accept to about 1×10^6 particles/spill, in spite of the fact that calculations based on E802 data rates indicated that another factor of two or three should have been possible.

3.1. THE BEAM AND TARGET

3.1.2 Beam Definition and Counting

The most basic event definition in the experiment is determining when a valid beam particle has hit the target. To do this, and to determine a global start time for the experiment, a set of scintillators and phototubes upstream of the target is used [Keh91]. The first elements in the chain are the UDEW (Up-Down-East-West) counters, four scintillators coupled to Hamamatsu 2431 phototubes and arranged in two pairs with a thin gap surrounding the beam line between the two scintillators of each pair. These counters are located about 4 m upstream of the target and serve as beam halo veto counters, eliminating events in which the beam particles are far off axis, due perhaps to collisions with residual gas in the beam line or grazing collisions with the edges of the beam collimators or with the inside wall of the beam pipe.

The main beam counters, BTOT, BTOF and HOLE sit in a configuration about 1 m upstream of the target (see Figure 3-3). Each of the three scintillators is made of Bicron BC418 and is instrumented with a pair of Hamamatsu 2083 phototubes. The first counter is BTOT which measures $2'' \times 3'' \times 0.040''$ and makes the principal measurement of the charge of the beam. Again, perhaps because of interactions with the walls of the beam pipe, it is possible that beam particles are not actually ^{28}Si . The output of the phototube coupled to BTOT is split and sent through two discriminators which are set high and low on the analog signal. The low discriminator is meant to fire whenever a charged particle passes through BTOT, and the high discriminator is meant to fire only when a particle with a charge of at least 14 passes through the counter. Each of these discriminator outputs is counted on a scaler visible in the counting house, and the difference between the number of events firing each of these discriminators can serve as a useful diagnostic. A large number of events firing the low level, but not the high one, may indicate a sag in the discriminator level.

The next element is BTOF which measured $3/4'' \times 1-5/8'' \times 0.020''$ for the February 1991 run and $3/4'' \times 18'' \times 0.020''$ for the March 1992 run. It is vacuum-coupled to the phototubes, and in order to obtain the best timing resolution the light from the scintillator is actually taken from the face of the plastic rather than through a more conventional optical coupling to the edge of the counter. The timing resolution of BTOF is 45 ps and this counter provides the global start time for the experiment. This counter was one of the first unexpected casualties of the very intense E859 beam which was as much as a factor of ten higher than was typical during E802. This radiation

CHAPTER 3. EXPERIMENTAL DESCRIPTION

exposure to the high beam rate quickly damaged the BTOF plastic, causing it to become yellowed and reducing its light output. This was first noticed in the ratio of counts seen on the BTOT scalers compared to the BTOF one. Many events that triggered the high level BTOT failed to do the same for BTOF. To remedy this, a pragmatic if unusual solution was tried for the second season of E859 running. The small BTOF counter of 1991 was replaced with a long rectangular design mounted in an assembly that allowed it to be moved along its length in steps of 1 cm. Whenever the performance of the counter seemed to have degraded sufficiently (usually this was when BTOF/BTOT dropped to less than 90%) the counter was stepped, bringing an area of undamaged scintillator into the beam.

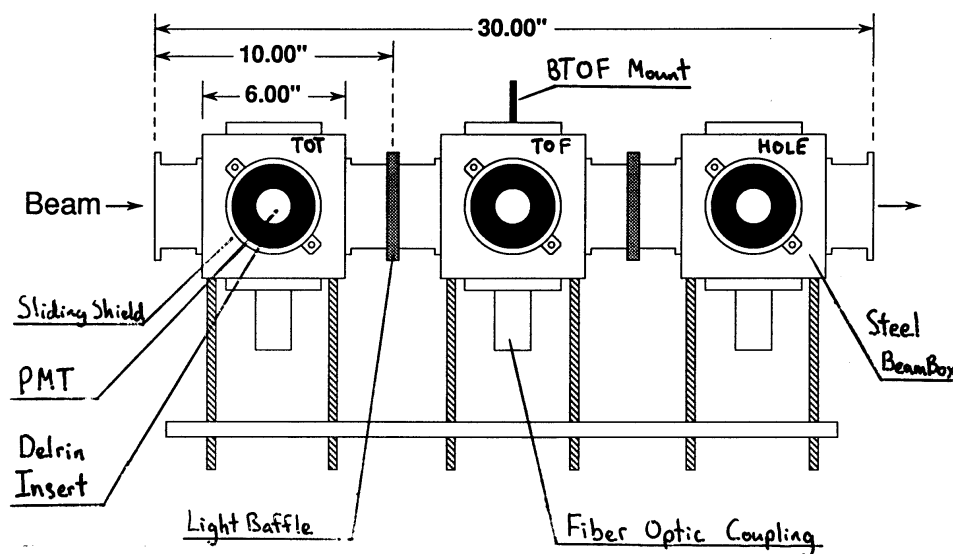


Figure 3-3: External view of the beam counter assembly. The evacuated boxes are made of soft iron meant to shield the phototubes from stray magnetic fields.

Following BTOF is HOLE, a counter similar to BTOT except that it has a hole 1 cm in diameter cut into its middle. It measures $2'' \times 3'' \times 0.118''$ and it used to verify that the beam is still steered straight ahead. BTOT, BTOF and HOLE were all mounted inside three large soft iron boxes. The high magnetic permeability of these boxes was meant to shield the phototubes from stray magnetic fields, presumably those emitted by the Henry Higgins dipole magnet 3 meters downstream.

The final element of the beam counting and defining detectors is the bull's-eye (BE), a rectangular scintillator measuring $7.6\text{ cm} \times 10.8\text{ cm} \times 0.16\text{ cm}$ coupled to two Hamamatsu 2083 phototubes and

3.1. THE BEAM AND TARGET

mounted at the end of the beam pipe, 11.7 meters downstream of the target. This detector measures the charge remaining in the projectile fragment, and is used to determine when the beam projectile suffered an interaction in the target.

3.1.3 The Target Assembly

The target assembly used in E859 is the same as was used in E802. It is a belt with 15 individual target holders which rolls around two wheels whose axles are perpendicular to the beam. A remotely controlled electric motor drives one of the wheels, moving targets in and out of the beam spot. The actual targets are foil disks 2.2 cm in diameter mounted in a holder on short standoffs which are attached to the belt so that they are parallel to the gear axes. As the wheel turns it brings a target holder around and places it in the path of the beam. See Figure 3-4 for a diagram of the mechanism. The whole mechanism is inside an aluminum box surrounding the beam pipe. The part of the box

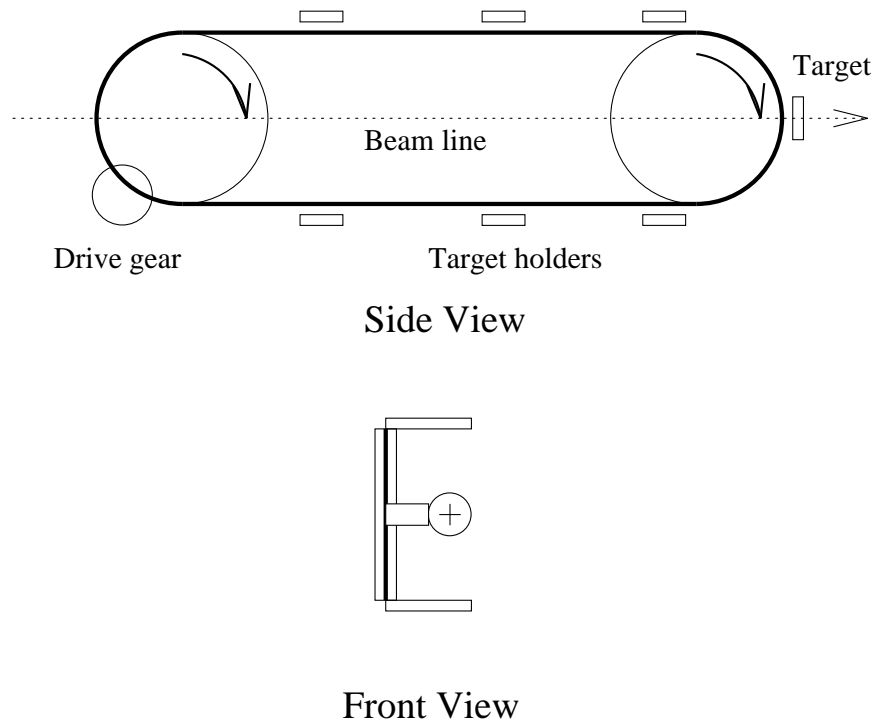


Figure 3-4: Schematic view of the target assembly. The side view show the two gears of the target movement with the drive gear. The front view shows more clearly how the individual target holders drop in front of the beam when the gears are rotated.

CHAPTER 3. EXPERIMENTAL DESCRIPTION

just downstream of the target is a hemispherically shaped section called the *snout*. It is made of 2 mm aluminum and is therefore is a significant contributor to the total radiation length of material in the spectrometer.

Each of the holders can be loaded with a target, or can be left empty for background studies. The targets that are relevant for the present single particle analysis are shown in Table 3.1. Aside from knowing its material composition, the single most important quantity characterizing a target is its thickness, usually measured in mg/cm^2 or quoted as a fraction of an interaction length for the Si projectile. The thinnest interaction length target used in the collection of the E859 kaon data is 1% ^{197}Au ; the thickest is 6% ^{27}Al . The main benefit of a thinner target is that there is less multiple scattering of the produced particles, giving better momentum resolution. The main benefit of a thicker target is that the rate of interaction is high, reducing the importance of the empty target correction.

Target	mg/cm^2	Fraction
Al 3%	817	0.0253
Al 6%	1630	0.0506
Au 1%	944	0.0103
Au 2%	1888	see Section 4.8.1
Au 3%	2939	0.0312

Table 3.1: Targets used in E859 single particle data taking. The targets were produced and characterized by the AGS target group. The names of the targets give their nominal thickness as a fraction of an interaction length for the Si projectile. The measured target fractions are shown in the last column.

3.2 Event Characterization

More information is extracted from the spectrometer data by looking at how that data changes as a function of some global feature of the event. It would be nice to select events based on the impact parameter of the event, because small impact parameter events, or *central* events, maximize the overlap of the projectile and target nuclei. These events are as different from p-p or p-A collisions as A-A collisions can get, and provide the best opportunity for observing phenomena not seen in

3.2. EVENT CHARACTERIZATION

the simpler collisions. However, most events are not central, so by looking at data which has not been selected for small impact parameter, one is not only averaging over all impact parameters, but most of the sample comes from peripheral collisions. Unfortunately, it is not usually possible to directly measure impact parameter, and it has to be inferred from signals that can be measured. E859 has several detectors to provide global *characterization* of events. Two of these are the Target Multiplicity Array, or TMA, and the Zero Degree Calorimeter, or ZCAL. Both detectors will be described here, but the usefulness of the ZCAL for much of the E859 data analysis has been lessened due to poorer resolution compared to that obtained during E802 and a fairly significant beam rate dependence to the ZCAL output (see Section 4.11).

3.2.1 The Target Multiplicity Array

The Target Multiplicity Array (TMA) is one of the principal event characterizing detectors in the experiment. It counts charged tracks emanating from the target, measuring the *multiplicity* of the event. The multiplicity is assumed to be related to the volume of the participant region and hence to the impact parameter of the event. Event selection based on cuts on the TMA spectrum provides the main source of centrality classification used in this thesis. See Chapter 6 for a discussion of the relationship between the impact parameter and the TMA signal as seen in models.

This description of the TMA follows the discussion in Tony Abbott's thesis [Abb90], except where changes have been made to the TMA configuration since then. There are two parts to the TMA. The first part called the *barrel* is a cylindrical detector 60 cm in diameter coaxial with the beam and surrounding the target. The second part called the *wall* is a nearly planar detector just downstream of the target. A perspective view of the TMA is shown in figure 3-5. As designed, the TMA barrel is built of 24 rectangular panels each parallel to the beam axis. In E859, two of these panels were removed so that the new Phoswich array could have an unimpeded view of the target; the two diametrically opposite panels were also removed so that the TMA would remain azimuthally symmetric. The wall is constructed of 22 panels, but several panels that overlap the spectrometer acceptance have been removed. The barrel covers the pseudorapidity range from 1.3 to -1.1 (30° to 143°); the wall covers pseudorapidities from 2.95 to 1.0 (6° to 40°). In the azimuthal angle, the wall and barrel cover all 2π , except for the regions covered by the removed panels as noted above.

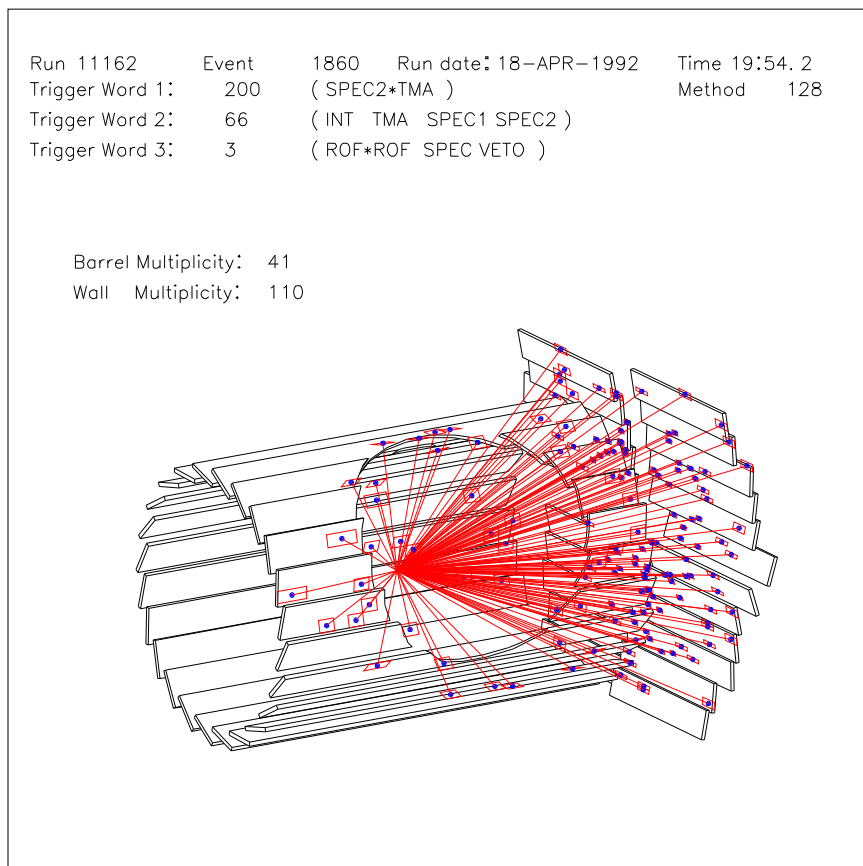


Figure 3-5: A perspective view of the TMA taken from the event display (EDISP), showing tracks from a high multiplicity event. The large hole in the detector is not, as far as we are aware, really there. It is a cut-away drawn in order to show the tracks more clearly. The cylindrical portion is the *barrel* and the flat portion is the *wall*. Each of the rectangular pieces is called a *panel*. Several of the panels in the barrel have actually been removed so that the PHOSWICH arrays might have an unimpeded view of the target.

3.2. EVENT CHARACTERIZATION

Each panel of the TMA is constructed of parallel plastic streamer tubes glued together and then to a foundation made of G10 fiberglass covered in copper foil. The tubes have a rectangular cross section, measuring $1.5\text{ cm} \times 1.0\text{ cm}$ for the tubes in the barrel, to $0.87\text{ cm} \times 0.87\text{ cm}$ for the tubes in the wall. Each tube has a single $50\mu\text{m}$ diameter anode wire running down the center held at high positive potential in an atmosphere of 70-30 argon-isobutane. Along the outside of the tube are a series of electrically distinct copper *pads*. When a particle passes through a tube, it ionizes the argon-isobutane mixture, which leads to an electron avalanche. The copper pad has a signal induced on it by this accumulation of charge, which is then read out by the TMA electronics.

3.2.2 The Zero Degree Calorimeter

The Zero Degree Calorimeter, or ZCAL, is a many ton sandwich of alternating steel and scintillator plates sitting on top of an impressive steel mount² just in front of the concrete beam dump at the end of the experiment, 11.7 m downstream of the target. It is used to measure the energy remaining in the projectile fragments travelling forward in a cone centered on the beam axis with a half angle of 1.5° . At the 5° spectrometer setting, with the beam pipe fitted through holes in the yoke of the magnet and the GASC, the conical acceptance is limited to a half angle of 0.8° . Since peripheral events will leave much of the beam projectile undeflected and central events can completely obliterate the projectile, the strength of the signal in the ZCAL is inversely correlated with the impact parameter of the collision. However, as will be discussed in Section 4.11, problems with the ZCAL performance during E859 have made its use as an event selector questionable, but it will be used in conjunction with the TMA to measure the forward energy of events selected on the basis of multiplicity.

The calorimeter measures $60\text{ cm} \times 60\text{ cm} \times 1.8\text{ m}$ and is made of 138 repeated units of 10 mm thick low-carbon steel and 3 mm thick scintillator plates [B⁺ 89]. The scintillator is an acrylic doped with naphthalene (PS15A), and sheets of titanium oxide-coated mylar between the scintillator and the steel are used to diffuse the produced light and protect the acrylic from scratches. The scintillation light emitted from the edges of the acrylic is first wavelength shifted by optical plates mounted on the sides of the calorimeter and then brought to the eight Thorn EMI 9822 photomultiplier tubes by UVA acrylic light guides. The total depth of the calorimeter is 8.9 nuclear interaction lengths, and there are 1.8 nuclear interaction lengths of material from the center outward. The calorimeter

²Designed by a visiting Russian scientist, the mount seems clearly capable of supporting several ZCAL's.

is divided into two sections, H1 with 32 units of steel and scintillator, and H2 with 106 units. The damage from the accumulated radiation exposure of 7 years of heavy-ion running, and the

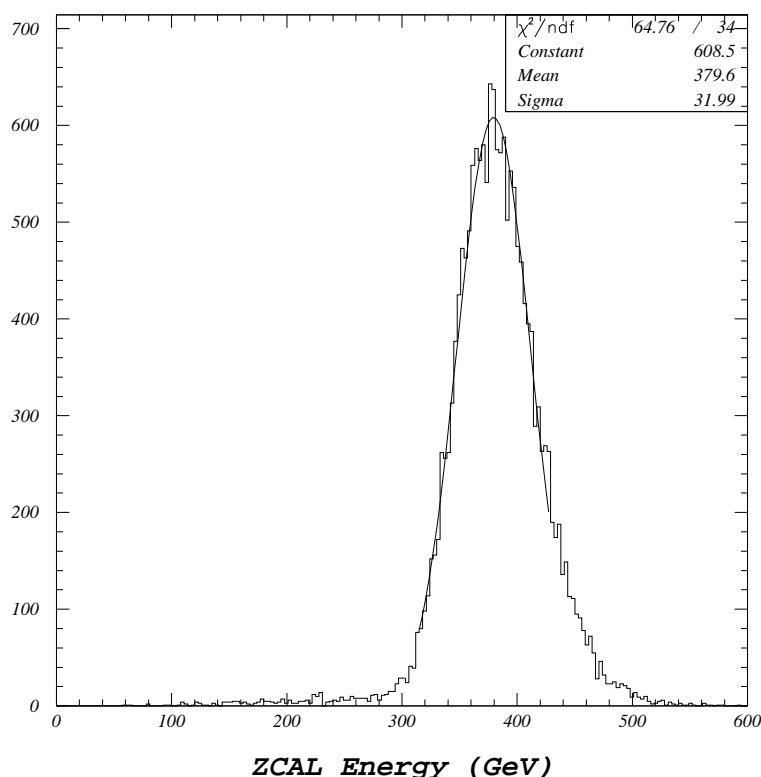


Figure 3-6: ZCAL energy distribution, showing a resolution of $1.64 \text{ GeV}^{1/2}$, typical of E859.

high beam rates of E859 have apparently taken their toll on the ZCAL, as the light output and resolution worsened significantly during the first E859 run. The energy resolution reported for the ZCAL during E802 was $\sigma/\sqrt{E} = 0.73 \text{ GeV}^{1/2}$ [B⁺89]. The performance more typical of the E859 running is illustrated in figure 3-6, where the resolution is $\sigma/\sqrt{E} = 32/\sqrt{380} = 1.64$, or more than twice as wide as the E802 number. See Section 4.11 for more details on the ZCAL performance.

3.3. THE SPECTROMETER

3.3 The Spectrometer

The E859 spectrometer is also called the Henry Higgins spectrometer after its most prominent feature, a 1.5 Tesla-meter dipole magnet which has kept the name given in its early use in the Cambridge Electron Accelerator.³ The main spectrometer, including the magnet, stretches over 9 meters from target to the veto counter behind the gas Čerenkov detector. The spectrometer can pivot about the target, from 5° out to 44° , has a solid angle acceptance of 25 msr, and has a particle identification system usable from 500 MeV/c up to 3 GeV/c for pions and kaons and up to 5 GeV/c for protons. Near the front end of the spectrometer, just upstream of the magnet are two drift chambers, T1 and T2, a segmented scintillator, F0 (not shown), and a time-projection chamber (TPC) (not shown). Just downstream of the magnet are two more drift chambers, T3 and T4, and the two multiwire trigger chambers, TR1 and TR2. Next is a time-of-flight wall (TOF), backed by a gas Čerenkov detector (GASČ) and the back counter (BACK). In the following sections, each of these detectors will be described in more detail.

3.3.1 The TPC and F0

The first element of the spectrometer is F0, a small segmented array of scintillators arranged in two staggered planes of vertical slats. Each identical element of F0 measures $1.2\text{ cm} \times 0.64\text{ cm} \times 12.8\text{ cm}$. The main function of F0 has been to serve as a fast input in the definition of a spectrometer trigger (see Section 4.8.2). Downstream of F0, between T1 and T2 is a small TPC whose utility was being investigated during the 1991 run of E859, but was never used for any of the physics analysis and was removed before the 1992 run. Therefore, the most relevant characteristic of the device for the present work is its thickness measured in radiation and interaction lengths, which is approximately the same as the drift chambers.

3.3.2 The Drift Chambers

Multiwire proportional drift chambers provide the primary source of particle tracking information in E859, and the design and operation of these type of detectors is exhaustively described in an article by Sauli [Sau77]. A typical chamber looks like an open rectangular frame across which are

³How the magnet received its name in the first place is a subject of some controversy.

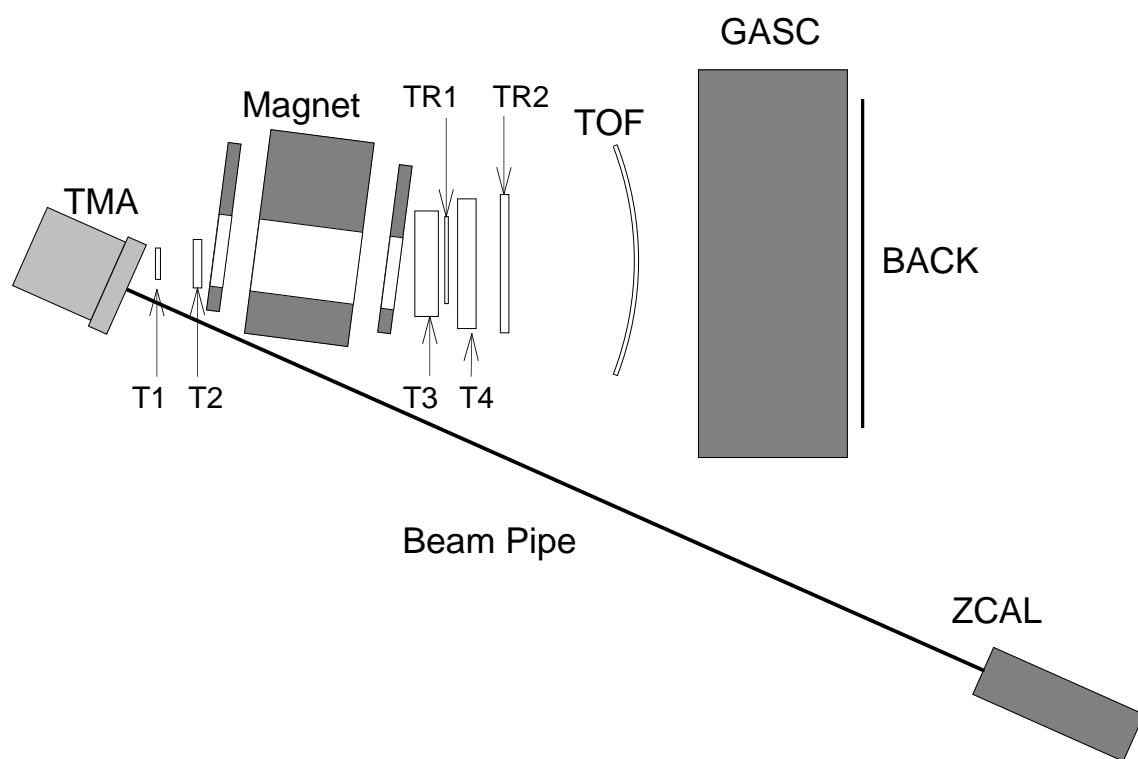


Figure 3-7: Plan View of the Spectrometer

3.3. THE SPECTROMETER

strung a number of parallel wires. The volume of the chamber is enclosed with windows made of thin aluminized mylar, and the interior is flooded with an easily ionizable gas mixture. The chamber is mounted on the spectrometer chassis so that the face of the chamber is normal to the general direction of oncoming particles. When a particle passes through the chamber, a signal is generated on the wire nearest the particle's path, and by knowing the location of the wire, one obtains some information about the particle's trajectory. Detectors like this have the disadvantage that one is typically unable to determine where along the length of the wire a particle passed. Because of this, these type of detectors are said to be *projective*. But, by combining the information from chambers with wires at different orientations, the spatial location of a part of a particle's trajectory can usually be determined.

Design and Construction

The fundamental unit in a drift chamber is the *drift cell*, a high voltage anode sense wire surrounded by several cathode wires or foils (see Figure 3-8). In some drift cell designs, as in chambers T2-T4, additional field wires are used to help fine tune the shape of the electric field. When a high energy particle passes through the cell, it leaves a trail of ionized gas molecules in its wake, called primary ionization. The liberated electrons often have enough kinetic energy of their own to directly ionize several other molecules in a process called secondary ionization, and the whole cloud of electrons begins drifting toward the sense wire, driven by the potential difference maintained between the sense and field and cathode wires. As this cloud nears the sense wire, the electric field gradient becomes very intense, accelerating the electrons to a high enough velocity that they again begin ionizing gas molecules. This electron avalanche can increase the number of freed electrons by a factor of 10^4 to 10^5 . The electron collection on the sense wire generates a signal, and if one also instruments the sense wire with a TDC, the electron drift time can be measured, and from a calibration, one can obtain the distance of the primary ionization from the wire. This can give, as in the E859 drift chambers, a spatial resolution of as fine as $150\text{--}200\mu\text{m}$.

Many parallel drift cells are assembled into a single *plane*. All the sense wires in a plane are parallel⁴, and planes of several different orientations, called *views*, are used in the spectrometer's tracking chambers. Table 3.2 lists the different types of planes and the orientation of their wires,

⁴Roughly. A machining error left T2 with wires whose orientation changes slightly across the chamber.

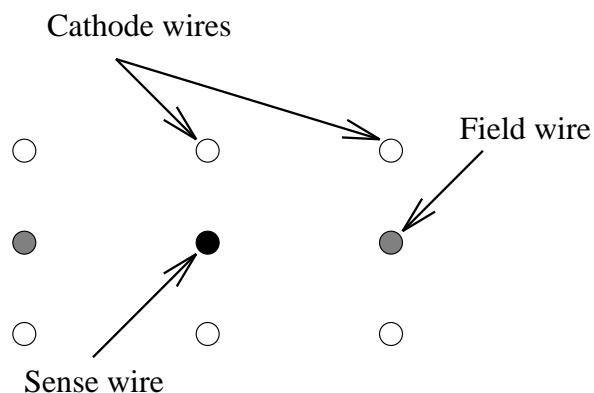


Figure 3-8: Typical drift cell design. This view is from one end of the drift cell looking along the length of the wires. The sense wire is kept at a large positive voltage, perhaps 2 kV. The cathode and field voltages are large and negative, between 600 V and 2 kV, and adjusted as needed to shape the electric field for high collection efficiency.

where the angles are measured clockwise from the positive y axis in the spectrometer coordinate system.

View Name	Orientation
x	0°
y	90°
u	$30^\circ (45^\circ)$
v	$-30^\circ (-45^\circ)$
w	(27°)

Table 3.2: Tracking Chamber Wire Orientations. The numbers in parentheses refer to the orientation of those planes in T1.

T1, designed, built and operated by Koos van Dijk of BNL, is the first chamber in the spectrometer and sits 104 cm downstream of the target. It has a 4 mm wire pitch to provide adequate segmentation over its small area, and the wires are directly soldered to a frame made of printed circuit board material. The design of T1 was an attempt to maximize the signal output for an ionizing track, so $10\ \mu\text{m}$ diameter sense wires are used to maximize the electron avalanche. The planes are separated from one another by a conductive cathode foil, and all 10 frames are stacked and glued directly together. The planes are grouped into 5 adjacent pairs sharing the same orientation. There are x , y ,

3.3. THE SPECTROMETER

u , v , and w views.

The chambers T2-T4 were designed by George Stephans, and they were sheperded through construction and testing at MIT by Marjorie Neal. The chamber packages are segmented into modules and each module contains either two or three planes. All the planes in one module have wires in the same orientation. The basic construction is a rectangular frame made entirely of G10 fiberglass, as in the case of T2, or of slats of G10 connected by bars of aluminum, as is the case in T3-T4. The wires are strung by hand through holes drilled in the G10 frame using a crimping technique which holds the wires in place. Each end of the wire is threaded through a stainless steel tube which is then crimped using a pneumatic jaw, holding the wire in place. On one end of the wire, a spring is used to keep tension on the wires to prevent sagging as the wires stretch and settle into place. The cathode and field wires are made of $100\text{ }\mu\text{m}$ diameter copper-beryllium alloy. The sense wires are made of $30\text{ }\mu\text{m}$ diameter gold plated tungsten.

T2 was redesigned for E859 and has 3 planes each of x , y , u and v views. T3 and T4 have 2 planes each of u and v views, and 3 planes of x and y . T3.5 has 3 planes of x views, with the last plane having resistive wires instrumented with an ADC in addition to the TDC at the end of each wire. It was intended that using the ADC information, a charge division technique would be used to determine the position of the hit along with wire, but resolution problems with the ADC's have kept this additional information from being realized.

Electronic Readout

The 8-channel preamplifiers and 16-channel discriminators used to read out the hits on T2-T4 were designed by Charles Parsons, Vasilios Vutsadakis and Robert Ledoux. Since the meter-long sense wires make fine radio antennae, the preamplifiers take for each channel a differential input from a sense wire and one of the adjacent field wires. Any signals induced on the wires by radio waves will, to a large extent, cancel in the difference between the two wires. The signal is differentiated and amplified by a Motorola 733 operational amplifier followed by a line driver and carried over a shielded ribbon cable to the discriminators. From there, the signal is sent to LeCroy 1879 Fastbus pipeline TDC's which digitize the time with a bin size of 2 ns.

Gas Supply

The ionization gas used in chambers T2-T4 is premixed 50-50 argon-ethane, a fairly standard mixture with low diffusivity, good electron avalanche gain and linear drift velocity over a large range in electric field strengths [Sau77]. T1 uses a mixture of argon-isobutane which has similar characteristics. Low diffusivity improves the spatial resolution of the chamber. A high gain gas gives a reasonable signal on the sense wire without requiring excessive voltage or very thin wires, improving the signal-to-noise ratio. Since even a well designed chamber will have an electric field whose magnitude may vary significantly over the volume of the drift cell, a constant drift velocity simplifies the calibration of the drift chambers and improves the spatial resolution. In reality, the drift velocity is not quite linear over the entire cell, and the actual calibration curve of drift distance versus drift time is obtained from the data itself by projecting tracks to sense planes and using the distance from the wire to the fitted track as an independent measure of the distance of the hit from the wire. The plot of distance versus time is fit with a cubic polynomial and the coefficients of this polynomial form the calibration which is stored in the RDB. With T1 as the only serious exception, the drift velocity is a constant $50 \mu\text{m/ns}$ to a good approximation. Figure 3-9 shows a schematic of the gas supply. Two bottles at a time are fitted with regulators and are connected to the main gas manifold. Gas is drawn from only one bottle at a time, but having two bottles ready means that we can switch from an empty bottle to a full one in a matter of a couple of minutes without having to lower the high voltage on the chambers. After the main manifold, the argon-ethane is bubbled through a 0°C alcohol bath, introducing a small amount of alcohol into the gas. This procedure reduces the buildup of carbon whiskers on the wires of the chamber.

High Voltage Supply

The high voltages for the tracking chambers are supplied in two ways. Some of the voltages require a fair amount of attention, and these voltages are therefore provided by a rack of Bertan high voltage supplies in the counting house where they may be monitored and adjusted even when beam is in the area. The Bertans also have a sensitive trip circuit which turns off the high voltage to a chamber when a spark occurs preventing it from developing into a corona discharge. Voltages supplied this way include all of the sense and field voltages as well some of the cathode voltages on T2. T2 receives special attention because the old chamber design used in E802 had some trouble

3.3. THE SPECTROMETER

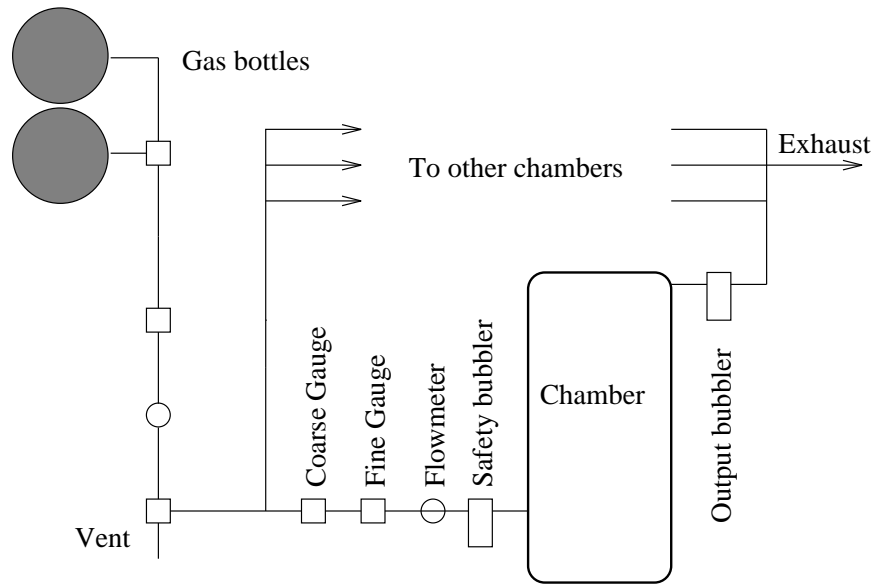


Figure 3-9: Schematic of the gas supply for the chambers T2-T4. The two shaded circles at left represent the argon-ethane supply tanks. The gas flows through a main manifold, is distributed in parallel to all the chambers and is collected together again for a common exhaust. See text for more details.

with sparking. The new design suffers no such problem. The other voltages are supplied by a LeCroy 4322 high voltage supply which is controlled through an interface installed in BNL859, a VAXStation 3100.

3.3.3 The Trigger Chambers

The two trigger chambers, TR1 and TR2, are multiwire proportional chambers which were originally part of the Multiparticle Spectrometer (MPS) experiment [EK80] and were recycled for E859 as part of the hardware of the LVL2 trigger. They are located 440 cm and 500 cm from the target, and each has a single x -plane of 150 and 256 sense wires, respectively. The sense wires are 1 mil gold plated tungsten, with a pitch of 0.25" [Etk79]. TR1 subtends a much smaller solid angle than any of the other chambers, cutting severely into the acceptance, but it was originally intended that it would sit between T3 and the magnet where its acceptance would have been comparable with the other chambers. Once it was discovered that there was not enough room to mount the chamber there, it was moved behind T3 and its x location was adjusted to try to maximize its acceptance.

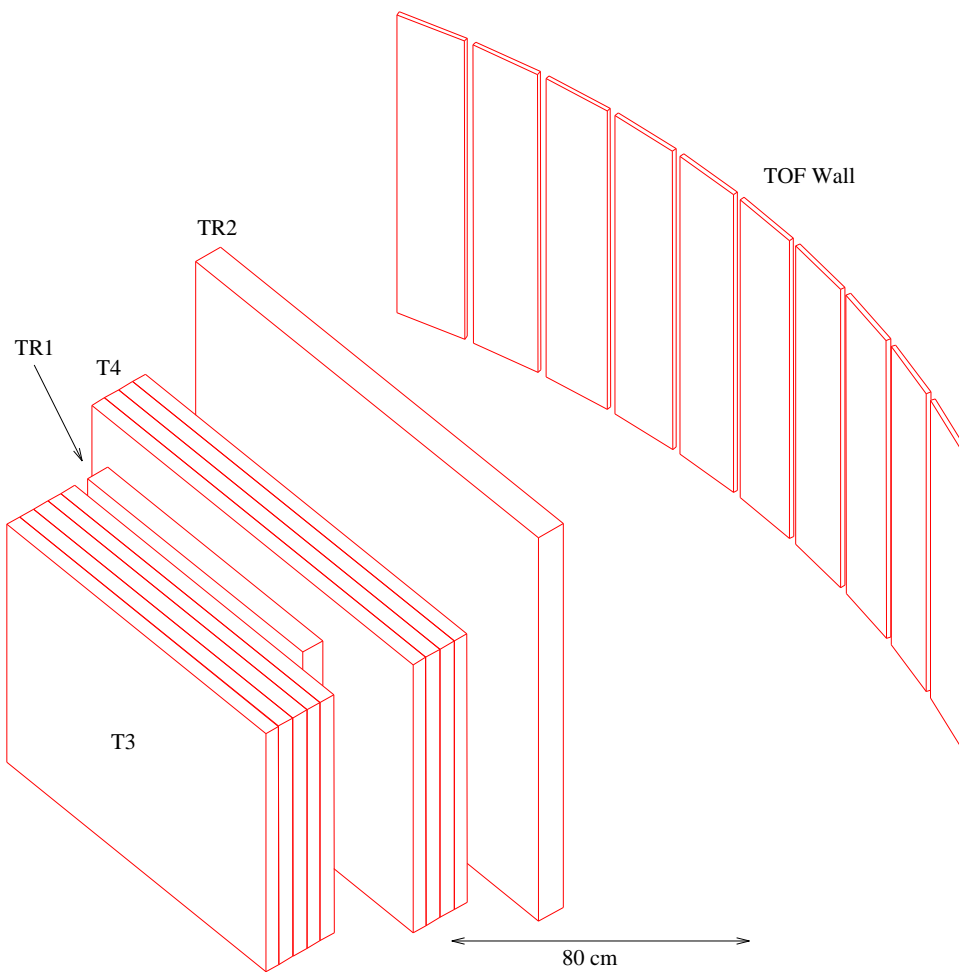


Figure 3-10: View of Detectors Behind Magnet

3.3. THE SPECTROMETER

Electronic Readout

The trigger chambers are read out using a system of chamber-mounted cards and associated CAMAC rack-mounted electronics called PCOS III (for Proportional Chamber Operating System) purchased off-the-shelf from LeCroy Corporation[LeC]. The time of the hit is not digitized, as it is on the tracking chambers, only the wire number of the fired wires is read out. The basic elements in the system are

- 2735PC Amplifier/Discriminator Card

A 16 channel preamplifier and discriminator cards with ECL outputs, mounted directly on the trigger chamber. Each card receives power and a reference voltage for the discriminator from a common power supply on the experimental floor.

- 2731A Delay and Latch Module

Each latch receives inputs from two 2735PC's, and provides two outputs: a prompt signal from the frontplane and a latched signal readout from the backplane.

- 2738 Crate Readout Controller

Each CAMAC crate contains one 2738 to control the 2713A's

- 4299 CAMAC Interface

This module coordinates the readout of all the 2738 crate controllers and is the one module that is directly addressed from BNL859.

When one of the wires in a trigger chamber is hit, the corresponding channel in the 2735PC fires. The 16 channels of a single amplifier card are sent over a standard ECLline 17-pair twisted pair ribbon cable to the input of the 2731A where two things take place. The 2731A provides a frontplane output called a *prompt OR* which is used in the LVL1 trigger decision. A logical OR is taken of all the wires on each of TR1 and TR2 and a logical AND is taken of those two signals. This result, $TR1 \wedge TR2$, is used as part of the SPEC trigger logic. At the same time, the signals from the hit wires propagate through an internal delay line in the latch whose length is set via software. If the event satisfies the LVL2 trigger, the trigger supervisor sends a signal to the crate controller and it is distributed along the backplane of the CAMAC crate to the latches. Any of the wire signals

that emerge from the delay in time with this signal are latched by the 2731A, and they are then read out in sequence by the crate controller and sent to the LVL2 trigger.

3.3.4 The Time of Flight Wall

The time-of-flight (TOF) wall is an arc-shaped segmented hodoscope about 660 cm from the target (see Figure 3-10). The wall is divided into 10 panels of 16 vertical slats. The first slat of each panel measures $3.2\text{ cm} \times 1.6\text{ cm} \times 78\text{ cm}$ and is made of SCSN-38 plastic scintillator. Each of the other 15 slats is half as wide, measuring $1.6\text{ cm} \times 1.6\text{ cm} \times 78\text{ cm}$ and is made of BC404 plastic scintillator. Both ends of each slat are instrumented with a Hamamatsu R2083 photomultiplier tube[S⁺86, Sak92]. The calibration of the timing constants for the TOF wall has been changed for the E859 analysis and a description of the procedure is given in Appendix E.

3.3.5 The Gas Čerenkov and Back Counter

The Gas Čerenkov, or GASČ, is a velocity threshold detector made of 40 cells arranged in 4 horizontal rows of 10 cells filled with Freon-12 and equipped with a light-gathering spherical mirror and a photomultiplier tube. Each of the cells has the shape of a truncated pyramid with the narrow end pointed toward the target and the mirror mounted near the downstream end of the cell. The two rows of cells nearest the $y = 0$ midplane of the spectrometer are large cells, 115 cm long, while top and bottom rows are smaller cells 84 cm long (see Figure 3-11). The Freon-12 (CCl_2F_2) in the GASČ is kept at a pressure of 3.8 atmospheres and has an index of refraction at that pressure of 1.004. Kaons above 1.8 GeV/c will fire the GASČ. The Back Counter is a planar pad detector, segmented in both the horizontal and vertical directions. There are 64 columns of 24 pads, each of which measures $12\text{ cm} \times 10\text{ cm}$. The Back Counter uses the same technology as the TMA to detect hits. A gas volume containing an anode wire is surrounded with cathode pads which are connected to preamplifiers and discriminators. The Back Counter sits immediately behind the GASČ and serves to verify whether tracks make it through the GASČ.

3.3. THE SPECTROMETER

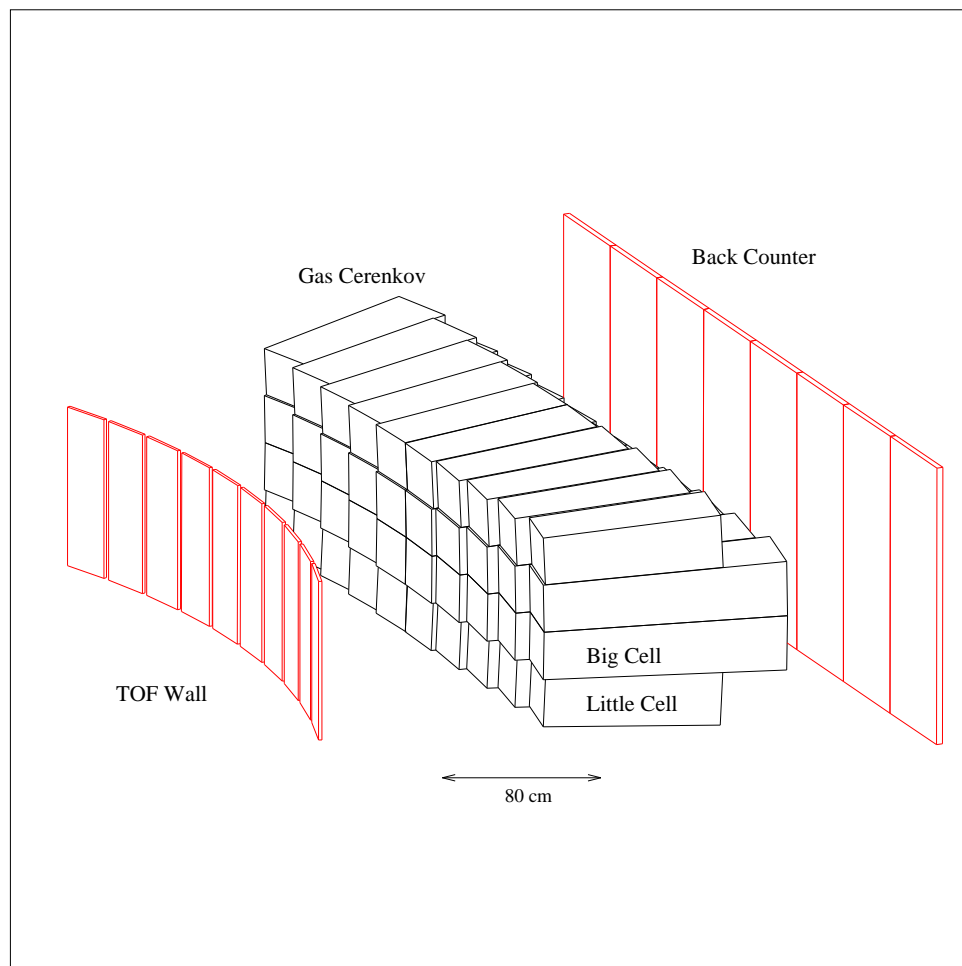


Figure 3-11: View of the Gas Čerenkov and Back Counter.

3.4 The Data Acquisition System

The E859 data acquisition system, also called the DAQ or the front end, is the conglomeration of electronics, interfaces, and computers that collects data from the detectors of the experiment, decides whether to keep or reject each event, formats the data and writes it to tape. The E859 DAQ is basically the same one used in E802. It has a maximum throughput of 100-150 events per spill and is described in detail in several BNL memos and theses [WLem, Col92]. A new DAQ has been designed and implemented by Kareem Ashktorab since the final run of E859, so the following section is meant to serve as documentation of what was done rather than as a reference for future users. A diagram of the DAQ hardware is shown in Figure 3-12, which aside from the Fastbus and CAMAC crates, sits in several VME crates in the electronics room of the counting house.

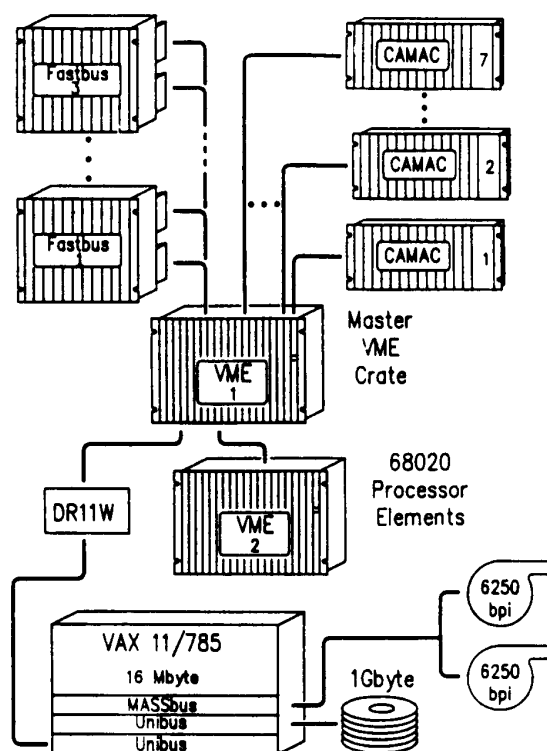


Figure 3-12: The data acquisition hardware. Data is collected from the detectors by the Fastbus and CAMAC crates at top. The Master VME crate contains interfaces to the peripheral crates. The Processor elements translate and format the raw data into a complete event, which is sent over the link to the data acquisition VAX where it is buffered and written to tape or disk.

3.4. THE DATA ACQUISITION SYSTEM

The nexus of the front end is the Trigger Supervisor, a VME crate filled with custom-designed boards, whose purpose is to orchestrate the collection of data. It distributes timing and control signals to other pieces of electronic equipment and determines whether a particular event should be kept or not. From the point of view of the Trigger Supervisor, the experiment is divided into partitions, where each partition roughly corresponds to a distinct detector subsystem of the experiment. For instance, the TOF partition includes the TOF wall, and the TRCK partition includes T2 through T4.⁵ Each partition is represented by a board in the Trigger Supervisor and has inputs for several different trigger signals. The Trigger Supervisor can be configured to enable or disable any of the trigger inputs of each partition by using the program, TS_MANAGE. For example, the SPEC trigger, a logical AND of signals from F0, the trigger chambers, and the TOF wall indicating the passage of a particle through the spectrometer, is connected to one of the trigger inputs of the TOF partition. If this is the only trigger condition enabled in the Trigger Supervisor, only events satisfying the SPEC trigger will be written to tape. The Trigger Supervisor can also coordinate data collection when several triggers are enabled, with scaledowns governing how frequently each trigger controls the collection of an event.

The rest of the data acquisition system sits in a rack of VME crates adjacent to the Trigger Supervisor. One crate contains interfaces to Fastbus and CAMAC crates which are located on the experimental floor. The CAMAC interfaces are Motorola 68000-based boards manufactured by Xycom, one for each CAMAC crate, which it controls through a crate resident Kinetic Systems controller. The interface to the Fastbus crates is provided by a custom interface board which communicates with the LeCroy 1821 segment manager resident in each Fastbus crate. This same crate also contains the Chairman, a Motorola 68010-based board, which governs these interfaces and ships the raw data they provide up to the Processor elements to be formatted. The raw data of the Fastbus TDC's and ADC's consist of a channel number and a value. The Processor elements are Motorola 68020-based computers which translate this raw channel number into more meaningful things like chamber and wire number, and they format the data into the YBOS banks which are eventually written to tape. On the side of this same crate is also the infamous *black button*. It is small and black and concave and it resets the crate containing the Chairman. It is used whenever the front end crashes. We have all pressed the black button. The data is written directly to 6250

⁵T1 is in its own partition, for historical reasons

bpi 9-track tapes, which can be filled in as little as 15 minutes when the spectrometer is at forward angles where particles are most abundant.

The LVL2 trigger provides the front end with an event veto. If an event does not satisfy the physics setup of the trigger, it generates a veto and the trigger supervisor drops the event and issues a clear to the detectors.

3.5 LVL2 Trigger

Certainly the main feature distinguishing the hardware of E859 from that of E802 is the addition of a second level trigger which accepts or rejects events based on the type and number of identified particles in the spectrometer. In this section, I will describe the hardware of the LVL2 trigger and describe how it functions. The software used to control the trigger, the database used to record how the trigger was configured for different runs, and the software trigger tests that were developed are described in Appendix C. The performance of the trigger is discussed in Section 4.8, and a study of biases in the data introduced through the use of the trigger is discussed in Section 4.6.

3.5.1 Hardware of the LVL2 Trigger

The LVL2 trigger is basically a hardwired special purpose computer. It consists of several CAMAC crates filled with modules that have been tediously (and often incorrectly) wired together by hand with twisted pair ECLline signal cables. The basic hardware elements of the trigger are:

- 2375 Data Stack (DS)

Data stacks are used in the LVL2 trigger as buffers of information. One is used as a circular buffer of struck TR1 wire numbers, the others as first-in-first-out (FIFO) buffers of TOF slat numbers and TOF up and down times.

- 2371 Data Register (DR)

The data register is a very expensive one-word memory. It latches a single value which may then be read out. It is used in the FERET (see below) interrogation circuitry.

- 2372 Memory Lookup Unit (MLU)

These modules are the workhorses of the LVL2 trigger. They are initialized with a list of

3.5. LVL2 TRIGGER

numbers which may then be retrieved one at time by specifying an index into the list. Though the total amount of storage in the MLU is fixed, the MLU allows a tradeoff between the number of indices and the amount of data available at each index. For instance, you may have 1 bit of information available at 65,536 addresses, or 8 bits available at each of 8,192 addresses.

- 2376A Data Array (DA)

This module is initialized by loading it with a list of numbers and providing it with a search width of the selected value. Then, you may provide a further number and ask if any of the numbers in the original list are within the search width. It is used to see if any of the wires hit on TR2 is within a wire or two of the predicted wire number taken from various combinations of TR1 and TOF.

- 2378 Arithmetic Logic Unit (ALU)

Although capable of a number of elementary arithmetic operations, in the LVL2 trigger this module is used to add the up and down time of flight.

- 4301 Driver Module

The Driver Module controls the TFC's and FERA's, sending out stops, starts and clears.

- 4303 16 Time-to-Charge Converter (TFC)

The TFC is a very accurate current source which is used in combination with a FERA to provide a time of flight measurement.

- 4300B ADC (FERA)

FERA stands for Fast Encoding Readout and ADC. It is used to digitize the current provided by the TFC. It provides 11 bits of dynamic range with a conversion time of $8.5 \mu s$. Used together with the TFC (the combination is called a FERET), it provides fast digitization of the time of flight.

- ECL-NIM Converter

These are used throughout the trigger as *inspection points*.

The complexity of the trigger wiring makes it difficult to discern its functioning directly from the plans, but for the record, a circuit diagram of the LVL2 trigger is shown in Figure 3-13. A

E859 Level-2 Trigger

October 26, 1993

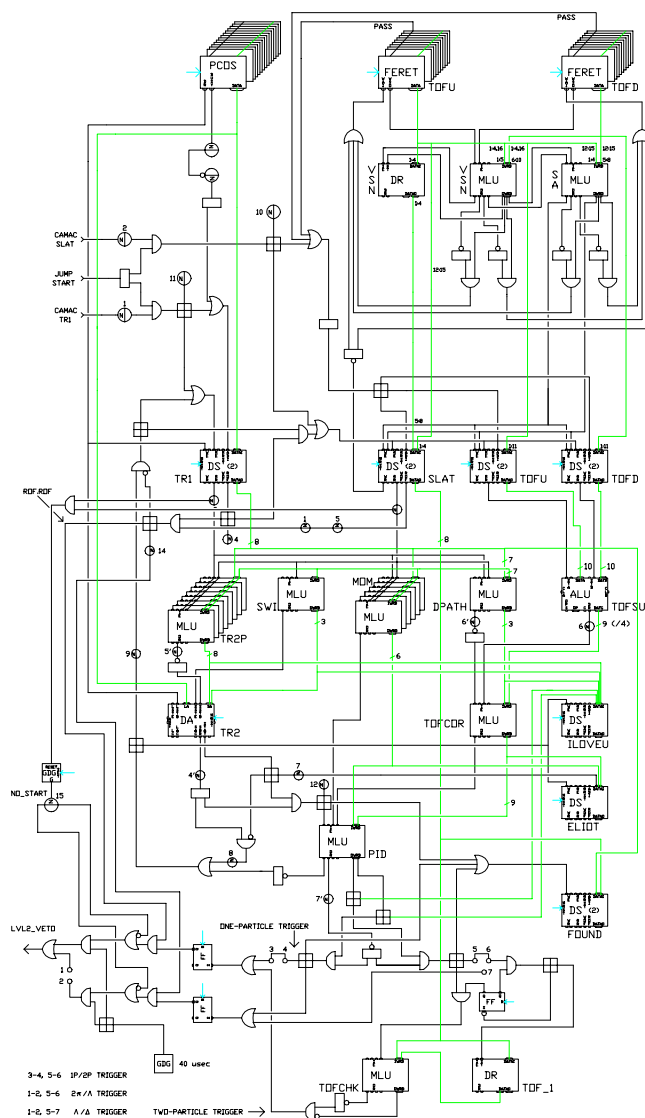


Figure 3-13: LVL2 trigger diagram. The basic flow of data through the trigger circuitry is from top to bottom. The block at upper right interrogates the TOF wall, the block at upper left provides computer control for testing. The data stacks and data array at middle hold the basic data inputs to the trigger. There is a loop at middle left that finds tracks and a block at middle right that determines p and β for found tracks. The pid MLU at lower center decides whether those values for a track constitute a desired particle. The lowest part of the circuit counts tracks for multiparticle triggers and sets the veto override at lower left for all type of triggers.

3.5. LVL2 TRIGGER

somewhat less cluttered flowchart of the trigger decision logic for the case of a single-particle trigger is shown in Figure 3-14.

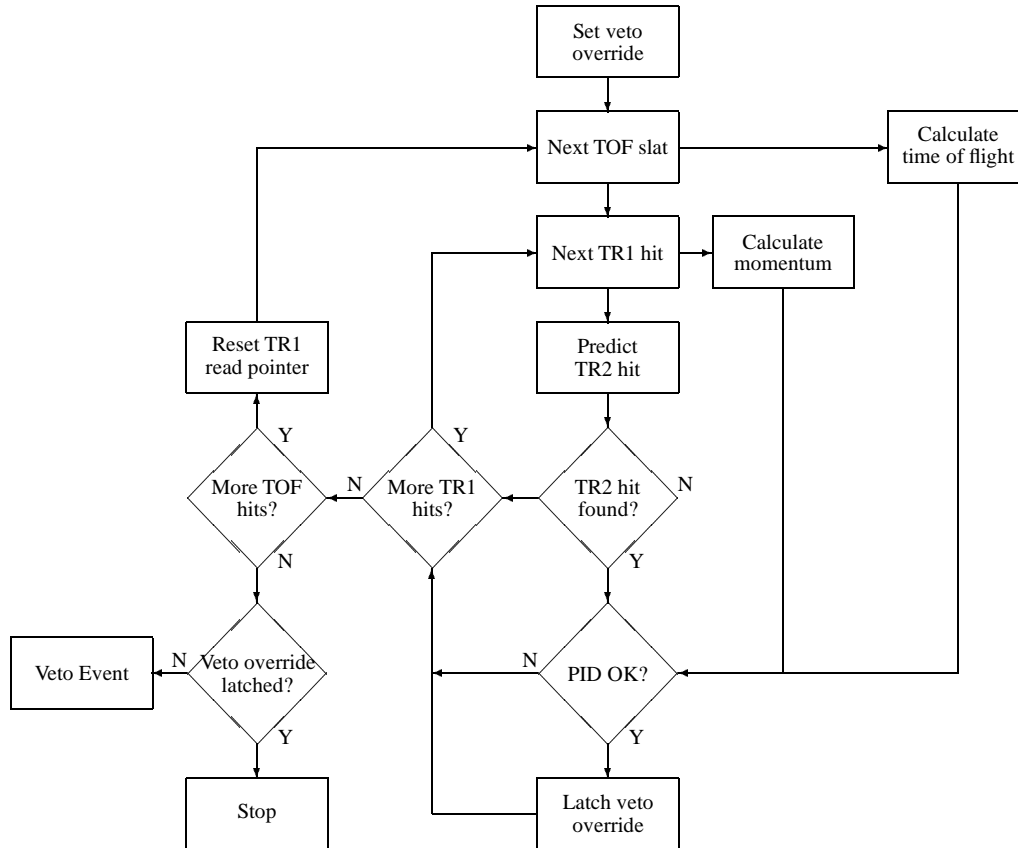


Figure 3-14: LVL2 flowchart for a single-particle trigger. The trigger is initialized by resetting all of the CAMAC modules and a flip-flop that can be set if a particle satisfying the trigger is found. An analog to a Fortran nested DO loop is performed over TR1 and TOF hits looking for aligned TR2 hits. The mass is calculated for found tracks, and if it satisfies the trigger, the flip-flop is set, preventing the event from being vetoed. If all of the hits are examined without finding the desired particle, the event is vetoed.

3.5.2 Operation of the LVL2 trigger

The LVL2 trigger serves as a veto for the TOF partition. What that means is that when the TOF partition generates an event, it will be kept unless the LVL2 trigger vetos it. In particular, for the single particle data taking, the LVL2 trigger was used as a veto for the SPEC trigger. It was used in

two basic ways, as a *tracking* trigger in which it only required the presence of tracks in the event, and as a *PID* trigger, in which particle identification requirements were also placed on the event. I will explain the tracking trigger operation first, because it is simpler, and then I will describe the additional parts of the PID trigger.

Tracking Trigger

Before each event, the LVL2 trigger is initialized. All of the data stacks and data arrays are initialized, and most importantly, the veto latching flip-flop is reset to false. If this flip-flop never gets set during the event, the event is kept.

After an event, data is loaded into the DS_TR1 data stack and the DA_TR2 data array from the PCOS III electronic readout of the trigger chambers (see Section 3.3.3). The FERET's begin digitizing the TOF wall times of flight, a process which takes $8\mu s$. Once they have finished digitizing, the slat number and up and down times for each slat begin to be read out of the FERA's and written into DS_SLAT, DS_TOFU, DS_TOFD data stacks, respectively. As soon as the first TOF slat is in place, the trigger begins its loop over TR1 wires. For each TOF slat, it takes each TR1 wire number in turn from the data stack and consults the MLU_TR2P lookup table to predict the TR2 wire that lies on a straight line between them. It looks in the DA_TR2 to see if that wire was hit. The data array has a programmable *search width* so that it doesn't require an exact match between the prediction and any of the entries in the data array, but will accept as a match anything within the search width of the lookup value.

If no match is found, the loop immediately proceeds to the next TR1 wire. DS_TR1 is configured as a circular buffer, so when the last wire has been read, it generates a *read overflow* and resets its read pointer to the first entry. That overflow causes the TOF data stacks to advance to the next slat. If there are no more entries in the TOF data stack, a condition called *ROF·ROF* is set. That means that both the TR1 and TOF data stacks have their read overflows set, and they have both examined all the data in the event. The trigger is done, and it sets the veto bit true.

However, if a match in the TR2 data array is found, the data word output of MLU_TR2P is set and forms the input to MLU_PID. For the tracking trigger setup, this MLU is filled with ones, and its output is set whenever MLU_TR2P is set. In the case of a one particle trigger, the data word of MLU_PID is used to change the state of another flip-flop which inhibits the veto flip-flop. Once a

3.5. LVL2 TRIGGER

condition satisfying the trigger has been found, the event cannot be vetoed.

PID Trigger

When the trigger is being used as a PID trigger, quite a bit more goes on. While a given TR1 wire and TOF slat combination is being checked against the list of TR2 hits, the TR1 wire and TOF slat number and times are being used in the other part of the circuit. MLU_MOM uses the TR1 wire and TOF slat to lookup a momentum for the track. They are also used as input to MLU_DPATH to lookup a path length for the track. The ALU averages the up and down TOF times and this is used with the path length as input to MLU_TOFCOR to lookup a β for the track. Combined with the momentum value from MLU_MOM, this gives enough information to calculate the mass of the track.

Whenever the tracking part of the trigger finds a track, MLU_PID is interrogated with the momentum and β of the track as inputs. The lookup table is binned in such a way that only certain combinations of momentum and β set the output true. If the output is set, it proceeds just as when the tracking trigger alone found a track—it set the flip-flop which inhibits the veto from being set.

When the PID trigger was used for collecting kaons, a mass window from $350 \text{ MeV}/c^2$ to $700 \text{ MeV}/c^2$ was typically used for the K^+ , and a window from $350 \text{ MeV}/c^2$ to $1300 \text{ MeV}/c^2$ was used for the K^- . The different windows were used to reduce the number of protons satisfying the K^+ trigger, while allowing for the collection of \bar{p} 's along with the K^- . Above a momentum of $2.5 \text{ GeV}/c$ all masses were allowed to satisfy the trigger, which compensates for the progressively worse mass resolution at higher momenta. For some of the running period the widening of the mass cuts occurred at $2.0 \text{ GeV}/c$ instead.

CHAPTER 3. EXPERIMENTAL DESCRIPTION

Chapter 4

Data Analysis

This chapter discusses the chain of analysis leading from raw data to final results. The first sections describe analysis which is common to all of the E859 data: track reconstruction and particle identification. After that the chapter is arranged topically, discussing various corrections and procedures specific to the single-particle kaon analysis.

4.1 Overview of Data and Analysis

The E859 single-particle kaon data set consists of over 11 million events taken during two running periods, one beginning in February 1991 (Feb91) and another in March 1992 (Mar92). The beam for both running periods was fully stripped ^{28}Si accelerated to 14.6 A·GeV/c. Five different spectrometer angle settings (5° , 14° , 24° , 34° , and 44°) and two different magnetic field strengths (2 kG and 4 kG) at both polarities were used (one exception, 5° running used only 4 kG).

The data was taken in individual runs of about 40,000 events, which fills a 200 megabyte 9-track tape, and takes about 30 minutes, more or less, depending on the exact trigger mix and the beam rate. Two types of targets were used, ^{27}Al and ^{197}Au . Table 4.1 summarizes the numbers of particles collected for the different systems in the single-particle running.

All of the single-particle data analyzed here were taken with a first-level SPEC trigger. Most runs also used the second-level (LVL2) veto in conjunction with the SPEC trigger to enhance the collection of rare triggers. Instead of collecting all particle types during every run, the trigger was often configured to select only one particular species, K^- for instance. This means that most runs

System	PID	5°	14°	24°	34°	44°	Total
Minimum Bias (in thousands)							
Si+Al	K ⁺	5	25	16	47	27	120
	K ⁻	6	12	14	7	5	44
Si+Au	K ⁺	9	62	19	47	14	151
	K ⁻	30	20	9	8	2	69
Central (in thousands)							
Si+Al	K ⁺	1	6	3	9	5	24
	K ⁻	1	3	3	1	1	9
Si+Au	K ⁺	2	15	5	11	4	37
	K ⁻	6	5	2	2	1	16

Table 4.1: Summary of statistics for E859 single particle kaon runs.

have no unbiased pions or protons, and in spite of the trigger, have only relatively small numbers of rare particles, making some run-to-run checks for consistency difficult. Runs in which the decision of the LVL2 veto was overridden were also taken to provide a way to check for biases introduced by the trigger. This is discussed in more detail in Section 4.6. Runs were also taken in which the LVL2 veto was configured in its track-finding mode in which it merely requires a straight-line coincidence of hits in TR1, TR2 and the TOF wall. In these runs, the LVL2 veto served as a super SPEC trigger.¹ These *NOPID* runs enhanced the collection of all particles in proportion to their natural abundance, and serve mainly to increase the usable statistics of pions and protons. Finally, a number of target-out runs were taken so that an appropriate subtraction of background could be made for the target-in runs.

The analysis chain begins with reconstructing tracks in the spectrometer and identifying the particles. Allowances are made for particle decays and inefficiency in reconstruction and particle identification, and then several corrections are applied to the data for specific problems that have been identified. The particles are binned, either in m_{\perp} versus y or p_{\perp} versus y , and transverse spectra in slices of rapidity are plotted from the binned data and fit with empirically motivated functions. These curves are then integrated to give the yield as a function of rapidity.

¹The term in vogue today would be SPEC++.

4.2. TRACK RECONSTRUCTION

The first part of the analysis is common to all the E859 data. There are three creatively, if not entirely accurately, named *passes* to which all of the data is subjected. During the first stage, PASS0, the data is consolidated from over 300 9-track tapes onto 50 8 mm tapes, calibrations and pedestals for some detectors are recorded in the collaboration database, and quite a few diagnostic histograms are generated. The second stage of analysis, PASS12, is primarily the track reconstruction pass. The final stage, PASS3, is the particle identification pass, and it has been run officially for the first time in the E802 collaboration's history on the E859 data. In addition to these major stages, there are a few special purpose analyses of subsets of the data. These include the TOF calibration pass (see Appendix C) which determined the timing calibrations for the time of flight wall, and the GASČ photoelectron threshold analyses [Sun94].

The main analysis module of PASS12, a new track reconstruction code called AUSCON, and the main module of PASS3, the particle identification code PICD, will be discussed in more detail in the following sections.

4.2 Track Reconstruction

The information that is used to reconstruct the tracks of particles in the spectrometer are the hits on the drift chambers T1–T4, trigger chambers TR1 and TR2 and the TOF wall. With these hits, the job of finding tracks then amounts to a complicated connect-the-dots problem. Designing, writing, debugging and testing reconstruction programs are probably the largest sinks of manpower and CPU time in the collaboration. This is partly because it is one of the most complicated pieces of software in the entire analysis chain, and partly because the reliable performance of the reconstruction program is of central importance to the quality of the analyzed data. It is also because everyone honestly thinks that he can write a better program. For the E802 data analysis, RECONSTRUCT, a program written by Martin Sarabura [Sar89] and Huan Huang was used [Hua90]. For the E859 analysis, a new program written by Peter Rothschild called AUSCON was used instead, and a detailed description of the algorithm and the code can be found in his thesis [Rot93]. I will give a brief overview of how AUSCON works and describe the procedure used to quantify its performance.

4.2.1 Overview of Algorithm

There are at least as many schemes for track finding as code authors, but one useful way in which some different algorithms can be classified is into *local* and *global* codes. RECONSTRUCT is a local code; it searches for small clusters of hits on individual chambers that form straight lines, then it tries to combine these track segments into the full track representing the particle's trajectory. AUSCON, on the other hand, is a more global code; it sketches a complete track using rough information, then searches for supporting hits within a search width about that initial guess and uses the found hits to refine the track. The reason for this approach is that it seems to make the algorithm less sensitive to effects like multiple scattering and missing or extra hits that may confuse the picture when viewed at a fine level of detail. AUSCON also uses the new tracking information provided by the detectors TR1, TR2 and T3.5 which were added after RECONSTRUCT was written.

AUSCON begins looking for tracks in the detectors behind the magnet. It does this because the environment there is less cluttered than in front of the magnet—many low momentum tracks have been swept out of the acceptance by the magnet, some particles have decayed, and some tracks not coming from the target do not make it through the magnet. There are certainly some sources of background for the rear chambers, such as tracks from interactions in the beam pipe, or spray off of the magnet yoke, but on the whole the rear chambers are still much cleaner. AUSCON starts with the detectors segmented in the bend plane: the x modules of the drift chambers, the trigger chambers TR1 and TR2, and the TOF wall. The segmentation of the detectors along this dimension is finer than in other directions, and since the magnet primarily spreads tracks out along this dimension, the task of track finding is somewhat easier. AUSCON forms its initial track guesses by drawing straight trajectories between hits on the TOF wall and hits on TR1. A search width of ± 1.5 cm about this line is used to collect hits on the x planes of T3, T4 and TR2. A similar loop over as yet unused hits on TR2 is performed, in order to find tracks that failed to produce a hit on TR1. Each collection of x hits is then fit with a straight line, and if one assumes the target position, this line determines the entire x projection of the trajectory.

Next, hits from the y modules are collected and added to each track. Since the TOF wall has both x and y information for each hit, this is done by taking the y location of the TOF hit for each x track, positing a target position and interpolating a path through the y module of the drift chambers behind the magnet. Again, a search width is drawn about this path and hits are collected. The

4.2. TRACK RECONSTRUCTION

segmentation in the y direction is not as fine as in the x direction, so it is possible at this stage for multiple x tracks to collect some of the same y hits. Pairs of y hits at the extreme ends of the track are connected with a line, and that line is combined with the already known x line to allow one to check whether there are enough hits on the u and v modules to support a track. If more than one track can be verified, the algorithm only keeps the track with the best fit to a straight line.

Each of these tracks is projected through the magnet using an effective edge model of the magnet, in which the real magnetic field is approximated with a constant field of fixed width. The strength, width and location of the field are chosen to reproduce the effects of the real field. This simplifies the projection of a track, so that, assuming a target position and knowing the track vector behind the magnet, the trajectory of the track in front of the magnet may be determined analytically. Next, hits are collected on T1 and T2 in a search width about the projection. The track density in front of the magnet makes it possible that more than one real track in T1 and T2 will be found within the search width, so AUSCON filters the candidates by imposing a matching cut. A cut is placed on the angle between the trajectory projected from the segment behind the magnet and the fitted segment in front of the magnet. If more than one candidate survives this, the T1T2 track with the best χ^2 is associated with the T3T4 track. A cut is also made on the projected track origin, requiring it to come within ± 2 cm of the run-by-run fitted target position. This cut was not properly applied when the PASS12 was run—the cut was placed at ± 2 cm about the nominal target position of $(0, 0, 0)$, not the fitted position, so a module was added to the PASS3 program which applied a symmetric cut about the correctly fitted target position. Since some of the tracks had been thrown out during PASS12 because they failed the original cut, the new cut had to be somewhat tighter than ± 2 cm, but for most runs the difference is small.

4.2.2 Momentum Determination

AUSCON calculates the momentum of found tracks by determining the magnitude of the bend in the magnet and then assuming that the portion of the particle's trajectory in the magnet can be well approximated as a segment of a circle. The magnet is modelled as a uniform field of constant strength with sharply defined edges. The width of the field in this approximation is fixed at 146.3 cm and it has an integrated $B \, dl$ of 1.5 Tesla-meters at its maximum field strength. A schematic of a particle trajectory through a magnet is shown in figure 4-1. In a uniform magnetic field, neglecting

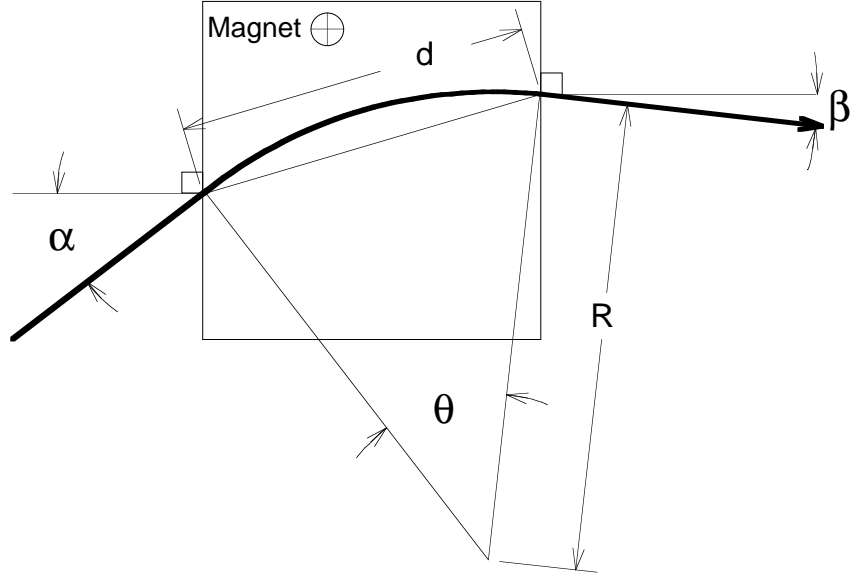


Figure 4-1: Determination of momentum from bend angle. This figure defines quantities used in formulae in the text.

energy loss, the momentum can be calculated from the Lorentz force law

$$\vec{F} = \frac{q}{c} \vec{v} \times \vec{B} = \frac{mv^2}{R} = \frac{qvB}{c}. \quad (4.1)$$

If we consider a track whose motion is entirely in the plane perpendicular to the magnetic field, then, in the units GeV/c, Tesla and meter, this may be written

$$p = \frac{qBR}{c} \approx 0.3BR. \quad (4.2)$$

For a track whose bend is entirely in the plane, the radius of curvature, R , and hence the momentum can be calculated from the two angles, α and β in the following way (see Figure 4-1)

$$\begin{aligned} \theta &= \alpha + \beta \\ R &= \frac{d}{2 \sin \frac{\theta}{2}} \\ p &= \frac{0.3Bd}{2 \sin \frac{\theta}{2}} \end{aligned} \quad (4.3)$$

4.3. PARTICLE IDENTIFICATION

If the track momentum has a small y component, there is a correction to the magnitude of the momentum because the projection into the xz plane of a small length ds of arc length is shortened. This makes the curvature of the track seem higher. The correction is

$$p' \approx p \times \sqrt{1 + \left(\frac{dy}{ds}\right)^2}. \quad (4.4)$$

The single track momentum resolution was discussed at some length in an early E802 memo [ZJ88]. There are several contributions to the momentum resolution, and the relative importance of each term depends on the total momentum of the track. This will be discussed in more detail in Section 4.3.2.

4.3 Particle Identification

For the E859 analysis, an extended particle identification (PID) scheme based on the work of Shigehiro Hayashi was used [H⁺93]. The code implementing the algorithm, PICD, differs in many ways from the earlier standard, PIAD, but embodies in a consistent way many of the features of the particle identification schemes which were already being used by others in their private analyses. The main difference between PICD and PIAD is that where the old algorithm used cuts in m versus p to separate different particle species, the new code uses cuts in $1/\beta$ versus p . The utility of this change is that the mass of a track does not have to be calculated. The nonzero resolution of the time of flight system means that it is possible to measure an unphysically short flight time for a particle, leading to a superluminal velocity and an imaginary mass. By making the mass calculation unnecessary, these problems are avoided. In this section I will give a summary of the PICD algorithm, show how the actual cuts in the code are determined, discuss the various calibrations, discuss how well the code performed, and examine sources of contamination, especially in the identification of kaons.

4.3.1 Overview of Algorithm

As stated above, PICD identifies particles principally through cuts in $1/\beta$ versus p which are then augmented with charge, GASČ and BACK counter requirements. The locations of the $1/\beta$ cuts are determined by calculating the expected width, σ , of the $1/\beta$ distribution as a function of momentum,

and placing the cuts at $\pm 3\sigma$ about the nominal curve for each particle. In addition, for most regions in the $1/\beta$ versus p decision space, a lower cut is put on the TOF wall ADC signal. At higher momenta, the cuts for different particles begin to overlap. For example, with 120 ps intrinsic timing resolution for the TOF wall, the pions and kaons begin to overlap at 1.8 GeV/c. Once particles begin to overlap, the GASČ and BACK counter are used to separate them, up to a momentum at which the heavier, and hence slower, particle also begins to fire the Cerenkov detector.

4.3.2 Determination of Cuts

In order to place the $1/\beta$ cuts properly, one must calculate the expected width of its distribution as a function of momentum. This width will have contributions from the intrinsic timing resolution of the TOF wall and uncertainties in the particle's momentum. The momentum term can be written as

$$\begin{aligned} d(1/\beta)_p &= d(E/p) = d\left(\sqrt{\frac{p^2 + m^2}{p^2}}\right) \\ &= -\frac{m^2}{p} \frac{1}{\sqrt{p^2 + m^2}} \frac{dp}{p} \end{aligned} \quad (4.5)$$

and the contribution arising from timing uncertainties can be written as

$$\begin{aligned} d(1/\beta)_t &= d(ct/L) = \sqrt{\left(\frac{c}{L}dt\right)^2 + \left(\frac{ct}{L^2}dL\right)^2} \\ &= \frac{ct}{L} \sqrt{\left(\frac{dt}{t}\right)^2 + \left(\frac{dL}{L}\right)^2}, \end{aligned} \quad (4.6)$$

where dt is the intrinsic timing resolution of the TOF wall and dL is the uncertainty in the path length, all other things being fixed. In E802, the quoted intrinsic timing resolution, dt , of 75 ps for the TOF wall was obtained using a single slat with coincidence scintillators in a secondary beam. In E859, the TOF wall intrinsic timing resolution is calibrated using identified particles, and a resolution of 120 ps is found instead (see Appendix E for details). If we use either of these values for the timing resolution, a time-of-flight of 25 ns, and a path length of 660 cm with an uncertainty of 1 cm, then the $\frac{dt}{t}$ term makes a much larger contribution to the uncertainty in $1/\beta$ than the uncertainty in the path length. Because of this, the PICD code uses a constant path length and neglects the $\frac{dL}{L}$ contribution to the uncertainty in $1/\beta$.

4.3. PARTICLE IDENTIFICATION

The momentum term and the timing term are then added in quadrature to give the total uncertainty in $1/\beta$

$$d(1/\beta)^2 = d(1/\beta)_p^2 + d(1/\beta)_t^2. \quad (4.7)$$

Using the expression for momentum from Equation 4.3, one can relate the uncertainty in momentum to an uncertainty in measuring the bend angle

$$p = \frac{0.3Bd}{2 \sin(\theta/2)} \quad (4.8a)$$

$$dp = -\frac{0.3Bd}{4} \frac{\cos(\theta/2)}{\sin^2(\theta/2)} d\theta \quad (4.8b)$$

$$\frac{dp}{p} = -\frac{1}{2} \frac{\cos(\theta/2)}{\sin(\theta/2)} d\theta \quad (4.8c)$$

$$\approx -\frac{1}{2} \frac{1}{\theta/2} d\theta \quad (4.8d)$$

$$= -\frac{d\theta}{\theta}. \quad (4.8e)$$

The uncertainty in θ comes from contributions due to the spatial resolution of the drift chambers and due to multiple scattering. Referring to Figure 4-1, one obtains that the bend angle can be written as $\theta = \alpha + \beta$, so the uncertainty in θ is $d\theta^2 = d\alpha^2 + d\beta^2$ which may be expressed in terms of the chamber resolution dx as

$$d\theta = \frac{\sqrt{2}dx}{D} \quad (4.9)$$

where D is the distance between chambers, and dx is the spatial resolution of the chambers, which is assumed to be the same for all the drift chambers.

The effect of multiple scattering on the uncertainty in θ is discussed in a paper by Highland [Hig75], and the spread in θ obtained there is

$$d\theta = \frac{17.5}{p\beta c} \sqrt{\frac{X}{X_R}} (1 + \varepsilon(L)) \quad (4.10)$$

where X/X_R is the number of radiation lengths of material traversed and $\varepsilon(X)$ is given by

$$\varepsilon(X) = 0.125 \log_{10}\left(\frac{X}{0.1X_R}\right). \quad (4.11)$$

Adding Equations 4.9 and 4.10 in quadrature and using

$$p = \frac{0.3Bd}{2 \sin \theta/2} \approx \frac{0.3Bd}{\theta}$$

gives

$$\begin{aligned} \left(\frac{dp}{p}\right)^2 &= \left(\frac{d\theta}{\theta}\right)^2 = \left(\frac{1}{\theta} \times \frac{\sqrt{2}dx}{D}\right)^2 + \left(\frac{1}{\theta} \times \frac{17.5}{p\beta c} \sqrt{\frac{X}{X_R}(1 + \varepsilon(X))}\right)^2 \\ &= \left(\frac{p}{0.3BL} \frac{\sqrt{2}dx}{D}\right)^2 + \left(\frac{p}{0.3BL} \times \frac{17.5}{p\beta c} \sqrt{\frac{X}{X_R}(1 + \varepsilon(X))}\right)^2 \end{aligned} \quad (4.12)$$

$$\equiv (C_1 p)^2 + (C_2 \times \frac{1}{\beta})^2 \quad (4.13)$$

The reason for lumping all of the constants into C_1 and C_2 is that the values to use for some of the underlying constants are somewhat unclear. For example, the spatial resolution dx , depends to some extent on details of the track reconstruction algorithm—the chambers may have $200 \mu\text{m}$ intrinsic position resolution, but if the reconstruction code systematically chooses the wrong hits to assign to the track, the effective resolution will be worse. It also depends on whether one should use the single plane resolution to specify values for these constants. The dependence of the expression on p and $1/\beta$ has been separated out and the formula is fit to data to extract C_1 and C_2 . Finally, putting everything together, one obtains

$$d(1/\beta)^2 = \left(\frac{c}{L} dt\right)^2 + (C_1 p)^2 + \left(\frac{C_2}{\beta}\right)^2. \quad (4.14)$$

Setting the scale for the contribution of the different terms in the expression, Vince Cianciolo has shown that the contribution of the spatial resolution to the overall uncertainty is small compared to contribution from multiple scattering [Cia94].

A summary of the particle types assigned to regions in $1/\beta$ versus p space is shown in figure 4-2. Each sweeping band shows the 3σ contours of the distribution for different particles. Within a band, the different regions in the diagram correspond to the different types of additional cuts placed on the data. There are several regions that are important for the kaon analysis. At the lowest momenta, TOF alone is enough to identify kaons. Beginning at a momentum of roughly $1.8 \text{ GeV}/c$, the GASČ and BACK counter are also examined to make the PID decision. The exact momentum value at

4.3. PARTICLE IDENTIFICATION

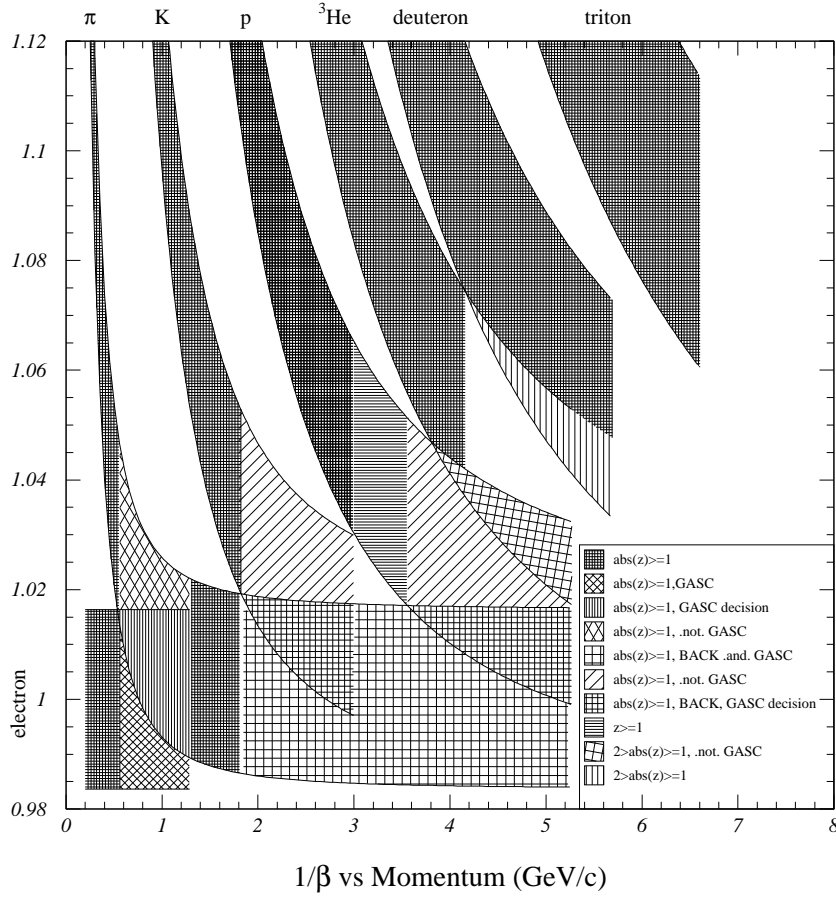


Figure 4-2: PICD Particle identification cuts for a 4kG magnetic field setting assuming 120 ps intrinsic timing resolution on the TOF wall. The bands represent cuts placed at the $\pm 3\sigma$ contours of distributions for the different particles. The differently hatched regions correspond to additional types of cuts placed on the data. In the diagram, the electron band also applies to positrons. In the legend, z is the charge of the particle, as determined by the energy loss in the TOF slat.

which this switch-over occurs depends slightly on the magnetic field, because the width of the PID bands, and hence the momentum at which the 3σ pion and kaon contours overlap, depends on the momentum resolution which depends on the magnetic field. In the PID region above 1.8 GeV/c and outside of the pion band, a track must be BACK counter verified and not fire the GASČ to be called a kaon. If the GASČ fires or the track is not BACK counter verified, it is not identified at all. These unidentified particles may be real particles that share a TOF slat, giving a spurious time-of-flight to one of the tracks, or they may be uncommonly large multiple scattering events, or something else may have fired the GASČ. In the region of the kaon band that overlaps the pion band, the decision is slightly different. BACK counter verification is still required, but if the GASČ fires, the track is a pion, otherwise it is a kaon. Depending on the fraction of real pions that fail to fire the GASČ and the ratio of pions to kaons in this momentum region, this is possibly a source of pion contamination of the kaons. This contamination will be examined in Section 4.5. Even though the kaons outside the pion 3σ band can be uniquely identified by TOF alone, the requirement that the GASČ not fire is demanded of all kaons above the π -K separation limit so that they are all subjected equally to the same PICD biases. For instance, if this were not done, then the kaons which need the GASČ in order to be separated from the pions would also show the effect of the $\sim 10\%$ absorption in the GASČ, while the kaons outside the pion band would not be affected by this.

4.4 Reconstruction and PID Efficiency

After a particle is emitted from a collision many things conspire to keep you from actually detecting it. Absorption and multiple scattering in the material of the spectrometer, inefficient detectors and particle decay can all prevent a particle originally headed into the spectrometer acceptance from being reconstructed and identified. In order to properly calculate particle yields, one needs to know the probability, ρ , that an emitted particle will be detected and properly identified. Then, when a particle is seen in the experiment, you assume that it actually represents $1/\rho$ particles that started out toward the spectrometer. This probability is called the *efficiency*, and it has contributions from the efficiency of track reconstruction and the probability of properly identifying the type of particle that made the track. In principle the efficiency for each particle species is a function of many variables: the kinematic variables of the track, the multiplicity, the spectrometer angle setting, and so on. In

4.4. RECONSTRUCTION AND PID EFFICIENCY

practice, it is only mapped as a function of a few variables, with the variation in the efficiency as a function of momentum having the largest effect. In this section, the efficiency for single kaons is determined; in the next section the effect of the GASČ on the efficiency is investigated. These two effects are treated as independent and are multiplied together to give a weight that is used particle by particle when filling the cross-section histograms.

In large part, the efficiency is determined by generating an ensemble of single-particle events using the E859 Monte Carlo (a simulation of the experiment built upon the GEANT package from CERN) and then using the PASS12 and PASS3 programs to reconstruct and identify the tracks. The number of events in which the particle or particles in question are correctly identified divided by the total number of events generated is the efficiency. GEANT is used to determine the efficiency of single-particle events as a function of momentum; other contributions to the efficiency are handled differently. The degree to which event multiplicity reduces the efficiency is taken directly from the study made by Peter Rothschild [Rot93]. He generated ensembles of 10,000 events for each of several multiplicities of 1 GeV/c protons in the the spectrometer. By reconstructing the events and counting how many of them contained the original multiplicity, he estimates that each additional fully reconstructed track in the spectrometer reduces the reconstruction efficiency by 2.3%. This parameterization of the effect of multiplicity has been used without modification in calculating the kaon cross sections.

To determine the momentum dependence of the efficiency, events are generated as input to the Monte Carlo by fixing p , and then randomly choosing θ and ϕ until the particle is within the spectrometer acceptance, as determined by a version of the same analytic routine used to calculate the geometric acceptance of the spectrometer in the cross section code (see Section 4.7). This does lead to an averaging over the angular coordinates that is not exactly like the data, but it is not thought to have a big effect on the results. Ensembles of 2000 single particle events each are generated in momentum steps of 0.1 GeV/c from 0.4 GeV/c to 2.9 GeV/c. The number of events in which the original particle is reconstructed and properly identified are counted and divided by the 2000 events generated to give the efficiency. The results as a function of momentum are shown in Figure 4-3. The Monte Carlo results are fit piecewise with smooth functions and those functions are used when filling cross section histograms to assign a weight to each particle. The dotted lines show the analytic decay curves for kaons and pions as a function of momentum. The number of

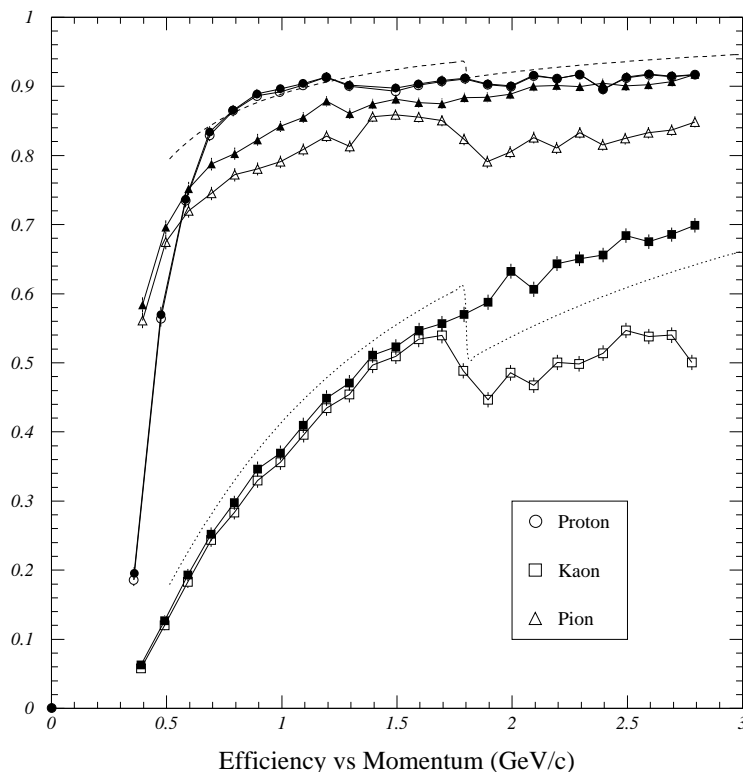


Figure 4-3: Efficiency for reconstructing and identifying various particles in the spectrometer as a function of momentum. The filled symbols mark the efficiency for track reconstruction alone, the open symbols mark the efficiency for reconstruction and proper identification. The solid lines are just to connect related symbols. The dotted line shows the decay curve for kaons, based on Equation 4.15. The dashed line is the same curve for pions. The abrupt drop in the decay curves at about 1.8 GeV/c occurs because above that momentum the GASČ is required to separate pions and kaons, and as part of that decision the particles are required to travel an additional 300 cm for BACK counter verification. This only affects the PID efficiency, as track reconstruction only uses information out to the TOF wall. In addition, there is some absorption in the GASČ, further increasing the difference between the reconstruction and PID efficiencies.

4.4. RECONSTRUCTION AND PID EFFICIENCY

particles surviving a flight distance L is derived from the exponential decay law

$$N = N_0 \exp\left(-\frac{t}{\gamma\tau}\right) = N_0 \exp\left(-\frac{L}{\beta\gamma c\tau}\right) = N_0 \exp\left(-\frac{Lm_0}{pc\tau}\right) \quad (4.15)$$

where L is the path length travelled by the particle, p is the momentum, m_0 is the rest mass and τ is the lifetime of the particle, which is often given instead in the combination $c\tau$. Kaons have $c\tau = 370$ cm, pions have $c\tau = 780$ cm [Gro90].² As the plot shows, for unstable particles at low momenta, decay is the most important reason for particle loss—only 41% of the kaons at 1.0 GeV/c could be expected to survive to the TOF wall. Even if a particle decays before the TOF wall, there is a chance that it will be reconstructed, especially if it decays very near the TOF wall. Since applying a correction based on the survival fraction as given in Equation 4.15 implicitly assumes that none of the decaying particles is reconstructed, this would result in an overcorrection to the data. Charles Parsons has shown that this makes a noticeable difference in the efficiency curve for reconstructing pions [Par92], but given the difference in the Q of the principal decay channels for pions and kaons, $\pi \rightarrow \mu\nu$ and $K \rightarrow \mu\nu$, one would expect this to be much less of a problem for kaons. For kaons between 1 and 2 GeV/c, the mean angle that the muon makes with respect to the incident direction of the kaon ranges from 10° to 20° , which makes it unlikely that the track will be reconstructed. The abrupt drop in the surviving fraction occurs when the GASČ is needed for particle identification, because the particle is then required to survive an extra 300 cm to the BACK counter for verification.

As a further check on the sensibility of the GEANT results, Table 4.2 shows what happens to the reconstruction and PID efficiency for 1 GeV/c protons as more and more mechanisms that can cause particle loss are turned on (protons are used so that decay is not an issue). If hadronic interactions and multiple scattering in the GEANT simulation are turned off, and the chambers are given perfect efficiency, all protons thrown in the acceptance are both reconstructed and identified. Turning on hadronic interactions causes a 3-5% loss in the number of protons. This rate of loss should be fairly constant for all momenta and particle species. Turning on multiple scattering causes another 1% loss, but for protons at 1 GeV/c this would not be expected to be a large factor. Finally, randomly discarding 2% of the hits per plane in each of T2–T4, and 15% of the hits in

²For protons, the current lower limit is roughly $c\tau \geq 10^{33}$ light-years.

T1 (T1 is quite a bit less efficient than the other chambers), causes another 5% loss. It's not

Description	Reconstruction	Total
No Losses	100%	100%
Hadronic Interactions	$96.4 \pm 0.6\%$	$96.4 \pm 0.6\%$
Multiple Scattering	$94.7 \pm 0.7\%$	$94.3 \pm 0.7\%$
Chamber Inefficiency	$89.3 \pm 1.0\%$	$89.0 \pm 1.0\%$

Table 4.2: Contributors to PID inefficiency for 1 GeV/c protons on the spectrometer. In each succeeding line a further mechanism for particle loss is turned on. In the top line, no processes are enabled, resulting in 100% efficiency for reconstruction and for reconstruction plus particle identification. Hadronic interactions are then turned on, resulting in a loss of 3% of the protons. Multiple scattering is enabled in the next line, causing only a slight loss at this momentum. In the last line, a chamber-dependent inefficiency per plane is introduced. This final entry has the same processes enabled as is used to generate the plot of efficiency as a function of momentum shown in Figure 4-3.

very straightforward to calculate beforehand the effect on the reconstruction efficiency of chamber inefficiencies. AUSCON is designed to handle some missing hits when it tries to find tracks in the spectrometer, making it somewhat robust with respect to hit loss. However, the inefficiencies on each plane are not independent quantities, as they are being treated here. If a track passes through an unusually inefficient region in a drift cell on one plane of a module, it is likely that it will pass through the corresponding region of the next plane, leading to correlated inefficiencies. So, it is a bit of a cheat to treat the planes as independent. However, several different efforts at visual scanning of tracks in the spectrometer have led to results for track reconstruction in basic agreement with the Monte Carlo results.

4.5 Effect of the GASČ on Kaon Identification

Above the point at which the pion and kaon $1/\beta$ versus p bands begin to overlap (~ 1.8 GeV/c), the GASČ information is used in the particle identification decision for kaons. The effect of the Čerenkov detector on the identification of kaons is quite important, especially considering that at 5° over half of the kaons are above this π -K TOF separation limit. Above this threshold, and below the 2.9 GeV/c limit where kaons cease to be identified (because they also begin to fire the GASČ)

4.5. EFFECT OF THE GASČ ON KAON IDENTIFICATION

the PID decision has three distinct regions (refer to Figure 4-2). In all three regions BACK counter verification is required to identify any particle. In the region at highest $1/\beta$, the kaons can be unambiguously separated from the pions by TOF alone, but if the GASČ fires the particle is not identified. In the region of the kaon band that overlaps with the pions, if the GASČ fires, the particle is called a pion; if it does not, the particle is called a kaon. Finally, in the region at lowest $1/\beta$, where the pions can be unambiguously separated from kaons by TOF alone, if the GASČ fails to fire, the particle is not identified. The study of the GASČ efficiency will take advantage of these different regions to select pions or kaons above the TOF separation limit that can still be uniquely identified by time of flight, and by studying the behavior of the GASČ for these particles, we can estimate what happens in the overlap region where the detector has to be used to tell pions from kaons.

There are two effects related to the GASČ that can influence the number of kaons that are identified. One is the rate at which kaons appear to fire the GASČ, even though they are below threshold. This could be due to the production of δ -rays in the GASČ, or kaons decaying into muons. This part of the contribution is a single-particle effect due to physics related to the kaons alone, and should already be taken into account in the GEANT simulation used to determine the efficiency in Section 4.4. A more likely reason the GASČ would fire for a true kaon is a background track above the threshold velocity. Since the PICD algorithm adds together the ADC signals from adjacent GASČ cells, a track pointing to the same cell as the kaon, or any of the surrounding cells, can make it appear that the kaon fired the GASČ. This masking of kaons is a multiparticle effect, and because of this, it is expected that the problem will be greatest at 5° , where the particle multiplicities are the highest. The other effect that distorts the number of kaons is contamination by pions that fail to fire the GASČ. The importance of this effect depends on the π/K ratio for the particular conditions of the run being examined. It will be different for different targets, for different angle settings, for different magnetic fields. Unfortunately, there are not enough statistics to really determine the magnitude of the effect for each of the different TMA cuts used in this analysis, so a study of the minimum bias data will be made and the importance for other event selections will be estimated.

4.5.1 Multiparticle GASČ Effects Leading to Kaon Loss

If a high velocity particle hits the same GASČ cell that a kaon points to and fires it, the kaon will be misidentified. By examining the rate at which uniquely TOF identified kaons fire the detector, we can estimate the losses, which can become quite severe for the 5° spectrometer setting. One can select particles above the π -K separation threshold whose TOF is consistent with a kaon PID hypothesis and are outside the pion PID band and look at the number that fire the Čerenkov detector and are BACK counter verified. These particles are presumably real kaons which, for whatever reason, point to a GASČ cell that has fired. For an accurate estimate of the rate at which this happens to real kaons, it is especially important that we know the sample of particles that we're using are not pions. So, in addition to the these cuts, I have imposed additional $1/\beta$ cuts to keep the sample free of particles near the π -K boundary. At 5° , the fraction of these particles that fire the GASČ is a strong function of where on the TOF wall the particle hits. This is shown in Figure 4-4, where the fraction is plotted as a function of the TOF panel number hit by the track (n.b.: higher panel numbers are nearer the beam pipe). Away from the beam, the rate is 10–15%, while near the beam the rate quickly rises to $\sim 35\%$. This rate remains unchanged even if a cut to remove events in which two reconstructed tracks point to the same cell is imposed. Therefore, the effect is likely due to tracks not coming from the target, perhaps due to downstream interactions in the beam pipe, which scatter into the GASČ and fire the detector. Also shown in the figure is the rate for back angles (34° and 44°) for which perhaps $\sim 5\%$ of the kaons fire the detector, consistent within the statistics with having no dependence on TOF panel number. There seems to be a baseline rate of 10% at forward angles, smoothly decreasing as one rotates the spectrometer backward, with an exceptional rate at extremely forward angles. The effect at 5° is parameterized as a 10% effect up to panel 5, then a linear increase up to 35% for panel 8, the limit of the acceptance for 5° . At other angles, the effect is parameterized as a flat 5%.

4.5.2 Pion Contamination of Kaons

To estimate the pion contamination of the kaons, we examine the fraction of pions outside the overlap region in $1/\beta$ versus p that fail to fire the GASČ. Figure 4-5 shows the fraction of BACK counter verified tracks firing the GASČ as a function of $1/\beta$ for a slice in momentum from 1.8 GeV/c to 2.2 GeV/c. Between these momenta, the tails of the kaon and pion bands have just begun to

4.5. EFFECT OF THE GASČ ON KAON IDENTIFICATION

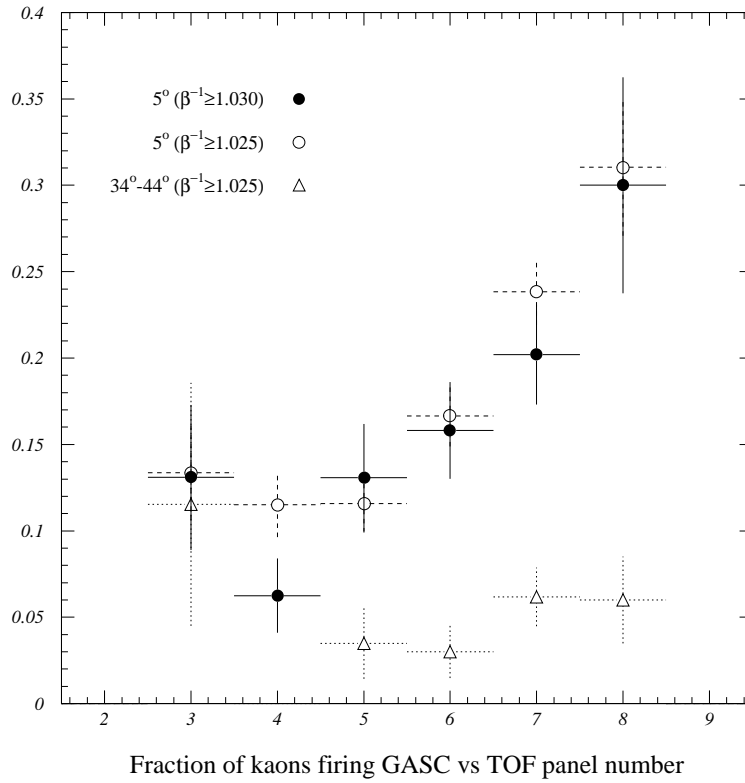


Figure 4-4: Fraction of TOF identified kaons firing the GASČ versus TOF panel number, where higher panel numbers are nearer the beam pipe. The kaons selected are outside the pion PID band, and to eliminate the possibility that the rise in the fraction of kaons firing the GASČ is due to a tail of the pion distribution, two different $1/\beta$ cuts have been tried as well. The rise is clearly seen in the 5° data, and is not seen in data taken from back angles.

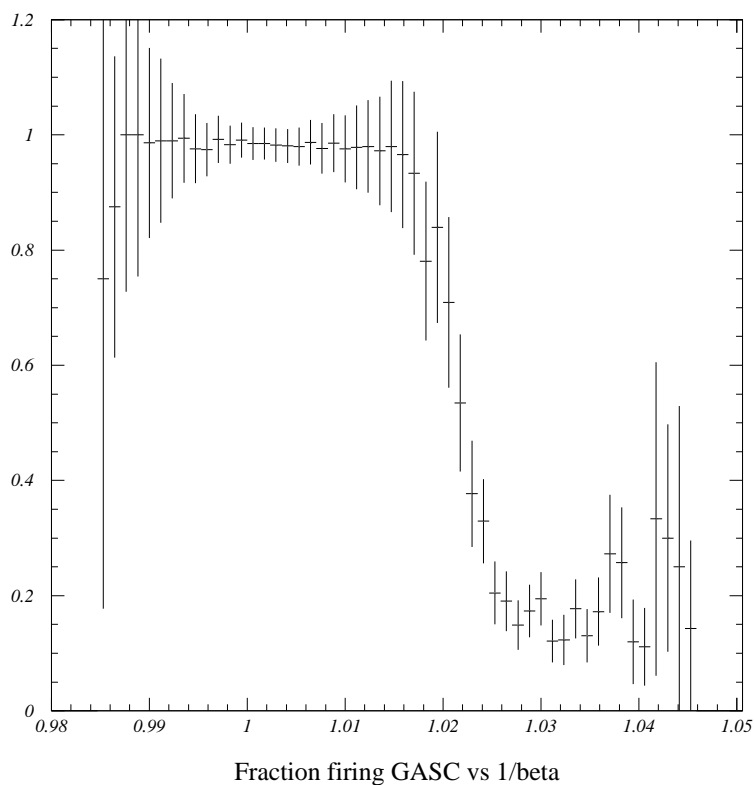


Figure 4-5: Fraction of tracks firing the GASČ for BACK counter verified tracks in Si+Au data taken at 14° for the momentum range $1.8 < p < 2.2 \text{ GeV/c}$. The large broad peak at left is the middle of the pion band, showing that about 1.5% of the pions fail to fire the detector. The data at right is a part of the kaon band, showing that about 10–15% of the kaons do fire the GASČ, which would cause them not to be identified.

4.5. EFFECT OF THE GASČ ON KAON IDENTIFICATION

overlap, but the peak of the kaon band is still well outside the $\pm 3\sigma$ pion band. Therefore the pions are relatively uncontaminated by the kaons, and vice-versa. The fraction of pions near the center of the pion region, ($0.995 < 1/\beta < 1.01$), that fail to fire the GASČ is 1.5%, and is fairly flat in $1/\beta$ over the width of the pion region. A similar examination of the pions uniquely identified by TOF as a function of momentum shows that the fraction of these pions firing the GASČ as a function of momentum is independent of momentum. Since the fraction is flat in these two views, I assume that it is flat throughout the kaon overlap region also and use that to calculate the contamination of kaons.

The seriousness of the pion contamination depends on a few things: the relative abundance of pions and kaons, the fraction of the data that depends on the GASČ for identification, and whether the contamination is a flat function of (y, m_{\perp}) . For instance, if the π/K ratio were 100:1 and 1% of the pions were misidentified as kaons, half the identified kaons would actually be pions. At back angles, where only a small portion of the m_{\perp} distribution requires the GASČ, even this degree of contamination makes little difference to the extracted m_{\perp} slope, or the dn/dy . However, above $y \approx 1.8$, where all of the kaon data requires the Čerenkov information, this would have a big effect. In addition, if the contamination is not uniformly distributed in m_{\perp} , it will change the slope of the m_{\perp} distribution. Much of the 5° kaon data depends completely on the GASČ, so the following corrections have special significance for that spectrometer setting.

Since only the pions in the overlap region can be misidentified as kaons because of the GASČ, I plot in Figure 4-6, the ratio of all kaons to pions in the overlap region multiplied by the 1.5% that are expected to be misidentified, as a function of momentum for Si+Au minimum bias data taken at 5° . At threshold (~ 1.8 GeV/c), there is no overlap of pions and kaons (at the 3σ level), so no contamination. As the momentum increases, the contamination becomes more and more severe, rising to as much as $\sim 30\%$ for K^- and $\sim 10\%$ for K^+ . The same correction is applied to both the Si+Al and Si+Au data.

4.5.3 Corrections Applied to Data

To assemble the two effects, multiparticle kaon masking and pion contamination, into a single correction for the kaon data, define two quantities, C_K and C_{π} as the fraction of *true* kaons and pions that fire the GASČ. C_K refers to all the true kaons above the π -K momentum separation limit,

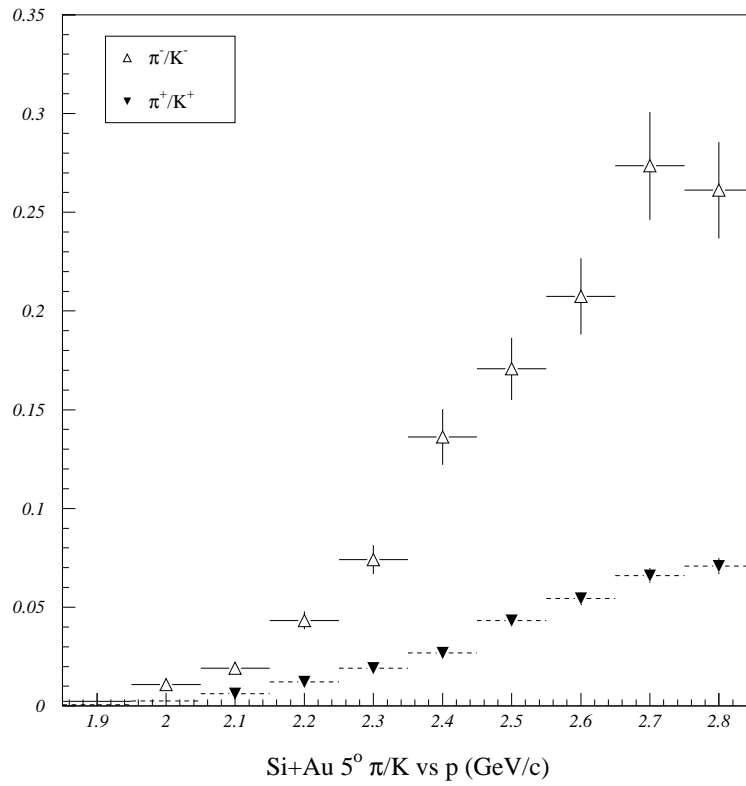


Figure 4-6: K/π Ratio versus p for GASČ Correction

4.5. EFFECT OF THE GASČ ON KAON IDENTIFICATION

while C_π only refers to the true pions above that limit that are in the region of $1/\beta$ versus p that overlaps with the kaons. This is done because those are the only pions that could possibly become kaons if the GASČ fails to fire. As discussed above, C_K is primarily a function of angle, while C_π is a constant 98.5%. Using these quantities, we can express the number of *measured* kaons and pions, K_m and π_m , in terms of the true numbers of kaons and pions, K_t and π_t as

$$K_m = (1 - C_K)K_t + (1 - C_\pi)\pi_t \quad (4.16)$$

and

$$\pi_m = C_K K_t + C_\pi \pi_t. \quad (4.17)$$

Substitute Equation 4.17 into Equation 4.16 to give

$$K_m = (1 - C_K)K_t + \frac{1 - C_\pi}{C_\pi}(\pi_m - C_K K_t), \quad (4.18)$$

Solve for the number of true kaons,

$$K_t = \frac{C_\pi K_m - (1 - C_\pi)\pi_m}{C_\pi(1 - C_K) - C_K(1 - C_\pi)}, \quad (4.19)$$

and rearrange to put this explicitly in term of quantities (e.g., π_m/K_m) that we have just determined

$$K_t = \left(1 - \frac{1 - C_\pi}{C_\pi} \frac{\pi_m}{K_m}\right) \frac{K_m C_\pi}{C_\pi(1 - C_K) - C_K(1 - C_\pi)}. \quad (4.20)$$

The coefficient C_K is determined as a function of TOF panel for 5° and 14° data, because these are the two angle settings most affected by the GASČ correction. At back angles, the pion spectrum is softer, resulting in fewer pions above the π -K threshold, and less of the kaon p_\perp distribution is dependent on the GASČ, making the effect of any correction less important. Because of this, the effect of the pion contamination is neglected except for 5° and 14° . At the other spectrometer angle settings, the effect of the kaon masking is set to a constant 5%. The fraction π_m/K_m is taken from the parameterization as a function of momentum shown in Figure 4-6.

4.6 LVL2 Trigger Biases

A *bias* in a trigger arises when the trigger has unaccounted for inefficiencies that are dependent on some feature of the data. For example, one might design a trigger to reject events not containing kaons, but find that it also rejected events with more than one particle in the spectrometer. Since the probability of having two or more particles in the spectrometer should be correlated with the overall multiplicity of the event, you may wrongly conclude that there is a dearth of kaons in high multiplicity events. When using any trigger, one has to worry about such sources of possible bias, and the LVL2 trigger is, of course, no exception. However, there are two features of the LVL2 trigger that make checking it for bias somewhat difficult.

- First, the LVL2 veto is not a simple trigger. It is not just a discriminator threshold on an analog signal, but uses a wide variety of input data and makes a complicated calculation to determine whether to reject an event.
- Second, the LVL2 trigger is a very selective trigger. To check the trigger for biases against kaons, you have to look through untriggered data, identify kaon-containing events and see if there are any systematic problems in the decision that the trigger would have made for those events. The rarity of kaons means that you will necessarily have poor statistics for this type of search, and you may not be able to identify problems with a great deal of certainty.

In order to study the efficiency of the LVL2 trigger, runs were taken in which the LVL2 decision was recorded but not allowed to actually determine whether or not the event was kept. Using these *veto out* runs one can plot the number of events that contain kaons but would have been rejected by the LVL2 trigger. In two such runs, 10884 and 10885, 988 events containing at least one kaon were found by the offline combination of AUSCON and PICD. Of these, 15 events had the veto bit in trigger word 2 set, indicating they would have been vetoed by the LVL2 trigger, and these events were further examined using the event display, EDISP. Plotting the tracks of the kaons, the hits corresponding to the kaon were located in the event and checked to see if any reason could be found for the trigger rejecting the event. Three events were found to be missing trigger chamber information and were eliminated from the sample. The LVL2 trigger cannot make allowances for missing trigger chamber hits, so the reason for the discrepancy between the offline and online

4.6. LVL2 TRIGGER BIASES

decision in these three events is clear. The loss of particles due to trigger chamber inefficiency is an issue separate from losses due to decisions made by LVL2 trigger, and is not counted as a LVL2 trigger bias.

The distribution in momentum versus mass of the remaining twelve events is shown in Figure 4-7. The open symbols show the offline determination of mass and momentum, given the track as reconstructed by AUSCON and the time-of-flight recorded in the LVL1 TOF banks. The filled symbols show the mass and momentum calculated using the LVL2 emulator. The straight lines in

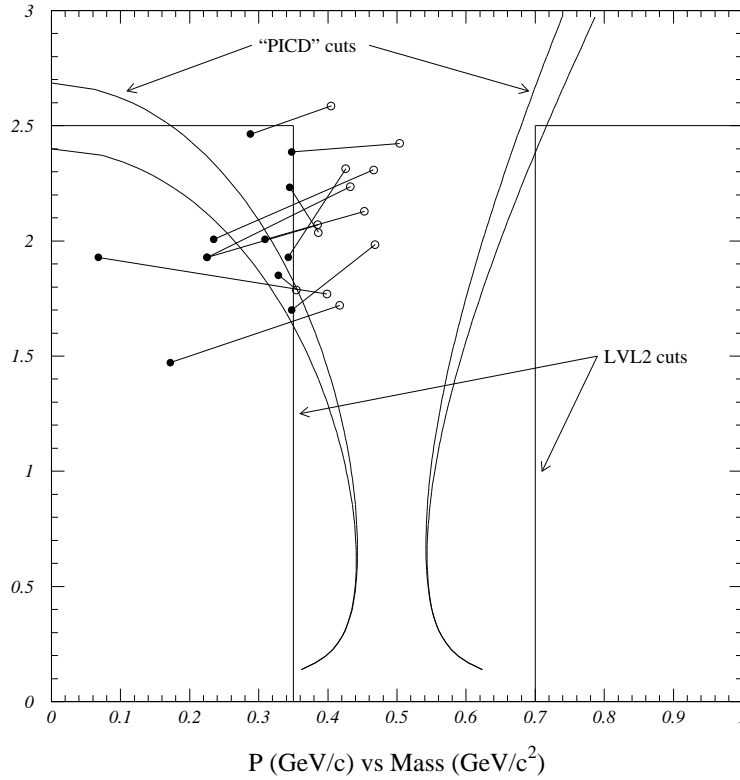


Figure 4-7: Online and offline masses for rejected kaon events. The LVL2 trigger accepts events when the online calculation of the particle mass lies within the region marked as *LVL2 cuts*, positioned about the nominal kaon mass of $0.494 \text{ GeV}/c^2$. The open symbols are the masses for kaons calculated offline by AUSCON, the filled ones are calculated in the same manner as is done in the LVL2 trigger. The straight lines are the momentum versus mass cuts used online, the curved lines show two sets of PICD-type $1/\beta$ versus p cuts. The inner set (labelled “PICD” cuts) are for a TOF resolution of 120 ps; the outer ones are for a resolution of 150 ps.

Figure 4-7 represent the online p versus m cuts used in the LVL2 trigger. The cuts for these runs accepted masses between $0.350 \text{ GeV}/c^2$ and $0.700 \text{ GeV}/c^2$ up to $2.5 \text{ GeV}/c$; above that momentum, all masses were accepted. The cuts are placed asymmetrically about the nominal kaon mass of $0.494 \text{ GeV}/c^2$ because the mass of the pion is fairly close to the mass of a kaon, and the cut had to be pulled in slightly compared to the placement of the cut on the proton side of the mass region to avoid swamping the trigger with pions. The curves in the figure represent what the PICD type $1/\beta$ versus p cuts for two different choice of intrinsic TOF wall timing resolution look like in LVL2 decision space. The narrower flaring cuts about the kaon mass correspond to an intrinsic resolution of 120 ps, the wider cuts 150 ps. The PICD cuts are also asymmetric, especially at higher momenta, because the effect of timing jitter on a calculated mass is not the same for positive and negative shifts in the timing.

Some of the points shown in Figure 4-7 may be the result of a misidentification of the kaon in the offline analysis, rather than a failing on the part of the LVL2 trigger. Two such problematic events are shown in the following figures. A plan view of the detectors behind the magnet is shown in figure 4-8 for event 24996 of run 10885, a 2kG B polarity run at 14 degrees. The upper of the two tracks was identified as a kaon by the offline software, but not by the LVL2 trigger. A scenario consistent with the diagram shown is that the upper track decayed between T4 and TR2, with one of the decay products producing the TR2 and TOF hits just above the two tracks. The TOF slat pointed to by the reconstructed track probably belongs to the lower track, which was reconstructed as a proton both by the online and offline algorithms. In this case, the LVL2 trigger was probably correct in not finding a kaon in the event.

A plan view of the detectors in front of the magnet is shown in Figure 4-9 for event 13004 of the same run. Here the reconstructed target position is not at $x = 0$ as is assumed in the LVL2 trigger, but at $x = 1.8\text{cm}$. This difference in target position changes the momentum of the track and therefore the calculated mass. Though it doesn't show in the figure, the hits that AUSCON used to verify the track from behind the magnet actually look as though they come from the beam pipe, not the target. Calculating the mass of the track using utilities available inside EDISP, it appears that it is most likely an electron, but the apparent misassignment of hits has stiffened the track, raising the momentum and the mass, making it appear to be a kaon. Events like these are difficult to call LVL2 trigger problems, and are more properly lumped in with a systematic error due to improper

4.6. LVL2 TRIGGER BIASES

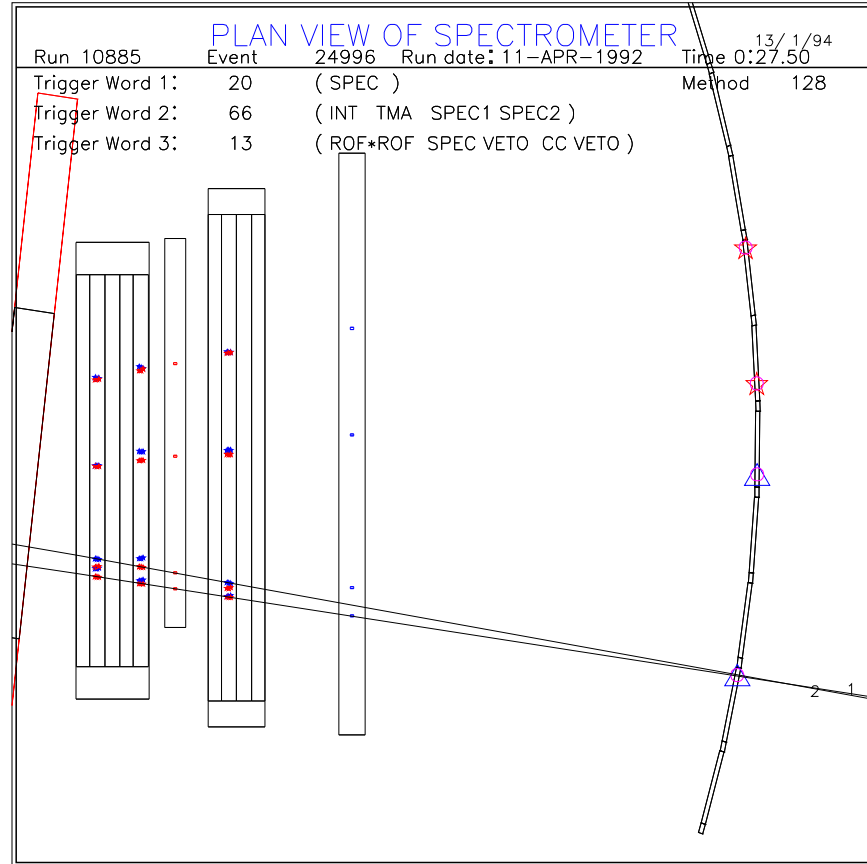


Figure 4-8: Possible decay masquerading as a kaon in the offline analysis. Shown in the figure from left to right are T3, TR1, T4, TR2 and the TOF wall. The upper track in this event is called a kaon by the offline analysis code, but the veto bit for the event was set by the LVL2 trigger. The struck TOF slat appears to be used for both tracks. A more likely interpretation is that the upper track decays after T4 sending a decay particle toward the upper right of the figure and generating a hit on TR2 and the TOF wall.

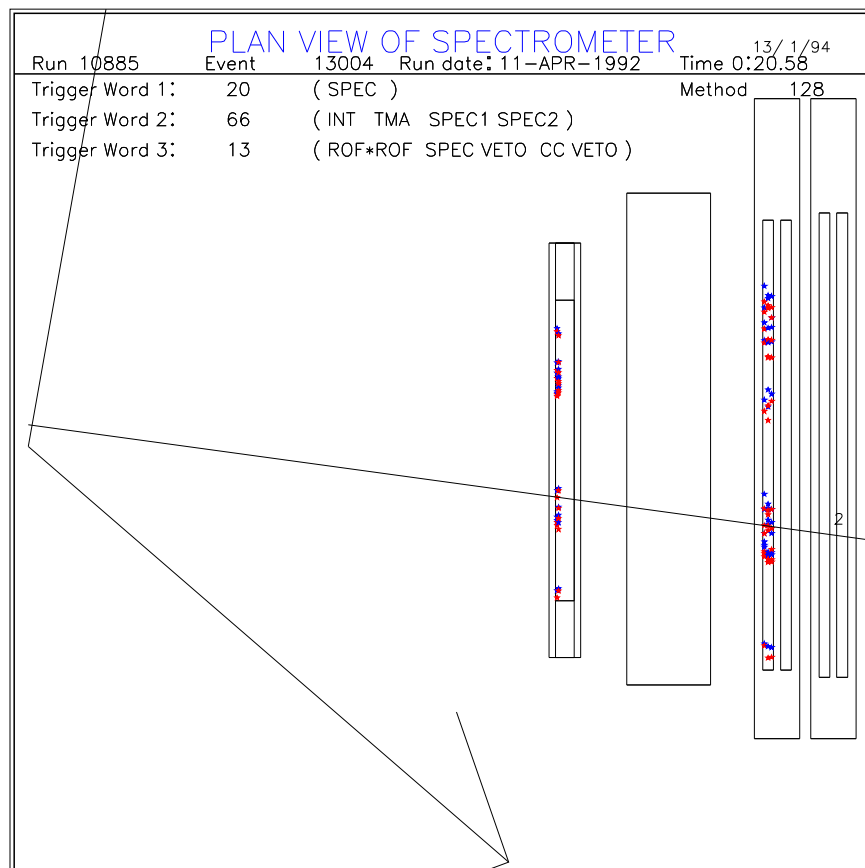


Figure 4-9: Reconstructed target position creating kaon. Shown in the figure from left to right are T1, the TPC and T2. The nearly horizontal line across the figure is the projection of a track back toward the target (located at the intersection of the two oblique lines at left). The projected x target location is off by 1.8 cm which causes the online and offline determination of the momentum to differ significantly. The LVL2 trigger does not identify the track as a kaon, which the offline analysis does.

4.7. SPECTROMETER ACCEPTANCE

reconstruction. If we eliminate such events from the sample, we are left with only $\sim 4\text{--}5$ events out of the 988 original events in the two runs that could be considered LVL2 failures. This is a systematic effect of $\sim 0.5\%$, so no attempt to correct the data will be made.

As is shown in Figure 4-7, there is a roughly triangular region where the 150 ps intrinsic timing resolution $1/\beta$ versus p cuts are wider than the online mass cuts. Particles that fall into this region will be rejected by the trigger, but would have been identified as kaons by the offline analysis. To determine the magnitude of the bias this introduces in the kaon spectra, take Gaussian timing distribution of kaons whose width at a particular momentum is calculated, as in the PICD code, as a summation in quadrature of an intrinsic timing resolution, a momentum independent spatial resolution, and a momentum dependent multiple scattering contribution. Integrate this Gaussian in $1/\beta$ from a value corresponding to the LVL2 mass cut out to 3σ . If we divide this by the integral between $\pm 3\sigma$, we obtain the fraction lost. The result is shown in Figure 4-10. The peak of this distribution is at 2.5% at 2.5 GeV/c (above which all particles are kept), and quickly falls off at lower momenta. If this distribution is convoluted with a normalized momentum spectrum and integrated, the total fraction of kaons lost is determined to be 0.2%. These numbers represent a nearly worst case. The LVL2 mass cuts shown here do not open up until 2.5 GeV/c. For much of the data taking, these mass cuts open up at 2.0 GeV/c, instead of 2.5 GeV/c, which reduces the mismatch of the $1/\beta$ cuts and the mass cuts to nearly zero.

The result of this analysis is that the LVL2 trigger appears to throw out no more than 2.5% of the kaons at any value of momentum, with the integrated number over all momenta more like 0.2%. This is to be compared with the 0.5% actually counted in the data, which given the statistics are entirely consistent with one another. Even though this bias is momentum dependent, it is small compared to other sources of systematic error, and no correction factor due to this bias will be applied to the data.

4.7 Spectrometer Acceptance

The calculation of the phase space acceptance of the spectrometer used in the present analysis is based on an analytic approach devised by Charles Parsons and Brian Cole, which I have extended so that it is tied directly to the chamber geometry constants used in the rest of the analysis. If one

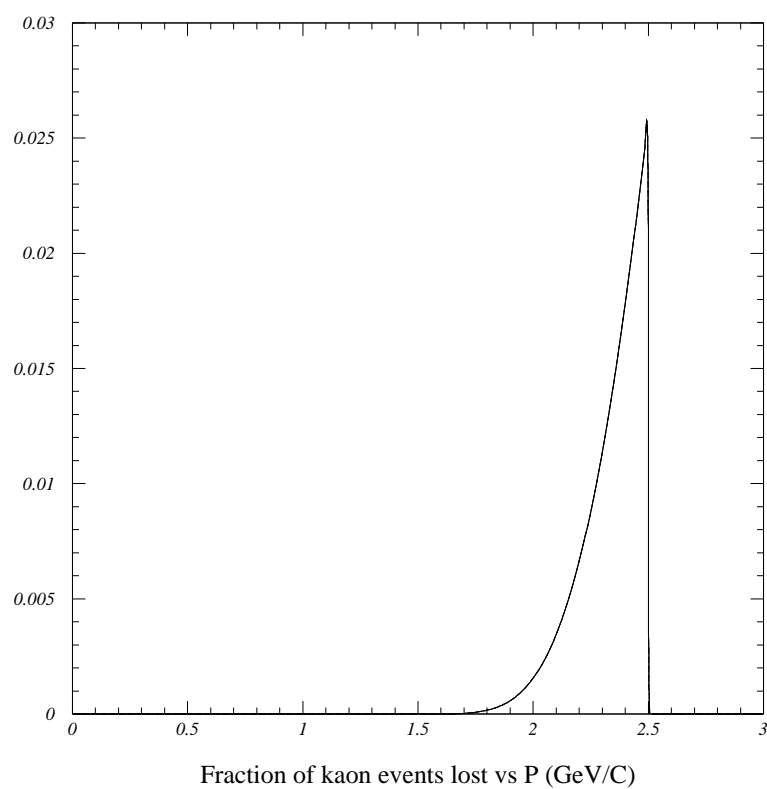


Figure 4-10: Expected fraction of kaon events lost due to overlap of a 150 ps sigma Gaussian timing distribution with the online mass cuts used in the LVL2 trigger. See text for more details.

4.8. TRIGGER CONDITIONS

makes a magnetic thin lens approximation, all of the bend in a particle's track takes place at the midpoint of the effective edge field, and this simplifies the description of a trajectory to a straight line starting at some origin, a kink in the middle of the magnet, and a straight trajectory through the rest of the spectrometer. An analytic expression for a condition on the initial and final trajectories can be found, given that the track is required to pass inside the x dimension of the chambers and the TOF wall. The region of intersection of the constraints imposed by all of the detectors represents the acceptance. Details of the procedure are described in Appendix D. The only provision made for including the constraints on the acceptance introduced by the GASČ is to restrict the TOF wall acceptance to slats 20 to 150. Figure 4-11 shows the TOF slats struck by particles that also fire the GASČ, showing that this is a reasonable cut.³

For the cross section analysis, the acceptance as a function of (y, p_{\perp}) , (y, m_{\perp}) , or (p, θ) is precalculated and stored in histograms, where the number in each bin represents the fraction of the particles in that bin that are inside the acceptance. These histograms are then used to assign bin-by-bin weights to similarly binned histograms of raw or decay corrected counts. The acceptance depends on the angle setting of the spectrometer, the magnetic field and the location of the beam spot, so a pass through the runs is made and a new acceptance histogram is generated whenever one of these quantities changes (the threshold for beam spot location changing is 1.5 mm). Figure 4-12 shows the total acceptance for kaons. The acceptance extends to low p_{\perp} (down to about 100 MeV/c near mid-rapidity) in part due to the significant amount of 2 kG low field and 5° running that was done.

4.8 Trigger Conditions

This section discusses the triggers (BEAM, INT, SPEC and LVL2) that were used to select the events studied in this thesis. The systematic variations in the INT trigger are then examined in some detail, and a problem with the Au 2% data is pointed out. The performance of the LVL2 trigger is also discussed.

³n.b: The first panel of TOF slats (1–16) was not instrumented during E859.

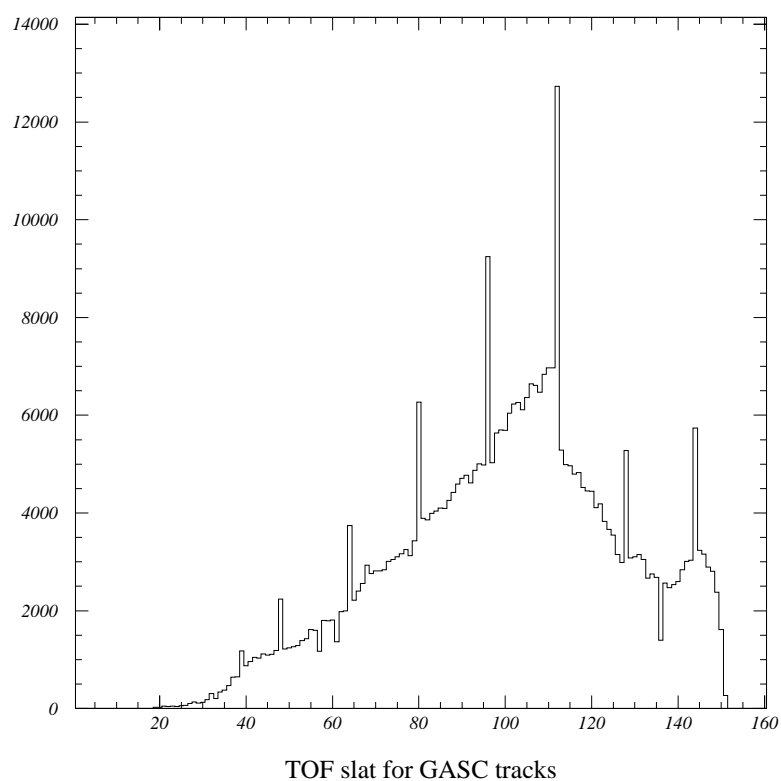


Figure 4-11: TOF slat for tracks firing GASC. The fiducial acceptance for all momenta is restricted to slats 20–150 so that tracks outside the GASC are not accepted. The spikes in the histogram arise because every 16th slat is twice as wide as the others.

4.8. TRIGGER CONDITIONS

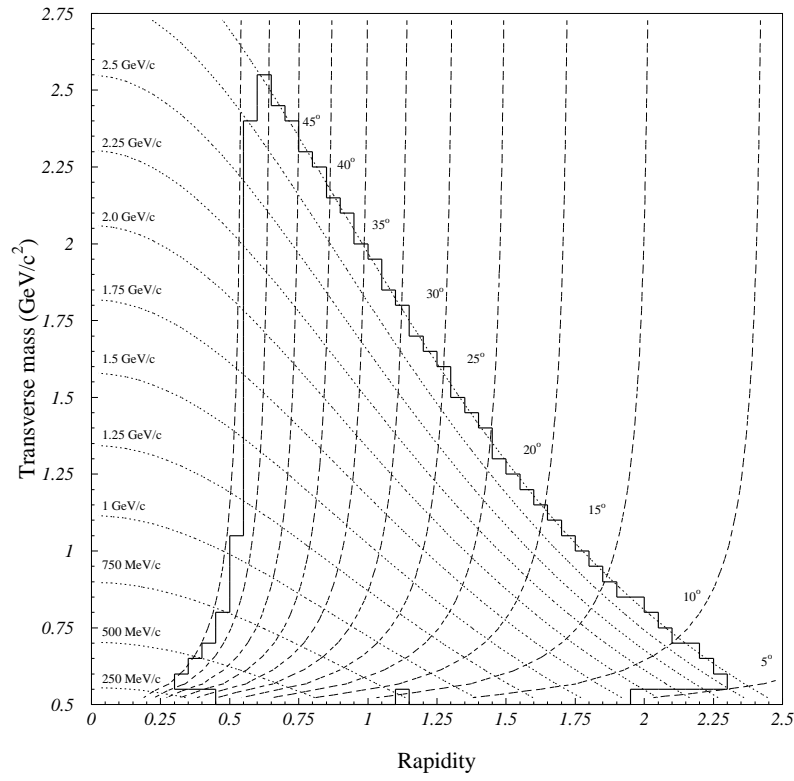


Figure 4-12: Kaon $y - m_{\perp}$ acceptance, including the extended momentum range given by the GASČ. The low m_{\perp} acceptance arises because the 2 kG magnetic field setting was used for a significant fraction of the single-particle kaon data collection. The upper right hand edge of the acceptance is due to the upper momentum limit for which kaons can be separated from pions.

4.8.1 BEAM and INT Trigger

The most fundamental trigger in the experiment is BEAM—all other triggers require it. BEAM is set when a particle of the proper charge is incident on the target, and it is formed from the following combination of beam counter signals, where PRE is set if the beam particle was preceded within 100 ns by another particle (see Section 3.1.2 for definitions)

$$\text{BEAM} = \overline{\text{UDEW}} \wedge \text{BTOT} \wedge \text{BTOF} \wedge \overline{\text{HOLE}} \wedge \overline{\text{PRE}} \quad (4.21)$$

If BEAM is set, but another particle follows within $1\mu\text{s}$, the FOLLOW bit is set. All events in which PRE is set are automatically dropped by the DAQ, and all events in which FOLLOW is set are later eliminated from further analysis. Additional offline charge cuts on the beam counters, $12.0 < Z_{\text{BTOT}} < 16.0$ and $11.7 < Z_{\text{BTOF}} < 16.5$, were used to further clean up the beam. During typical single particle data collection, the DAQ scaledowns were set so that about 5% of the events written to tape were BEAM events. Since the beam scaler which counts the total live beam for the run doesn't know about these later cuts, the amount of beam that it records is scaled down by the fraction of BEAM events which are found to pass both the FOLLOW and beam counter charge cuts. A cut on this fraction, called CBEAM in much of the cross section code, is made during the offline analysis, and runs in which CBEAM is less than 60% are discarded. This is a looser cut than was used in earlier analyses, but as the high beam rates and poor beam structure have increased the number of FOLLOWS from 5–10% during E802 to 15–25% during E859, some relaxation of the cut was necessary.

The INT trigger is used to select events that have had an interaction in the target. It is defined as a BEAM event that also shows a low signal in the bull's-eye, indicating a loss of charge on passing through the target,

$$\text{INT} = \text{BEAM} \wedge \overline{\text{BE}}. \quad (4.22)$$

Figure 4-13 shows the bull's-eye charge distribution for Si+Au 3% events for INT and BEAM triggers.

The hardware cut on the bull's-eye signal is set manually on the floor by adjusting a discriminator threshold on the bull's-eye phototube signal and corresponds to a loss of ~ 1.4 units of charge from the beam peak of 14 units. During E802, the width of the beam peak, as measured by the bull's-eye

4.8. TRIGGER CONDITIONS

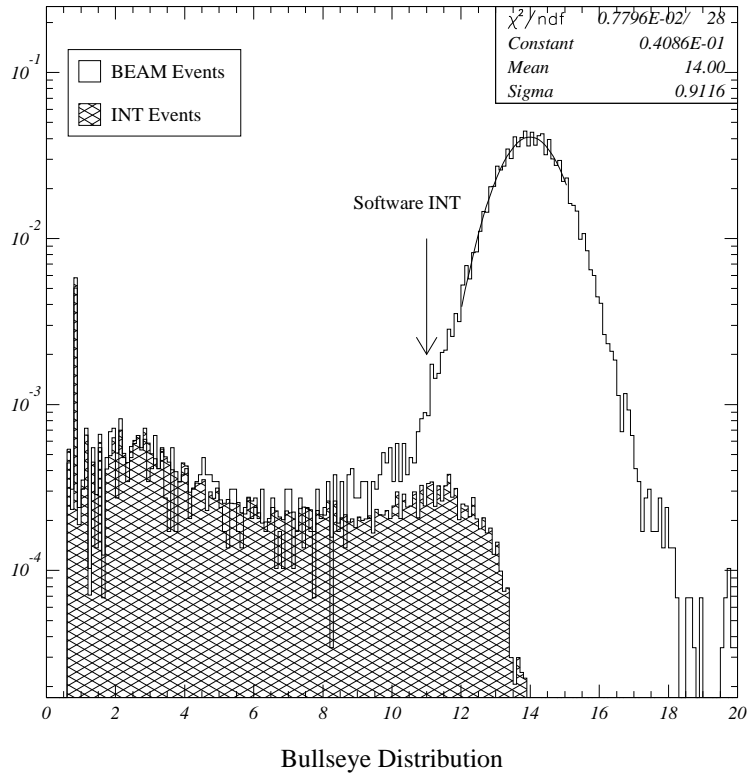


Figure 4-13: Bull's-eye charge distribution for BEAM and INT events for Si+Au 3% data, showing the location of the beam peak at 14. The plain histogram shows the distribution for BEAM events, while the hatched histogram shows the distribution for INT events. For these runs, the hardware INT cuts was set at $BE = 12.6$. The arrow indicates $BE = 11$, where a software cut was placed on the bull's-eye distribution to study the consistency of the interaction rate.

ADC, was about 0.4 units. Therefore, INT selected events more than 3σ away from the beam. In E859, the width of the beam peak in the bull's-eye increased to 0.8 units, so that a cut at 12.6 is only 1.5σ away from the beam. This change in the width may be due to any number of things, but one possibility is an additional source of noise, perhaps a ground loop, on the input to the bull's-eye ADC. Since the cut sits right at the edge of the beam peak, any drift in the cut can cause quite a few more BEAM events to be called INT. This effect can be seen in the E859 data by looking at the beam normalized bull's-eye distribution for INT events, shown in Figure 4-14, for two runs, one taken during Feb91, the other during Mar92. The earlier run clearly shows that INT has begun to include part of the beam peak. The effect of the classification of so many beam particles as INT events is reflected in the INT/BEAM ratio for all targets, but is especially visible in the empty target runs since there is so little strength in the histogram away from the beam peak.

INT Cross Section Consistency

Because there is a variation in the calculated INT rate, even with target out subtraction, as a function of time, there is a question of what interaction cross section to use for the different targets. These are physically the same targets as used in E802, and the interaction rate of these targets has been measured several times before [Blo90, Par92]. As a check of the analysis, we want to make sure that we can reproduce the rates measured before. Determining the interaction rate for the various targets used in the analysis begins by calculating the simple ratio of the number of INT events (correcting for the scaledown) to the total beam for the run. However, INT events are generated even when no target is in place, and this contribution to the ratio must be taken into account. During most of the Feb91 and Mar92 running period, a typical target out contribution amounted to 0.9% interaction per beam particle. This is nearly the same rate as the thinnest target used in this analysis, Au 1%. In the early part of Feb91, however, a rate of over 1.0% was more typical. As discussed above, the INT trigger depends crucially on the discriminator threshold set for the bull's-eye phototube signals, and the high rate in Feb91 appears to have been due to a difference in the threshold setting. This is shown in Figure 4-14. A changing INT rate complicates the target out correction, however, so a tighter software cut was applied to the bull's-eye charge spectrum to make the INT rate more uniform. The cut was placed at 11.0 units of charge. The effect of this on the target out INT/BEAM rate is shown in Figure 4-15. In the figure the rate is shown for all empty target runs and as a function of

4.8. TRIGGER CONDITIONS

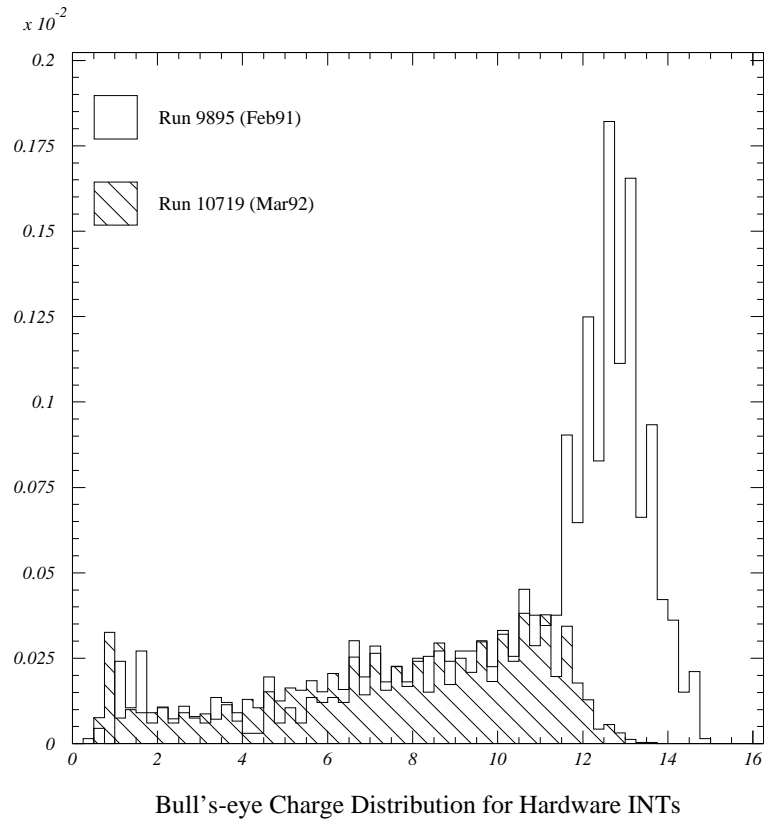


Figure 4-14: Bull's-eye charge distribution for INT events in empty target runs. The horizontal axis is in units of charge. The plain histogram is the distribution for run 9895, taken early in the Feb91 run, the hatched one for run 10719, taken midway through the Mar92 run. The distribution for run 9895 shows that INT includes quite a bit of the beam peak, which would be centered at 14 with a sigma of 0.8

different cuts on the bull's-eye charge spectrum. The early Feb91 runs show an INT/BEAM rate of 1.1% dropping to 0.9% by the end of the running period. This variation in the early runs disappears entirely when the software cut is applied, with the rate a nearly constant 0.74%. A tighter software cut at 10.0 units of charge, doesn't seem to have any further effect on the INT/BEAM variation. The dip in the INT/BEAM rate near the end of the running period was due to a particularly bad 24 hour period of beam, and none of those runs, target in or target out, are used in the analysis. This is discussed in more detail below.

INT Masking and the Au 2% Data

The INT/BEAM rate for the empty target runs near the end of the Mar92 running period show a dip in the rate regardless of the cut applied. The drop in the rate may be an effect due to a combination of high instantaneous beam rate and details of the timing of gates in the bull's-eye electronics. It appears that it is possible for a BEAM particle which is not also an INT to trigger a discriminator in the bull's-eye electronics whose width can overlap a closely following particle. If that particle is an INT, the bull's-eye will appear to have fired, falsely classifying the second event as a BEAM and masking the INT. Unfortunately, by the time this hypothesis was developed, the beam electronics had been disassembled, making it impossible to check directly. Those people most familiar with the setup of the electronics remain, on the whole, agnostics, but it seems the most likely explanation for the observed behavior. The fact that the strange INT rate appears to last for a single 24 hour period, coincidentally a Monday, may make the hypothesis even more plausible.

During that 24 hour period, all of the E859 Au 2% data was taken. A comparison of the calculated Si+Au cross section for the Au 1%, Au 2%, and Au 3% targets, which should all result in the same value, shows the Au 2% result low by $\sim 20\%$, and with a large amount of dispersion in the calculated value among the Au 2% runs. The Au 2% was taken under quite different conditions than the rest of the runs used in the single-particle kaon analysis. It was taken as part of the 2K correlation running, but with single K^- and \bar{p} also satisfying the LVL2 veto. In principle, it is valid to use this data for K^- analysis, but as it seems to have serious systematic problems, it will not be used in the present work.

4.8. TRIGGER CONDITIONS

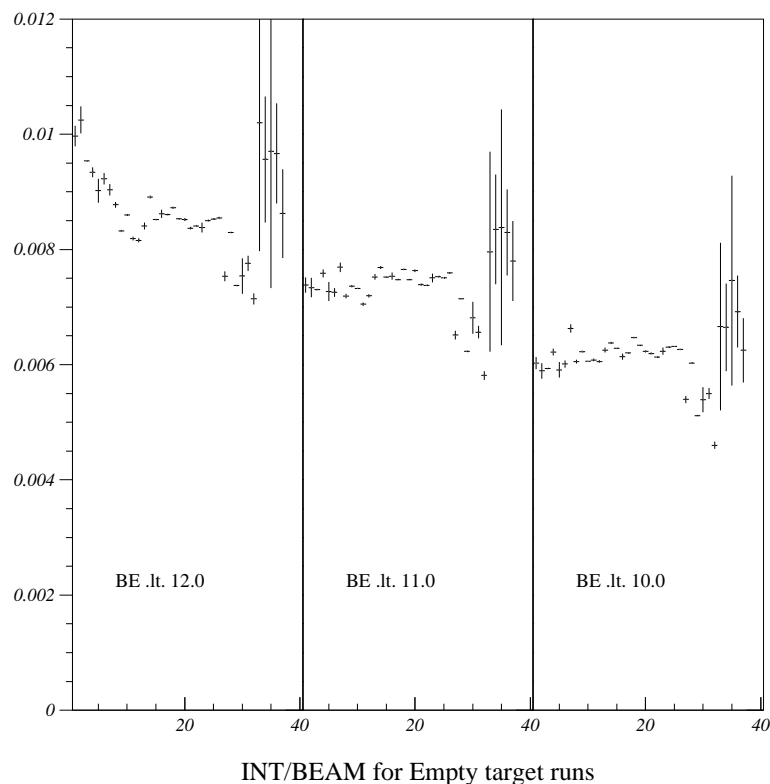


Figure 4-15: INT/BEAM for empty target runs. The horizontal axis is just the ordinal number of each empty target run as it occurred in the data set. The first panel shows the rate when a software cut on the bull's-eye charge spectrum is placed at 12.0 units. There is a fair amount of variation in the rate, especially for the Feb91 runs where the rate drops 18% over the course of the running period. The second and third panel show this same rate for cuts at 11.0 and 10.0, respectively. Already for a cut at 11.0, all of the Feb91 variation has disappeared. The dip in the rate for the late Mar92 runs take place during one 24 hour period of exceptionally poor beam. No runs during that period are used in the analysis.

4.8.2 SPEC Trigger and LVL2 Veto

The spectrometer trigger, SPEC, and its associated second level veto, LVL2, are the key to the present kaon analysis. Before E859, the SPEC trigger was the most selective, unbiased single particle trigger available in the experiment. The SPEC trigger is a level one trigger made of a series of coincidence requirements on several more basic triggers. The definition of SPEC is

$$\text{SPEC} = \text{BEAM} \wedge \text{TOF} \{ \wedge \text{F0} \} \{ \wedge \text{TR1} \wedge \text{TR2} \}. \quad (4.23)$$

F0 is true if any of the slats in F0 is hit, and TOF is true if any of the slats in the time of flight wall is hit. The terms in braces were sometimes, but not always required. Part of the way through the Mar92 run, TR1 and TR2 were included in the definition of the SPEC trigger. The reasoning was that, since the LVL2 veto will reject events with no hits on either of TR1 or TR2, no additional bias was introduced by requiring TR1 and TR2 in the level one trigger. It also allowed the SPEC trigger to take advantage of the trigger chambers to improve its selectivity.

The LVL2 veto is used to reject SPEC events that don't meet further criteria. Many different configurations were used for the LVL2 veto (see Appendix C for terminology), and only runs taken with certain configurations of the trigger are appropriate for certain analyses. The standard RUN_INFO database entry made for each run does not contain specific enough information to separate runs into the appropriate analysis categories, so a simple ASCII text file, RUN.TYPE.DAT was assembled with a numerical run type identifier put in by hand for each run from data recorded in the run sheets. The header of that file reads

```
! The known run types are:
!      0: Unknown, bad, or not kaon run
!      1: K+K- (includes p-)
!      2: K-   (includes p-)
!      3: K+
!      4: NoPID
!      5: K+K- veto out
!      6: K- veto out
!      7: K+ veto out
```

4.8. TRIGGER CONDITIONS

! 8: Kaon run, but unknown trigger condition.
! 9: P- dedicated

This file is parsed by a routine of the same name and the run identifier is then used in the cross section analysis to guarantee that the only the intended runs are used at each stage in the analysis.

The types of mass and momentum cuts for each of these triggers is shown in Table 4.3.

General Name	K ⁺ Mass Range	K ⁻ Mass Range	Maximum PID Momentum
K ⁺ K ⁻	350-700 MeV/c ²	350-1300 MeV/c ²	2.5 GeV/c
K ⁻	N/A	350-1300 MeV/c ²	2.5 GeV/c
K ⁺	350-700 MeV/c ²	N/A	2.5 GeV/c

Table 4.3: LVL2 Mass and Momentum Cuts

The figure of merit used for the LVL2 veto is the *rejection factor*, R , which for the current data set is defined as

$$R = \frac{N_{\text{LVL1}}}{N_{\text{LVL2}}} \quad (4.24)$$

where N_{LVL1} is the number of LVL1 triggers, and N_{LVL2} is the number of LVL2 events accepted. Of course, N_{LVL1} should only include those LVL1 triggers subject to the LVL2 veto, primarily SPEC triggers. The rejection factor varies depending on the exact running conditions from about 3 for Si+Au at 5° for a K⁺K⁻ trigger, to about 70 for Si+Al at 44° for the same trigger. The very high rejection factors at back angles are not actually that useful, since a trigger is only useful if it allows you to increase the intensity of the beam, and we could not raise the beam to take advantage of the extreme selectivity of the LVL2 veto at back angles. Radiation safety limits kept the beam below 2×10^6 ions/spill, and at the back angles it sometimes took 3 hours to fill a tape with events. If we had it to do over again, constructing a less restrictive trigger requirement for the back angles, using a NOPID LVL2 veto for example, might have improved the physics throughput of the experiment. Table 4.4 lists the rejection factors typical of the E859 data taking.

Even with the LVL2 veto, the fraction of accepted events that actually turn out to contain a kaon in the offline analysis is fairly small. The fact that events without kaons can mimic kaon-containing ones, at least in the eyes of the LVL2 veto, limits the ultimate selectivity of the trigger.

An analogy that we found useful when trying to understand the behavior of the LVL2 trigger is

System	Angle	NOPID	K^+K^-	K^+	K^-
Si+Au	44°	1.2	25		70
	34°	1.2	13		
	24°	1.2	7		25
	14°	1.2	4		14
	5°			2.0	2.5
Si+Al	44°	1.2	20		
	34°	1.2	15		
	24°	1.1	10		32
	14°	1.1	7		20
	5°			2.4	2.7

Table 4.4: E859 single particle rejection factors. The NOPID configuration is just a tracking trigger with no particle identification requirements. The K^+K^- and K^- configurations almost always included \bar{p} as well. Entries are only filled for configurations that were actually used.

of two resistors in parallel. The analog of current is the flow of events through the trigger to tape, and the resistance is provided by the selectivity of the trigger. A very selective trigger presents a high resistance to writing events to tape; a low selectivity one passes events to tape easily. The rate at which undesirable events are able to mimic desired ones establishes the significance of the second resistor in the net

$$\frac{1}{R} = \frac{1}{R_{\text{real}}} + \frac{1}{R_{\text{fake}}} \quad (4.25)$$

It does not do any good to select events that are rarer than the rate at which ordinary events are able to fool the trigger.

4.9 Invariant Cross Sections and Yields

This section discusses what a cross section is and how it is calculated in the present work. Consider particles emerging from an event.⁴ Discretize the final state momentum space and count the number of particles of type i that appear in each d^3p bin. That number is the *differential yield*, d^3n_i/dp^3 , for species i . Its value will depend on how we select events; central events tend to produce lots of

⁴This section is modelled after the discussion in the review article by Ole Hansen [Han90].

4.9. INVARIANT CROSS SECTIONS AND YIELDS

particles and so have large differential yields, while peripheral events have much smaller differential yields. If events are selected by exactly specifying the final state, the measurement is *exclusive*. If events are selected without any requirements on the final state, except the detection of a particle of type i , the measurement is *inclusive*. The middle ground, selecting events with an incomplete specification of the final state, is a *semi-inclusive* measurement. The kaon production results presented here as a function of cuts in the event multiplicity are semi-inclusive measurements. Taking the differential yield and integrating it over all momentum space gives the total yield of species i in the event

$$n_i = \int \frac{d^3 n_i}{d^3 p} d^3 p. \quad (4.26)$$

If we repeat the measurement for an ensemble of N events we obtain the average yield per event

$$\langle n_i \rangle = \frac{1}{N} \int \frac{d^3 n_i}{d^3 p} d^3 p. \quad (4.27)$$

Though the total yield is a Lorentz scalar, the number per momentum volume element, $d^3 n_i / d^3 p$, is not and depends on the frame in which it is measured. To rewrite this in a Lorentz invariant form, begin with the explicitly invariant four-momentum volume element $d^4 p$ and use a delta function $\delta(p^\mu p_\mu - m^2)$ to restrict the four-momentum to the mass shell. The delta function is also Lorentz invariant since its argument is invariant. Using the relation $\delta(f(x)) = \sum_i \frac{1}{|f'(x_i)|} \delta(x - x_i)$ where $\{x_i\}$ is the set of zeros of $f(x)$ [CTDL77], this can be rewritten as

$$\begin{aligned} \int d^4 p \delta(p^\mu p_\mu - m^2) &= \int d^4 p \delta(E^2 - p^2 - m^2) \\ &= \int \frac{d^3 p}{2E} \end{aligned} \quad (4.28)$$

which shows that the combination $d^3 p / E$ is a Lorentz invariant. Equation 4.27 then becomes

$$\langle n_i \rangle = \frac{1}{N} \int E \frac{d^3 n_i}{d^3 p} \frac{d^3 p}{E}. \quad (4.29)$$

The next step is to express this in terms of the variables used in the analysis. Change from (p_x, p_y, p_z) to (y, p_\perp, ϕ) and use the relations $E = m_\perp \cosh y$ and $p_z = m_\perp \sinh y$ to write the Jacobian of this

change of variables as

$$\begin{aligned} dp_x dp_y dp_z &= p_\perp dp_\perp d\phi dp_z \\ &= p_\perp dp_\perp d\phi E dy. \end{aligned} \quad (4.30)$$

This leads to a final expression for Equation 4.27

$$\begin{aligned} \langle n_i \rangle &= \frac{1}{N} \int E \frac{d^3 n_i}{dp^3} \frac{d^3 p}{E} \\ &= \frac{1}{N} \int E \frac{d^3 n_i}{E p_\perp dp_\perp dy d\phi} \frac{E p_\perp dp_\perp dy d\phi}{E} \\ &= \frac{1}{N} \int \frac{d^3 n_i}{p_\perp dp_\perp dy d\phi} p_\perp dp_\perp dy d\phi. \end{aligned} \quad (4.31)$$

The quantity

$$dn(y, p_\perp, \phi) = \frac{d^3 n_i}{p_\perp dp_\perp dy d\phi} \quad (4.32)$$

is the invariant yield [Bak]. In the present work, we do not measure the reaction plane of the collision, and assume that after many collisions, the azimuthal angle dependence of the invariant yield is averaged over, leading to the double differential expression

$$dn(y, p_\perp) = \frac{d^2 n_i}{2\pi p_\perp dp_\perp dy}. \quad (4.33)$$

Using the relation $p_\perp dp_\perp = m_\perp dm_\perp$, the invariant yield may also be written as

$$dn(y, m_\perp) = \frac{d^3 n_i}{2\pi m_\perp dm_\perp dy} \quad (4.34)$$

The invariant cross section can be calculated instead if the number of produced particles is normalized by the target thickness and the incident beam flux instead of number of events. The differential cross section is proportional to the probability that an event will produce a particle of the desired type in the specified momentum region. The invariant yield has an advantage in situations where the trigger cross section is not known terribly accurately. In E859 many differential yields are reported as a number “per central event”, for instance. If the cross section for a central event is well known, then the differential cross section for the production of the particle may be calculated [Par92].

4.9. INVARIANT CROSS SECTIONS AND YIELDS

In calculating the invariant cross sections and yields from the data, the following expression based on Equation 4.34 is used [Blo90]

$$dn(y, m_{\perp}) = \frac{1}{2\pi m_{\perp}} \frac{N(y, m_{\perp})}{N_{events}} \frac{acc(p, \theta, \phi) wgt(p, L, i)}{dy dm_{\perp}}, \quad (4.35)$$

where $N(y, m_{\perp})$ is the actual number of identified kaons found in a (y, m_{\perp}) bin, $1/acc(p, \theta, \phi)$ is the fraction of the full 2π azimuthal range accessible to the particle, and $wgt(p, L, i)$ is a weight assigned to the particle, which, among other things, includes a decay correction factor for a particle of type i travelling a distance L with momentum p . This factor, and the effect of absorption are determined using the E859 Monte Carlo. The weight also includes a factor for reconstruction and particle identification efficiency and a factor accounting for the efficiency of the GASČ (see Section 4.4). The number of events, N_{events} , that satisfy a particular trigger is calculated by specifying the cut for the trigger as a fraction of the total inelastic cross section for the target and then multiplying this fraction by the target cross section and the amount of beam collected for the run.

4.9.1 Matching Data for Different Target Thicknesses

For each of the Si+Au and Si+Al data sets, targets of two different thicknesses were used. For the aluminum data the two targets had thicknesses of 817 mg/cm² and 1630 mg/cm². For the gold data the two targets were 944 mg/cm² and 2939 mg/cm² thick. In calculating yields, the data is normalized directly to the beam, meaning that the number of events in the denominator of the expression for the invariant yield, Equation 4.35, is determined by multiplying the amount of beam for the run by the trigger cross section, which in turn is expressed as a fraction of the interaction cross section for the target. Therefore to get the proper matching of particle yields throughout the entire data set, it is important to make sure that the interaction cross section for the two target thicknesses are consistent with one another. In other words, if you determine that the 2939 mg/cm² gold target represents a 3% target, meaning that it produces a target out corrected INT/BEAM rate of 3%, the 944 mg/cm² target had better be very close to a $\frac{944}{2939} \times 3\% = 0.96\%$ target. This is especially important since the choice of target when taking data was correlated with the spectrometer angle; thick targets were used at back angles where there are relatively few particles in the spectrometer

to increase the rate of events, thin targets at forward angles (where the majority of particles are) to keep the rate low enough that the DAQ can keep up. This also leads to a correlation in rapidity and m_{\perp} . Particularly for the gold data, the forward rapidity m_{\perp} spectra gets their low m_{\perp} contribution from the 944 mg/cm² target and their high m_{\perp} contribution from the thicker target.

To measure the interaction rate for a target, count the number of INT events, multiply by the INT scaledown, divide by the amount of beam for the run, and then subtract off the empty target interaction rate. If this is done for the E859 data, quite a bit of variation in the rate is seen as a function of run number. Since the target thicknesses haven't been physically remeasured since the BNL target group produced them for the first E802 run in 1986, there was some concern that the variation might be due to nonuniformities in the target thickness, and that as the beam impinged on different regions of the target in different runs, there would be more or less material for the beam to interact with. The thinnest gold target is only about 0.5 mm thick, so 10% variations in the interaction rate can be accounted for by 50 μ m variations in thickness. However, the interaction rate is also determined by where on the bull's-eye signal the INT discriminator is set, and it is easy to imagine that the output of the bull's-eye phototubes might sag during intense beam, leading to variations in the interaction rate. If a tight software cut on the bull's-eye distribution is made, the resulting definition of INT should be insensitive to slight sagging in the phototube output. If the interaction rate for this INT definition is plotted for empty target runs for a few choices of bull's-eye cut, the resulting rate becomes quite stable (see Figure 4-15). This is consistent with the variation in interaction rate being due to variation in the INT definition.

Several authors have directly measured the interaction cross sections for the different targets [Blo90, Par92], and as a check on the consistency of the data, I will too. To check the target-in interaction rate, a set of runs from a period during the Mar92, runs 10510 to 10600, was selected. Over the course of these 90 runs, all of the different targets in the single-particle kaon analysis, including two empty target runs, were used (Au 2% is an exception, but see Section 4.8.1). Using these runs reduces the chance of systematic errors due to large changes in the fundamental INT rate. Figure 4-16 shows the INT/BEAM rate, with no target out subtraction, for the runs during that period. The dotted lines are fits to the data which we can use to compare different target thicknesses. Of course, the cross section per scatterer for targets of the same material should agree. Table 4.5 shows a comparison for the different targets when the target out rate is subtracted from

4.9. INVARIANT CROSS SECTIONS AND YIELDS

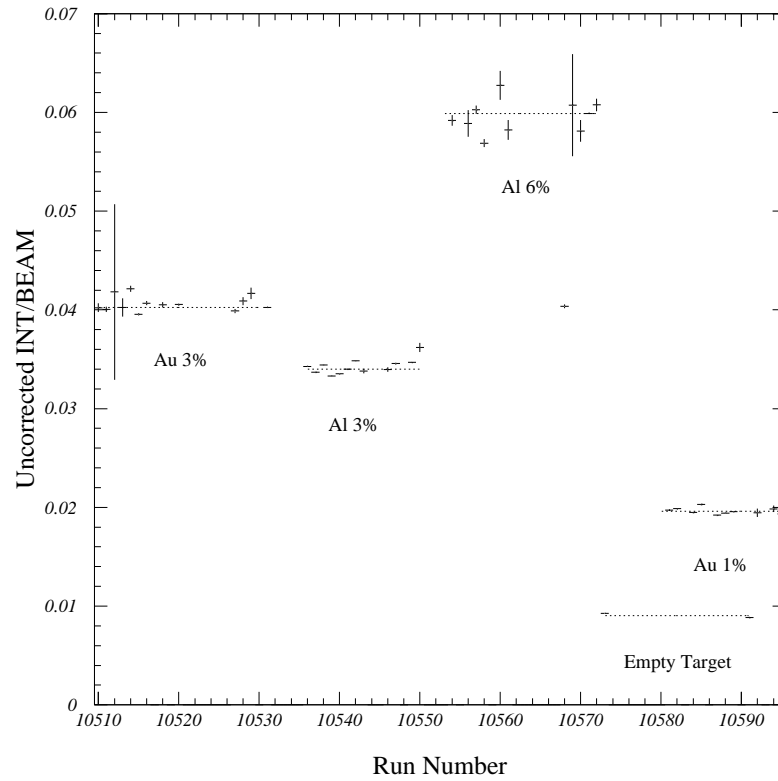


Figure 4-16: Interaction rates for a series of runs in Mar92, used as a check of the constancy of the target cross section. Plotted is the number of INT events divided by the amount of beam, taking the appropriate scaledowns into account. Nominally, this should be constant. However, variations in the INT cross section, due perhaps to sagging in the bull's-eye phototubes, causes variations in the rate measured.

the target in rate and the result, f , is converted to a cross section per scatterer via

$$\begin{aligned} cs &= f \left(\frac{\text{mg}}{\text{cm}^2} \right)^{-1} \frac{\text{mg}}{\text{g}} \frac{\text{g}}{\text{mole}} \frac{\text{mole}}{6.02 \times 10^{23}} \frac{\text{mb}}{\text{cm}^2} \\ &= f \left(\frac{\text{mg}}{\text{cm}^2} \right)^{-1} \frac{\text{g}}{\text{mole}} \frac{1}{6.02 \times 10^{-7}}. \end{aligned} \quad (4.36)$$

Good agreement is seen, assuaging fears of warped targets, but the actual target thickness used in the analysis is taken from previous measurements, in order to avoid trivial differences in the yields reported.

Target	mg/cm ²	INT/BEAM	Corrected INT/BEAM	$\sigma_{\text{INT}}^{\text{Si+A}}$ (mb)
Empty		0.0090		
Al 3%	817	0.0340	0.0250	1370 ± 5
Al 6%	1630	0.0599	0.0509	1399 ± 5
Au 1%	944	0.0196	0.0106	3678 ± 12
Au 3%	2939	0.0424	0.0334	3727 ± 13

Table 4.5: Interaction rate consistency check. The measured interaction rates for the different targets used in the single-kaon analysis are shown, as is a target-out interaction rate for the same running period. The empty target rate is subtracted from the target-in rate to give the values in the fourth column. Using the target thicknesses, these values are converted into silicon-nucleus interaction cross sections, which for the two thicknesses of gold differ by less than 3%, the aluminum values by less than 1%.

4.10 TMA Data Analysis

This section discusses the analysis of the TMA, the principal event characterization detector used in this thesis. Using the TMA, the variation in kaon production can be examined as a function of multiplicity, and indirectly, as a function of centrality. Later, in Section 4.11 the average number of projectile participants for each of the TMA cuts discussed here will be determined, correlating the TMA and ZCAL, and allowing the study of kaon production as a function of the number of projectile participants. This section addresses several issues concerning the TMA, in particular questions about the response of the TMA to the high intensity beam of E859, how corrections to the multiplicity spectrum are made for empty target contributions, and how cuts on the multiplicity

4.10. TMA DATA ANALYSIS

distribution are made.

4.10.1 General Features of TMA Distribution

To orient the reader, Figure 4-17 shows the beam-normalized multiplicity distribution seen in the TMA for INT events for the Si+Au 3%, Si+Al 3% and empty targets used during taking data for the single-particle kaon runs. The general outline of the TMA response can be understood by keeping in mind that the number of pions, and hence most of the produced particles, scales approximately with the number of binary collisions suffered by the projectile and target participants [Blo90]. Consistent with a geometry-dominated view of heavy-ion collisions, most of the cross-section is peripheral, leading to very few particles in the TMA, which accounts for the large cross section near zero multiplicity. The Si+Au distribution shows a broad, gently sloping region over the mid-multiplicities which arises because the amount of the gold nucleus that the silicon projectile interacts with increases only slowly with decreasing impact parameter once the impact parameter is small enough that the silicon nucleus is completely occluded by the gold. This leads to a slow increase in the number of binary collisions and consequently a slow increase in the multiplicity. In striking the aluminum target, a nearly symmetric collision for the silicon projectile, the amount of overlap increases rapidly with decreasing impact parameter, for all centralities, so there is no broad region similar to the gold. A central Si+Au collision produces many more particles than a central Si+Al collision, so the gold distribution extends much farther out in multiplicity. In fact, empty target reactions often produce higher multiplicities than the aluminum target, leading to a large target out correction for the aluminum data. If one were to compare this distribution with similar ones shown in a number of E802 papers, it would be quickly seen that the maximum multiplicity shown here is significantly lower than during E802 [Par92]. As described in Section 3.2.1, several panels were removed from the TMA during E859, and this has reduced the maximum multiplicity seen in the TMA for Si+Au 3% from about 240 to about 160.

The multiplicity distribution for the Si+Au 3% data extends to values about 10-15% higher than for the Si+Au 1% data. One thing which might be expected to account for this is the difference in the production of δ -electrons for targets of different thicknesses. The thicker target will produce more δ 's, and this will consequently shift the TMA distribution out. The number of delta electrons

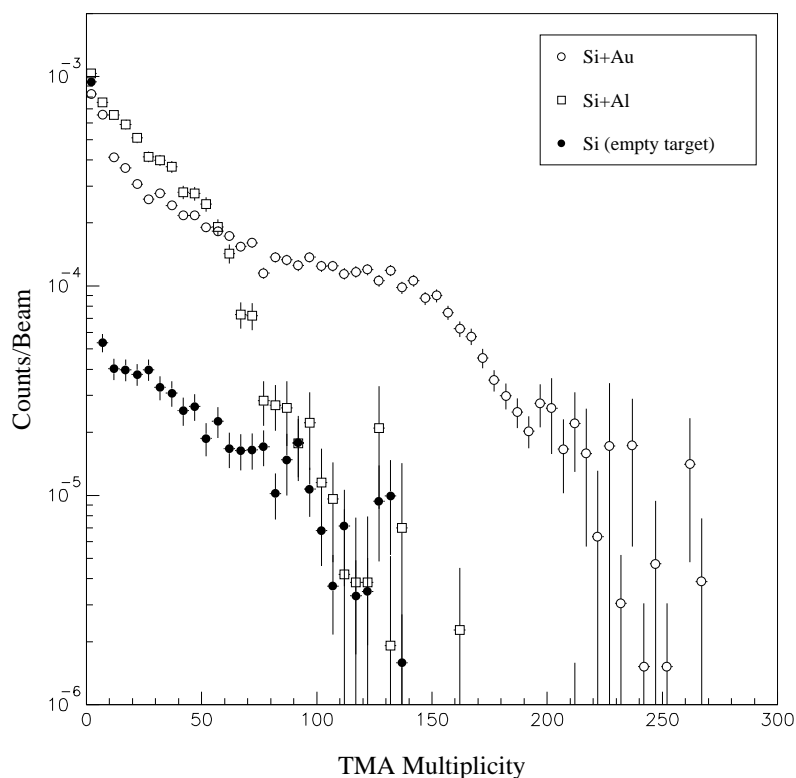


Figure 4-17: TMA distribution for INT events for the different targets used in taking the E859 kaon data. All distributions have been divided by the amount of beam, taking the INT and BEAM scaledowns into account. The broad, gently sloping mid-multiplicity region for the gold targets is because of the slow change in the amount of the gold nucleus that the silicon projectile has to pass through once complete overlap has occurred. Note that the empty target TMA distribution extends even beyond the aluminum target in TMA distribution.

4.10. TMA DATA ANALYSIS

produced with energy greater than a lower kinetic energy threshold E_1 is [Gro90]

$$N(E \geq E_1) = \frac{1}{2} \frac{x}{E_1} \left(0.3071 \text{ MeV cm}^2 \text{ g}^{-1} \right) \frac{Z}{A} \frac{z^2}{\beta^2} \rho \quad (4.37)$$

where x is the thickness of the material, Z and A and ρ are the charge and mass number and mass density of the target. The charge and velocity of the projectile are denoted by z and β , respectively. We use a kinetic energy threshold of 25 MeV for a particle to make it out of the target assembly and into the TMA [Abb90]. Since the number of δ -electrons depends on the projectile charge squared, most of the production will come from the passage of the initial silicon ion through the target, rather than the passage of the produced particles through the rest of the target. This means that the contribution of the δ 's to the TMA signal have nothing to do with the charged particle multiplicity or the centrality of the collision. As long as the number of δ 's is small, however, and as long as the TMA threshold is determined for each different target separately, this should be a small effect, and no attempt is made to correct the TMA distribution for the number of δ 's. The difference between the TMA distribution for the Au 3% and for the Au 1% targets, however, may be understood by calculating the difference in the number of δ 's expected to be produced by a silicon ion passing through each of the two targets. In a thin target, the projectile should travel on average through one-half of the target, so there should be an excess of δ -rays produced in the thicker gold target over the production in the Au 1% target equivalent to a silicon nucleus completely traversing a gold 1% of an interaction length thick. When reasonable values are put in Equations 4.37, the Au 3% produces ~ 10 more δ -rays than the Au 1% target.

Another effect which could cause the TMA distribution for the Au 3% target to extend to higher multiplicities is the additional conversion of the γ 's from π^0 decay into e^+e^- pairs. Each π^0 can give rise to as many as 4 charged particles. This signal is related to the number of produced particles, since the more π^0 's that are produced initially, the more e^+e^- pairs are created, which leads to a larger signal in the TMA.

4.10.2 Rate Dependence of TMA Signal

The higher beam rates of E859 have led to concern about the possibility of instrumental pileup in the TMA, which occurs when the signal seen in a detector from multiple beam particles is recorded

as though it came from only one beam particle because the beam particles arrived within too short a time interval. There is a gate on the beam counters 100 nsec wide preceding and following each particle to try and prevent this, but if the recovery time of a detector is much longer than this it will still be vulnerable to pileup. This is not so easy to protect against, as the beam counters will correctly record the passage of only one beam particle, but the detector will still have effects left over from the last event. This could be the case with the TMA. Particles generating signals in the TMA leave ionization behind, which must dissipate before the TMA is ready for another event. The time scale for this recovery can be estimated by using a drift velocity of $50 \mu\text{m/ns}$ over a drift distance of $\approx 1 \text{ cm}$. This drift takes 200 ns, so when beam particles begin arriving sooner than this, there is a good chance that ionization will still be present in the cells of the TMA and may cause extraneous hits for the second event.

One way to look for this effect is to plot the TMA distributions as a function of the *instantaneous* beam rate, which can be obtained from the ungated beam counter clock and scalers which record the time and total beam since the last beam particle, independent of whether or not the computer was busy when that occurred. Figure 4-18 shows the instantaneous beam rate for a series of runs near the end of the Mar92 silicon beam running. Though the average beam for these runs was about 8×10^5 particles/spill, as the figure shows, the distribution of rates is spread quite a bit. We can plot the TMA distribution for the 25% of the events with the lowest rate and compare that to the TMA distribution for the 25% of the events with the highest rate. This is shown in the upper panel of Figure 4-19. The relative difference of the two distributions is shown in the lower panel, and within the statistics, there is no significant difference between the two. There is some structure in the difference at the 10–20% level, but as this is much smaller than the rate dependence seen in the ZCAL, no attempt is made to correct the effect.

4.10.3 Determination of TMA Cuts

This section describes the procedure for setting cuts on the TMA multiplicity distribution corresponding to a particular fraction of the interaction cross section. It seems that the best way to explain how the multiplicity cuts are determined is to start by comparing it with the way that seemed correct when we first started thinking about it. If you are trying to select events with in the top $X\%$ of the multiplicity distribution, it would seem that you should proceed as follows: Histogram the

4.10. TMA DATA ANALYSIS

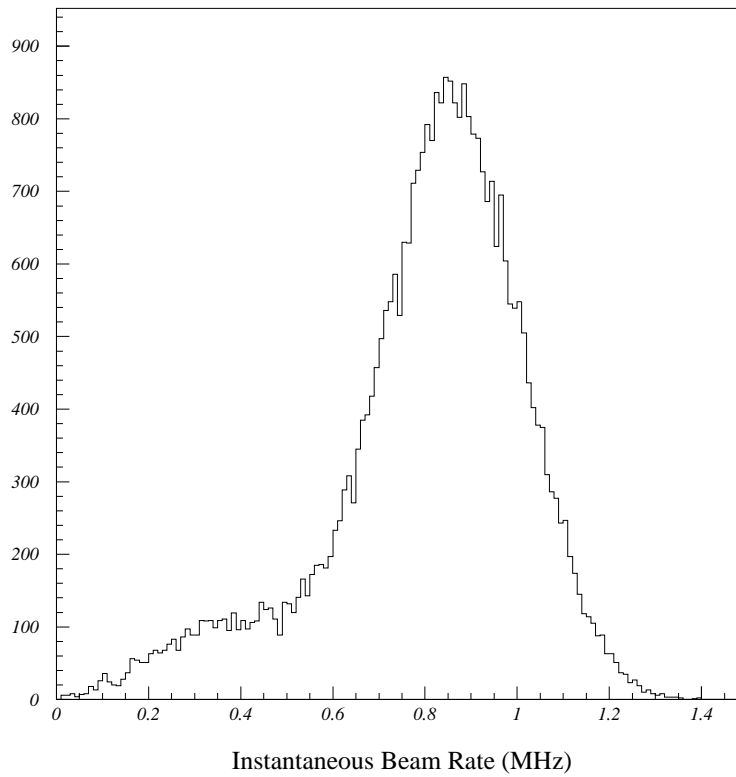


Figure 4-18: Mar92 instantaneous beam rate. This plot is for a series of runs taken as part of the 2π running, near the end of the Mar92 run period, run numbers 11168-11188. The average beam rate for these runs was 800-900k/spill, similar to the beam rates for the kaon runs.

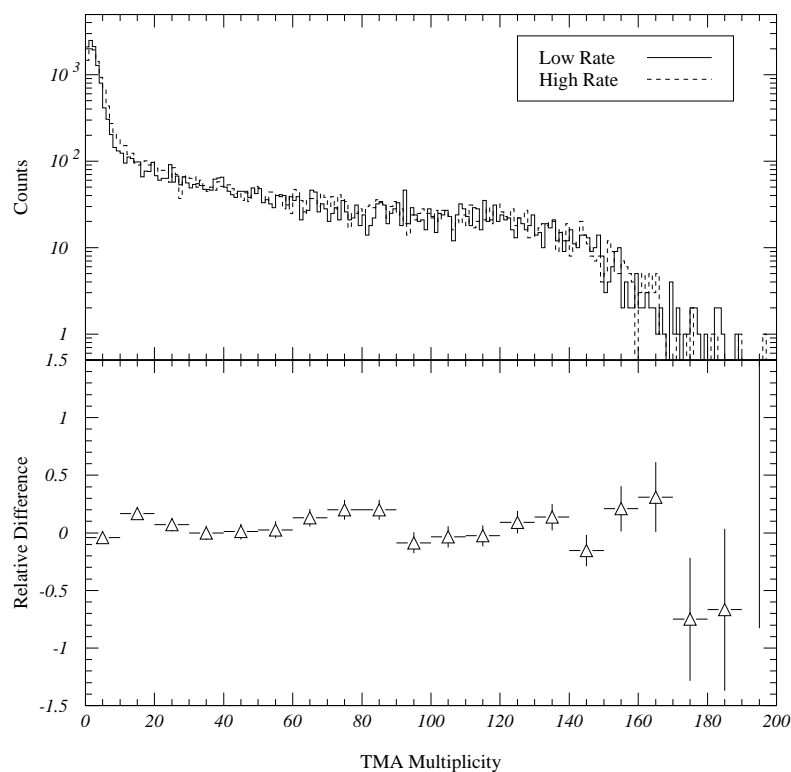


Figure 4-19: Rate dependence of TMA for Feb91 data. The top panel shows the TMA distribution for INT events for low (< 0.9 MHz) and high (> 1.3 MHz) events. The bottom panel shows the relative difference of the two distributions, $(H - L)/((H + L)/2)$. A constant fit to the relative difference is consistent with 1. There is some structure at the 10–20% level in the difference, but no attempt is made to correct the data.

4.10. TMA DATA ANALYSIS

TMA multiplicity for INT events, divide the histogram into a high and a low multiplicity bin such that the high bin contains $X\%$ of the events and the low bin contains $(1 - X)\%$ of the events. The TMA multiplicity dividing the two bins should determine the location of the cut. Unfortunately, there are problems with this procedure. The first is that a target out correction needs to be made to the multiplicity distribution. Events caused by collisions between the beam and something other than the target can generate a significant contribution to the TMA distribution. The second problem is that the very lowest part of the multiplicity spectrum (events producing very few particles in the TMA) is the result of very peripheral events, and the number of very peripheral events is very sensitive to the threshold on the bull's-eye counter. If the threshold drifts down slightly, many more BEAM events will be classified as INT events and will be included in the histogram. This will inflate the distribution for low TMA and will consequently pull down the location of the $X\%$ cut.

Instead, the technique used to determine the location of the TMA cut is as follows. The TMA multiplicity for INT events is histogrammed as above, normalized to beam (taking the BEAM and INT scaledowns into account), and an appropriate empty target TMA multiplicity distribution is subtracted. The integral of this histogram should be equal to the interaction rate of the target, up to some uncertainty due to INT discriminator fluctuation. The predetermined interaction rate of the target is multiplied by the fraction of the cross section desired and the histogram is integrated down from its high end until that amount of cross section is found. The TMA value to which you have to integrate determines the TMA cut. In the case of the aluminum target, the integration from the upper end actually begins at the point where the histogram (with its target out contribution subtracted off) hits zero. This is done to keep the target out contribution from affecting the TMA cut.

TMA Groups

The above procedure for determining the TMA cut can be performed run-by-run if there are enough statistics to reliably make cuts on the TMA distribution. The scaledowns for each run were chosen so that INT and BEAM events each accounted for about 5% of the events collected. For a full run of $\approx 40,000$ events, this gives 1000–2000 INT events, which is enough to accurately determine the TMA cut. Sometimes, however, the scaledowns were incorrectly set, resulting in too few INT events, and sometimes runs were ended before a full tape's worth of events could be taken,⁵ again

⁵Often this was followed by pressing the black button. See Section 3.4.

resulting in too few INT events. Because of this, a different strategy had to be followed. Runs were classified into groups, where each group has $\sim 5,000$ INT events. Care was taken to segregate different target and angle settings into different groups. The determination of good run groupings requires a fair amount of iteration, and the final run number ranges for the different groups used in this analysis are listed in Appendix G.

Once the groups have been chosen, the procedure for determining the location of the TMA cuts can be summarized in the following list. The first element in each item is the name of a COMIS routine used inside of CSPAW to perform the task described.

- RAWINT: Histogram raw TMA distributions for all runs.
- MTGRPAVG: Form the average beam-normalized TMA distributions for empty target groups.
- INGRPAVG: Form the average beam-normalized TMA distributions for target in groups.
- INGRPSUB: For each target in group, subtract the contribution of an appropriately chosen target out group.
- GRPSUM: Form running sums of the target in group averages by integrating down from the high multiplicity end of the histogram.

Given the output of GRPSUM, one can easily determine the TMA threshold to use for any desired fraction of the cross section. Multiply the target fraction by the desired fraction of the cross section. Find the bin in the running sum that just exceeds that value. The TMA multiplicity of that bin is the threshold to use. All events above that multiplicity are taken.

Statistics, Centrality and the Choice of Cuts

At this stage, the actual multiplicity cuts to use on the data can be determined. Whatever other cuts are made, the collaboration tradition is to report central results, where central is defined as the top 7% of the inelastic cross section. For the TMA, this means events in the top 7% of the multiplicity distribution, and the reason for this particular choice is that in the case of Si+Au, the inner 7% of the cross section corresponds to impact parameters small enough to ensure complete overlap of the

4.10. TMA DATA ANALYSIS

projectile and target given a completely geometric picture of the cross sections

$$\left(\frac{1.2 \times 197^{1/3} - 1.2 \times 28^{1/3}}{1.2 \times 197^{1/3} + 1.2 \times 28^{1/3}} \right)^2 = 9.9\%. \quad (4.38)$$

Other cuts may be made, however, limited only by the statistics available. Figure 4-20 shows the TMA distribution for Si+Al and Si+Au events containing a K^+ or a K^- . The TMA distribution shown should only be taken as approximate, since it is a combination of Feb91 and Mar92 data, which as discussed above, have multiplicity distributions that differ quite a bit. However, it is a good enough guide to the range of multiplicity cuts that may be reasonably made. The highest multiplicity hatched area in each histogram, labelled TMA1, corresponds to the top 7% of the INT cross-section. There are enough kaons in this cut to plot reasonable spectra, so using the statistics in that cut as a measure, the other cuts, TMA2–4 have been constructed to have similar statistics, for both Si+Al and Si+Au.

Since the events with kaons are skewed toward central collisions, as can be seen in the figure, the most peripheral cut that can be made on the data that still contains enough statistics to reliably plot and fit spectra is the outer 60% of the inelastic cross section. In the case of Si+Au, using the formula $r = 1.2A^{1/3}$ fm to calculate the radius of each nucleus, the impact parameter of a grazing collision is 10.6 fm, and the outer 60% of the cross section corresponds to collisions with impact parameters greater than 6.7 fm. In the case of Si+Al, the impact parameter of a grazing collision is 7.2 fm, and the outer 60% of the cross section corresponds to collisions with impact parameters greater than 4.6 fm.

4.10.4 Consistency of TMA Cuts

Part of the difficulty in getting the TMA cuts consistent is that the cuts are based on a quantity measured for INT while the data is plotted for SPEC events (most often with a LVL2 veto as well). A run, or group of runs, with few INT events may have large statistical fluctuations in the determination of multiplicity cuts, but those same runs may contain many kaons. Errors in setting the TMA cut for those runs could lead to large effects on the cross sections. In order to check the quality of the TMA groups chosen, we can plot spectrometer integrated kaon counts for each run. This is just the number of found kaons inside the spectrometer acceptance, with no correction for

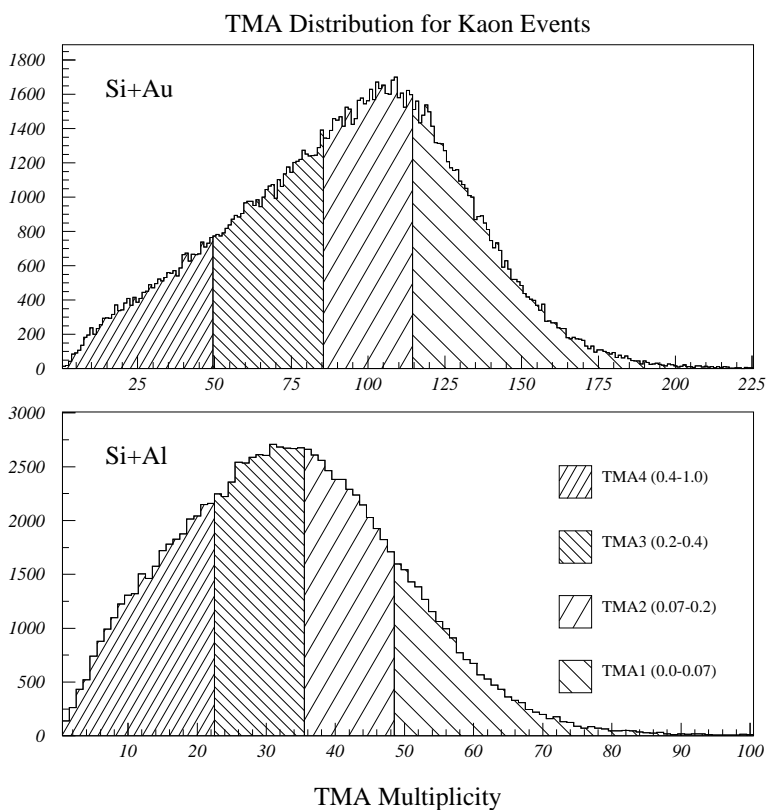


Figure 4-20: TMA distribution for events containing a K^\pm . The data is a combination of Feb91 and Mar92, so the exact multiplicities should only be taken as approximate, since the configuration of the TMA was changed between the two runs. The highest multiplicity cut, TMA1, corresponds to the uppermost 7% of the INT multiplicity spectrum. The other cuts have been designed to have similar statistics to the TMA1 cut.

4.11. ZCAL ANALYSIS

decay or reconstruction efficiency at all. For all runs within a spectrometer angle and magnetic field setting, this number should be the same.⁶ Often, after subdividing the data set appropriately, only one or two runs fall into each category. Nonetheless, the spectrometer integrated counts for these orphan runs can be compared to related categories to see if their values make sense. Figure 4-21 shows several examples of the consistency of the integrated counts for K^+ in Si+Au for the TMA1 cut. If any run is found far outside what is statistically plausible, the group of which it is a part is examined to see if the TMA response might have changed over the course of the runs making up the group. If so, groups can be subdivided or rearranged.

4.11 ZCAL Analysis

The ZCAL is used to measure the remaining forward going energy of the beam fragments. Dividing the ZCAL energy by the kinetic energy of the beam yields the number of projectile spectators—those nucleons in the beam that don't strongly interact with the target. The calorimeter is often used to select events, but here it will be used to measure the number of spectators for the different TMA cuts described in Section 4.10. The reason for using the ZCAL as a measurement tool rather than an event selector is due to adverse effects suffered by the ZCAL as a consequence of the high beam rates of E859. As will be shown, the result of these effects is to reduce the resolution of the calorimeter, so that selecting events based on ZCAL information would result in a bias, while using it to measure the forward energy of TMA-selected events just results in a less precise measurement than had the ZCAL worked better. Ron Soltz was the first to point out the utility of using the ZCAL this way, and that it might be possible to calibrate away the beam rate dependence in the ZCAL signal. As an added bonus, using the ZCAL in this way circumvents the question of the performance of the ZCAL at 5° , where the angular acceptance of the ZCAL is reduced to $\sim 0.8^\circ$ because the beam pipe passes through a hole in the yoke of the Henry Higgins magnet. Once the ZCAL distribution for a particular TMA cut is determined it should be applicable to any angle setting of the spectrometer, including 5° .

⁶In the local vernacular, this is referred to as the number of counts “per DNDYFACT”, the name of a variable in the cross section code.

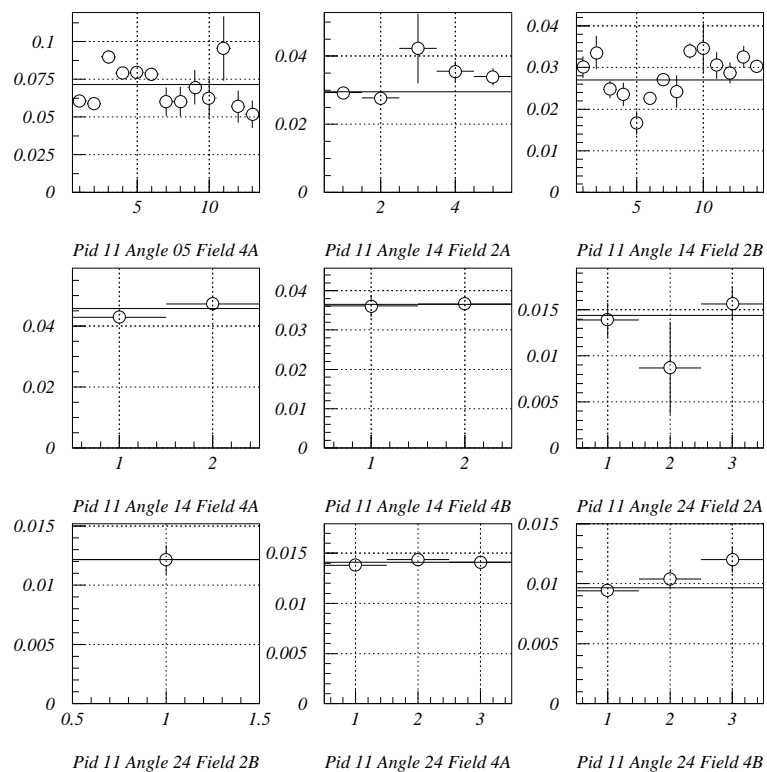


Figure 4-21: Spectrometer integrated K^+ counts for Si+Au TMA1 cut. Each panel shows the integrated number of counts in the spectrometer acceptance for each of the several runs that match the same combination of criteria. Only a subset of all the combinations is shown. Within each panel, fluctuations of order 10-15% are typical, which contributes to the systematic error in the determination of the yields.

4.11. ZCAL ANALYSIS

4.11.1 Rate Dependence of ZCAL Signal

The instantaneous beam rate is determined by looking at the beam counter ungated clock, which records the number of microseconds since the last event. The inverse of this time is a measure of the beam rate immediately preceding the current event. During the Feb91 run the beam rate was as high as $1.5\text{--}2.0 \times 10^6$ particles/spill, and the ZCAL signal began to show some rate dependence. This can be seen in Figure 4-22, where a profile histogram of the ZCAL energy distribution as a function of the instantaneous beam rate is shown for a $\text{BEAM} \wedge \overline{\text{INT}}$ events taken during a series of Feb91 runs. The ZCAL distribution remains relatively constant out to ~ 0.4 MHz, but then begins a linear rise with the rate. This rate dependence can be traced to relatively long ADC gates on the ZCAL which began to admit pileup for the high E859 beam rates. To counteract this, clipping circuitry was added to the ADC inputs between the Feb91 and Mar92 runs. Figure 4-23 shows the location of the beam peak in the ZCAL energy distribution for the Mar92 running, indicating that the change to the electronics has nearly eliminated the severe rate dependent pileup effects. However, as can be seen in Figure 4-24 which shows the ZCAL energy distribution for INT events for two different bins in rate, the ZCAL resolution has worsened in a way that is also beam rate dependent. At high rates, the distribution is broader, and worse, negative values are seen for $\sim 5\%$ of the events. The resolution is somewhat better at low beam rate.

4.11.2 ZCAL Distributions for TMA Gated Events

If we restrict ourselves to low rate events, the ZCAL is trustworthy enough that we can make a distribution of the ZCAL energy for each of the TMA cuts used for Si+Al and Si+Au. Figure 4-25 shows the difference in the ZCAL energy distributions for Mar92 Si+Al events satisfying the TMA1 cut (the most central 7% of the TMA distribution). The middle panel shows how both the mean and RMS of the distribution change when the events are also required to have a low instantaneous beam rate. The beam rate cut is applied to all events before making the cuts described in this section.

The ZCAL energy distributions can then be converted into the number of projectile participants, N_{part}^{proj} , by

$$N_{part}^{proj} = A_{proj} \left(1 - \frac{E_{ZCAL}}{T_{proj}} \right) \quad (4.39)$$

where A_{proj} is the number of nucleons in the projectile, E_{ZCAL} is the energy measured in the

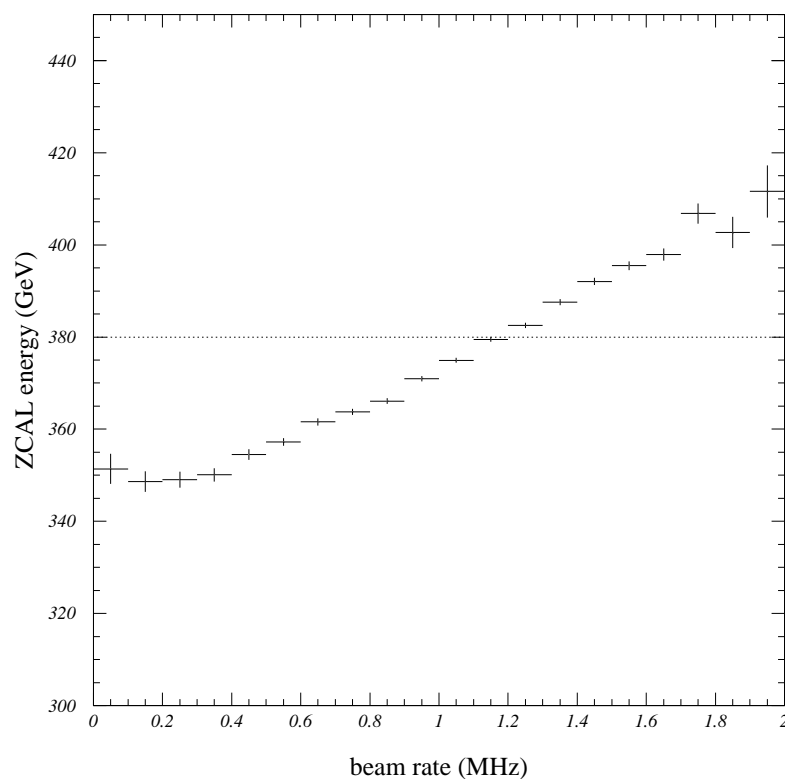


Figure 4-22: Feb91 ZCAL rate dependence. The figure shows a profile histogram of the ZCAL energy for $\text{BEAM} \wedge \overline{\text{INT}}$ events as a function of the instantaneous beam rate for a set of Feb91 runs. By looking at these events, the profile histogram tracks the location of the beam peak. The dotted line shows the value to which the complete ZCAL distribution is calibrated, 380 GeV. The ZCAL distribution remains relatively constant out to ~ 0.4 MHz, but then begins a linear rise with the rate.

4.11. ZCAL ANALYSIS

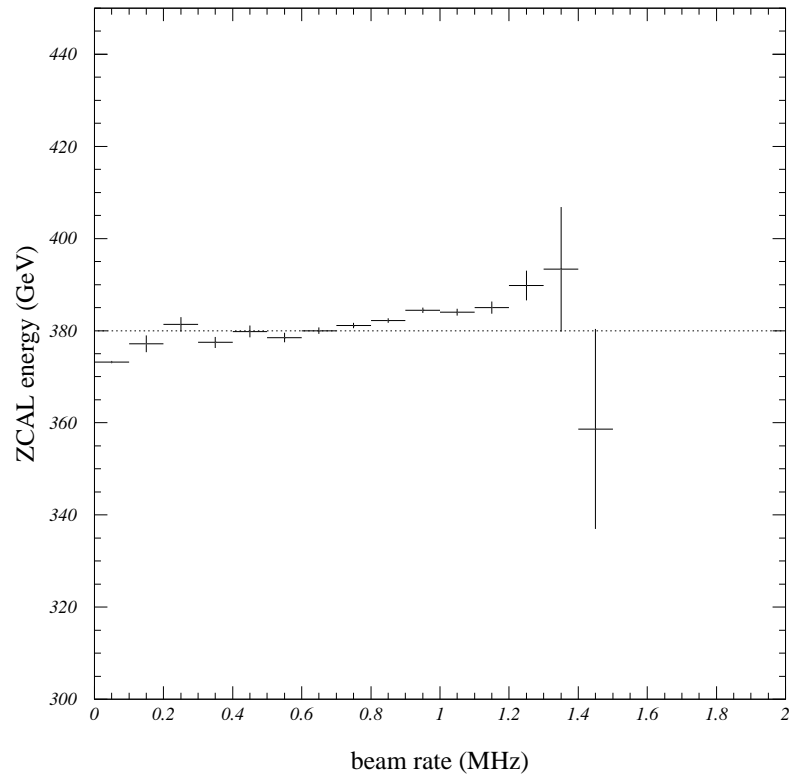


Figure 4-23: Mar92 ZCAL rate dependent beam peak. The figure shows a profile histogram of the ZCAL energy for $\text{BEAM} \wedge \overline{\text{INT}}$ events as a function of the instantaneous beam rate for a set of Mar92 runs. The change in the ZCAL electronics between the Feb91 and Mar92 runs has apparently eliminated most of the beam rate dependence in the location of the ZCAL beam peak. Again, the dotted line shows the energy value to which the complete ZCAL energy distribution is calibrated, 380 GeV.

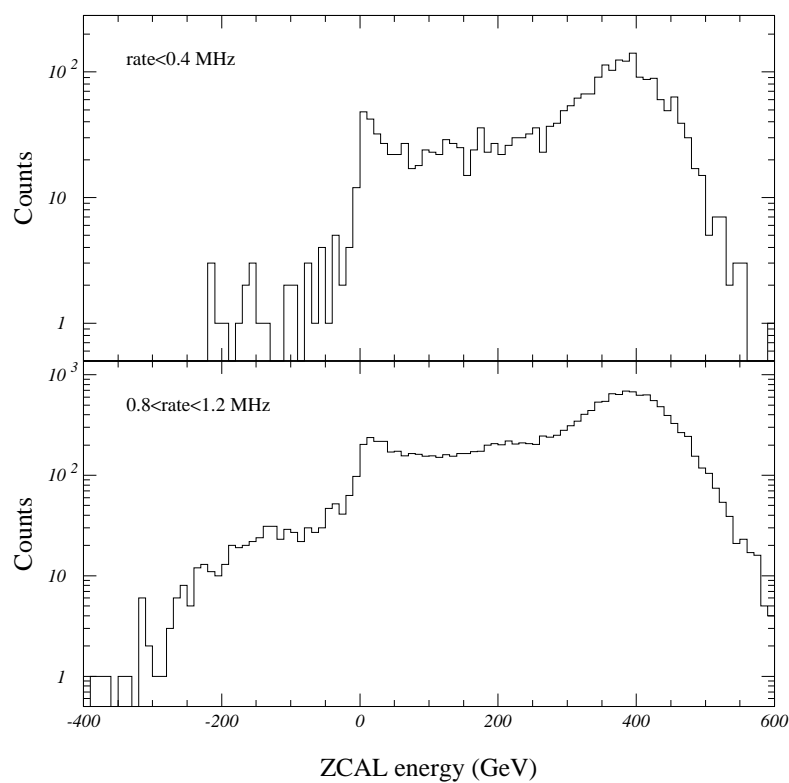


Figure 4-24: Mar92 ZCAL rate dependent resolution. The top panel shows the ZCAL distribution for relatively low beam rate INT events. The bottom panel show the same distribution for high beam rate events instead. At the higher rates, there is a worsened ZCAL resolution, with $\sim 5\%$ of the events actually recording negative ZCAL energies.

4.11. ZCAL ANALYSIS

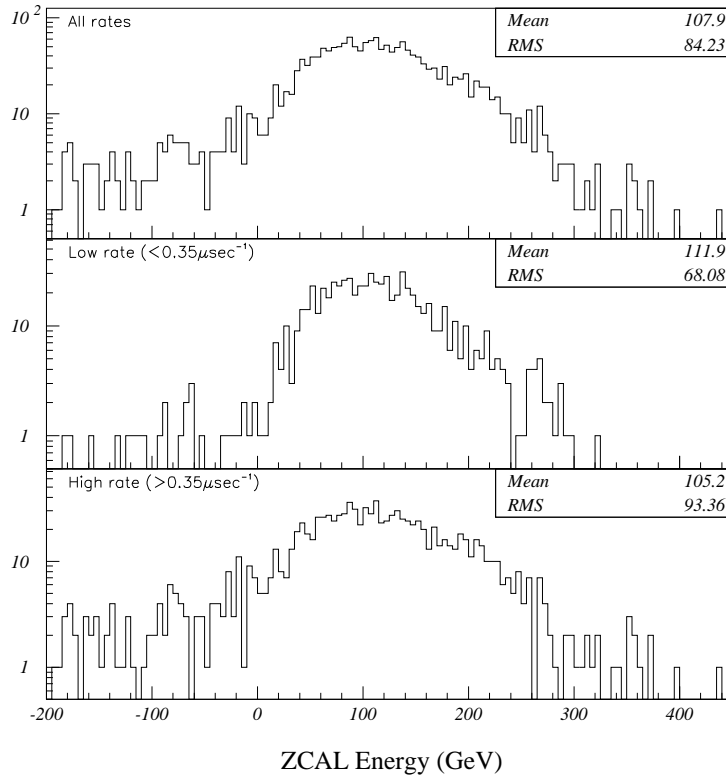


Figure 4-25: ZCAL distribution for Si+Al TMA1 events. This is an example of the type of effect seen by restricting the ZCAL measurement to low beam events. The top panel in the ZCAL distribution for all Si+Al events satisfying the TMA1 cut, with no restriction on the beam rate. The middle panel shows the same distribution for low rate events; the bottom panel shows it for high beam rate events. Comparing the low and high rate distributions, one can see that the low rate distribution is narrower with fewer negative ZCAL events than the high rate one. The mean and RMS of the two distribution are also different.

ZCAL, and T_{proj} is the total kinetic energy of the projectile nucleus. Table 4.6 lists the average and the RMS of the ZCAL and projectile participants for each of the TMA cuts for Si+Al and Si+Au. The fact that the ZCAL energies and the calculated number of projectile participants are skewed toward central collisions just reflects the fact that the kaon production is also skewed toward central events and the TMA cuts are designed to fairly evenly divide the kaon statistics among the four bins used. The two most central TMA cuts are only slightly separated, on average, in ZCAL energy, with quite a bit of overlap. The more peripheral cuts do better, and give a fair lever arm to the ZCAL measurement, but there is a good deal of overlap in the distributions for even the TMA4 cut.

System	Name	$\langle E_{ZCAL} \rangle$	E_{ZCAL}^{RMS}	$\langle N_{ZCAL} \rangle$	N_{ZCAL}^{RMS}
Si+Al	TMA1	118.3	58.5	19.3	4.3
	TMA2	161.8	68.0	16.1	5.0
	TMA3	229.8	72.1	11.1	5.3
	TMA4	318.2	55.8	4.6	4.1
Si+Au	TMA1	21.8	23.1	26.4	1.7
	TMA2	51.7	42.2	24.2	3.1
	TMA3	149.6	72.1	17.0	5.3
	TMA4	278.8	65.3	7.5	4.8

Table 4.6: Properties of ZCAL distributions for TMA gated events. Shown are the average and the RMS of the ZCAL energy distribution and the calculated number of projectile participants for each of the TMA cuts used in the analysis.

Chapter 5

Data Presentation and Discussion

This chapter presents the results of the data analysis and discusses the features and trends of the data. Invariant yields for kaons as a function of m_{\perp} and y are shown first. These distributions are then parameterized and integrated to give both transverse slopes and yields as a function of rapidity. The variation in the transverse and longitudinal distributions of kaons as a function of centrality is also presented. Sources of systematic error are examined and estimates of the magnitude of these errors are made. Data are presented for the production of K^{-} and K^{+} for two different systems, and for minimum bias data plus four different TMA cuts.

5.1 Slopes and Invariant Yields

The procedure used to calculate the invariant yields was described in Section 4.9. These yields, plotted in slices of rapidity as a function of m_{\perp} , are found to be well described by exponentials in m_{\perp} . As an example of the transverse distributions, Figure 5-1 shows the m_{\perp} spectra for the central $\text{Si}+\text{Au} \rightarrow K^{-}$ data.¹ The ordinate is the transverse kinetic energy, $m_{\perp} - m_0$, and the abscissa shows the invariant yield. Each of the distributions is a slice of the data 0.2 units of rapidity wide, and all except the topmost distribution have been divided by successive factors of 10 for display purposes. In the case of the minimum bias data, the statistics are good enough that rapidity bins 0.1 unit wide were used instead. The data slice of the topmost spectrum is centered at $y = 0.5$, and the central rapidity of each slice increases as one descends on the plot. The legend at right shows

¹The shorthand $\text{Si}+\text{A} \rightarrow K$ is used to mean both inclusive or semi-inclusive data.

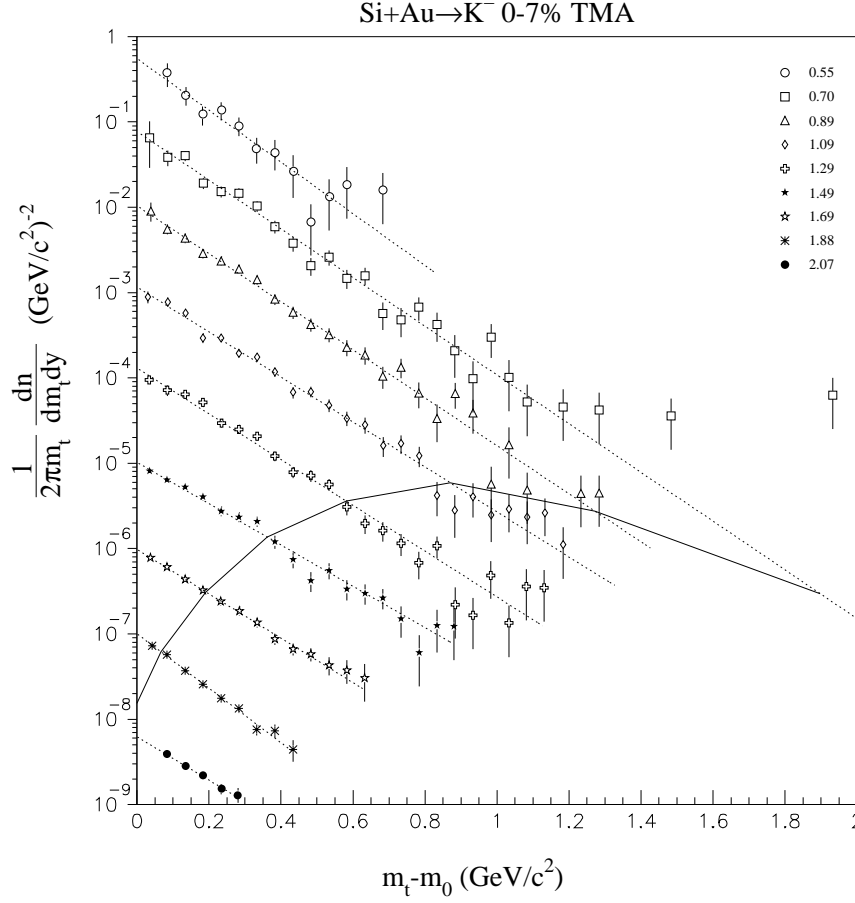


Figure 5-1: Central Si+Au→K⁻ m_{\perp} distribution. This is shown as an example of the data; the rest of the plots are presented in Appendix A. The horizontal axis is the transverse kinetic energy, $m_{\perp} - m_0$, and the vertical axis is the invariant yield per event. Each distribution is a slice of the data 0.2 units of rapidity wide, and the values at upper right show the average rapidity of the data in each slice. After the topmost slice, each distribution has been divided by successive factors of 10 for display purposes. The dotted lines are exponential m_{\perp} fits to the data. The solid line indicates the maximum momentum of π -K separation using TOF alone.

5.1. SLOPES AND INVARIANT YIELDS

the average rapidity for the data in each slice. Almost all of the data for the lowest rapidity slice comes from the 44° spectrometer setting. The mid-rapidity slices are made up of data from a few different spectrometer settings, and the highest rapidity slices are made entirely of 5° data (refer to Figure 4-12). The solid line which curves up from lower left indicates the π -K TOF separation limit; all data below and to the right of this line require the GASČ for particle identification. So that the reader may examine the quality of the data, the coverage in both m_\perp and y , and the degree to which the data may be described as exponential in m_\perp , the plots of the invariant yields as a function of m_\perp for K^+ and K^- for all systems and all TMA cuts are presented in Appendix A.

The explicit form of the function used to parameterize the data is (see Appendix F for details)

$$\frac{d^2n}{2\pi m_\perp dm_\perp dy} = Ae^{-m_\perp/B}, \quad (5.1)$$

where B is the *inverse slope parameter* (sometimes just called the *slope*). That the spectra should be well described by this function is basically an empirical observation, and in fact, it is already known from the E802 results that the pion invariant yields are better fit by exponentials in p_\perp and the protons by Boltzmann, or thermal, distributions [Par92]. To compare the difference between fits of exponentials in m_\perp and p_\perp to the data, Table 5.1 shows the χ^2 per degree of freedom for the two different parameterizations for data in slices of rapidity 0.2 units wide centered at $y = 1.3$. Not only do the data seem to be substantially better described by the m_\perp fits, but it also appears that the K^- may be slightly better fit by this parameterization than the K^+ . In his thesis, Brian Cole, showed that it was plausible that the nearly exponential m_\perp behavior of pions could be the result of superposing several curves, each of which was exponential in p_\perp^2 [Col92]. In bubble chamber data, where exclusive pion production can be studied, baryon, meson and vector meson decays each produced pions with an exponential in p_\perp^2 distribution—with each type of decay having a different slope.

It is possible that a similar mechanism is at work in the kaons. Hyperon decays such as $\Lambda(1520) \rightarrow NK^-$, vector meson decays such as $f_2(1720) \rightarrow K^+K^-$, and the decay of excited kaon states such as $K^* \rightarrow K\pi$ all have similar Q values. However, each of these three types of decays divides the available energy differently since the first involves a kaon and a heavier particle, the second involves two equally massive particles, and the third is a kaon and a lighter particle. For a

System	Fit Type	χ^2/dof	
		K^+	K^-
Si+Au min bias central	m_\perp	39.5/21	21.5/21
	p_\perp	253/27	240/27
	m_\perp	46.2/21	27.7/21
	p_\perp	83/27	64.8/27
Si+Al min bias central	m_\perp	33.2/21	28.6/21
	p_\perp	166/27	140/27
	m_\perp	16.4/21	31.1/21
	p_\perp	44.6/27	60.2/27

Table 5.1: Comparison of the χ^2/dof for different fits to the K^\pm transverse distributions. The distributions are better fit by exponentials in m_\perp than exponentials in p_\perp .

kaon produced in a decay of a given Q , the more massive the other daughter, the more energy the kaon receives. However, this additional energy will tend to distribute the kaon in rapidity.

To summarize what is found in the transverse spectra, we may plot the inverse slope parameters (B in the above fit function) for the kaons. Figure 5-2 shows a summary of the inverse slope parameters for the different systems and centralities as a function of rapidity. All systems and all centralities show an increase in the slope parameter from target rapidity to mid-rapidity followed by a decrease for rapidities above that.

The inverse slope parameters for the Si+Al data show very little variation as a function of centrality, where the most central data is defined as the top 7% of the TMA distribution, and the most peripheral is the lowest 60% of the TMA distribution. This may be an indication that the Si+Al system is not a large system compared to some characteristic size or volume related to kaon production; therefore it makes little difference whether one has a central or a peripheral Si+Al collision. The Si+Au slopes, on the other hand, show a substantial increase as one selects more central collisions. For a mid-rapidity slice, $1.2 < y < 1.4$, the K^+ slopes increase from $158 \pm 3 \text{ MeV}/c^2$ for peripheral events to $184 \pm 3 \text{ MeV}/c^2$ for central events. The K^- mid-rapidity slopes increase from $141 \pm 3 \text{ MeV}/c^2$ for peripheral events to $162 \pm 3 \text{ MeV}/c^2$ for central data. For comparison, the most central Si+Al slopes in the same rapidity range are $169 \pm 4 \text{ MeV}/c^2$ and $149 \pm 3 \text{ MeV}/c^2$ for K^+ and K^- , respectively.

5.1. SLOPES AND INVARIANT YIELDS

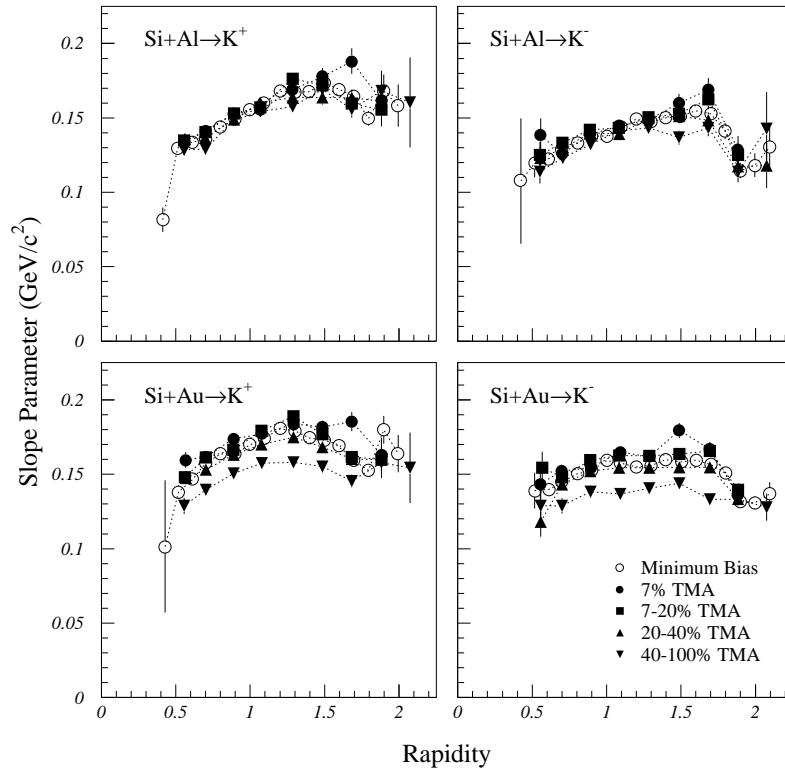


Figure 5-2: m_{\perp} slope parameter summary. The top panels show slope parameters for kaons from Si+Al collisions; the bottom panels for kaons from Si+Au. The panels on the left are K^+ 's and the panels on the right are K^- 's. All slope parameters are shown as a function of laboratory rapidity.

In the p-A results, the statistics for K^- are fairly poor, but the inverse slope parameters for both K^+ and K^- in Si+Au near $y = 1.3$ are about $160 \text{ MeV}/c^2$. Certainly there is not a $20 \text{ MeV}/c^2$ difference between the two. The slope difference between the K^+ and the K^- is apparently a nucleus-nucleus effect, and may indicate an increasing difference in the physical processes producing K^- and K^+ .

5.2 Average Transverse Momentum

The average transverse momentum for a distribution exponential in m_\perp is

$$\langle p_\perp \rangle = \frac{\int_{m_0}^{\infty} p_\perp A e^{-m_\perp/B} dm_\perp}{\int_{m_0}^{\infty} A e^{-m_\perp/B} dm_\perp} = \frac{\int_{m_0}^{\infty} \sqrt{m_\perp^2 - m_0^2} e^{-m_\perp/B} dm_\perp}{\int_{m_0}^{\infty} e^{-m_\perp/B} dm_\perp}. \quad (5.2)$$

The integral in the numerator of this expression has a solution of the form [GR80]

$$\int_u^{\infty} x(x^2 - u^2)^{\nu-1} e^{-\mu x} dx = 2^{\nu-1/2} \frac{1}{\sqrt{\pi}} \mu^{1/2-\nu} u^{\nu+1/2} \Gamma(\nu) K_{\nu+1/2}(u\mu). \quad (5.3)$$

Putting in $u = m_0$, $\nu = 3/2$, and $\mu = 1/B$, and combining this with Equation 5.2, we get the following expression for the average p_\perp [Che93]:

$$\langle p_\perp \rangle = (m_0/B) m_0 \frac{K_2(m_0/B)}{1 + m_0/B} e^{m_0/B}. \quad (5.4)$$

Figure 5-3 shows $\langle p_\perp \rangle$ for K^\pm versus rapidity for the most peripheral and the most central TMA cuts. These plots contain essentially the same information as the plots of slope parameter as a function of rapidity, since $\langle p_\perp \rangle$ can be calculated knowing only the slope parameter and the rest mass, but it puts it into a form for which there might be a little bit more physical feeling. It also makes it easier to compare to p-p results. For central Si+Au near mid-rapidity, the K^+ have an average p_\perp of $466 \pm 4 \text{ MeV}/c$, while the K^- have an average of $426 \pm 6 \text{ MeV}/c$. In p-p collisions, the average p_\perp for K^- at this energy is $\sim 395 \text{ MeV}/c$, for K^+ is $\sim 415 \text{ MeV}/c$ [Che93]. The increase in $\langle p_\perp \rangle$ is presumably due to the additional collisions in A-A.

5.2. AVERAGE TRANSVERSE MOMENTUM

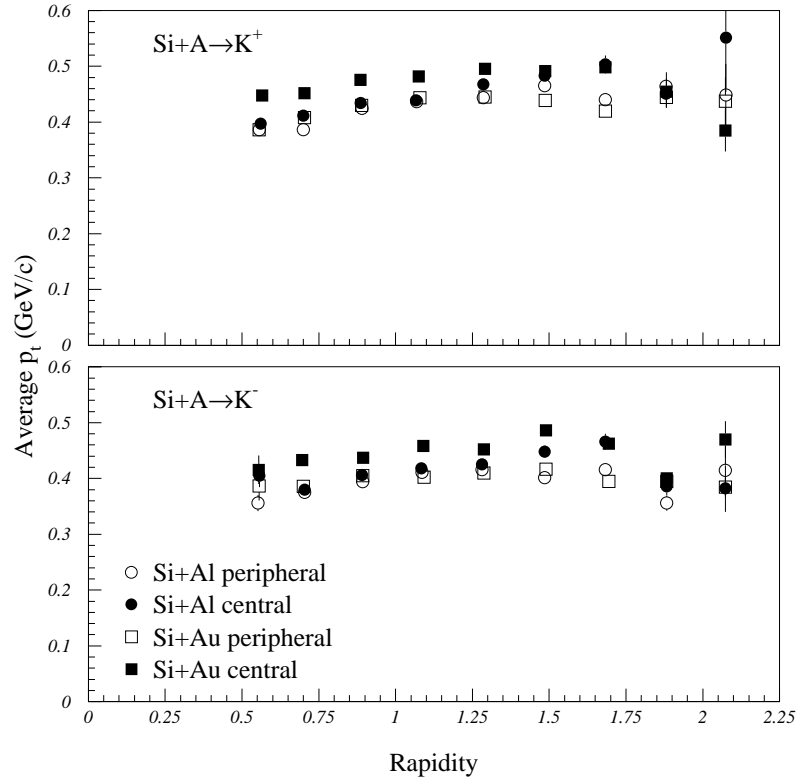


Figure 5-3: Average p_{\perp} versus rapidity for Si+Al and Si+Au. The top panel is for K^+ ; the bottom panel shows K^- . The K^+ consistently have $\sim 20\text{--}40$ MeV/c larger $\langle p_{\perp} \rangle$ than the K^- . Si+Al shows essentially no difference between peripheral and central collisions for both K^+ and K^- , while Si+Au shows a difference of $\sim 20\text{--}40$ MeV/c. This difference seems to disappear as one moves forward in rapidity toward y_{NN} .

5.3 Rapidity Distributions

If the fits to the m_{\perp} distributions are integrated over all m_{\perp} , the yield, dn/dy , in each slice of y may be determined. The integration involves an extrapolation outside of the range of m_{\perp} for which there is actually data, so there will be a systematic error associated with each dn/dy point, inversely related to the amount of m_{\perp} coverage the slice has. Integrating the invariant yield over m_{\perp} gives

$$\frac{dn}{dy} = \int_{m_0}^{\infty} 2\pi m_{\perp} A e^{-m_{\perp}/B} = 2\pi AB^2(m_0 + B)e^{-m_0/B}. \quad (5.5)$$

Figures 5-4–5-7 show the dn/dy distributions for K^+ and K^- as a function of rapidity for minimum bias data and for data gated on different TMA cuts. For all the systems, as one would expect, the amplitude of the dn/dy distributions grows with more central collisions.

Figure 5-4 and Figure 5-5 show the dn/dy distribution for kaons in Si+Al. For K^+ the peak value of the dn/dy grows from 0.160 ± 0.006 for the most peripheral TMA cut to 1.25 ± 0.04 for the most central cut. For K^- , the peak climbs from 0.043 ± 0.002 in peripheral collisions to 0.32 ± 0.01 in central collisions. One can exploit the near symmetry of the Si+Al system to reflect about y_{NN} the data measured over the rapidity range $0.5 < y < 2.1$ and obtain nearly complete rapidity coverage. This allows a check on the quality of the data by looking at the degree to which the reflected and unreflected data overlap in the mid-rapidity region. As can be seen from the figures, the data in the region of overlap seem to be in substantial agreement. In the case of the minimum bias data, where the statistics allow the dn/dy to be plotted in bins 0.1 unit wide, there are 5 data points above $y = 1.72$ providing quite a bit of overlap.

Figure 5-6 and Figure 5-7 show the dn/dy distribution for kaons in Si+Au. The Si+Au data does not have the same reflection symmetry as the Si+Al system, so it is a little tougher to argue that we have complete coverage. However, for the central Si+Au data at least, the yields peak well below mid-rapidity, so the yields have fallen by 20–50% before the rapidity coverage ends near $y = 2.1$.

Table 5.2 summarizes the features of the kaon rapidity distributions. The parameters of Gaussian fits to the dn/dy distributions are shown. In the case of Si+Al, the mean of the Gaussian is fixed at $y = 1.72$ and only the amplitude and the width are allowed to vary. For Si+Au, the fit is from the lowest rapidity data points to $y = 1.8$. This is done because the distribution begins to flatten at

5.3. RAPIDITY DISTRIBUTIONS

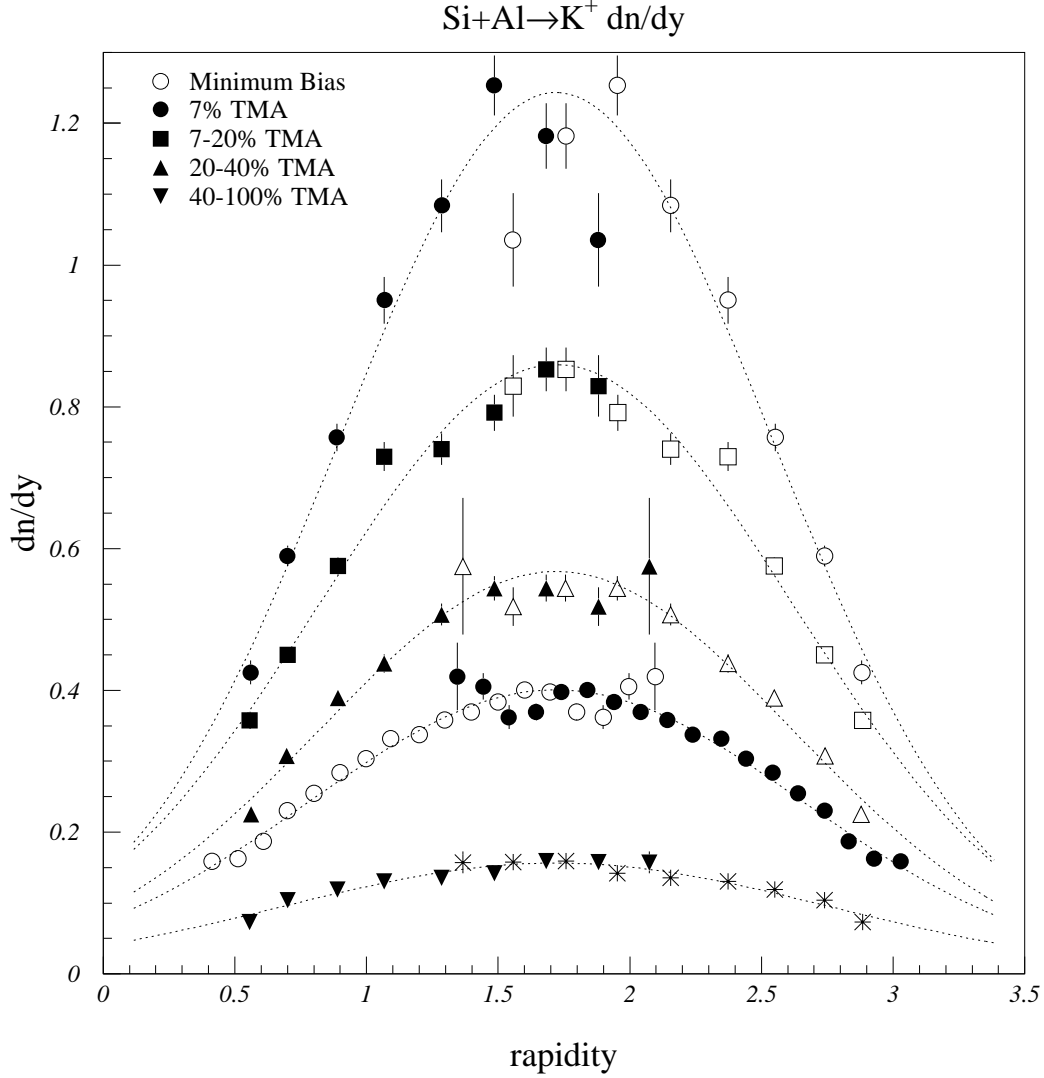


Figure 5-4: $\text{Si+Al} \rightarrow \text{K}^+ \text{ dn/dy}$ distributions. The filled symbols in the range $0.5 < y < 2.1$ are the actual data for different TMA cuts, the open circles in that range are the minimum bias data. The points extending up to $y = 3.0$ are obtained by reflection about $y_{\text{NN}} = 1.72$, the nucleon-nucleon center-of-mass rapidity. The lowest dn/dy points are for the peripheral TMA cut, the highest points are for the central TMA cut. The dotted line shows Gaussian fits to the unreflected data with the mean fixed at $y = 1.72$.

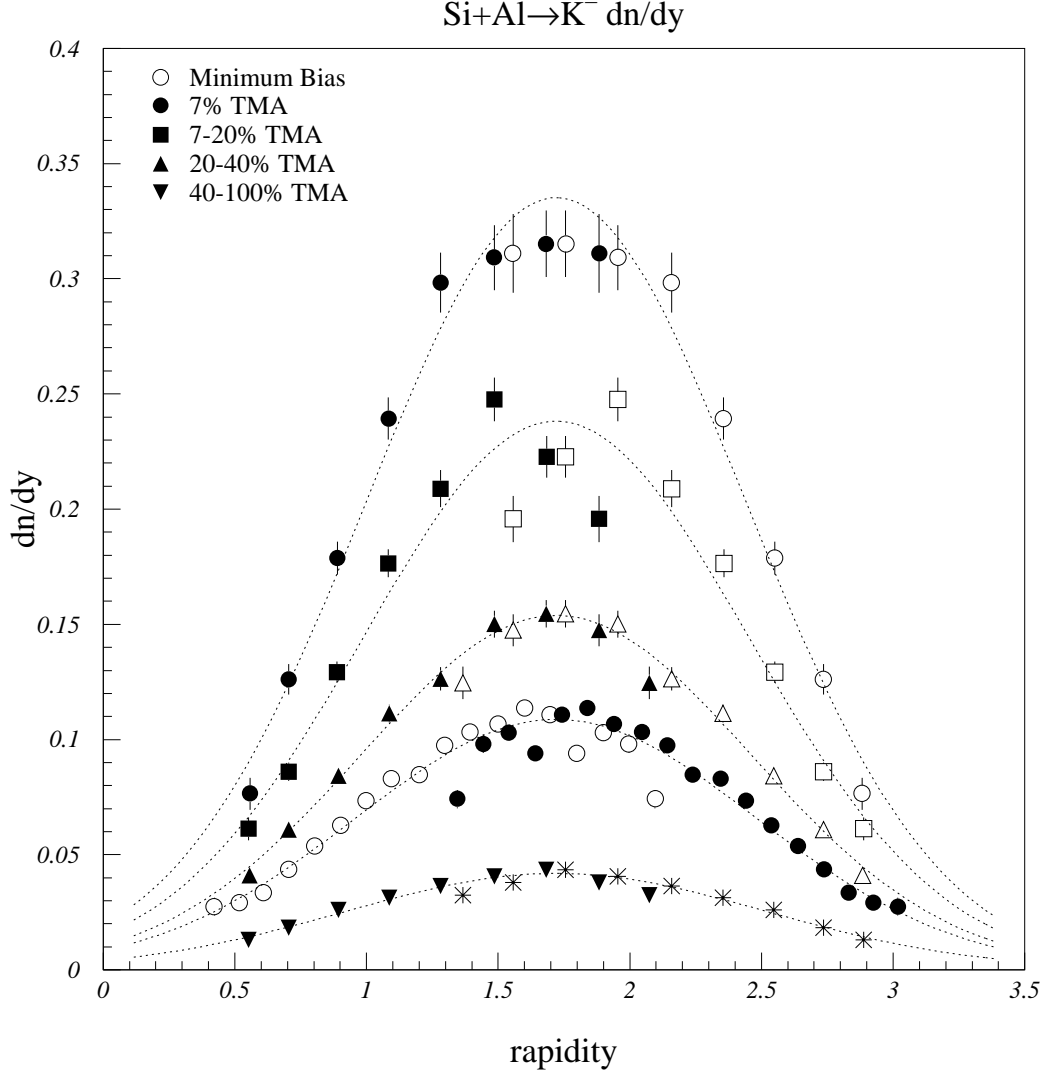


Figure 5-5: $\text{Si}+\text{Al} \rightarrow \text{K}^- \text{ dn/dy}$ distributions. The filled symbols in the range $0.5 < y < 2.1$ are the actual data for different TMA cuts, the open circles in that range are the minimum bias data. The points extending up to $y = 3.0$ are obtained by reflection about $y_{\text{NN}} = 1.72$, the nucleon-nucleon center-of-mass rapidity. The lowest dn/dy points are for the peripheral TMA cut, the highest points are for the central TMA cut. The dotted line shows Gaussian fits to the unreflected data with the mean fixed at $y = 1.72$.

5.3. RAPIDITY DISTRIBUTIONS

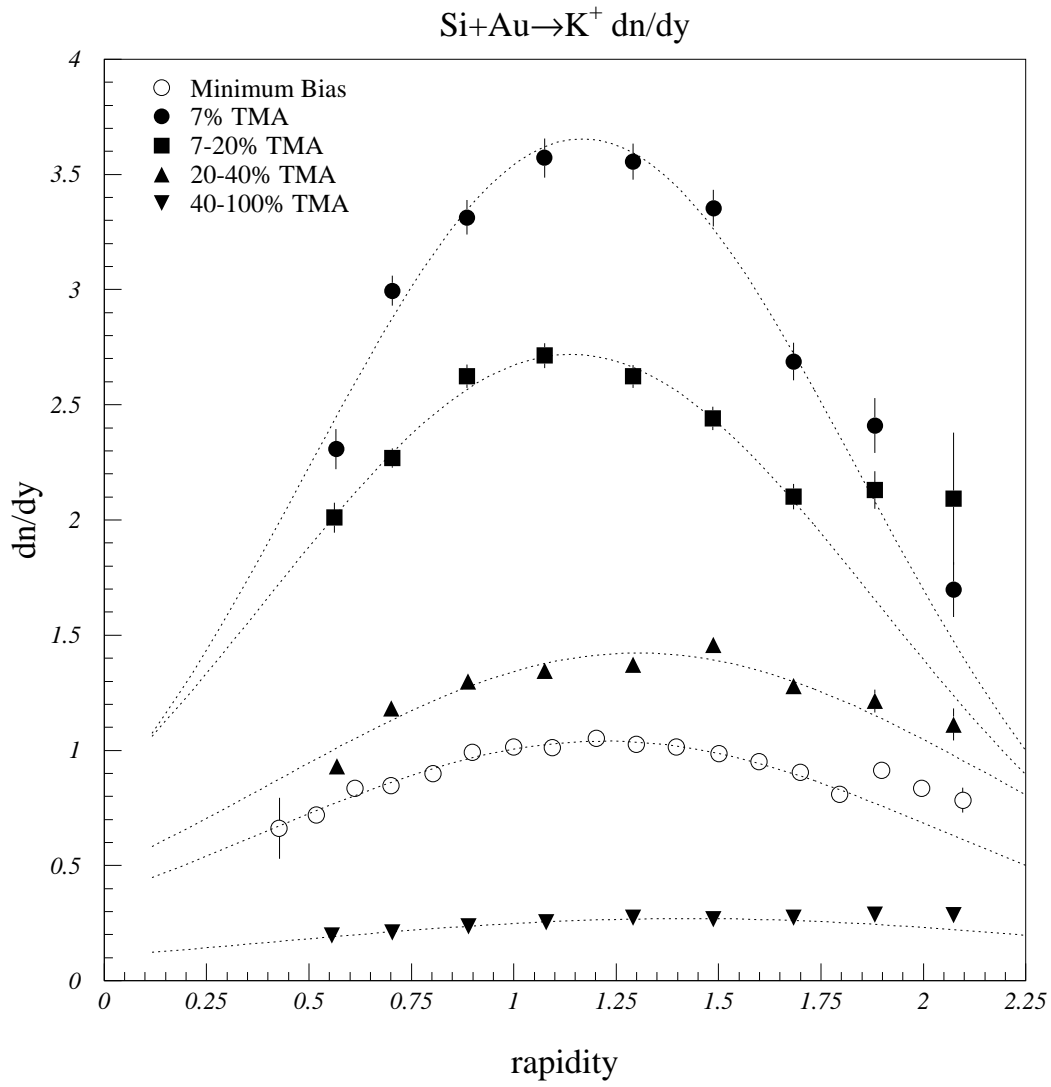


Figure 5-6: $\text{Si}+\text{Au} \rightarrow \text{K}^+ \text{ dn/dy}$ distributions. The lowest dn/dy points are for the peripheral TMA cut, the highest points are for the central TMA cut. The open circles are minimum bias data plotted in bins 0.1 unit of rapidity wide. The dotted lines show Gaussian fits to the data points near the peaks of the distributions.

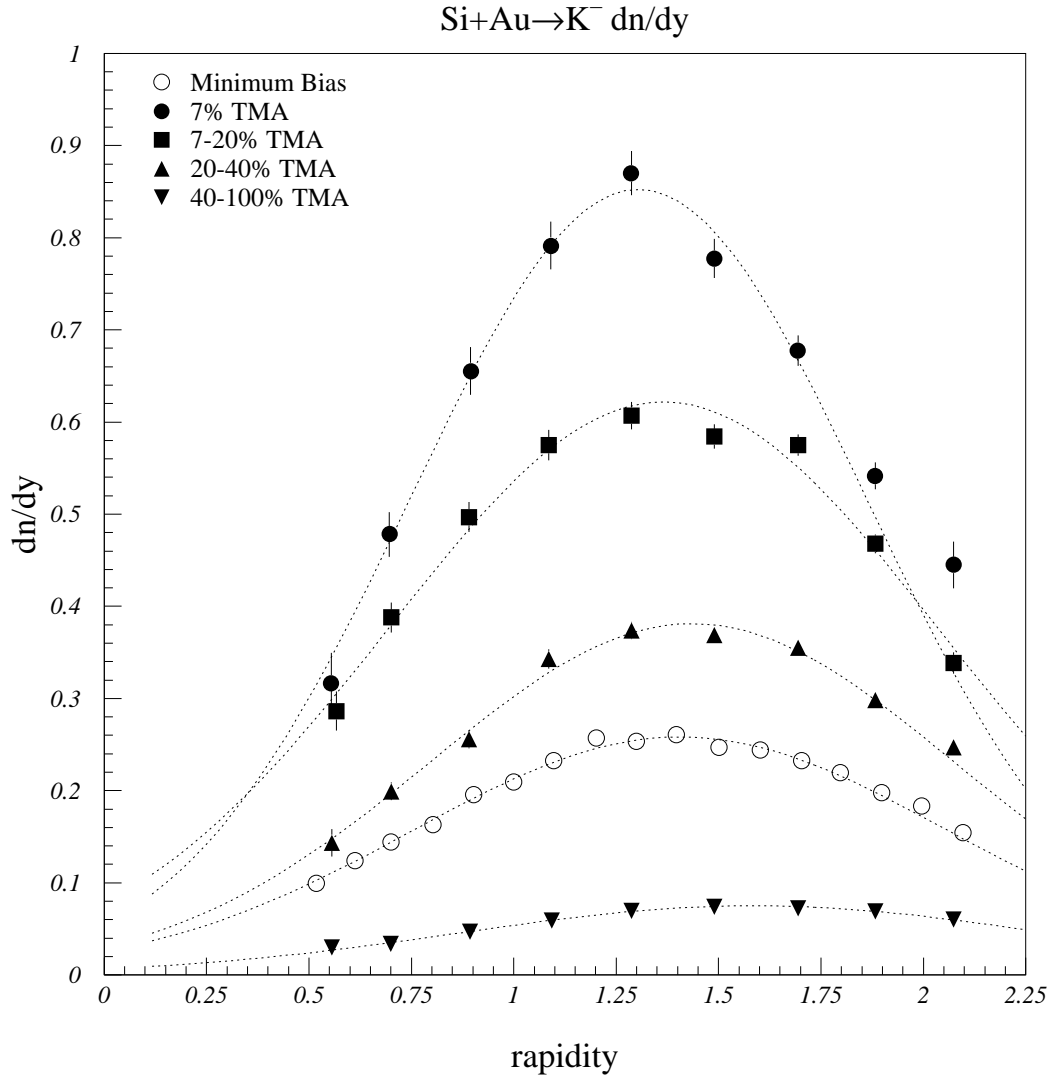


Figure 5-7: $\text{Si}+\text{Au} \rightarrow \text{K}^- \text{ dn/dy}$ distributions. The lowest dn/dy points are for the peripheral TMA cut, the highest points are for the central TMA cut. The open circles are minimum bias data plotted in bins 0.1 unit of rapidity wide. The dotted lines show Gaussian fits to the data points near the peaks of the distributions.

5.3. RAPIDITY DISTRIBUTIONS

Si+Al \rightarrow K ⁺	Amplitude	Mean	Sigma	Yield
0–7% TMA	1.25 \pm 0.02	1.72	0.82 \pm 0.01	2.56 \pm 0.04
7–20% TMA	0.86 \pm 0.01	1.72	0.90 \pm 0.02	1.94 \pm 0.04
20–40% TMA	0.57 \pm 0.01	1.72	0.90 \pm 0.02	1.29 \pm 0.03
40–100% TMA	0.16 \pm 0.003	1.72	1.04 \pm 0.03	0.42 \pm 0.01
Si+Al \rightarrow K [−]	Amplitude	Mean	Sigma	Yield
0–7% TMA	0.34 \pm 0.02	1.72	0.71 \pm 0.04	0.61 \pm 0.03
7–20% TMA	0.25 \pm 0.02	1.72	0.71 \pm 0.04	0.44 \pm 0.04
20–40% TMA	0.16 \pm 0.01	1.72	0.73 \pm 0.04	0.29 \pm 0.02
40–100% TMA	0.04 \pm 0.003	1.72	0.78 \pm 0.05	0.08 \pm 0.005
Si+Au \rightarrow K ⁺	Amplitude	Mean	Sigma	Yield
0–7% TMA	3.65 \pm 0.05	1.17 \pm 0.01	0.67 \pm 0.03	6.1 \pm 0.3
7–20% TMA	2.72 \pm 0.03	1.14 \pm 0.01	0.75 \pm 0.03	5.1 \pm 0.2
20–40% TMA	1.42 \pm 0.02	1.30 \pm 0.03	0.89 \pm 0.06	3.2 \pm 0.2
40–100% TMA	0.27 \pm 0.01	1.53 \pm 0.14	1.16 \pm 0.19	0.8 \pm 0.1
Si+Au \rightarrow K [−]	Amplitude	Mean	Sigma	Yield
0–7% TMA	0.85 \pm 0.02	1.30 \pm 0.01	0.56 \pm 0.02	1.19 \pm 0.04
7–20% TMA	0.61 \pm 0.02	1.39 \pm 0.02	0.67 \pm 0.04	1.10 \pm 0.06
20–40% TMA	0.38 \pm 0.01	1.44 \pm 0.02	0.64 \pm 0.03	0.61 \pm 0.03
40–100% TMA	0.07 \pm 0.001	1.55 \pm 0.05	0.69 \pm 0.05	0.12 \pm 0.01

Table 5.2: Parameters of kaon rapidity distributions obtained by Gaussian fits. In Si+Al, the mean of the Gaussian was fixed to $y = 1.72$, a condition of the symmetry of the system. Only statistical errors are shown.

the highest rapidities for the central data. Also, for the peripheral K^+ yields, a jump in the dn/dy at high rapidity which appears to be related to the 5° data causes a fit to the whole distribution to overestimate the integral.

There is a trend in the data for the widths of the rapidity distributions to become more narrow for the more central cuts. This can be seen graphically in Figure 5-8. The widths become more narrow

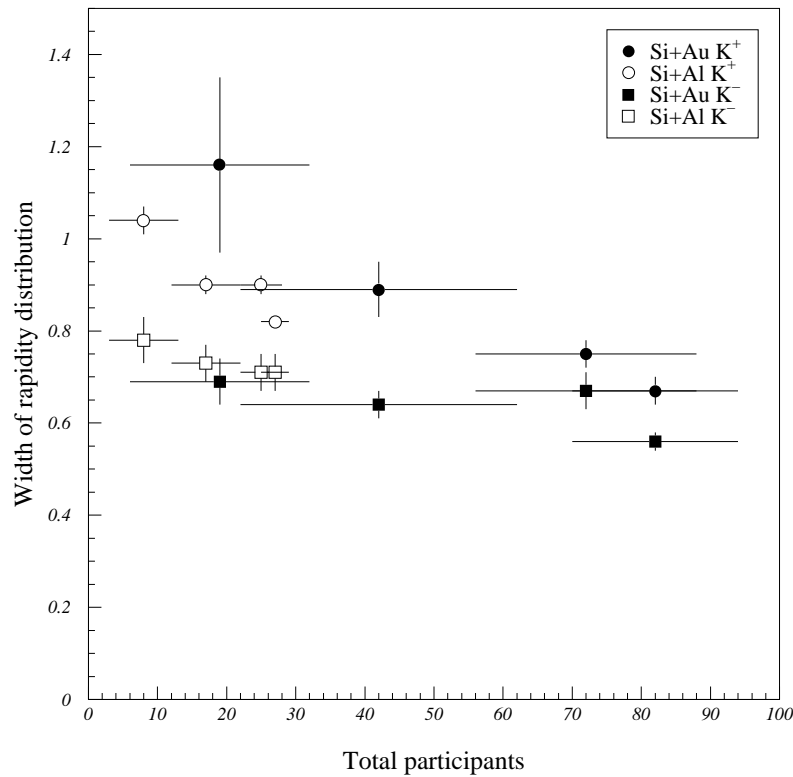


Figure 5-8: Widths of kaon rapidity distributions. As in the plots of yields versus total participants, the horizontal bars represent the root-mean-square of the underlying distribution of participant number. As the number of participants increases, the widths of the kaon rapidity distributions tend to become narrower. There is about a 25% decrease in the widths in going from the most peripheral Si+Al to the most central Si+Au.

at the same time as the peak of the kaon distribution in Si+Au is shifting backward in rapidity. This means that the whole kaon distribution is not shifting back uniformly, but that a peak in the distribution is growing at $y = 1.0-1.3$.

5.4. SCALING OF KAON YIELDS

5.4 Scaling of Kaon Yields

Another way to characterize the kaon production is to look at the total yields as a function of the number of participating nucleons, though exactly what is meant by a participant needs a small amount of clarification. Here we mean to count primary nucleons struck by other primary nucleons, and not nucleons struck by produced secondaries. These participants are essentially the subset of all the nucleons contained in a clean-cut collision volume.

We begin by determining the number of projectile participants, N_{part}^{proj} , for each of the different TMA cuts. In Section 4.11, we determined the ZCAL distribution for the TMA cuts. This can be converted into the number of projectile participants using

$$N_{part}^{proj} = A_{proj} \left(1 - \frac{E_{ZCAL}}{T_{proj}} \right) \quad (5.6)$$

where A_{proj} is the number of nucleons in the projectile, E_{ZCAL} is the energy measured in the ZCAL, and T_{proj} is the total *kinetic* energy of the beam, 380 GeV. In the case of a symmetric system such as Si+Al, doubling N_{part}^{proj} gives the total number of participants. In an asymmetric system such as Si+Au, we have to use a model to extract the total number of participants. In his thesis, Matt Bloomer used the nuclear geometry code taken from the model FRITIOF to determine the numbers of projectile, target and total participants [Blo90]. In Figure 5-9, taken directly from his thesis, he shows the relationship between the number of projectile participants, N_{part}^{proj} and the average number of target participants, N_{part}^{targ} . Of course, the sum of N_{part}^{proj} and N_{part}^{targ} is the total number of participants. Using points read off of this figure, we can determine the distribution of total participant number for the events in each of the TMA cuts placed on the data. This was done for both Si+Al and Si+Au, in spite of the simpler method available in the case of Si+Al, in order to treat both systems in the same way. The large range in E_{ZCAL} for each of the TMA cuts means that, even though the average number of participants is well-determined for each cut, it is the average of a wide, asymmetric distribution. In plotting the yields versus the number of participants, a horizontal error bar is used, not to represent the error on the average, but to show the RMS of the underlying distribution for which the average is calculated.

Next, we have to determine the total kaon yields. Again, in Si+Al, the symmetry of the system helps. A Gaussian, with its mean fixed at $y_{NN} = 1.72$, is fit to the data. In Si+Au, there is more

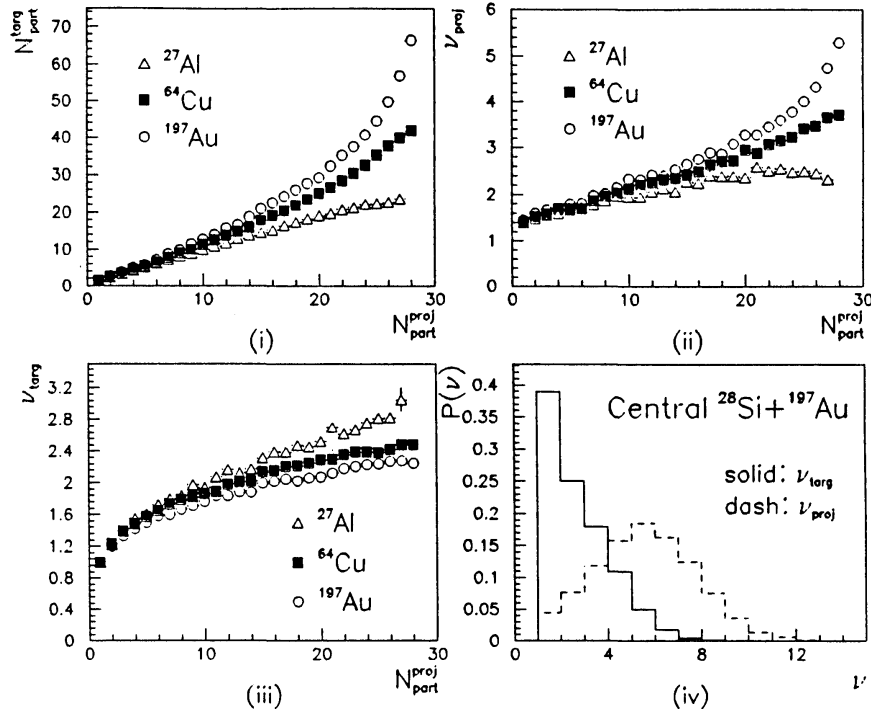


Figure 5-9: $N_{\text{targ}}^{\text{proj}}$ vs $N_{\text{proj}}^{\text{targ}}$ within FRITIOF [Blo90].

5.5. PARTICLE RATIOS

uncertainty when extrapolating the yields to all of phase space. In the most central collisions, the peak of the kaon distribution has moved back to $y = 1.1$ – 1.2 , so integrating a Gaussian fit to the peak captures most of the yield before extrapolating outside the measured rapidity range. In the peripheral cuts, the peak of the distribution moves forward to $y = 1.4$ – 1.6 , so that less of the yield is in a rapidity range covered by the spectrometer. On the other hand, for the peripheral cuts, the asymmetry of the system should play somewhat less important role, and one would be very surprised to see the yields in the forward rapidity range behave wildly differently from the measured data at backward rapidities.

Determining the yields in this way and plotting them versus the total participants calculated as described gives the results shown in Figure 5-10. The yields are well-described as linear in the total number of participants for both K^+ and K^- over most of the range in centralities, with $N_{K^+} \approx 0.082N_{part} - 0.6$ and $N_{K^-} \approx 0.016N_{part} - 0.09$. There may be some saturation in the yields in the most central collisions, but a separate fit to those data points shows only a very slight change in the linear coefficient.

The linear behavior of these trends should not be taken as evidence that little in the way of new physics is occurring. Matt Bloomer showed in his thesis that the yields of pions increased linearly with the number of binary collisions, implying that each new nucleon-nucleon interaction has a similar probability of creating a pion in the final state. But, the typical energies involved in these collisions are well above the pion creation threshold, so even nucleons that have already suffered several collisions may still have enough energy to create a pion in subsequent collisions. Kaons, on the other hand, are energetically more expensive to create, so the probability of creating kaons decreases quickly with the number of collisions suffered by a primary nucleon. As will be argued in Chapter 6, the linear behavior may be something of a coincidence; as nucleon-nucleon collisions create fewer kaons, the meson-meson and meson-baryon reactions create more, with the result being a linear increase with the number of participants.

5.5 Particle Ratios

Another interesting feature of the kaon data is a seeming independence of the K^+/K^- ratio on the centrality cut applied to the data. In fact, there seems to be only a weak target dependence

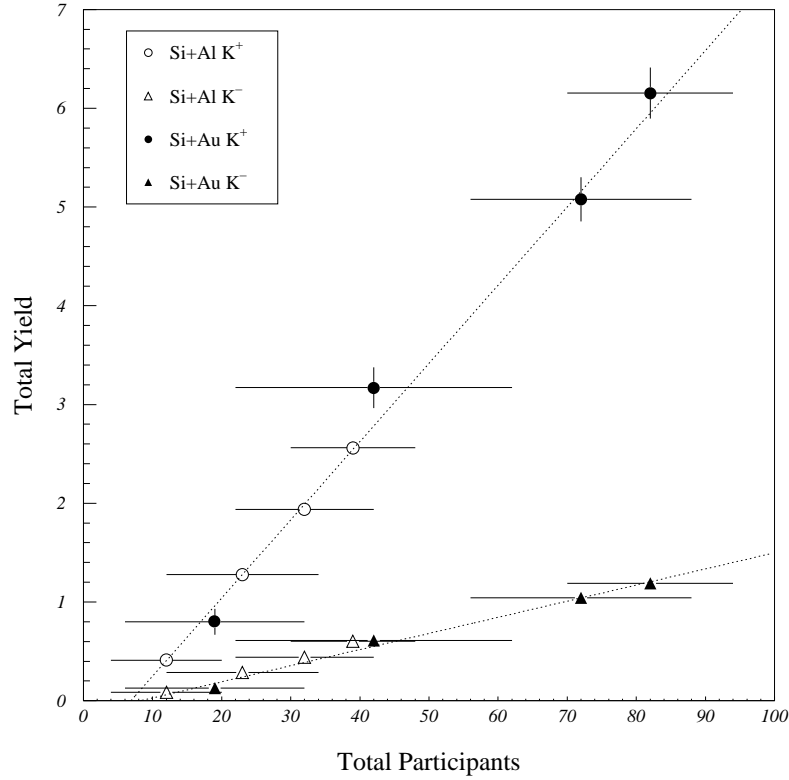


Figure 5-10: Kaon yields versus total participants in Si+Al and Si+Au. Each data point is for events in one of the TMA cuts. The total yields are determined by Gaussian fits to the rapidity distributions, the Si+Al data is reflected about y_{NN} first to take advantage of the near symmetry of the system. The number of participants is determined from the E_{ZCAL} and FRITIOF (see text). Because of the large range in E_{ZCAL} for each of the TMA cuts, the horizontal bars are used to represent the RMS of the E_{ZCAL} distribution.

5.5. PARTICLE RATIOS

to the ratio, as well. The ratio is formed from the data shown in Figures 5-4 through 5-7. For

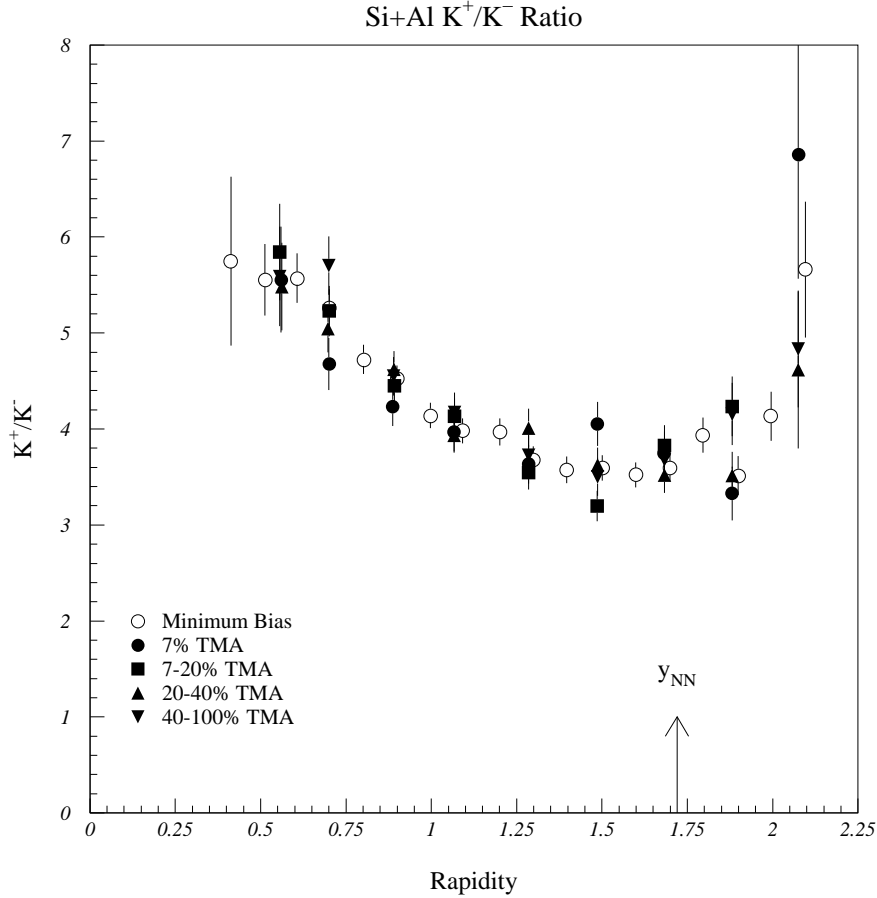


Figure 5-11: Si+Al K^+/K^- ratio of dn/dy versus rapidity

each multiplicity cut, the ratio as a function of rapidity is formed by dividing the K^+ dn/dy by the K^- dn/dy bin by bin. Figure 5-11 shows the ratio for Si+Al for all of the different TMA cuts and for minimum bias events as well; Figure 5-12 show the ratio for the same selection of Si+Au events. Near mid-rapidity, the ratio is ~ 3.5 – 4.5 and it rises steadily as one goes back toward the target rapidity. The ratio reaches a maximum of ~ 6 in Si+Al and ~ 7 in Si+Au. There is only a 5–10% difference as the events selection varies. This is somewhat surprising, given the different production mechanisms and the difference in the inelastic kaon-nucleon cross section for K^+ and K^- . In addition, for Si+Au the rapidity density of target protons changes by a factor of ~ 3 at

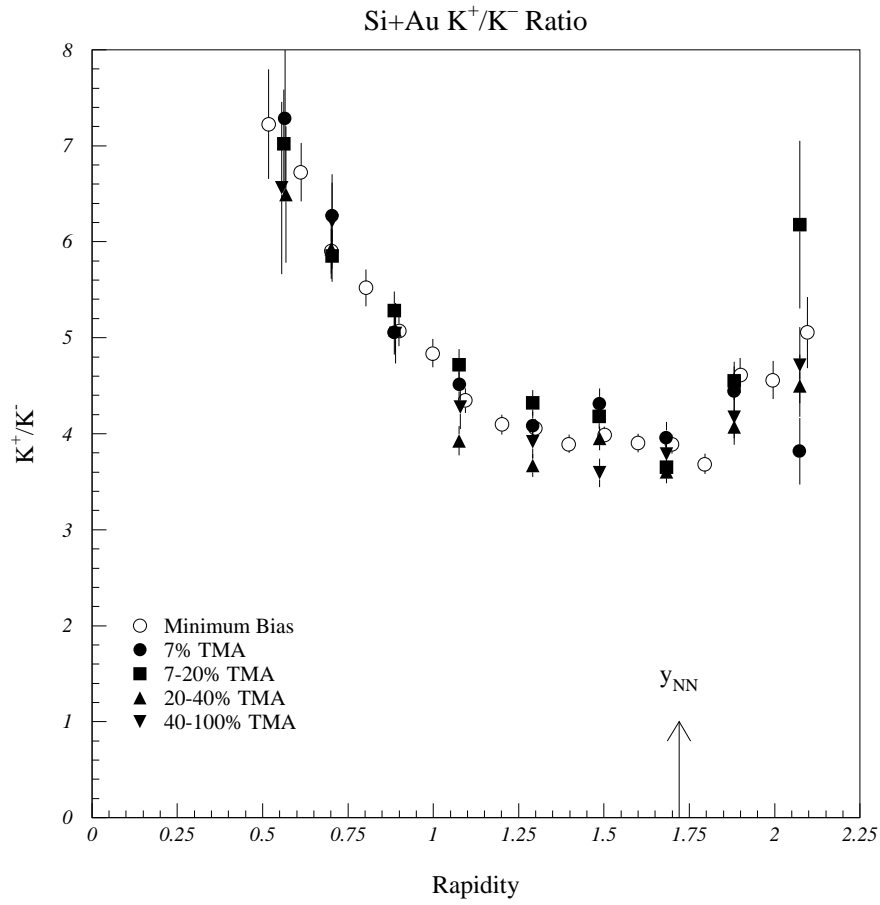


Figure 5-12: Si+Au K^+/K^- ratio of dn/dy versus rapidity

5.6. ESTIMATES OF SYSTEMATIC ERRORS IN THE KAON ANALYSIS

$y = 1.0$ in going from minimum bias to central events [Par92] (also see Appendix B). Also, the total yields of both K^+ and K^- increase by a factor of ~ 30 in going from the most peripheral Si+Al to the most central Si+Au (see Figure 5-10). This is an enormous change, but the K^+/K^- ratio is basically unaffected.

Figure 5-13 shows the ratios of yields and slopes for central events to the same quantities in peripheral events for both Si+Al and Si+Au. The top row of the figure shows the ratio of dn/dy 's. This emphasizes the point that even though the peak of the dn/dy distribution is at $y \approx 1.2$ for K^+ and at $y \approx 1.3$ for K^- in Si+Au, the greatest relative increase in the yield is coming from a point in rapidity even closer to the target, showing that the increase in both K^+ and K^- is influenced to a significant degree by the target baryons. The Si+Al yields show an increase that seems somewhat broad and flat about y_{NN} . Recalling the rapidity distribution of the Λ 's in p-p data shown in Figure 2-2 and the E810 Λ measurement shown in Figure 2-7, it does appear that the K^- and Λ distributions are similar in shape, though they differ in amplitude. The bottom row of Figure 5-13 shows similar ratios formed from the slope parameters. In Si+Al, over much of the rapidity range covered, there is little or no change in the slope in going from peripheral to central, although at higher rapidities, the slope does increase slightly. In going from peripheral to central Si+Au events, the kaon slopes increase by 10–15% over much of the rapidity range, with slightly higher increases toward the edges of the coverage.

5.6 Estimates of Systematic Errors in the Kaon Analysis

In order to know how much significance to assign to the results just presented, it is important to have an estimate of the systematic errors associated with the kaon measurements. There are several places in the data where systematic errors could be introduced. Some of them have already been alluded to in passing. Here, these contributions are discussed in detail.

5.6.1 Overall Normalization

The overall scale of the yields is set by the number we choose to use for the inelastic cross section of the Au and Al targets. This number suffers from rather large uncertainties. Variations in the bull's-eye can have an especially large influence on the interaction rate. As was shown in Section 4.8.1,

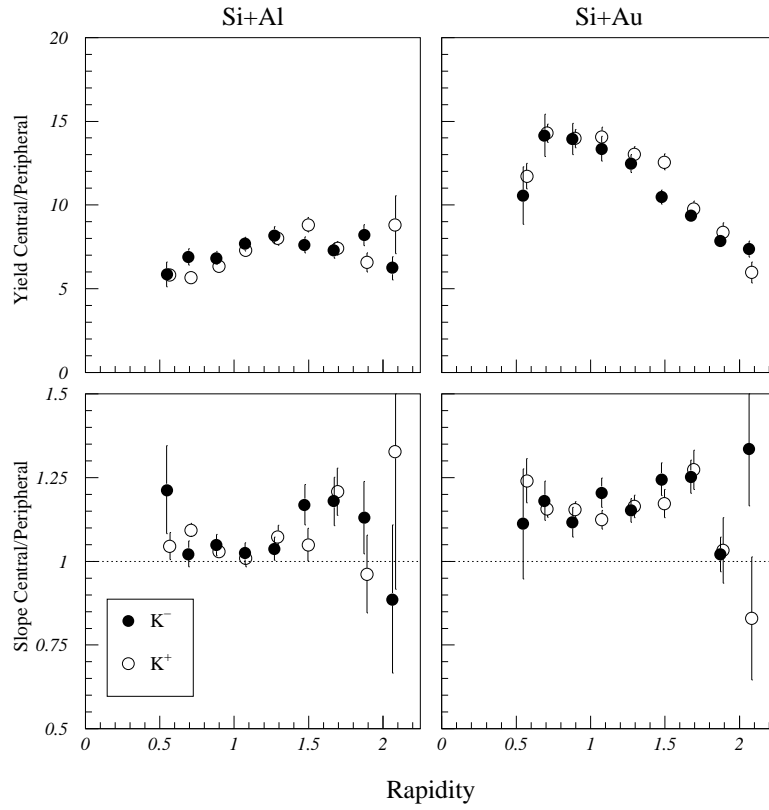


Figure 5-13: Comparison of central and peripheral yields and slopes. The top figures show the ratio of dn/dy in central events to the dn/dy in peripheral events, as a function of laboratory rapidity. The bottom row shows a similar ratio of slope parameters. The left column is for Si+Al, the right column for Si+Au.

5.6. ESTIMATES OF SYSTEMATIC ERRORS IN THE KAON ANALYSIS

other sources of variation in the interaction rate can be severe enough to discard the data. The interaction rate used in this thesis was adopted from earlier work, so it is appropriate to consider the systematic uncertainties quoted before. In both Matt Bloomer and Charles Parsons' theses, the interaction rate for the different targets is calculated from the target out corrected INT/BEAM rates, just as in Section 4.8.1. The run-to-run fluctuations in that rate, coupled with the overall uncertainty in the actual cut being made by the bull's-eye, leads to a 10–15% quoted systematic uncertainty in the overall normalization.

This uncertainty has its fullest effect in the peripheral cuts on the data. Since very few kaons are produced in extremely peripheral collisions of two nuclei, as can be concluded by examining the TMA distribution for events containing a kaon (see Figure 4-20), the peripheral TMA cuts are very sensitive to the value used for the inelastic cross section. Since all of the yields are normalized to the trigger cross section, expressed as a fraction of the inelastic cross section, multiplied by the amount of beam, a 10% change in the inelastic cross section will change the number of events we accept by 10%, but will have essentially no effect on the number of kaons collected, leading to a 10% change in the yields. In the more central cuts on the data, changing the number of events accepted by 10% also changes the number of kaons by $\sim 10\%$, so the uncertainty in the interaction cross section has less of an effect.

5.6.2 Relative Normalization of Different Targets

Since the data set for both Si+Al and Si+Au is made by combining data taken with targets of two different thicknesses, there is a systematic error associated with the relative normalization of the data. Since the choice of target was also correlated with rapidity, there is a systematic error introduced in the slopes and dn/dy 's due to changes in the relative cross section assigned to each target. This is especially true in Si+Au where the Au 3% target was not used for any of the 5° running, and the Au 1% target was used almost exclusively for 5° (there are a few 14° runs as an exception). The magnitude of this effect can be estimated by artificially adjusting the thickness of the two targets, and this has been done for Si+Au inclusive K^+ yields, under the assumption that the results so obtained will be applicable to all the other systems. The Au 1% target fraction was lowered by 5%, and the cross sections recalculated. This has the effect of raising the K^+ cross section for that target by 5%, since the same number of kaons will be produced by a target 5%

thinner. This only has an effect on the results forward of $y \approx 1.3$, since the Au 1% data were all taken at 5° , and that spectrometer setting only contributes to the higher y slices of the data. The net effect of the change is to lower the slopes by $\sim 1\%$, but only over the rapidity range $1.3 < y < 1.7$ where there is a scissoring effect between the 5° and the 14° data. At higher y , the 5° data stands alone, and the slope is unaffected. The dn/dy , which is unaffected at lower y , is smoothly raised until the highest y data is 5% higher after the change.

5.6.3 Uncertainty in TMA Cuts and Event Selection

As shown in Section 4.10, the spectrometer integrated kaon counts are consistent within a given TMA cut to no better than the 5–10%. Also, if the kaon yields change quickly as one makes small changes to the event selection, there will be some uncertainty in the reported yields due to uncertainties in event selection. On the other hand, if the yield per event changes only slowly, then very little error in the yields will arise from this cause. To check the magnitude of this systematic effect, the kaons yields were calculated for events in the top 10% of the TMA distribution, as well as for the top 7%. The differences are of order 5%, and thus the exact TMA cuts values are not a large source of systematic error.

5.6.4 Uncertainties in Slope and dn/dy

Though the χ^2 of the fits to the invariant yields indicate that the m_\perp form does a good job of parameterizing the data, the degree to which the data is not exactly an exponential in m_\perp represents a source of systematic error. To quantify this error, fits to subranges of the m_\perp coverage were made and the change in the slope calculated. In general, little change is seen when fitting only to portions of the data. Typical variations are 5–10%. However, since the coverage in m_\perp decreases steadily as y increases (refer to Figure 4-12), the slopes for large y , while representing good fits to the data, are marked by larger and larger systematic uncertainty. It is not clear how to quantify this error from the data itself, but later in Section 6.3, a comparison of fits to the output of RQMD with and without the experimental acceptance imposed gives some rough idea of the effect due to the reduction in acceptance.

5.7. DISCUSSION OF DATA

5.6.5 Total Systematic Errors

Taking all the sources of systematic error together, we can try to assign a total uncertainty to the data. This will be a function of the rapidity to some degree, since the conditions under which the data was collected changed for the 5° data. We estimate a systematic uncertainty of $\sim 5\%$ in the determination of the slope parameter up to $y = 1.6$, and $\sim 10\%$ for the higher rapidities, due to the decreased acceptance of the spectrometer. We also estimate a systematic uncertainty of 10–15% in the determination of dn/dy , principally due to uncertainties in determining the interaction cross section of the targets. For the Au target, this uncertainty increases at higher rapidities to $\sim 15\%$ because of the uncertainty in the relative normalization of the Au 3% and the Au 1% targets. However, in the case of the K^+/K^- ratios, much of the systematic normalization uncertainty cancels in the division.

5.7 Discussion of Data

Now that the results of the E859 kaon data have been shown, the main features of kaon production in Si+Al and Si+Au can be summarized fairly briefly. In addition, this section will try to pull together the disparate properties of kaons displayed in the previous sections and develop a coherent physics picture of the kaon production in these systems at AGS energies. There are many features of the data which are consistent with, though not conclusive evidence for, a unified picture of these collisions in which the K^+ are produced predominantly by associated production, while the K^- are produced through strangeness exchange reactions involving excited hyperonic intermediate states. Overall, one of the most striking features of the data is that, though there are substantial differences in the magnitudes of the slopes and yields of K^+ and K^- , the values for both signs seem to change systematically in quantitatively similar ways as the centrality of the event is varied.

One of the first things shown was that the transverse distribution of the kaon invariant yields are better described by exponentials in m_\perp than exponentials in p_\perp , and that the K^- may be more nearly exponential than the K^+ . Before E859, the data for heavy ion collisions at these energies did not have the statistics to distinguish conclusively between an exponential in p_\perp and an exponential in m_\perp for the K^- distributions, though it already seemed as though the K^+ followed the exponential m_\perp parameterization more closely [Par92]. In general, the K^+ slope parameters are larger than for

CHAPTER 5. DATA PRESENTATION AND DISCUSSION

the K^- by $10\text{--}20\text{ MeV}/c^2$. This may reflect the differences in the underlying processes creating the kaons. The K^+ are strongly created in associated production in relatively high energy collisions among primary nucleons. This process has a fairly low threshold, leaving a lot of energy in the center-of-mass system to push the K^+ to high m_\perp . The K^- 's which are produced in the initial battery of nucleon collisions, are produced in kaon pair production. This has a higher threshold than associated production, which leaves less energy left over to translate into m_\perp for the K^- . In addition, a large fraction of the K^- are produced by lower energy interactions among secondaries. This tends to reduce the degree to which the K^- populate the high m_\perp part of the distribution (this will be an issue later in comparing to RQMD).

The inverse slope parameters of the transverse distributions show some rapidity dependence, rising by $10\text{--}30\text{ MeV}/c^2$ as one moves from near target rapidity toward y_{NN} . Not all of the systems have the same degree of rapidity dependence, however. The $\text{Si}+\text{Au}\rightarrow K^-$ is flatter in rapidity than $\text{Si}+\text{Al}\rightarrow K^+$, for instance. In the rapidity dependence of their slopes, the kaons behave somewhat more like the protons than the pions. From E802 data, it is seen that the pion inverse slopes (especially for the p_\perp parameterization) are nearly flat as a function of rapidity and that the proton slopes show a strong rise with rapidity [A⁺94]. Many of the pions are presumed to be created in the decay of $\Delta(1232)$, which should help even out the rapidity dependence of the slopes by providing a source of pions throughout the rapidity range that all have similar m_\perp behavior. In the case of the kaons, if the decay of hyperon resonances such as the $\Lambda(1520)$ are a significant source of K^- production, this might also erase some of the rapidity dependence of the K^- slopes. The K^+ , on the other hand, do not have such a resonant interaction with the nucleons—there is no analog of the $\Lambda(1520)$ contributing to their yields. Therefore, the K^+ slopes are a reflection of the associated production channel which then gets slowly modified by additional collisions as the system gets larger. Since the K^+ have a relatively small cross section with nucleons, even this system dependence is muted.

In $\text{Si}+\text{Al}$, there is only a very slight dependence of the slope parameter on the centrality of the collision. This may indicate that the $\text{Si}+\text{Al}$ system is a small system by some measure related to kaon production and so it doesn't particularly matter whether one has a peripheral or central collision. Of course, the number of participants increases even in the $\text{Si}+\text{Al}$ system as one selects more and more central collisions, but the increase seen in kaon production in the central collisions may just

5.7. DISCUSSION OF DATA

be a linear compounding of processes already available in the peripheral collisions. The fact that the slopes change so little seems to show that the fundamental character of the kaon-producing processes does not change much. The kaon inverse slope parameters in Si+Au show a much more pronounced centrality dependence, with the slope parameter rising $\sim 20 \text{ MeV}/c^2$ in going from the most peripheral to the most central collisions.

The kaon rapidity distributions for the Si+Al system are well described as Gaussians, assuming the data is reflected about y_{NN} . The kaon rapidity distributions for Si+Au are also roughly Gaussians centered on a point in rapidity nearer the target, and with a flattening of the distribution toward the projectile rapidity. As one varies the centrality of the event sample, the peak of the dn/dy for Si+Au moves back toward the target rapidity, consistent with a picture of kaon production that is sensitive to the presence of the large number of target baryons. The total K^+ and K^- yields, obtained by integrating the Gaussian fits to the dn/dy distributions, are seen to scale linearly with the total number of participants. This is a bit surprising since kaons are relatively expensive to create. In the case of Si+Au the number of participants continues to increase even for impact parameters smaller than that needed to have the silicon nucleus completely occluded by the gold. The increased total number of participants have to share the fixed energy brought into the system by the silicon projectile. If the kaon production were to proceed only through NN collisions, more of these collisions would be taking place at lower and lower energies. So, as more and more participants are brought into play, one might expect the number of kaons created per participant to decrease. The fact that the number does not decrease may signal that more kaons are being created through processes other than NN collisions.

The widths of the rapidity distributions are seen to decrease slightly with increasing centrality, an effect strongest in $\text{Si+Au} \rightarrow K^+$. This is also seen in the pseudorapidity distributions of charged particles in the WA80 data [A⁺92c]. In the paper reporting the WA80 results, they speculate that the narrowing comes about because the particle production in the central rapidity region increases much faster than in the fragmentation regions, leading to an narrower distribution. At AGS energies, the fragmentation regions are not cleanly separated from the central regions, but the narrowing may come about for similar reasons. If there is a source of kaons near $y = 1.2 - 1.3$ whose contribution to the yields increases more strongly with centrality than the contribution of primary nucleon-nucleon governed kaon production, the distributions would be expected to become narrower. This is also

CHAPTER 5. DATA PRESENTATION AND DISCUSSION

consistent with a scenario of kaon production mediated by secondary collisions. For comparison, the widths of Gaussian fits made to the π^+ from Si+Au in the E802 data show little variation with centrality. The peripheral π^+ dn/dy has a rapidity width of $\sigma = 0.71 \pm 0.06$ and the central π^+ dn/dy has a width of $\sigma = 0.75 \pm 0.02$. It seems that pions are relatively easy to create, so as more energy is deposited in the system in central collisions, the pions can be created relatively uniformly over the full rapidity range. On the other hand, the increased kaon production relies on processes that only take place in a limited rapidity region—namely, interactions involving produced particles, such as meson-baryon and meson-meson collisions.

As shown in Section 2.1.2, the decay of the $\Lambda(1520)$ leads to a K^- rapidity distribution ~ 0.8 unit wide. If the contribution of this channel to K^- production becomes more important in heavier systems, it may serve to limit the degree to which the K^- rapidity distributions can narrow. In the production of K^+ there is no large resonance expected to contribute to the yields, so the rapidity distribution of the K^+ from associated production just depends on the energy available in the center of mass system. If the trends continue, it is possible that the K^- widths in Au+Au will be wider than the K^+ widths. The formation of a QGP in some of these very heavy ion collisions should erase some of this effect since the kaons would be produced through the direct combining of quarks and antiquarks, and not through the decay of hadronic resonances. As a function of centrality then, one might see the width of the K^+ first get narrower and then increase to become the same as the K^- width, as one goes through the QGP.

Finally, the insensitivity of the K^+/K^- ratio to the experimental collisions is quite an unusual result. The ratio is constant to within $\sim 10\%$ independent of centrality. In addition, there is only a slight target dependence, with the ratio near mid-rapidity essentially the same in both Si+Al and Si+Au at ~ 4 and rising to ~ 6 in Si+Al and ~ 7 in Si+Au. For a sense of scale, the proton dn/dy in Si+Au in a slice 0.2 units wide centered at $y = 1.3$ increases by a factor of about 20 in going from peripheral to central collisions (0.982 to 18.8 [A^+94], see Appendix B). Again, keeping associated production in mind, this can explain a large increase in the yield of K^+ , but shouldn't necessarily do the same for the K^- . It may however point to a mechanism for feeding the yield of K^- which operates in proportion to the abundance of K^+ . The obvious candidate for this is the hyperon which is produced alongside the K^+ . Ironically, the independence of this ratio may be a consequence of the momentum dependence of the kaon-nucleon cross section. From the p-p data, one can see that

5.7. DISCUSSION OF DATA

there is already a difference in the K^+ and K^- abundance at mid-rapidity of about a factor of 4 (refer to Figure 2-2). The K^- yields in p-p fall off more quickly than the K^+ as one moves away from mid-rapidity. For kaons near the target rapidity, the momentum spectrum is softer, and the bulk of the kaons have momenta below 1 GeV/c. For K^+ at these momenta, the cross section is nearly all elastic, with only 2-3 mb being inelastic. The K^- 's, on the other hand, have larger and larger inelastic cross section as their momentum falls. Below ~ 1 GeV/c, the K^- inelastic cross section with nucleons is ~ 40 mb. One expects the Λ 's to have inelastic cross sections typical of other baryons, 30–40 mb. Therefore at the back rapidities, most of the K^+ 's make it out of the collision unimpeded, but a stronger and stronger coupling grows between the hyperons and K^- 's via inelastic collisions with nucleons in strangeness exchange channels such as $N\Lambda \rightarrow NNK^-$. Since the Λ rapidity distributions are similar to the K^+ in both shape and amplitude, any mechanism which converts $\sim 10\%$ of the hyperons into K^- will produce enough K^- 's in the right regions of rapidity to keep the shape and magnitude of the K^+/K^- ratio relatively stable as the size of the collision volume increases.

Many of the characteristics of kaon production behave as one would expect. The yields increase with centrality, there are more K^+ than K^- , a difference which becomes amplified as one goes back toward target rapidities, and the slopes are intermediate between the pions and protons. On the other hand, there are some interesting features which may provide insight into the physics. For instance, the details of the shapes of the rapidity dependence of the slopes and yields which suggest sources of K^- beyond pair production in primary nucleon-nucleon interactions. Given the relatively large threshold for kaon pair production, it is interesting to see that secondary collisions, or cooperative effects², may play a large role in producing the K^- .

²These types of processes are often misleadingly referred to as *collective effects* in the literature. Thanks to C. Ogilvie for clarifying this point.

CHAPTER 5. DATA PRESENTATION AND DISCUSSION

Chapter 6

Model Comparisons

In this chapter, detailed comparisons will be made between the E859 single-particle kaon data and the output of RQMD version 1.08. The extent to which the model reproduces the data will be quantified, and then the physical processes responsible for kaon production within RQMD will be examined. Particular emphasis will be placed on the rapidity dependence of kaon production.

6.1 Overview

RQMD simulations have been compared to relativistic heavy-ion data for many different observables, such as baryon and meson distributions and two-particle correlations, and RQMD does fairly well at reproducing what is seen in experiments [Xu94, Cia94, Sol94]. The exception to this seems to be in the yields of pions which RQMD enthusiastically over-produces [Zac93]. The implications of this pion excess for kaon production will be discussed later.

Since many of the gross features of particle production in heavy-ion collisions, such as transverse energy spectra, can be explained largely in terms of nuclear geometry and energy and momentum conservation [Col92], a model which properly incorporates these will go a long way toward reproducing the proton and pion distributions. But, kaons account for only a small fraction of the produced particles, so they have little effect on the dynamics of the collision. On the other hand, the dynamics of the collision may have a large effect on the production of kaons, so comparing to the kaons provides a stringent test of a code.

There are two purposes behind making these comparisons. The first is to provide evidence

which can be used to help validate (or invalidate) the model by seeing how well it reproduces the data. Of course, even if the model output were to match the data down to the finest detail one could not claim that it had the correct physical picture. However, a code that can simultaneously match single particle spectra, multiparticle correlations and strangeness production could claim to have embodied some of the more important features of the physics. Fortunately, we won't have to deal with these fine shades of interpretation. We will be more concerned with discrepancies between the model and data of order 10–30%, and whether the model reproduces the general trends in the kaon production data.

The other reason for making the comparison is that in a model, one can investigate the importance of the different mechanisms which produce kaons. One can not learn about any *fundamental* physical processes this way, since the model only contains processes that were explicitly put in to begin with.¹ However, the complex dynamics of a relativistic heavy-ion collision may lead to the unexpected importance of certain mechanisms.

As an aside, another widely used code for simulating AGS energy heavy-ion collisions, ARC, was designed with the explicit motivation of reproducing AGS heavy-ion collisions within a very strict hadronic cascade prescription [PSK92]. At the time of this writing, the most recently distributed version of ARC is 1.9.5, which the authors of the code have said has known weaknesses in its parameterization of the rapidity dependence of primary kaon production [K^+ 93]. The parameterization used in the current version of ARC is flat as a function of rapidity, in marked contrast with the experimental data, which are peaked about mid-rapidity (see Figure 6-1). Therefore, while acknowledging that ARC simulations do seem to reproduce the general features of these collisions, I will restrict myself to detailed comparisons between data and RQMD. It is hoped that the comparisons can be extended in the near future to include ARC.

6.2 Synopsis of RQMD Algorithm

RQMD is in many ways similar to conventional cascade codes, though it has been described as taking a “maximalist” approach to modelling heavy ion collisions [Zaj93]. A concise exposition, summarized here, of the main ingredients in RQMD 1.08 may be found in Heinz Sorge's HIPAGS

¹With no slight intended against RQMD, the computer science term for this is *garbage in, garbage out*.

6.2. SYNOPSIS OF RQMD ALGORITHM

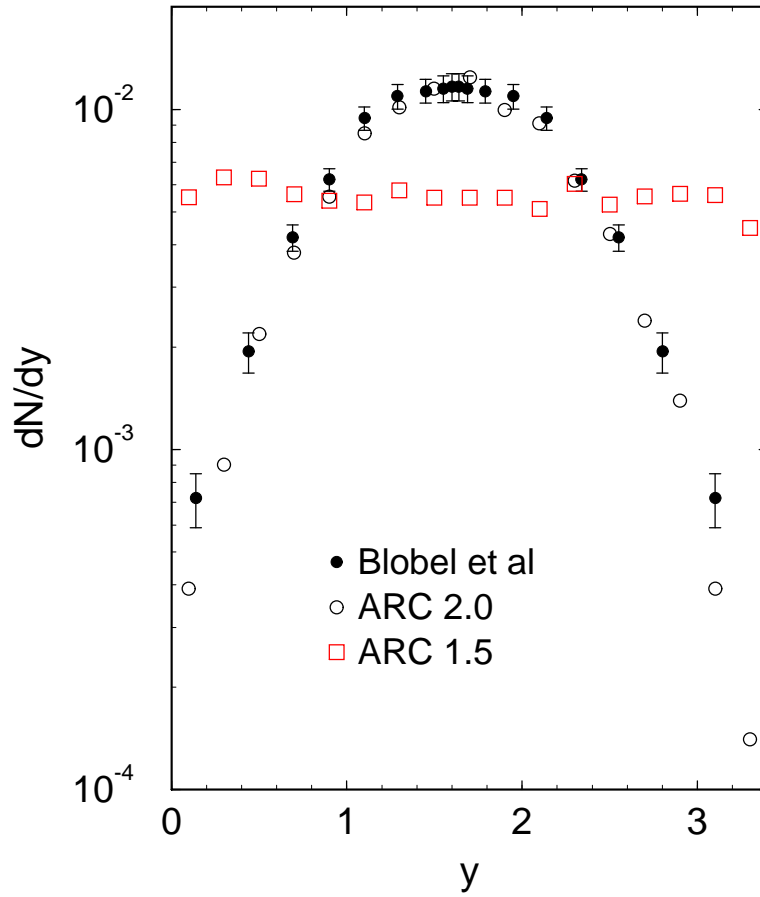


Figure 6-1: Rapidity distribution of primary K_s production in ARC 1.5 and ARC 2.0, showing the difference in the parameterizations [K⁺93]. Output of ARC prior to version 2.0 (this includes version 1.9.5) use an essentially flat distribution, while version 2.0 corrects this with a distribution peaked about mid-rapidity.

contribution [Sor93]. The incident nuclei are initially populated with nucleons according to a Woods-Saxon density profile and an impact parameter for the nuclear collision is chosen from a geometrically weighted distribution. Collisions between particles take place when they approach within a distance determined by their interaction cross section, $d = \sqrt{\sigma/\pi}$, as measured in their mutual c.m.s frame. For interactions below $\sqrt{s} = 2.0 \text{ GeV}/c^2$, the result of a collision becomes one of the known meson and baryon resonances. The measured branching ratios are then used to decide how these states should decay. For interactions above $\sqrt{s} = 2.0 \text{ GeV}/c^2$, RQMD employs a string formalism similar to that found in other codes such as VENUS [Wer89]. For AGS energies, however, this aspect of the model does not play nearly as large a role as it does at the 200 A-GeV CERN energies. All secondaries are allowed to reinteract with all other particles. In the initial battery of nucleon-nucleon interactions, the collision volume becomes populated with a large number of hadronic resonances such as Δ 's, ρ 's, N^* 's, and ω 's, produced through reactions like $\pi N \rightarrow \Delta(1232)$, $\pi\pi \rightarrow \rho(770)$ and $NN \rightarrow N\Delta(1232)$ [Sor93]. These resonances store some of the initial energy of the nucleon-nucleon collisions in their rest mass, bringing more energy to subsequent collisions than might otherwise be available.

For kaon production, especially for K^- production, the reinteraction of these excited states is quite important. At AGS energies, one expects the associated production channel $NN \rightarrow N\Lambda K^+$ to dominate primary strangeness production since it has a lower threshold (672 MeV) than other processes such as $NN \rightarrow NNK^+K^-$ (987 MeV) or $NN \rightarrow NN\Lambda\bar{\Lambda}$ (2.2 GeV). In RQMD, the kaon yields can also be affected by processes such as $\pi Y \leftrightarrow Y^* \leftrightarrow \bar{K}N$ which provides a way for the s quark, created in associated production, to shuttle back and forth between a Λ and a K^- .

The main weakness of RQMD, as with any cascade-like code, is the reliance upon a large number of unmeasured cross sections. As pointed out by Aichelin [Aic93], even those cross section for which there is experimental data, such as $pp \rightarrow p\Lambda K^+$, are not always reliably measured (see Figure 6-2). The cross sections for processes which have not been measured, or cannot be measured, are calculated using a Breit-Wigner resonance formula. An overall normalization factor is used to match the cross section calculated this way with the known values for πN interactions.

The RQMD calculations that will be shown are the result of $\sim 20,000$ Si+Au minimum bias events, $\sim 5,000$ Si+Au central events ($b < 5 \text{ fm}$), and $\sim 50,000$ Si+Al minimum bias events. Mean fields within the model were turned off, as they are not expected to play a large role at AGS energies.

6.2. SYNOPSIS OF RQMD ALGORITHM

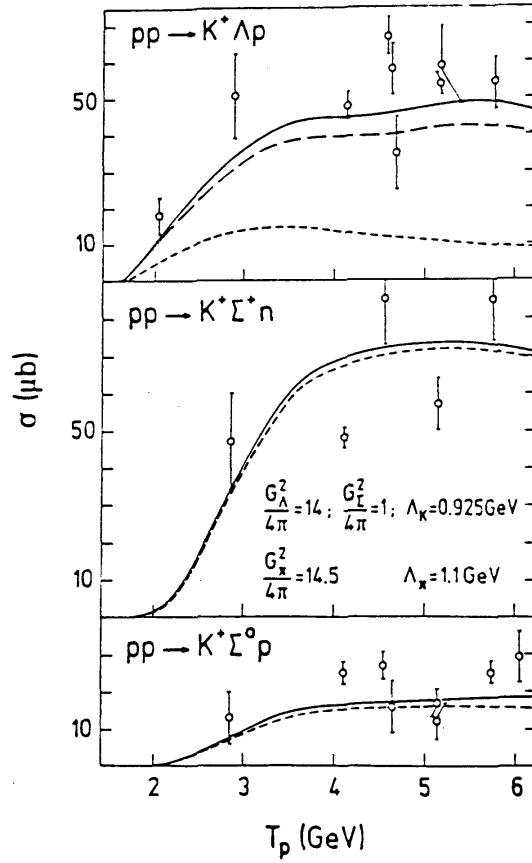


Figure 6-2: Compilation of world's data for several strangeness production reactions in p-p reactions expected to be important at AGS energies [Lag91]. As the figure shows, there are significant experimental uncertainties in the determination of the cross sections.

There are quite a few other options within RQMD and Table 6.1 shows which of these were enabled.

Switch	Value	Meaning
1	NA	<i>Unused</i>
2	NA	<i>Unused</i>
3	F	Use clock time for random number seed.
4	F	Pauli-blocking of collisions is performed
5	NA	<i>Unused</i>
6	T	Mean field is turned off.
7	NA	<i>Unused</i>
8	T	Collisions between two nucleons in the same nucleus not permitted if neither has previously suffered a collision.
9	F	Many particles (Δ , ρ , η) are allowed to decay.
10	F	Pauli-blocking not enabled for resonance decay products.
11	F	No Pauli-blocking when building the nucleus.
12	F	Normal (T disables collisions to study mean field).
13	T	Ropes enabled.
14	F	Turns off phase space output on logical unit 7.
15	F	Normal (T performs Fritiof simulation)
16	F	All unstable non-strange hadrons decayed at end of event.
17	F	Participant and Spectator zones kept separate, but spectator zone heated by participants.
18	F	Particle/Jet system decay.
19	F	Normal (T disables transverse motion).
20	F	Elastic collisions not written to logical unit 9.
21	T	T turns off spectator calculations. This default setting is F, but if switch 23 is T (also default) then this becomes T.
22	F	Normal (T overwrites data statements with input file).
23	T	Fast cascade (sets switches 6,8,21 to T).
24	F	Normal (F used for pA with mean field).

Table 6.1: RQMD switches. Courtesy of R. Soltz

6.3 Event Selection and Acceptance Issues

In comparing the output of RQMD to the data, an effort was made to select events by the same criteria used for real data. To do this, a definition of a minimum bias event for RQMD had to be designed. Also, a measure of the event multiplicity as similar to the experimental measure as possible had to be built.

In the experiment the interaction trigger, which defines the minimum bias event sample, is based on the signal seen in the bull's-eye scintillator. Designing a bull's-eye simulation for RQMD is not particularly easy since the signal in the bull's-eye grows like z^2 of the projectile fragments passing through it, but RQMD does not cluster its final state protons and neutrons into multiparticle fragments. Instead a different definition of a software interaction trigger was constructed using a simulation of the ZCAL. The interaction trigger requirement of a loss of ~ 1.4 units of charge from the beam was replaced with the requirement of a loss of at least two nucleon's worth of energy in the simulated ZCAL. As one would expect, the kaon yields in the peripheral cuts on the data are very sensitive to this definition. Table 6.2 shows what happens to the integrated kaon dn/dy in the most peripheral RQMD Si+Au events as this interaction definition is varied from no requirement (besides RQMD's own requirement of at least one nucleon-nucleon interaction) through the loss of one, two and three nucleon's worth of energy in the ZCAL.

ZCAL	K ⁺	K ⁻
0	0.43	0.10
1	0.50	0.11
2	0.55	0.12
3	0.61	0.14

Table 6.2: Systematic yield variation in peripheral RQMD event selection. The column labelled “ZCAL” is the minimum required energy loss in the ZCAL divided by the beam kinetic energy, giving the number of nucleons lost from the silicon projectile. The other two columns are the integrated kaon dn/dy 's for K⁺ and K⁻, respectively. As the minimum interaction requirement is strengthened, the kaon yields increase significantly.

The simulation of the TMA response was written by Ron Soltz. It counts all charged particles above a minimum kinetic energy cut of 25 MeV with $6^\circ < \theta < 143^\circ$ and $0 < \phi < 2\pi$, except for

two 30° gaps in ϕ and two missing panels in the forward wall of the TMA. Table 6.5 shows the multiplicity cuts used to define various event selections. Central events are then defined by a cut on

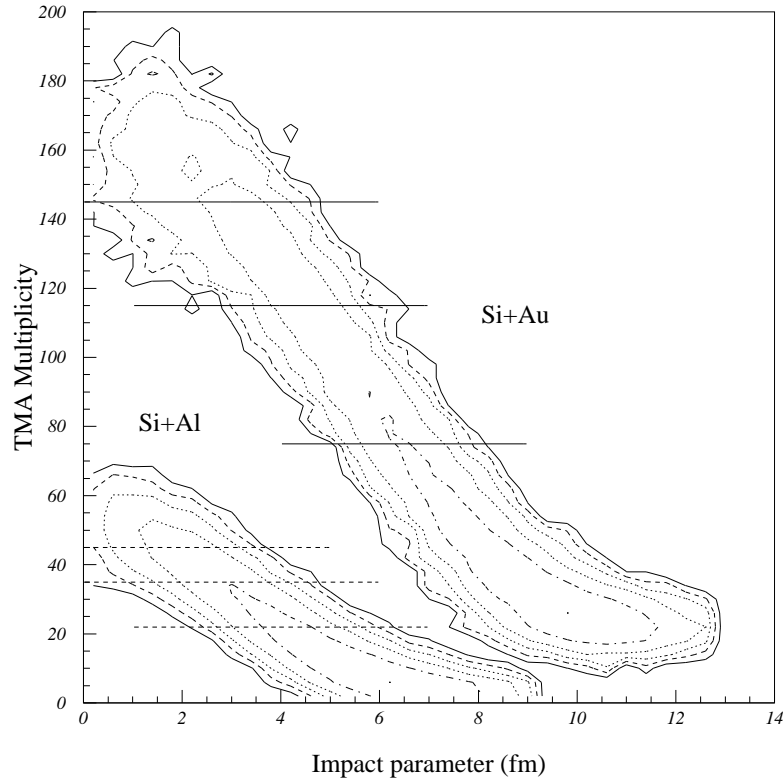


Figure 6-3: Simulated TMA versus impact parameter for RQMD minimum bias events. Over the middle range of multiplicities, the two quantities are usefully correlated. At the low end of the multiplicity distribution (peripheral events), there is some flattening of the correlation, limiting the ability of the TMA to select events with different impact parameters. The lines show where the TMA cuts used on the RQMD data are located.

this distribution rather than a cut in impact parameter, although there is a strong correlation between the two, as can be seen in Figure 6-3. This correlation in the model confirms the expectation that multiplicity cuts on the experimental data correspond reasonably well to impact parameter cuts. A fairly wide range of impact parameters do contribute to each multiplicity cut, but within reason, one is selecting large impact parameters by choosing low multiplicity events and small impact parameters by choosing high multiplicity events. The figure also shows that the smallest impact

6.3. EVENT SELECTION AND ACCEPTANCE ISSUES

parameters that can be chosen by looking for high multiplicity are not much less than 2 fm. Tighter cuts can be made on the event multiplicity, but these events will have impact parameters ranging up to 2 fm.

For a set of RQMD events generated with $b < 5$ fm, Figure 6-4 shows the difference in the events selected between a hard cut on impact parameter and a multiplicity cut for RQMD Si+Au events. Requiring high multiplicity tends to select slightly more central events than the $b < 5$ fm cut. Figure 6-5 shows what then happens to the K^+ dn/dy for a few different definitions of *central*

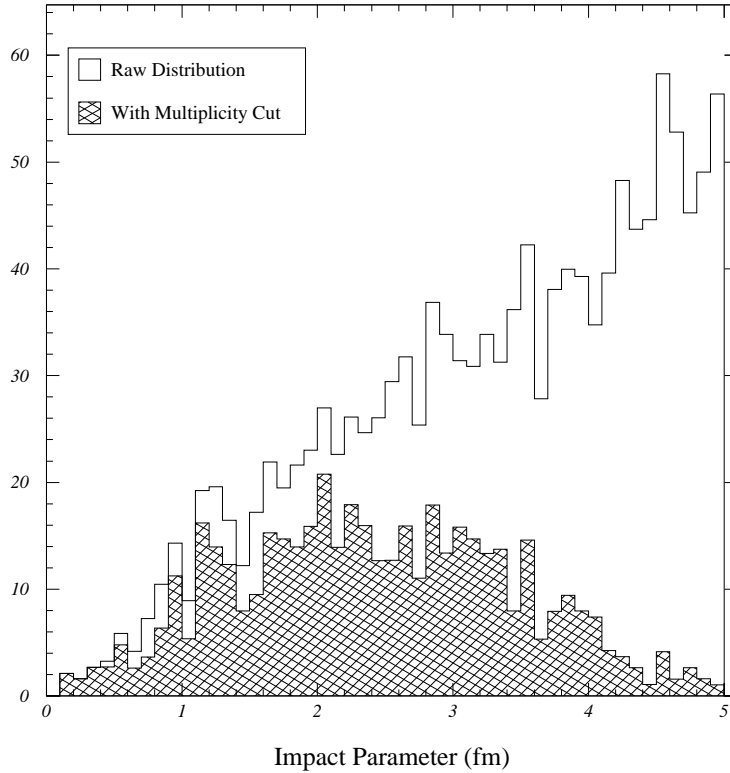


Figure 6-4: RQMD Si+Au impact parameter distribution for high multiplicity events. The plain histogram is the raw, geometrically weighted impact parameter distribution. The hatched histogram shows what happens to the raw distribution when a simulated upper 7% TMA multiplicity cut is imposed. The average impact parameter of the TMA selected events is 0.9 fm smaller than the average for all events with $b < 5$ fm.

events. The filled symbols show the yield of K^+ for multiplicity selected events; the open symbols

are for events selected on impact parameter. As the figure shows, the agreement is closest for impact parameters between 2 and 3 fm.

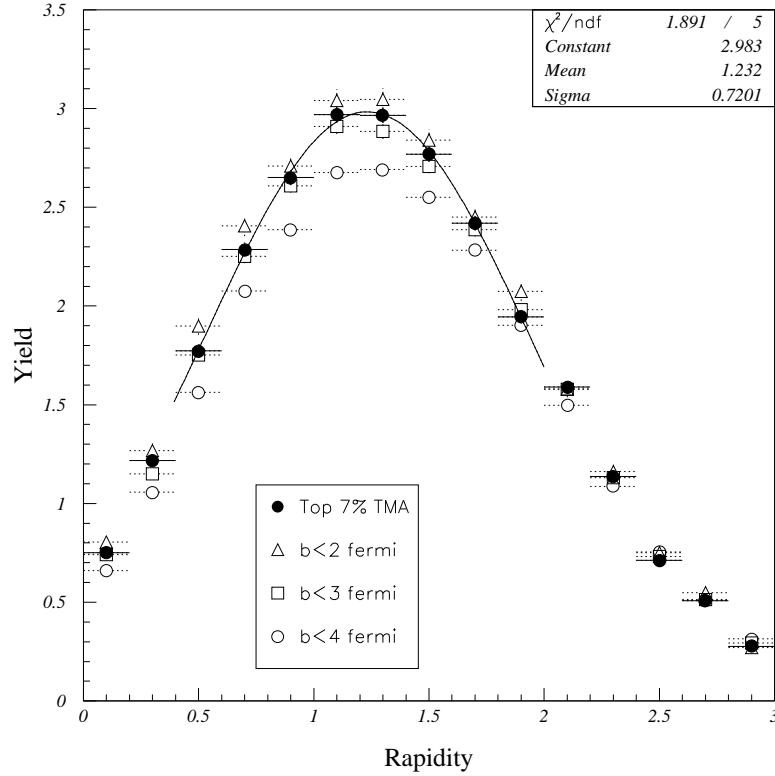


Figure 6-5: RQMD Si+Au K^+ dn/dy for different event selections. The solid line is a Gaussian fit to the peak of the dn/dy distribution for the high multiplicity cut. The agreement between the two ways of selecting events is best for impact parameters between 2 and 3 fm.

6.4 Kaon Yields and Slopes

As with the real data, the first results to examine are the invariant yields and the m_{\perp} inverse slope parameters. There are enough kaon statistics in the minimum bias and central RQMD simulations to treat the model output in exactly the same way as the data. Cross section histograms are filled and the experimentally accessible region is masked off using the same acceptance histograms as for real data. Then the same fitting routines used for the data are used to fit exponential m_{\perp}

6.4. KAON YIELDS AND SLOPES

distributions to the model output. A comparison of the slopes found in RQMD and the data for a slice in rapidity 0.2 units wide centered at $y = 1.3$ is shown in Table 6.3. The RQMD K^+ slopes

System	RQMD K^+	Data K^+	RQMD K^-	Data K^-
Si+Al minimum bias	157 ± 3	167 ± 2	184 ± 7	147 ± 2
Si+Al central	160 ± 3	169 ± 4	236 ± 27	149 ± 3
Si+Au minimum bias	163 ± 3	179 ± 2	188 ± 7	157 ± 2
Si+Au central	165 ± 3	184 ± 3	226 ± 10	162 ± 3

Table 6.3: Comparison of RQMD and data m_\perp inverse slope parameters. The units are MeV/c^2 . While the RQMD slopes for K^+ are somewhat smaller than for real data, the K^- slopes are quite a bit larger.

are lower than the data, and the K^- slopes are significantly higher than the data. The statistics for the K^- are fairly thin for fitting the data this way, but it does seem that RQMD is off the mark here. Figure 6-6 shows a direct comparison between the m_\perp distributions for K^- in central Si+Au for RQMD and E859 data. The first question that arises is whether the difference in the slopes between RQMD and the data in A-A collisions is generated during the A-A collision, or whether is is due to a bad parameterization of the p-p data. We generated 100,000 p-p events using RQMD, and the $p+p \rightarrow K^-$ m_\perp slope extracted from the RQMD events is $138 \pm 6 \text{ MeV}/c^2$, the $p+p \rightarrow K^+$ slope is $145 \pm 2 \text{ MeV}/c^2$. For comparison, the kaon slopes in the E802 p+Be data near $y = 1.5$ are $130 \pm 10 \text{ MeV}/c^2$ for K^- , and $150 \pm 5 \text{ MeV}/c^2$ for the K^+ [A⁺92a]. So, the kaon slopes in p-p events generated with RQMD seem to agree well with the data. Subsequent discussions with one of the authors of RQMD may have identified an inadvertently disabled πY channel in the present version of the code as the culprit [Sor]. Other meson-hyperon channels do not seem to have been affected. Preliminary results with a patched version of RQMD that properly incorporates the πY channel show an inverse m_\perp slope for central Si+Au $\rightarrow K^-$ of $204 \pm 14 \text{ MeV}/c^2$. The size of the statistical errors do not allow for a conclusive statement, but there is some indication that the modification to the code changes the RQMD K^- m_\perp slopes in the direction of the data.

The fitted slopes for RQMD are not greatly affected by the experimental acceptance, as can be seen in Figure 6-7. The figure shows the effect of fitting an exponential m_\perp distribution over the whole range and within the acceptance to RQMD output in three different slices of rapidity. There

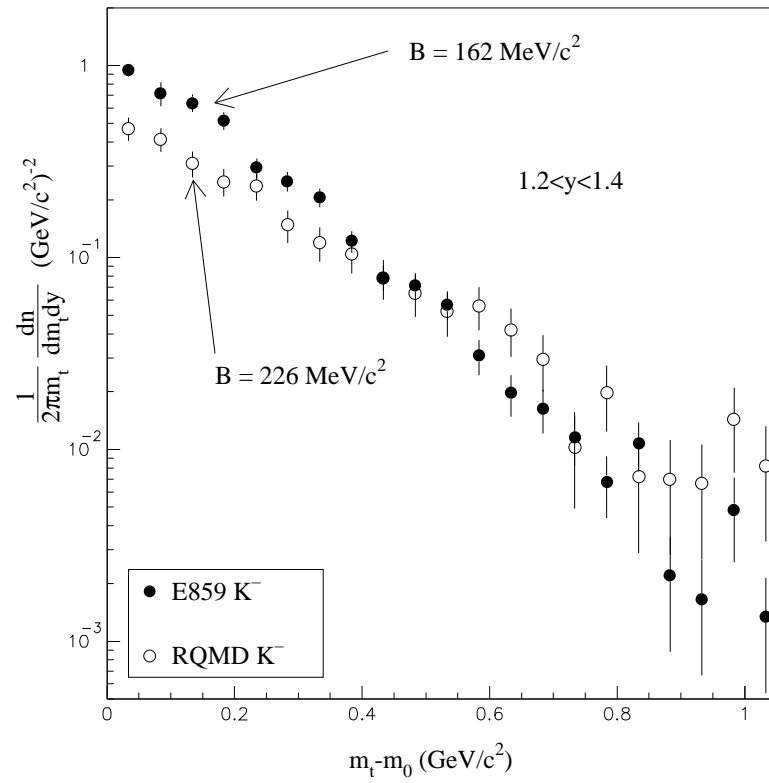


Figure 6-6: RQMD and E859 upper 7% TMA Si+Au \rightarrow K^- m_{\perp} distribution. The RQMD slope is significantly higher than the data.

6.4. KAON YIELDS AND SLOPES

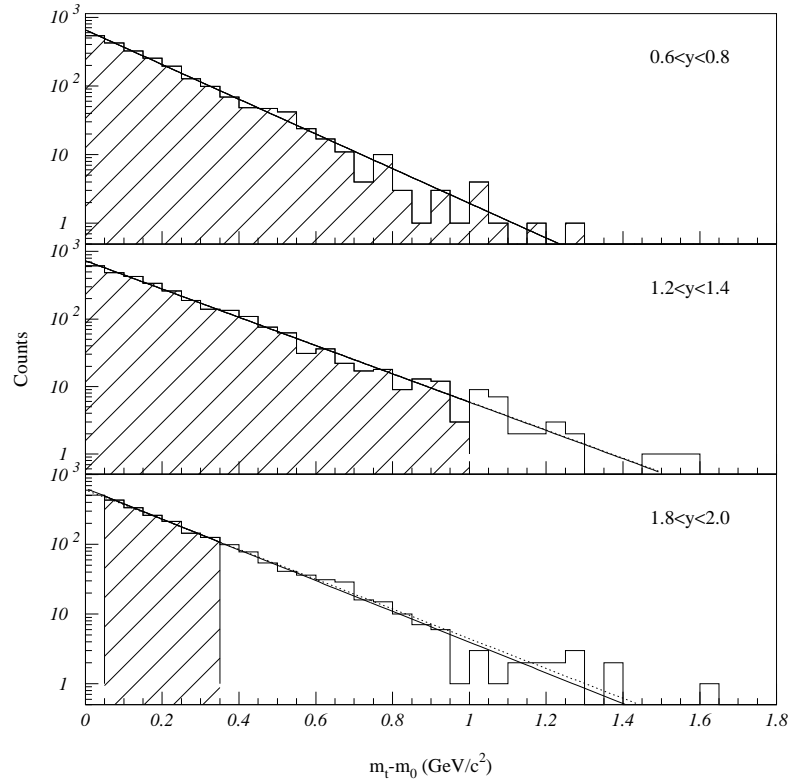


Figure 6-7: RQMD Si+Au \rightarrow K $^+$ slope systematics. The m_{\perp} distributions for low, medium and high y slices of the minimum bias data are shown. Two exponential m_{\perp} fits are made to each distribution. One, fit over the whole distribution, is shown as a dotted line. The other, shown as a solid line, is fit over only that part of the distribution inside the E859 acceptance, represented by the hatched area. The two fits are only distinguishable for the most forward slice, where imposing the acceptance reduces the slope parameter by ~ 2 MeV/c 2 .

is very little difference for any of the rapidities, the largest difference occurring for the slice with the least acceptance.

There are two ways to obtain the dn/dy for kaons in RQMD. One can take the fits to the m_{\perp} spectra described above and integrate them to give dn/dy as a function of rapidity. Or, one can just histogram the yields directly as a function of rapidity. The first method is certainly the more correct way, but as Table 6.4 and Figure 6-7 show, there is very little difference between the two methods. Also, the relatively limited statistics of the RQMD sample makes this type of analysis impossible for any of the more peripheral cuts. If we histogram the counts directly and make the

System	K ⁺ Fit	K ⁺ Count	K ⁻ Fit	K ⁻ Count
Si+Al minimum bias	0.28±0.01	0.29±0.01	0.074±0.003	0.074±0.003
Si+Au minimum bias	1.00±0.02	0.99±0.03	0.21±0.01	0.22±0.01

Table 6.4: Comparison of RQMD dn/dy from fits and counts.

event selection appropriately, the rapidity distributions for RQMD kaons for each of the four TMA cuts can be plotted. Figure 6-8 and Figure 6-9 show the kaon dn/dy distributions as a function of rapidity. The yields in each bin are obtained by simple counting, not by fitting an exponential in m_{\perp} to the transverse spectra and integrating. However, this is expected to have only a $\sim 5\%$ effect on the dn/dy . In general the RQMD yields are 10-30% lower than the data at the peak, but this difference essentially disappears near the edges of the experimental coverage. The one exception to this general characterization seems to be the peripheral Si+Au yields, for which the RQMD yields are slightly higher than the data. However, it should be noted again that there are considerable systematic uncertainties associated with comparing the peripheral cuts on the data and in the model.

6.5 Scaling of Kaon Yields in RQMD

A further comparison between the E859 kaon data and the output of RQMD can be made by looking at the change in total yields of kaons as a function of the number of participating nucleons. Using the simulated ZCAL and TMA, we calculated the number of participants in the same way as for real data, and then compare average number of participants for kaon events for the different TMA cuts

6.5. SCALING OF KAON YIELDS IN RQMD

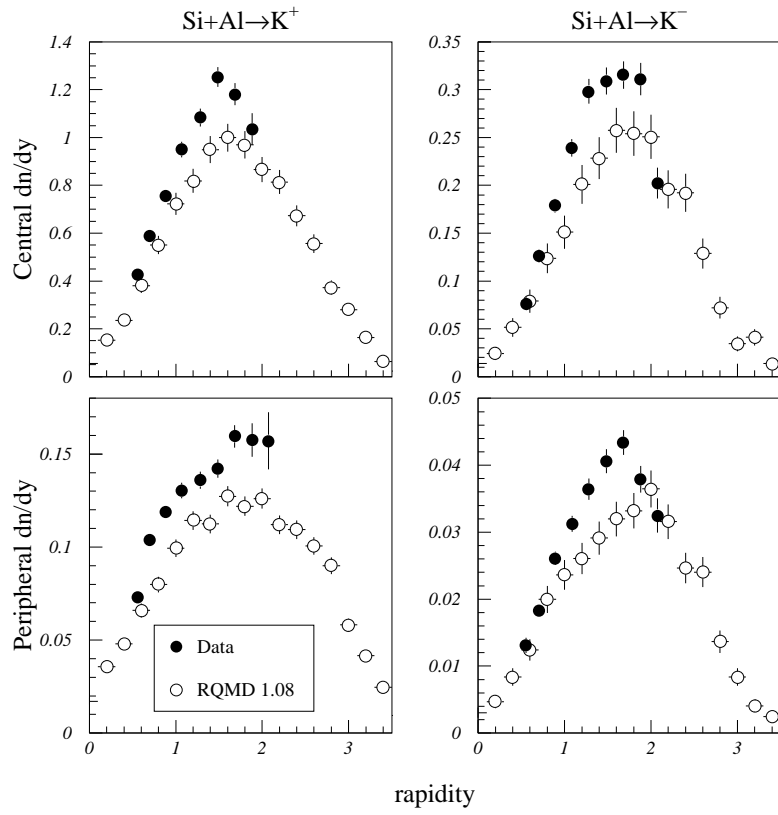


Figure 6-8: RQMD and measured Si+Al \rightarrow K dn/dy versus rapidity for the most central and the most peripheral TMA cuts.

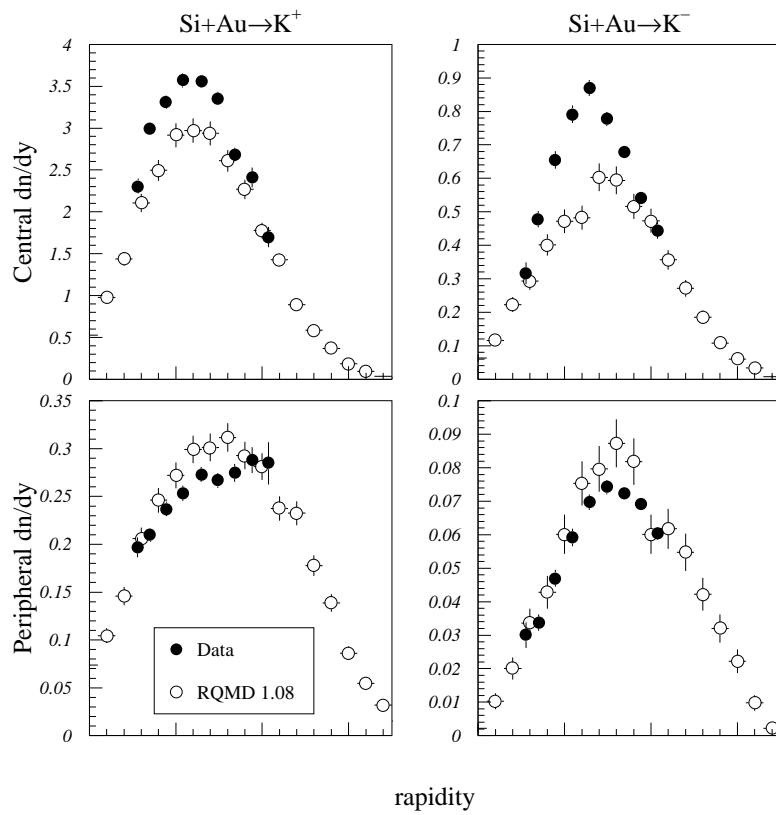


Figure 6-9: RQMD and measured Si+Au→K dn/dy versus rapidity for the most central and the most central TMA cuts.

6.6. K^+/K^- RATIO

with real data. Table 6.5 shows these values. The yields are plotted as a function of these cuts in

System	Name	Range	$\langle N_{proj}^{RQMD} \rangle$	RMS_{proj}^{RQMD}	$\langle N_{proj}^{Data} \rangle$	RMS_{proj}^{Data}
Si+Al	TMA1	44–	20.2	2.9	19.3	4.3
	TMA2	31–43	16.4	3.7	16.1	5.0
	TMA3	17–30	10.7	4.0	11.1	5.3
	TMA4	0–16	4.0	3.0	4.6	4.1
Si+Au	TMA1	143–	27.1	0.8	26.4	1.7
	TMA2	108–142	25.5	1.8	24.2	3.1
	TMA3	65–107	20.0	3.8	17.0	5.3
	TMA4	0–64	6.8	5.0	7.5	4.8

Table 6.5: Comparison of ZCAL for TMA cuts between RQMD and real data. The TMA cuts for the data are defined in Section 4.10 and the cuts on the RQMD simulated TMA response are made in a similar way. The simulated ZCAL response is histogrammed for events containing a kaon in the acceptance and satisfying each of the TMA cuts, and the average ZCAL energy is extracted. This is divided by the beam kinetic energy and subtracted from 28 to give the number of participants.

Figure 6-10. The kaon yields in RQMD rise linearly with the total number of participants, as do the E859 kaon yields. The figure shows a dotted line representing the linear fit to the E859 data, and a dashed fit to the RQMD data. For comparison, the equations of the linear parameterizations are

$$\begin{aligned}
 N_{Data}^{K^+} &= -0.6 + 0.08N_{part} \\
 N_{RQMD}^{K^+} &= -0.9 + 0.07N_{part} \\
 N_{Data}^{K^-} &= -0.09 + 0.016N_{part} \\
 N_{RQMD}^{K^-} &= -0.15 + 0.014N_{part}
 \end{aligned} \tag{6.1}$$

6.6 K^+/K^- Ratio

Using RQMD, we can also examine the ratio of K^+ and K^- . Figure 6-11 shows the K^+/K^- ratio for Si+Al with the E859 minimum bias Si+Al data superimposed. The RQMD results have much poorer statistics than the real data, but the peripheral RQMD ratio seems to substantially follow the trend of the data. There is a statistically marginal tendency for the central RQMD ratio to have a flatter rapidity dependence than the data or the peripheral RQMD ratio. A factor of four better

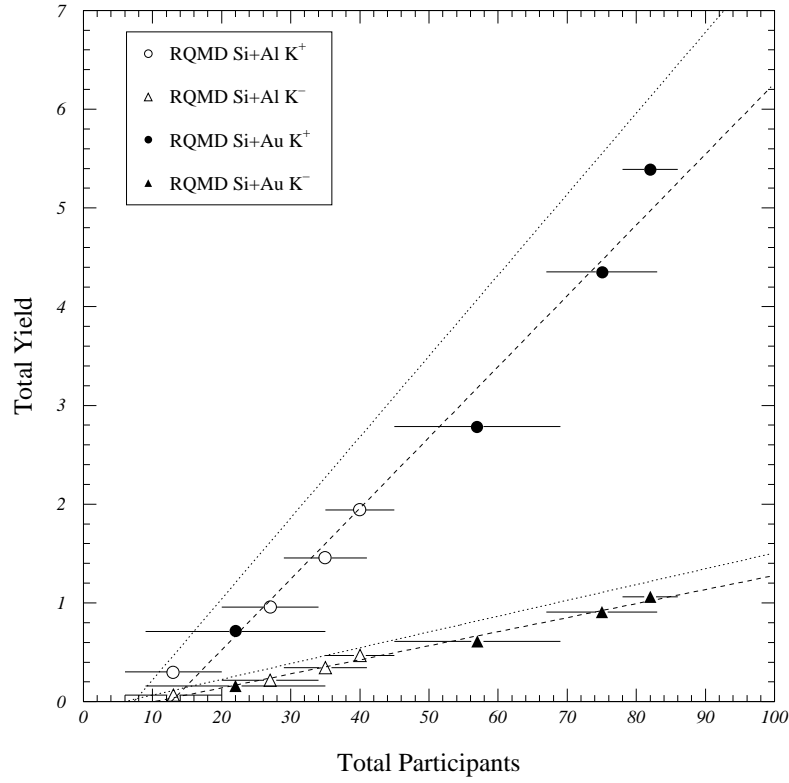


Figure 6-10: Scaling of RQMD total kaon yields with number of total participants. The yields are obtained by directly counting all kaons produced by RQMD. The total yields for the K^+ and K^- both rise roughly linearly with N_{part} . The only deviation from this trend seems to be for the one or two most central TMA cuts for the Si+Au data. The dashed lines are the linear fits to the RQMD data; the dotted lines are the linear fits to the E859 kaon data shown in Figure 5-10.

6.6. K^+/K^- RATIO

statistics would probably be enough to allow one to say conclusively whether the trends were really different or not. Figure 6-12 shows the K^+/K^- ratio for Si+Au with the E859 minimum bias

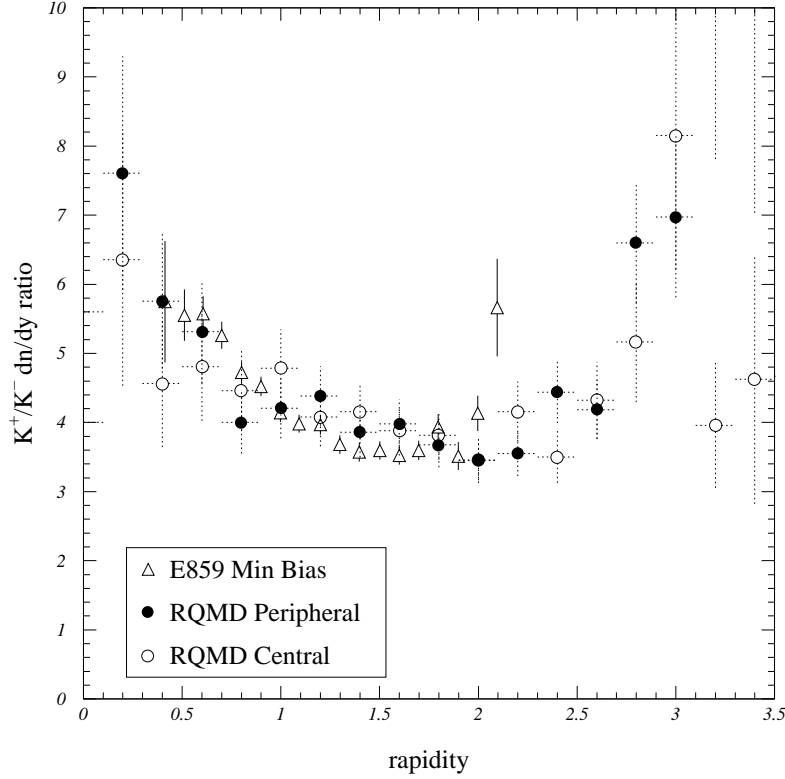


Figure 6-11: RQMD Si+Al K^+/K^- dn/dy ratio versus rapidity.

Si+Au data superimposed. Again, the peripheral RQMD ratio seems to follow the trend of the data, but the central ratio seems to differ somewhat. Part of this may be merely a statistical fluctuation, but it may be partly due to a missing $\pi Y \rightarrow NK^-$ channel (inadvertently disabled in RQMD 1.08, see Section 6.4). This channel works to increase the number of K^- 's, which would send the RQMD ratio in the direction of the data. Since this channel involves produced particles, one would expect its effect should be concentrated in rapidity around 1–1.2 (between y_{NN} and the target rapidity), which is where the effect is actually seen.

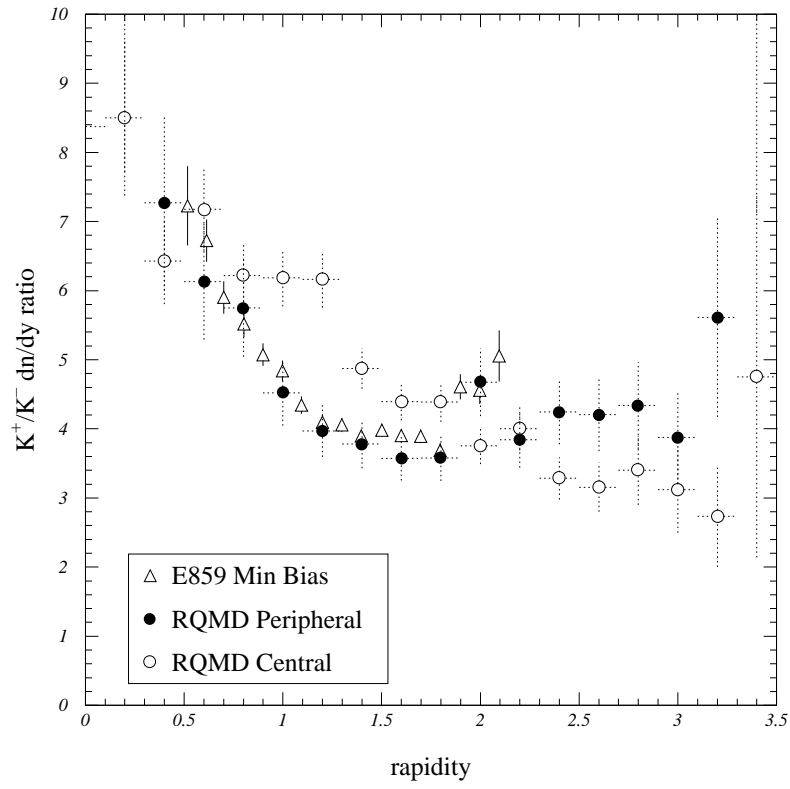


Figure 6-12: RQMD Si+Au $K^+/K^- dn/dy$ ratio versus rapidity

6.7 Kaon Production Mechanisms

Of course, the advantage of using a model is that you have direct access to the production mechanisms of the final state particles. We can look in the model to see the relative importance of the different contributions to the final K^+ and K^- yields. As described above, RQMD creates many of the final particles not directly, but via resonant or excited intermediate states. Figure 6-13 and Figure 6-14

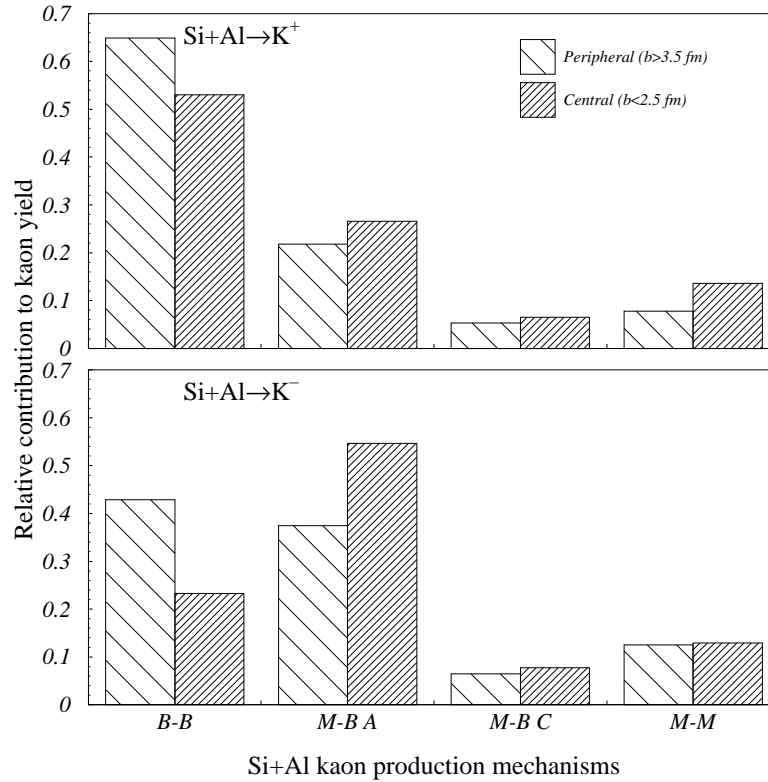


Figure 6-13: RQMD Si+Al→K production mechanisms. In each panel is a comparison of peripheral and central kaons, normalized to show the relative importance of each process. *B-B* means baryon-baryon collisions, *M-B A* means meson-baryon annihilations, *M-B C* means meson-baryon collisions, and *M-M* means meson-meson collisions. As a general rule, baryon-baryon collisions play a smaller role in central collisions. This is especially true for K^- .

show the relative importance of different mechanisms in RQMD that produce kaons for peripheral and central collisions. RQMD produces one file containing the momenta of all produced particles and a separate file which contains the momenta and production mechanism of the kaons. Because

the information for the whole event is not available in the strangeness production file, it is difficult to make the same multiplicity cuts as above using the TMA simulation. Instead, cuts on impact parameter have been used here to define central and peripheral. However, since we are not comparing the information in this section to experimental results, it is not so important.²

There are several categories of collisions shown in each bar chart. They are:

- *B-B*

Baryon-Baryon collisions. This includes associated production, $NN \rightarrow N\Lambda K^+$, and kaon pair production, $NN \rightarrow NNK^+K^-$, as well as more exotic channels involving baryon resonances such as $N\Delta \rightarrow N^* \rightarrow \Lambda K^+$.

- *M-B A*

Meson-Baryon annihilation. This includes channels such as $\rho N \rightarrow \Lambda K^+$, where the meson in the initial state does not appear in the final state.

- *M-B C*

Meson-Baryon collision. This includes channels such as $\rho N \rightarrow \rho N K^+ K^-$, where the initial meson also appears in the final state.

- *M-M*

Meson-Meson collision. This includes channels such as kaon pair production via pion annihilation, $\pi\pi \rightarrow K^+K^-$.

In peripheral collisions, baryon-baryon collisions are the main source of K^+ and K^- in both systems. In central collisions, meson-baryon collision quickly become more important. Meson-baryon interactions are the main source of K^- production in both central Si+Al and central Si+Au. Baryon-baryon collisions are nearly always the main source of K^+ . However, in central Si+Au the total of both types of meson-baryon interactions manages to just out produce the baryon-baryon channels.

We can also examine the production mechanisms as a function of rapidity. Figure 6-15 shows this for Si+Au for central and peripheral collisions. In peripheral K^+ production, the baryon-baryon channel is peaked about y_{NN} , but this peak moves back toward the target as one goes to

²We're not comparing apples to oranges, we're just having a close look at the apples.

6.7. KAON PRODUCTION MECHANISMS

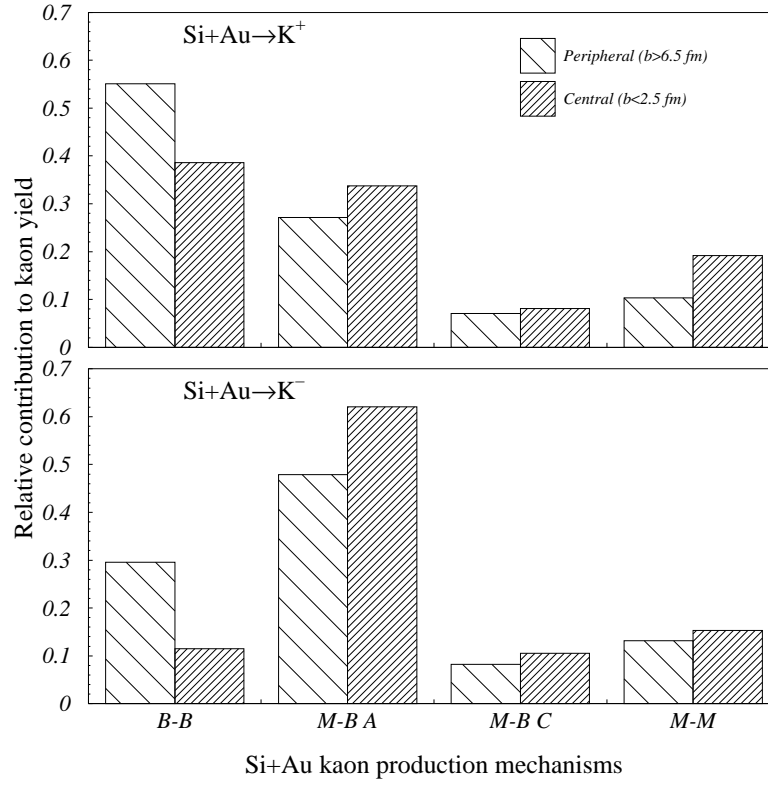


Figure 6-14: RQMD $\text{Si+Au} \rightarrow \text{K}$ production mechanisms. In each panel is a comparison of peripheral and central kaons, normalized to show the relative importance of each process. *B-B* means baryon-baryon collisions, *M-B A* means meson-baryon annihilations, *M-B C* means meson-baryon collisions, and *M-M* means meson-meson collisions. As a general rule, baryon-baryon collisions play a smaller role in central collisions. This is especially true for K^- .

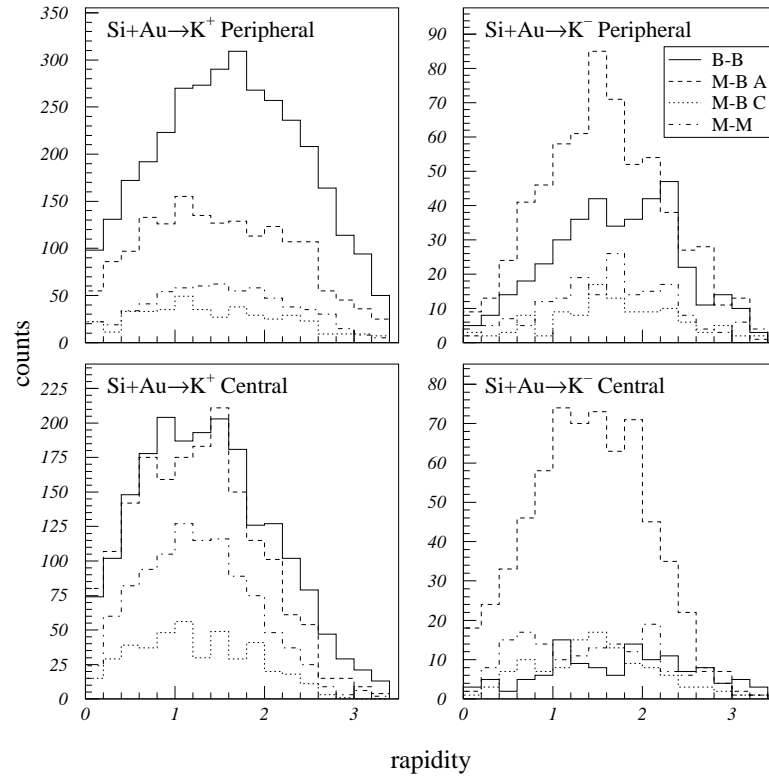


Figure 6-15: RQMD $\text{Si+Au} \rightarrow \text{K}$ production mechanisms versus rapidity

6.8. SUMMARY OF MODEL COMPARISON

central collisions. In K^- production, the baryon-baryon channel remains strongest near y_{NN} . These trends are consistent with the difference in the thresholds of kaon pair production and associated production with a Λ . The meson-baryon processes shows large changes in going from peripheral to central collisions. In K^+ production, it becomes as important as the baryon-baryon channels. In K^- production, it starts out as the dominant source in peripheral collisions, and grows even more important in central collisions. Since these processes involve at least one produced particle, they are peaked closer to the target rapidities than y_{NN} .

6.8 Summary of Model Comparison

In general, RQMD 1.08 does a reasonable job of reproducing many of the observables in the E859 single particle kaon data. However, the agreement between model and data should not be over-sold: there are several places where the model is in significant disagreement with the data. On the other hand, RQMD does reproduce the systematic trends in the data quite well, and there are many instances where the quantitative agreement between the model and the data is quite good.

The total yields that RQMD predicts are 10–15% lower than the data for all but the most peripheral data. However, as explained in Section 6.3, there are large systematic uncertainties inherent in comparing the peripheral model output to data. Most of the difference in the central yields occurs directly under the peak of the dn/dy distribution where RQMD is quite a bit too low. The disagreement is most serious for central $Si+Au \rightarrow K^-$, where RQMD predicts only about 70% of the K^- 's seen in the data.

There are also mixed results in the agreement between the m_\perp inverse slope parameters in RQMD and the data. The RQMD slopes for both central and minimum bias $Si+Al \rightarrow K^+$ are about $10 \text{ MeV}/c^2$ smaller than the data, while the K^+ slopes for $Si+Au$ are about $20 \text{ MeV}/c^2$ lower than the data. The statistical uncertainties on these numbers is about $3 \text{ MeV}/c^2$, and there are systematic uncertainties on the experimental data of a few percent, so I would argue that this is quite good agreement. The K^- slopes are a different story. The central $Si+A \rightarrow K^-$ slopes in RQMD are $\sim 70 \text{ MeV}/c^2$ higher than the data, and the RQMD slopes for K^- are larger than the slopes of the K^+ ; the opposite of what is seen in the data. The statistical uncertainties on the K^- model results are quite large, $\pm 10 \text{ MeV}/c^2$, but the effect is still significant.

Ironically, this discrepancy might be explained by interesting physics. If RQMD too strongly absorbs low momentum K^- the result might be consistent with the discrepancy seen in the yields and in the slopes. In fact, one might turn this around, and argue that the experiment sees evidence for less absorption of low momentum K^- than is predicted in a hadronic model. In a paper by Koch [KD89] discussing strangeness production in 2.1 A-GeV/c nuclear collisions, he argues that, “during the final expansion stage, the produced \bar{p} ’s and K^- ’s might not be so strongly depleted as naïvely expected.” This is because the annihilation rate of K^- is a strong function of the baryon density and falls rapidly as the system decouples.

RQMD does a good job at reproducing the widths of the dn/dy distributions and, in particular, reproducing the systematic decrease in those widths as the total number of participants increases. In RQMD, this is strongly correlated with an increase in the contribution of meson-baryon interactions to the yield of kaons, especially for K^- . RQMD tracks the trend in the data quite well and suggests a possible reason for this behavior in the widths.

Within the statistics, RQMD also seems to show a K^+/K^- ratio independent of centrality and system. The one exception to that seems to be the central Si+Au, but the dn/dy distribution for the K^- in that RQMD data set is oddly shaped, which may be simply a question of statistics. Since the mechanisms responsible for kaon production in RQMD vary significantly as one goes from peripheral Si+Al to central Si+Au, the stability of the ratio appears as a sort of complicated coincidence. In central Si+Au where one might expect the K^- production to lag behind the trend of the K^+ because of increased absorption, the contribution of meson-baryon interactions steps in to keep the yield as high as it is.

Finally, the mechanisms in RQMD responsible for kaon production vary quite strongly with centrality. For the most peripheral collisions, baryon-baryon collisions are the main source of K^+ and are also quite significant for the production of K^- . For the most central collisions, especially for Si+Au, meson-baryon interactions become much more important, competing strongly with baryon-baryon processes as the dominant source of K^+ ’s. The meson-baryon channels are the most important source of K^- ’s by far, responsible for nearly 75% of the K^- seen in central Si+Au.

While RQMD generally under-predicts the kaon yields, it is known to significantly over-predict the pion yields [Zac93]. Because of this, it may also over-rate the importance of meson-baryon interactions. However, many of the mesons during the collision are actually ρ ’s and ω ’s which

6.8. SUMMARY OF MODEL COMPARISON

would end up decaying into 2 and 3 pions if they did not interact with the hyperons and nucleons to produce the additional kaons seen in the central collisions. Quite a bit of the discrepancy between the pions yields of RQMD and what is seen in the data could be relieved by producing fewer heavy mesons in the initial stages of the collisions. This would reduce the number of kaons as well, because it would reduce the number of meson-baryon collisions. The number of pions should be affected more strongly, since a meson-baryon interaction leads to only one kaon, but allowing the heavy meson to decay can produce more than one pion.

From RQMD we learn a plausible reason for the trends seen in the E859 kaon data. As one creates a larger and larger collision system, the number of meson-baryon, and in particular meson-hyperon, collisions increases quickly, leading to an increase in the number of K^- which tracks the increase in the number of K^+ . The net effect is that central Si+Au collisions, where one would expect significant K^- absorption, have very nearly the same K^+/K^- ratio as peripheral Si+Al collisions. This is an interesting and significant point about the dynamics of relativistic heavy-ion collision at these energies. The large baryon number densities in these collisions allow for processes that not only augment the creation of strangeness, through the decay of massive nucleon and hyperon states, but provides a way for the created strangeness to be redistributed from the Λ 's and Σ 's to the K^- which ordinarily have a small primary production cross section. Simulations of Au+Au collisions at AGS energies have been begun, and it will be interesting to see if the RQMD model of these interactions is able to reproduce the details of strangeness production seen there.

Chapter 7

Summary and Conclusions

Distributions of K^+ and K^- produced by a $14.6 \text{ A} \cdot \text{GeV}/c$ ^{28}Si beam incident on targets of ^{27}Al and ^{197}Au have been measured over a large range in rapidity, $0.5 < y < 2.1$, and transverse momentum, $0.1 < p_{\perp} < 2.5$. These measurements are the most comprehensive charged kaon measurements made so far for heavy-ion collisions at these or any energies. The measurements have much higher statistics than similar data sets collected as part of E802, and the higher statistics have allowed a detailed look into the mechanisms of strangeness production. The following conclusions may be drawn from the data:

- The new data set has substantially better statistics than before, but where the data sets overlap the results are basically in agreement. For example, the peak of the central $\text{Si}+\text{Au} \rightarrow K^+$ dn/dy in the E802 data is $3.24 \pm 0.18 [\text{A}^+94]$; in the E859 data it is 3.57 ± 0.08 . The result of this difference in statistics is that within the statistical errors of the E802 data, the three dn/dy points from $y = 1.1$ – 1.5 all show essentially the same value, while the E859 data is clearly able to distinguish the maximum between $y = 1.1$ and $y = 1.3$.
- Many of the gross features of the kaon data are consistent with an orthodox picture of kaon production. The K^+ yields near y_{NN} are about a factor of 4 larger than the K^- yields, roughly the same as in p-p collisions at these energies. This is consistent with the expected dominance of the associated production $\text{NN} \rightarrow \text{NA}K^+$. The peak of the K^+ production in $\text{Si}+\text{Au}$ moves toward the target rapidity as more central events are selected. Again, this is what one would expect given associated production as the primary source of K^+ .

CHAPTER 7. SUMMARY AND CONCLUSIONS

- The inverse m_{\perp} slopes of both K^+ and K^- in Si+Al do not vary significantly with centrality, which is perhaps an indication that Si+Al is too small a system in which to see any significant change in the kaon production mechanisms. On the other hand, the m_{\perp} slopes in Si+Au increase by 10-20 MeV/c² in going from peripheral to central collisions, perhaps indicating that the larger number of collisions in the Si+Au system helps to populate the high m_{\perp} tail of the distribution.
- The inverse m_{\perp} slopes for the K^+ are 10-20 MeV/c² larger than the slopes for the K^- . Part of the reason for this may be the lower energy threshold for the process $NN \rightarrow N\Lambda K^+$ as compared to $NN \rightarrow NNK^+K^-$. The extra kinetic energy available in the associated production of a K^+ and a Λ allows the K^+ to be produced with higher m_{\perp} increasing the inverse m_{\perp} slope.
- The widths of the rapidity distributions for both K^+ and K^- decrease as the total number of participants increases. Therefore the kaon production is not increasing uniformly over the full rapidity range (as seems to be the case for the pions), but shows a peaking behavior.
- The integrated yields of both K^+ and K^- increase approximately linearly with the total number of participants. In going from peripheral Si+Al to central Si+Au the yields of both K^+ and K^- increase by a factor of ~ 30 .
- The K^+/K^- ratio demonstrates nearly unchanging behavior as a function of centrality and collision system. For all system, the ratio increases from 4 near y_{NN} to 6-7 near target rapidity. Meanwhile, in Si+Au the rapidity density of protons near $y = 1.0$ increases by a factor of nearly 20.

There are also several conclusions that can be drawn from the comparison with RQMD:

- The kaon yields in RQMD for central Si+Al and Si+Au are 10–30% too low, and most of this difference occurs at the peak of the kaon production. In the more peripheral cuts, the RQMD yields for K^+ and K^- agree well with the data in the case of Si+Au, but are still 20% too low in the case of Si+Al.
- The inverse m_{\perp} slope parameters for the K^+ in RQMD central Si+Au are about 10 MeV/c² lower than the data. The slopes for the K^- in the same system are ~ 70 MeV/c² higher than

the data. The significant discrepancy in the case of the K^- may have been traced to the lack of the $\pi Y \rightarrow NK^-$ process, which was inadvertently disabled in the version of RQMD used here. Preliminary indications are that enabling this process may move the RQMD m_\perp slopes in the direction of the data.

- The total yields of both K^+ and K^- in RQMD show a linear increase with the number of total participants as in the data. The linear coefficient of this increase for the K^+ is within 10-20% the same in RQMD and the data, and this is also true for the K^- .
- The widths of the kaon rapidity distributions in RQMD show the same narrowing with increased centrality as seen in the data.
- In going from peripheral Si+Al to central Si+Au, the relative contribution of baryon-baryon collisions to the K^+ yields decreases from 65% to 40%, while the contribution of meson-baryon collision increases from 27% to 43%. At the same time the contribution of baryon-baryon collisions to the K^- yields decreases from 42% to 12%, but the contribution of meson-baryon collisions increases from 43% to 74%. The interactions of secondaries plays a very large role in the production of K^- , and the importance of these processes increases with system size.

In explaining these results, it does not appear necessary to invoke the existence of a quark-gluon plasma. Though the one hadronic cascade code studied in detail here underpredicts the kaon production, it does seem to scale with system size like the actual data. So the code may have cross sections for some kaon production processes that are too small, but there seems to be an indication that the mechanisms which increase the production are modelled realistically. The current measurements also have some implications for some of the early observations made by the collaboration. In particular, the rise of the K/π ratio is almost certainly explainable without needing the quark-gluon plasma. While the pion production per participant is basically saturated in most collisions, the more central collisions bring into play processes which increase the strangeness production above what is seen in p-p data. At the same time, there are strangeness exchange reactions which help move some of this strangeness to the K^- 's from the Λ 's and Σ 's created in associated production with K^+ 's. Therefore, the K/π ratio, while not an indicator of QGP formation, does seem to indicate the importance of interesting dynamical effects in these collisions.

CHAPTER 7. SUMMARY AND CONCLUSIONS

There are several ways the current work could be extended. The AGS is now accelerating beams of ^{197}Au to 11.7 GeV/c per nucleon, offering the prospect of investigating strangeness production in a much heavier system than has yet been possible at these energies. Also, the symmetry of a collision like Au+Au effectively doubles the rapidity coverage of the experiment, reducing the uncertainties inherent in trying to determine the shapes of rapidity distributions or the yields of particles extrapolated to full phase space.

Though the K^+ and K^- differ in the magnitude of several measures, such as slopes and yields, one has to be struck by the similarity demonstrated between the K^+ and the K^- in the way these measures change with system size. It would be interesting to see if this similarity persists in the much larger Au+Au system. If strangeness exchange reactions involving the hyperons are a significant source of the K^- , the yields of K^- may increase significantly compared to the K^+ in Au+Au. Preliminary indications are that the K^+ yields continue to increase linearly with the total number of participant nucleons [Zac93]. If the K^- increase with the number of participants faster than the K^+ , it may be a strong clue to the dynamics of the collision.

Finally, it would be interesting to see the behavior of the kaon rapidity distributions in the larger system. If RQMD is correct, meson-baryon annihilations may account for nearly all of the K^- production. The fact that this mode of production proceeds via the decay of a hyperon resonance makes it difficult for the K^- to have a distribution in rapidity less than about 0.8 unit wide. There are no K^+ production channels with this kind of resonant behavior, so nothing prevents the K^+ distributions from becoming even more narrow. If the trends from the Si+A data continue, it is conceivable that the K^+ distributions would become narrower than the K^- distributions. The formation of a QGP would tend to erase this since it produces kaons without proceeding through a resonance.

The data analyzed in the thesis has provided a comprehensive view of kaon production in heavy-ion collisions at AGS energies. With high statistics, comparable in magnitude to the E802 pion data, it has been possible to make many different cuts on the kaon data for the first time and study systematic changes in the character of the kaon production. With the advent of the much heavier Au beams now available at the AGS, and the prospect of much higher energies which will be available at RHIC, the strangeness production data provided in these Si+Al and Si+Au collisions will serve as a needed benchmark for comparison. More than that, however, the present data help develop

a picture of nuclear collisions in which dynamics plays a central role in creating and distributing strangeness. Large numbers of resonances, strange and nonstrange, are created in the initial stages of the collision. These excited states interact among themselves and with the surrounding nuclear medium, helping produce strangeness, and then shuffling the created s and \bar{s} quarks among various strange mesons and baryons.

CHAPTER 7. SUMMARY AND CONCLUSIONS

Appendix A

Kaon m_{\perp} Distributions

This appendix presents the plots of m_{\perp} spectra of K^+ and K^- for Si+Al and Si+Au. For convenient reference, we repeat here the functional form of the fit to each spectrum,

$$\frac{d^2n}{2\pi m_{\perp} dm_{\perp} dy} = A e^{-B(m_{\perp} - m_0)}. \quad (\text{A.1})$$

The format of each data plot is basically the same, the data are plotted in bins 0.05 MeV/c² wide in m_{\perp} by 0.2 unit wide in rapidity (the minimum bias data is plotted with rapidity bins 0.1 unit wide). Several slices in rapidity are presented on each plot. The topmost slice corresponds to the lowest rapidity, usually a bin centered on $y = 0.5$; the lowest slice corresponds to the highest rapidity, usually a bin centered on $y = 2.1$. Each spectrum except the topmost has been divided by successive factors of 10. The line in each plot curving from lower left to upper right represents the GASČ threshold—all data to the lower right of this line require the GASČ for particle identification. The systematic error associated with each fit typically increases as one moves toward higher rapidity, both because the m_{\perp} coverage decreases, and because a larger fraction of the spectrum depends on the GASČ, for which there are substantial corrections due to pion contamination and kaon loss (see Section 4.5).

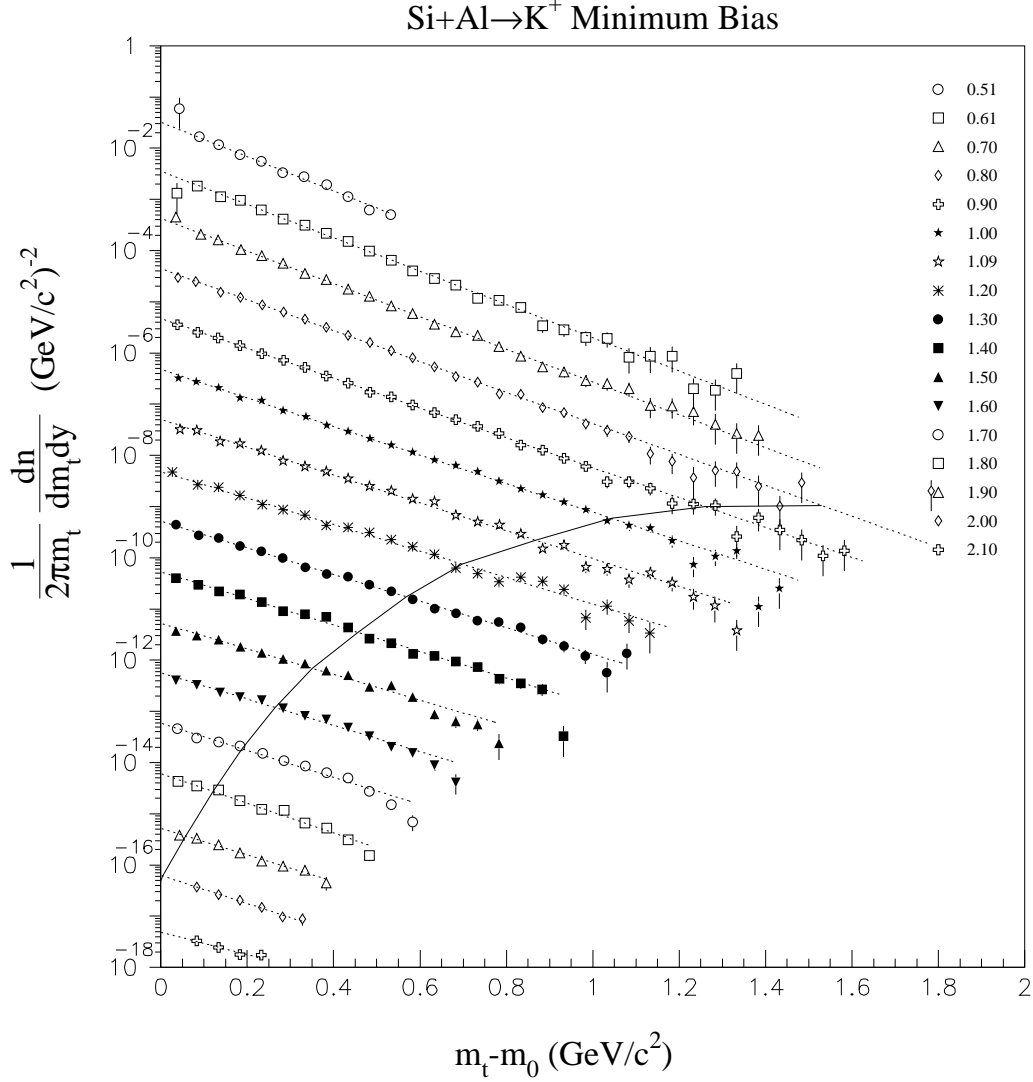


Figure A-1: Si+Al Inelastic K⁺ m_{\perp} Distributions. Data are plotted for slices in rapidity 0.1 units wide. Each slice after the topmost has been divided by successive factors of 10. Data to the right of the solid line in each slice requires GASČ for PID.

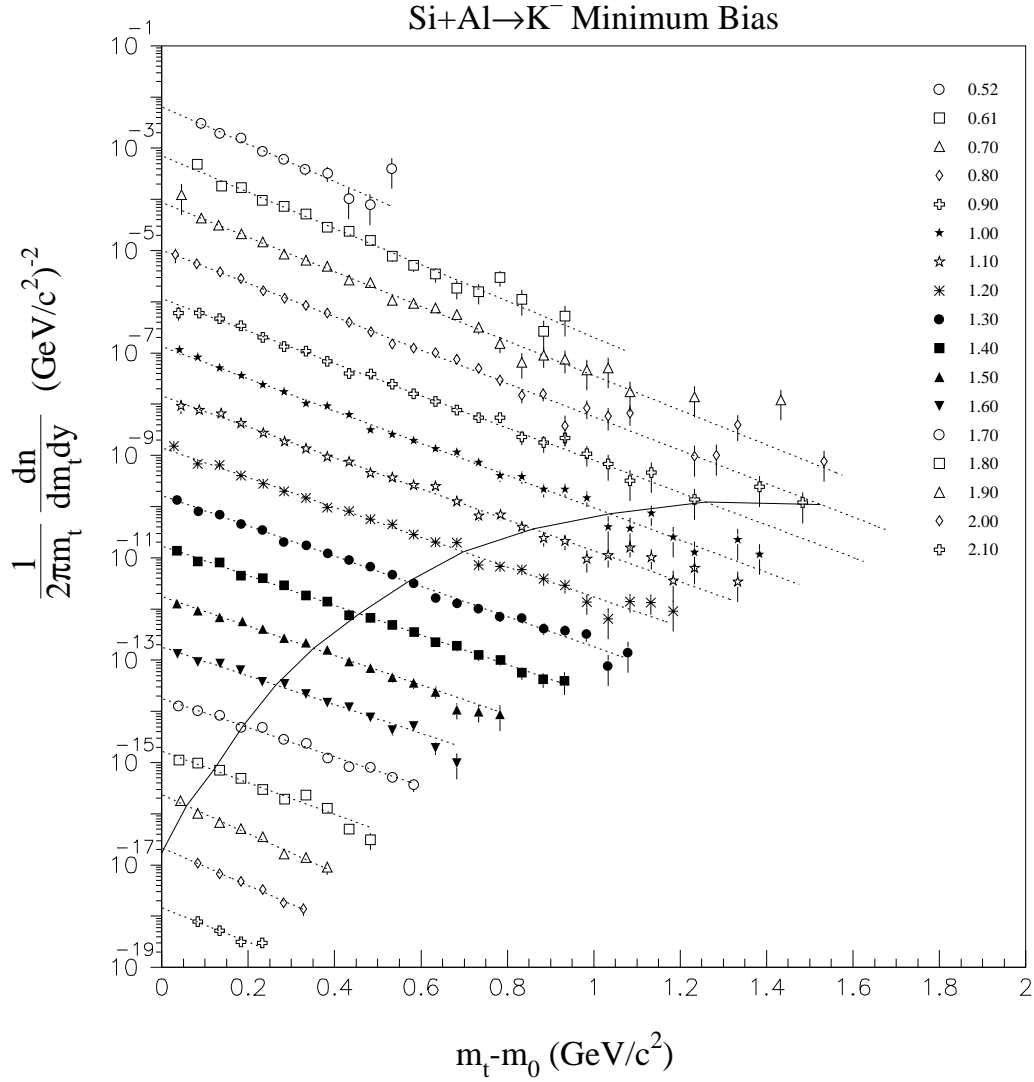


Figure A-2: Si+Al Inelastic K $^-$ m_{\perp} Distributions. Data are plotted for slices in rapidity 0.1 units wide. Each slice after the topmost has been divided by successive factors of 10. Data to the right of the solid line in each slice requires GASČ for PID.

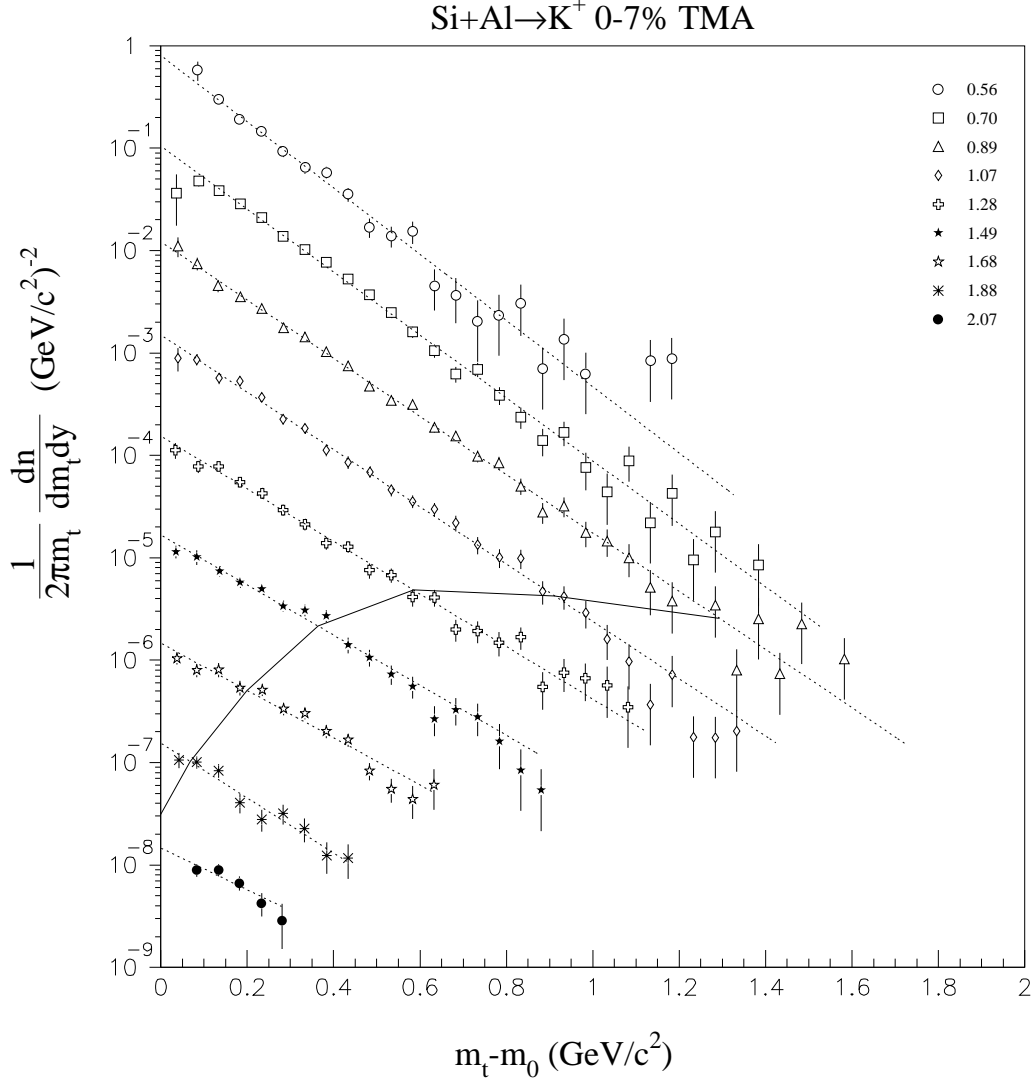


Figure A-3: Si+Al 0-7% TMA K⁺ m_{\perp} Distributions. Data are plotted for slices in rapidity 0.2 units wide. Each slice after the topmost has been divided by successive factors of 10. Data to the right of the solid line in each slice requires GASČ for PID.

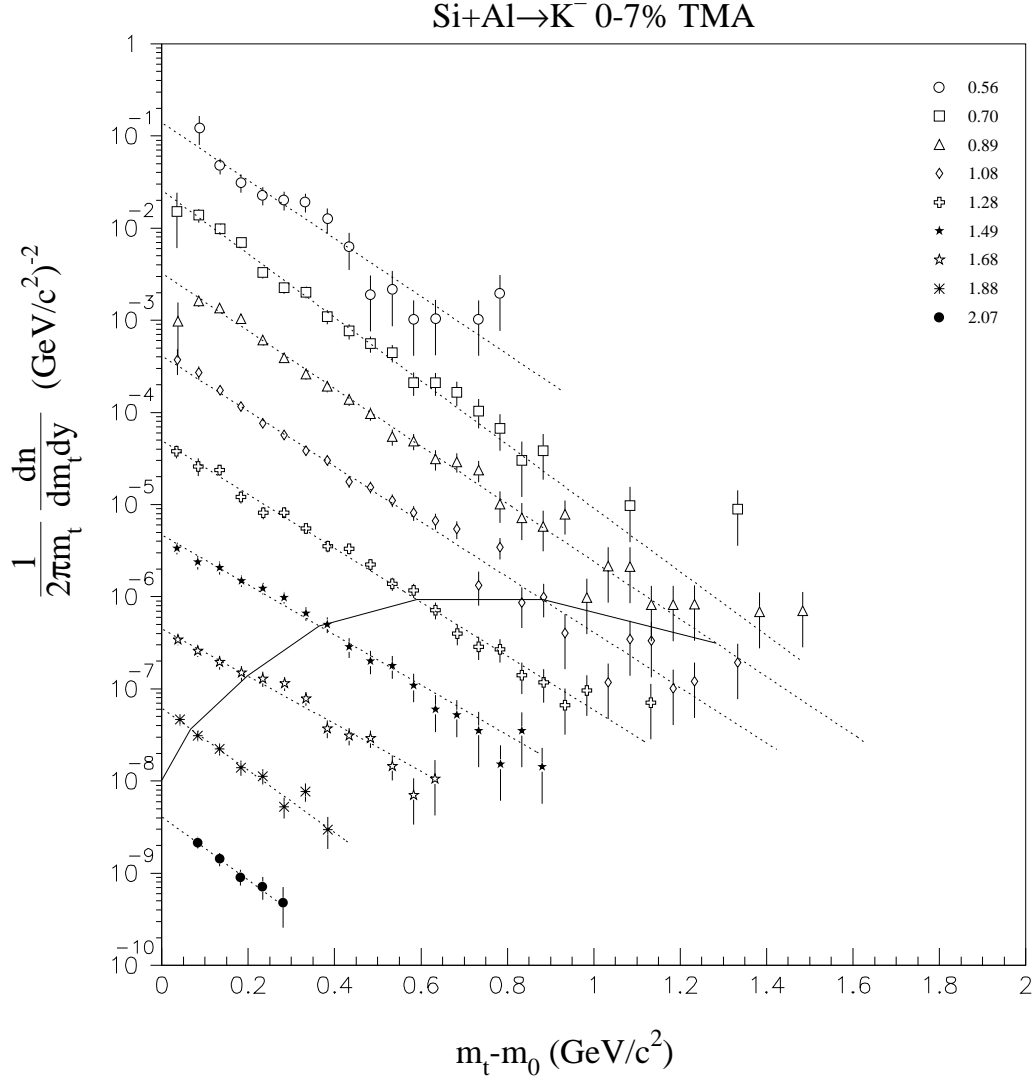


Figure A-4: Si+Al 0–7% TMA K⁻ m_{\perp} Distributions. Data are plotted for slices in rapidity 0.2 units wide. Each slice after the topmost has been divided by successive factors of 10. Data to the right of the solid line in each slice requires GASČ for PID.

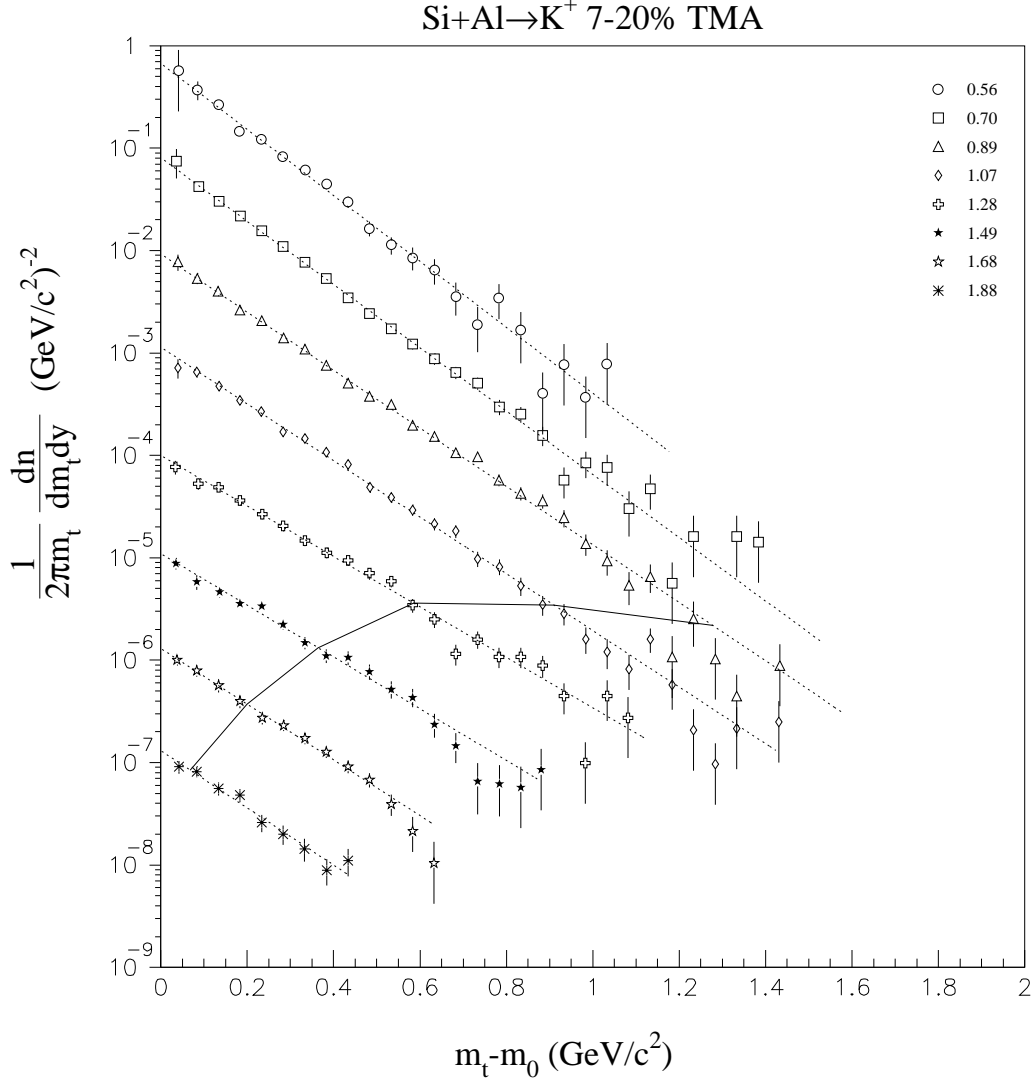


Figure A-5: Si+Al 7-20% TMA K⁺ m_{\perp} Distributions. Data are plotted for slices in rapidity 0.2 units wide. Each slice after the topmost has been divided by successive factors of 10. Data to the right of the solid line in each slice requires GASČ for PID.

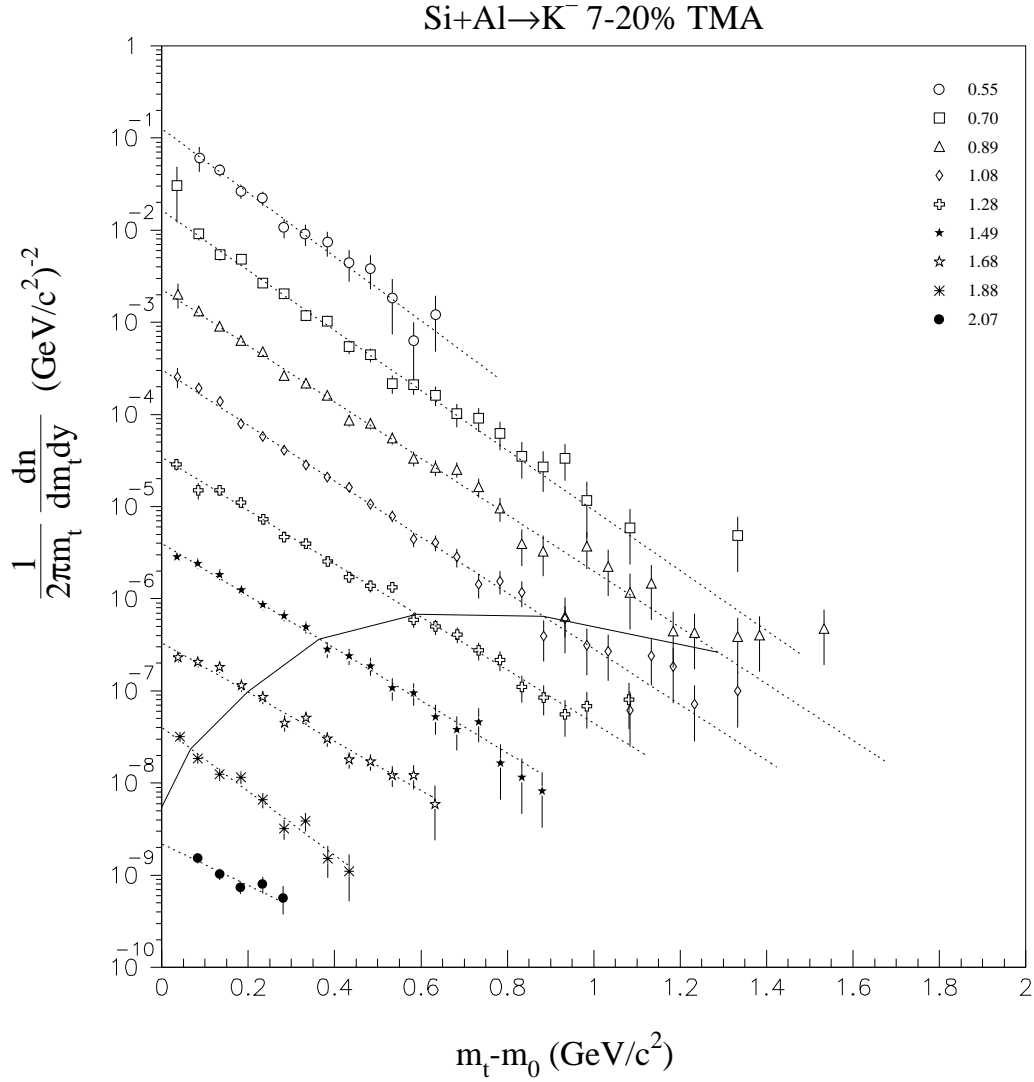


Figure A-6: Si+Al 7–20% TMA K⁻ m_{\perp} Distributions. Data are plotted for slices in rapidity 0.2 units wide. Each slice after the topmost has been divided by successive factors of 10. Data to the right of the solid line in each slice requires GASČ for PID.

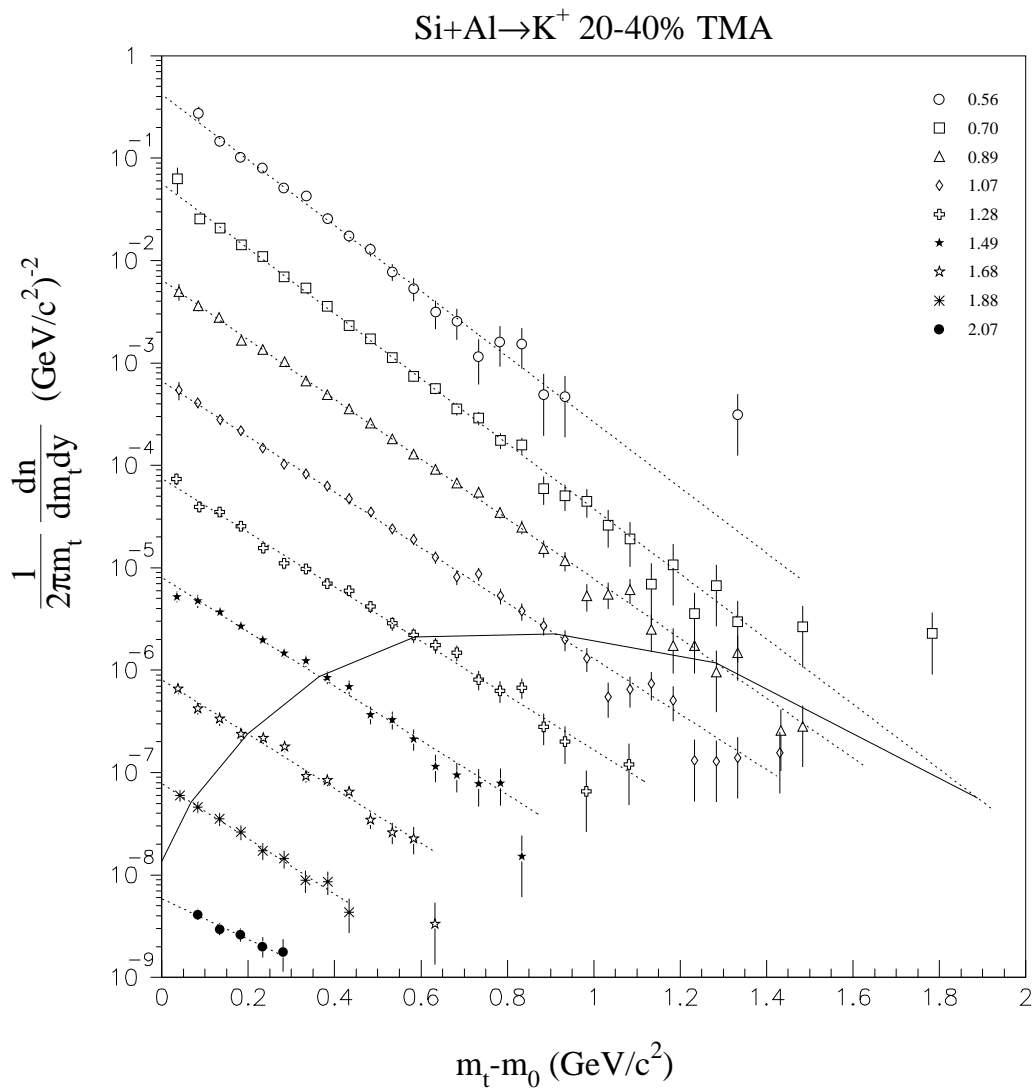


Figure A-7: Si+Al 20–40% TMA K⁺ m_{\perp} Distributions. Data are plotted for slices in rapidity 0.2 units wide. Each slice after the topmost has been divided by successive factors of 10. Data to the right of the solid line in each slice requires GASČ for PID.

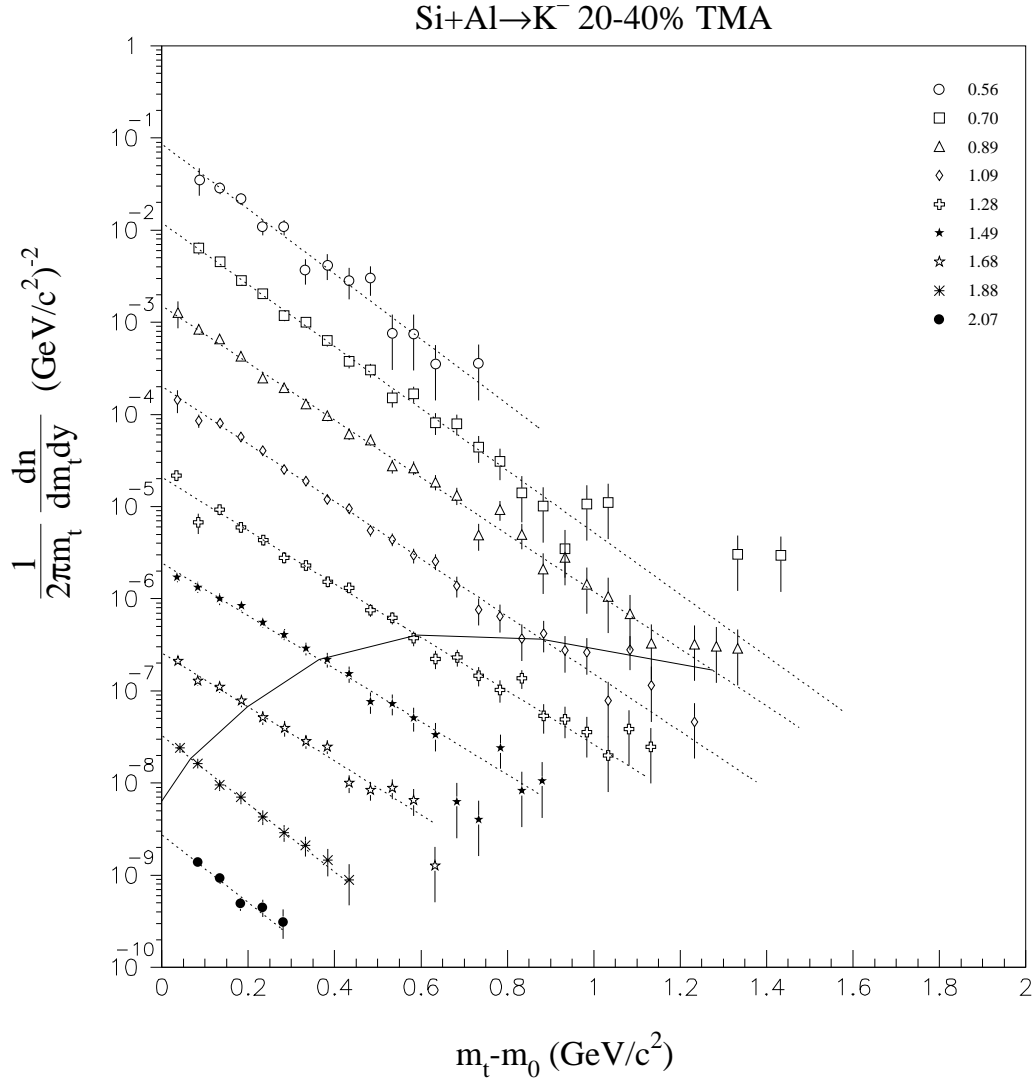


Figure A-8: Si+Al 20–40% TMA K $^-$ m_{\perp} Distributions. Data are plotted for slices in rapidity 0.2 units wide. Each slice after the topmost has been divided by successive factors of 10. Data to the right of the solid line in each slice requires GASČ for PID.

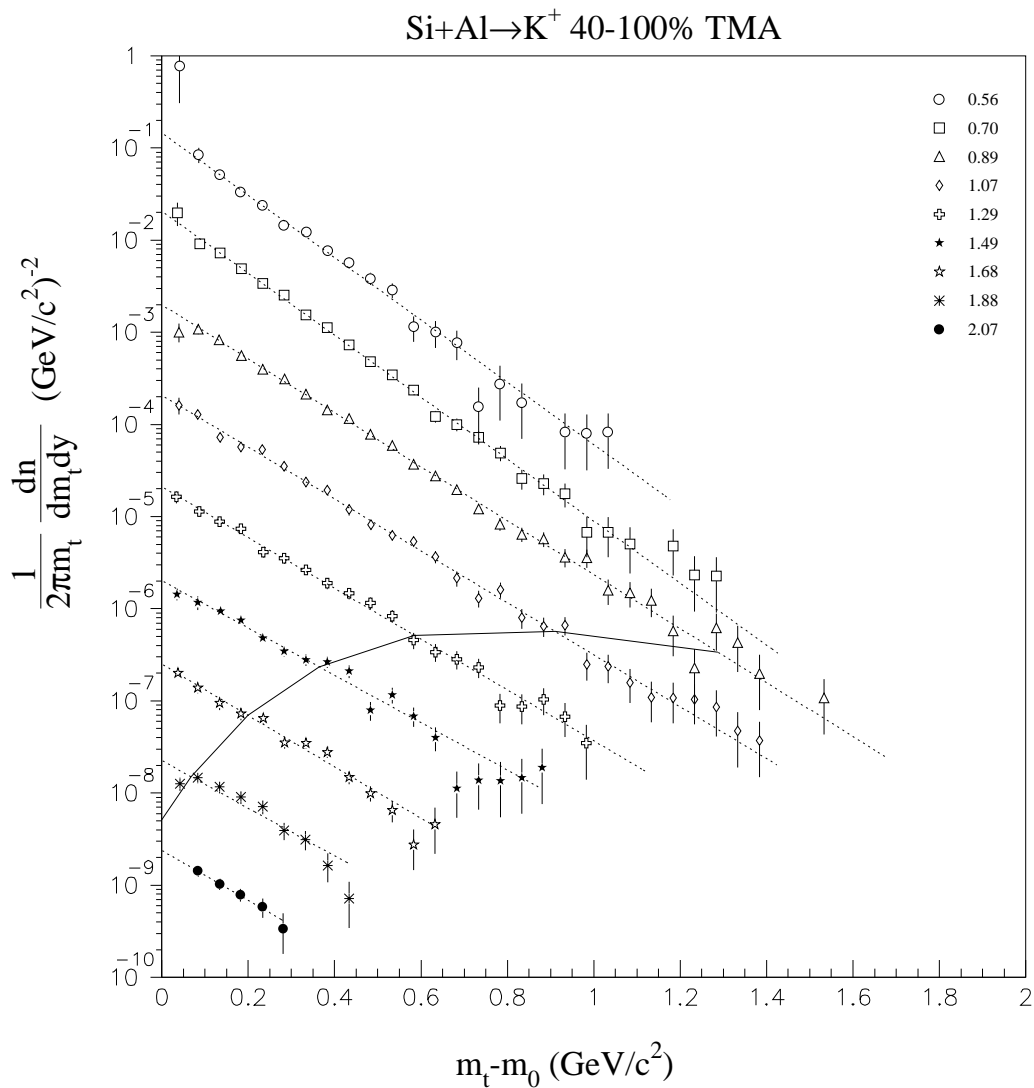


Figure A-9: Si+Al 40–100% TMA K⁺ m_{\perp} Distributions. Data are plotted for slices in rapidity 0.2 units wide. Each slice after the topmost has been divided by successive factors of 10. Data to the right of the solid line in each slice requires GASČ for PID.

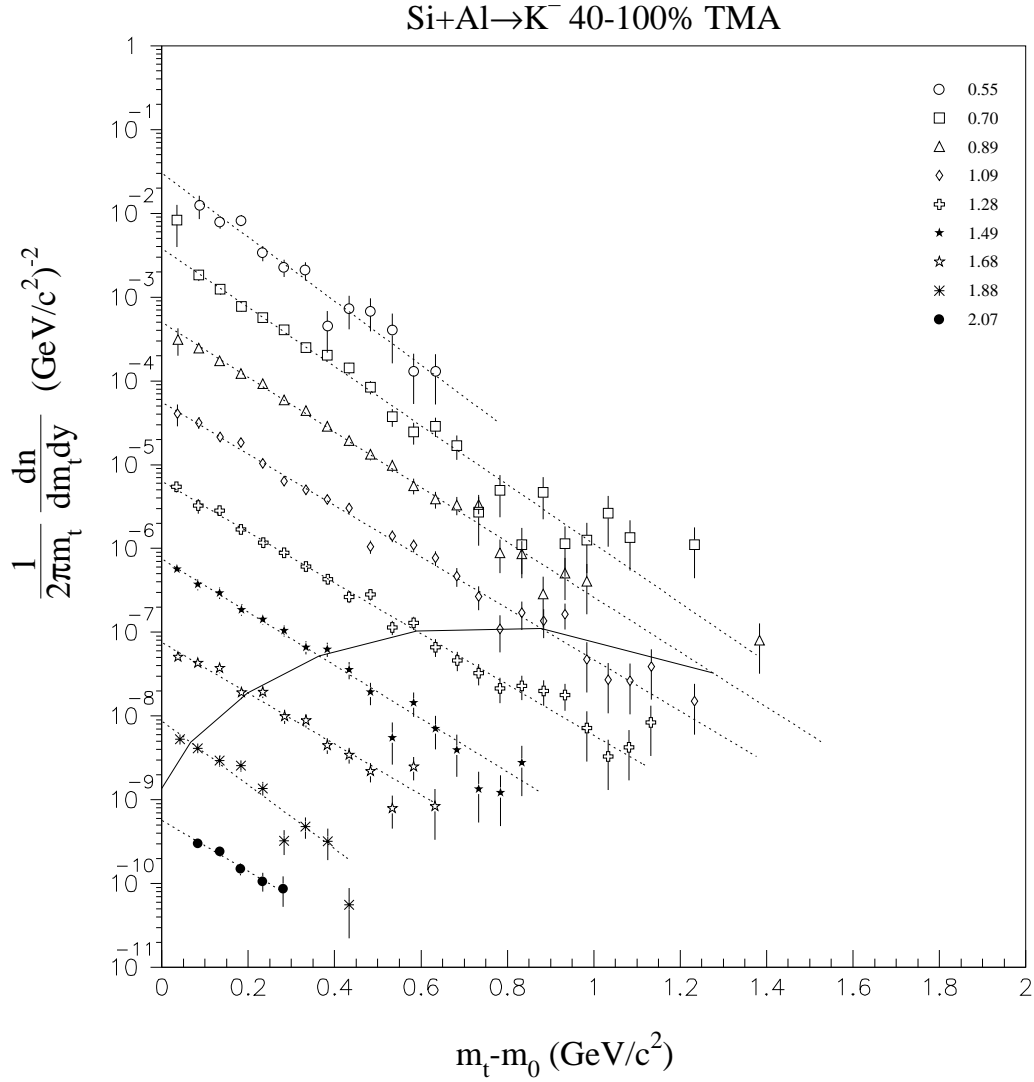


Figure A-10: Si+Al 40-100% TMA K⁻ m_{\perp} Distributions. Data are plotted for slices in rapidity 0.2 units wide. Each slice after the topmost has been divided by successive factors of 10. Data to the right of the solid line in each slice requires GASČ for PID.

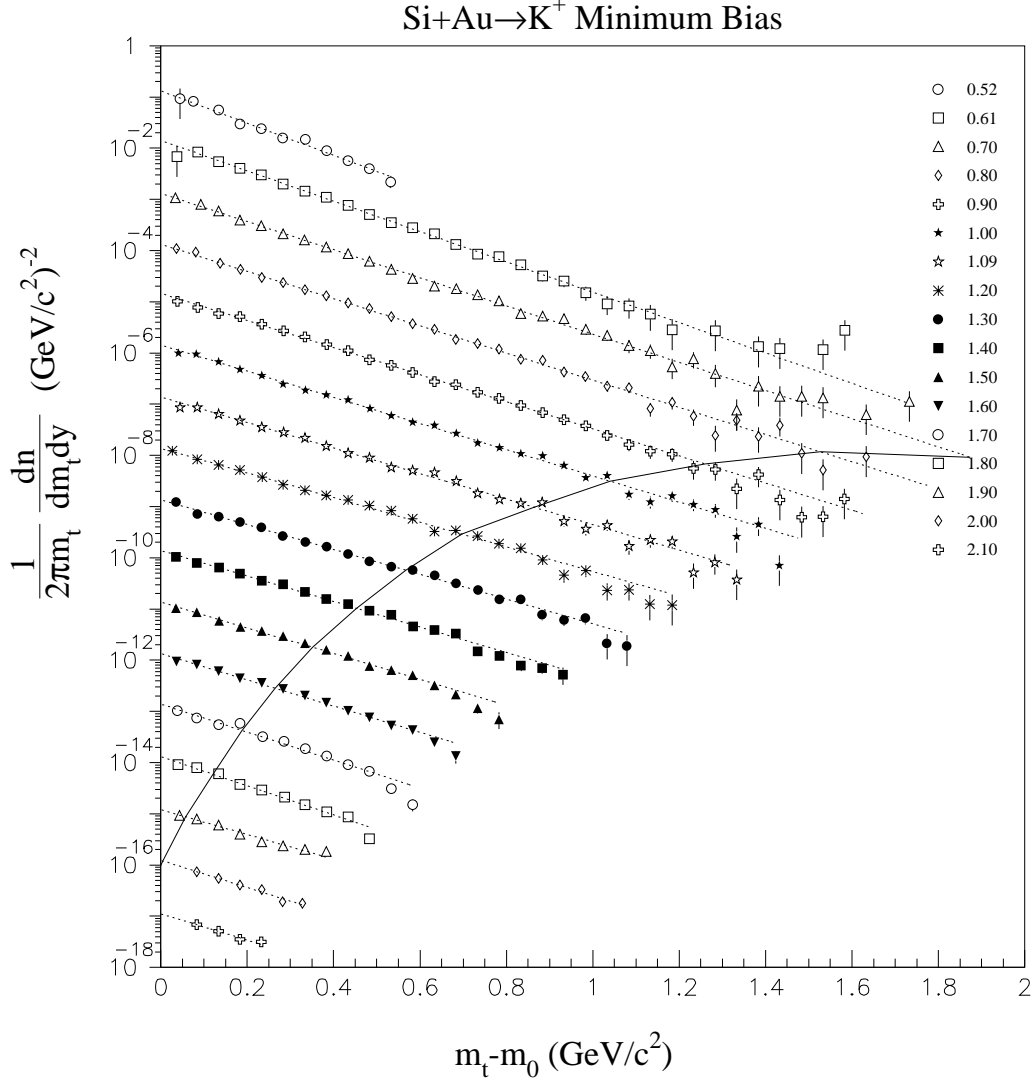


Figure A-11: Si+Au Inelastic K⁺ m_{\perp} Distributions. Data are plotted for slices in rapidity 0.1 units wide. Each slice after the topmost has been divided by successive factors of 10. Data to the right of the solid line in each slice requires GASČ for PID.

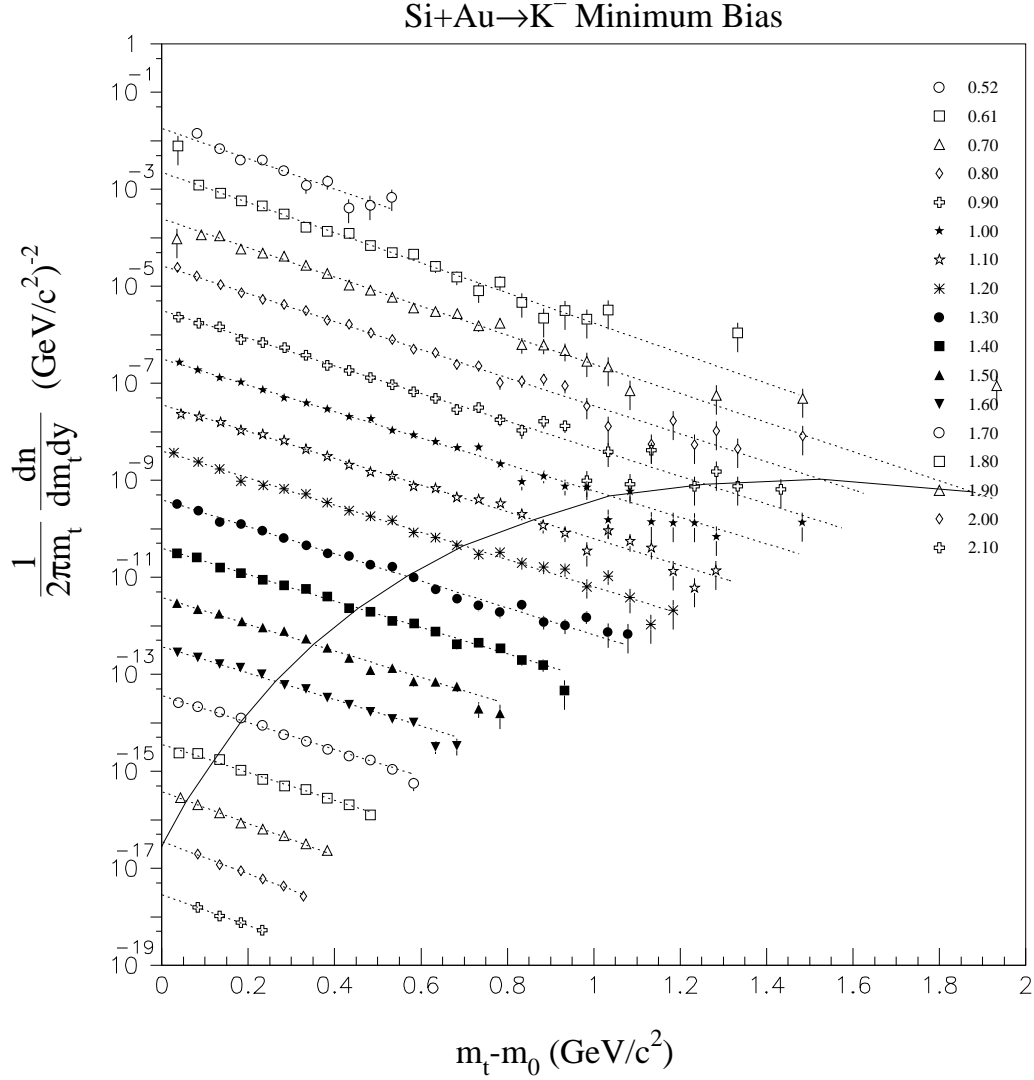


Figure A-12: Si+Au Inelastic K⁻ m_{\perp} Distributions. Data are plotted for slices in rapidity 0.1 units wide. Each slice after the topmost has been divided by successive factors of 10. Data to the right of the solid line in each slice requires GASČ for PID.

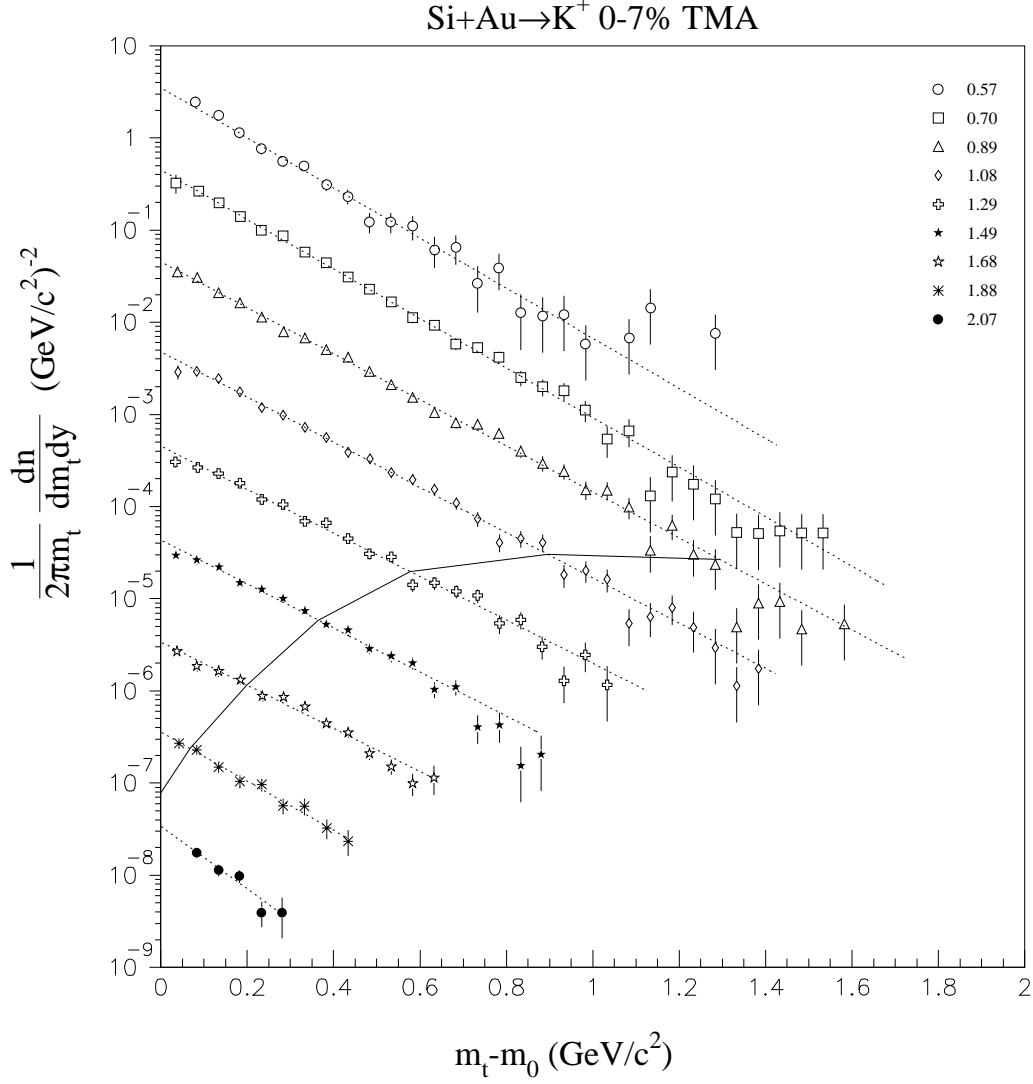


Figure A-13: Si+Au 0–7% TMA K⁺ m_{\perp} Distributions. Data are plotted for slices in rapidity 0.2 units wide. Each slice after the topmost has been divided by successive factors of 10. Data to the right of the solid line in each slice requires GASČ for PID.

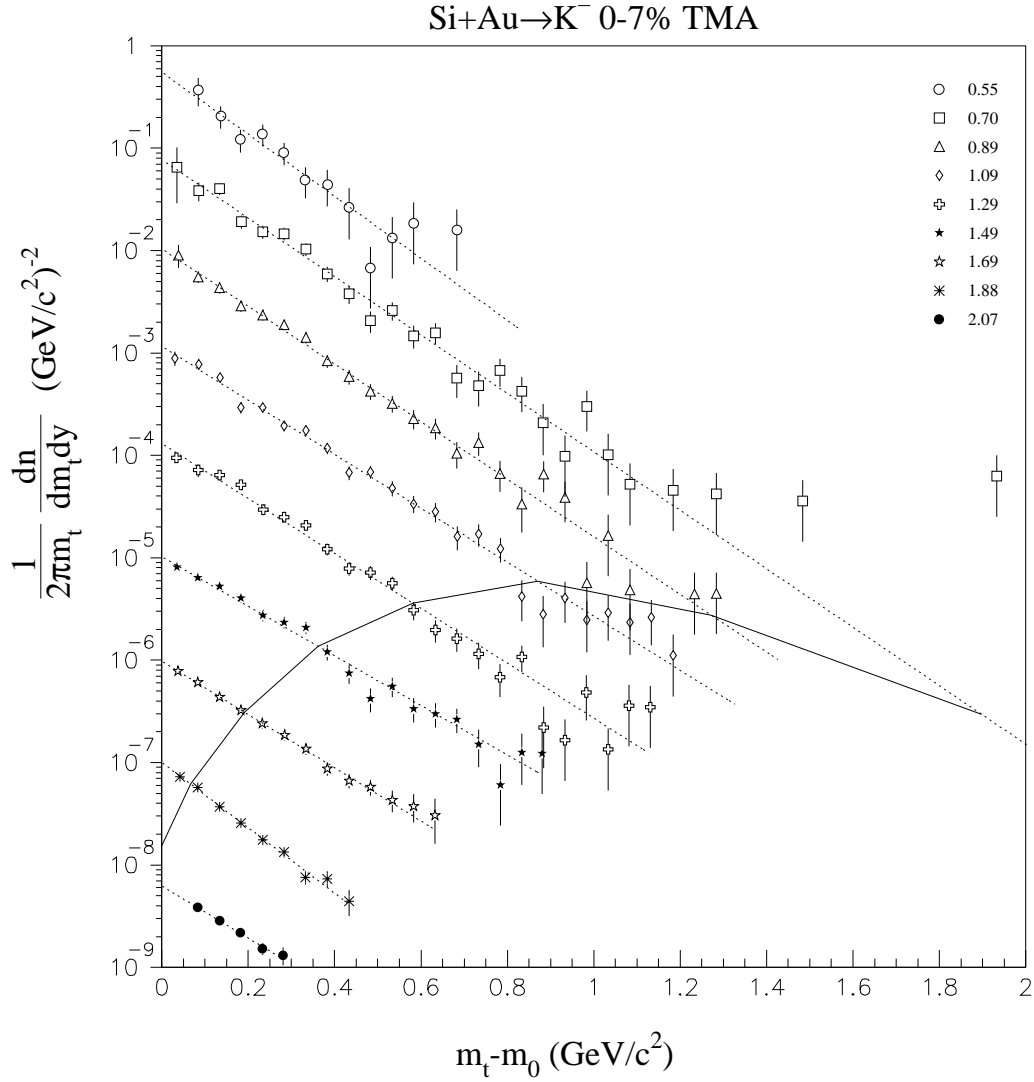


Figure A-14: Si+Au 0–7% TMA K⁻ m_{\perp} Distributions. Data are plotted for slices in rapidity 0.2 units wide. Each slice after the topmost has been divided by successive factors of 10. Data to the right of the solid line in each slice requires GASČ for PID.

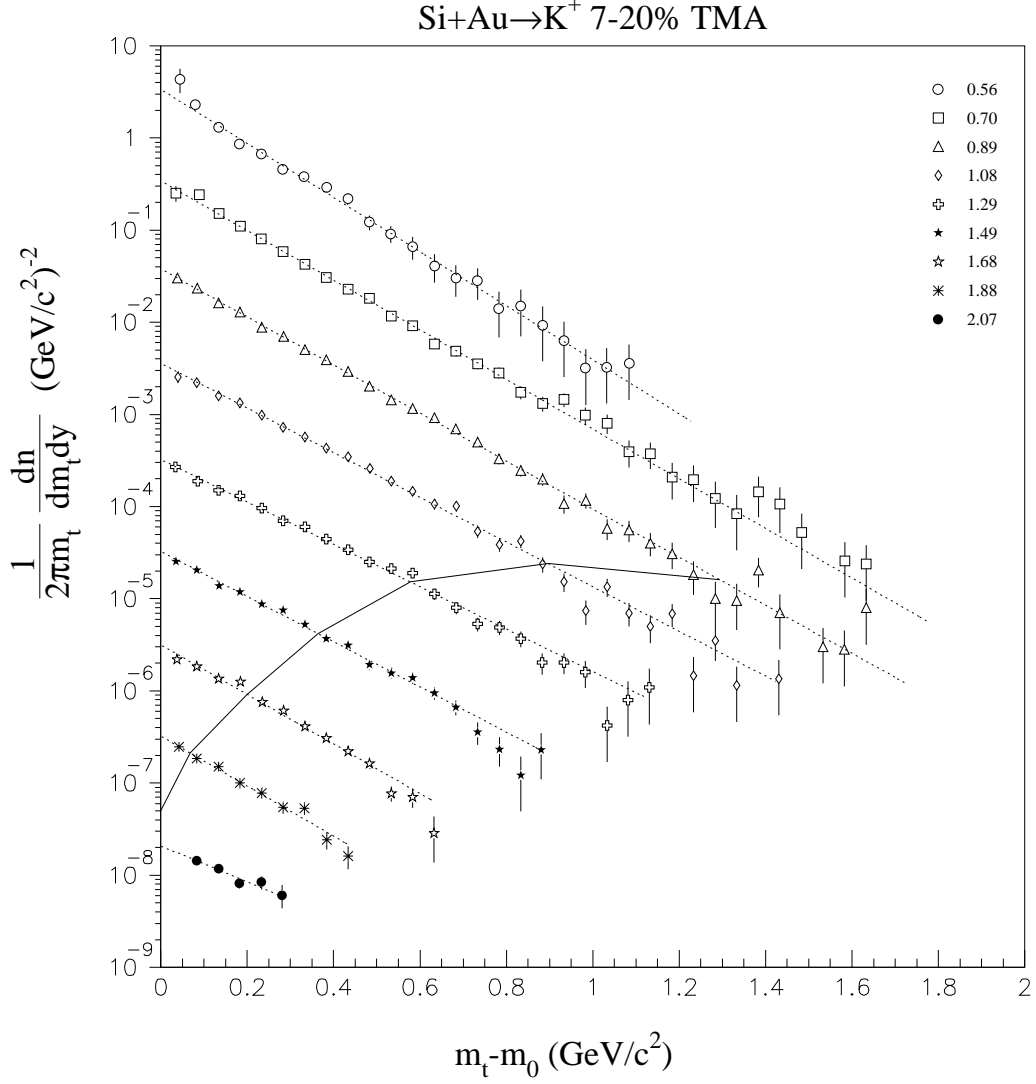


Figure A-15: Si+Au 7–20% TMA K⁺ m_{\perp} Distributions. Data are plotted for slices in rapidity 0.2 units wide. Each slice after the topmost has been divided by successive factors of 10. Data to the right of the solid line in each slice requires GASČ for PID.

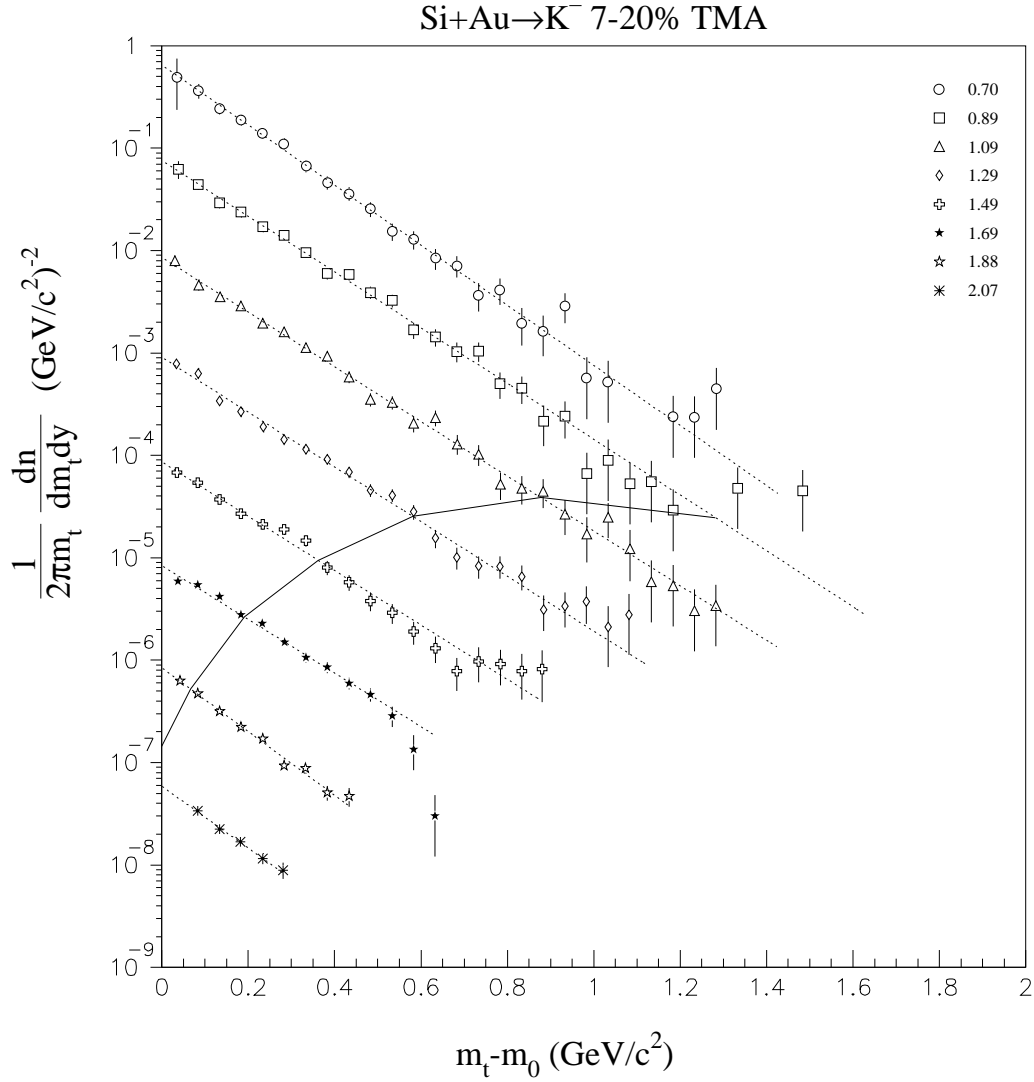


Figure A-16: Si+Au 7–20% TMA K⁻ m_{\perp} Distributions. Data are plotted for slices in rapidity 0.2 units wide. Each slice after the topmost has been divided by successive factors of 10. Data to the right of the solid line in each slice requires GASČ for PID.

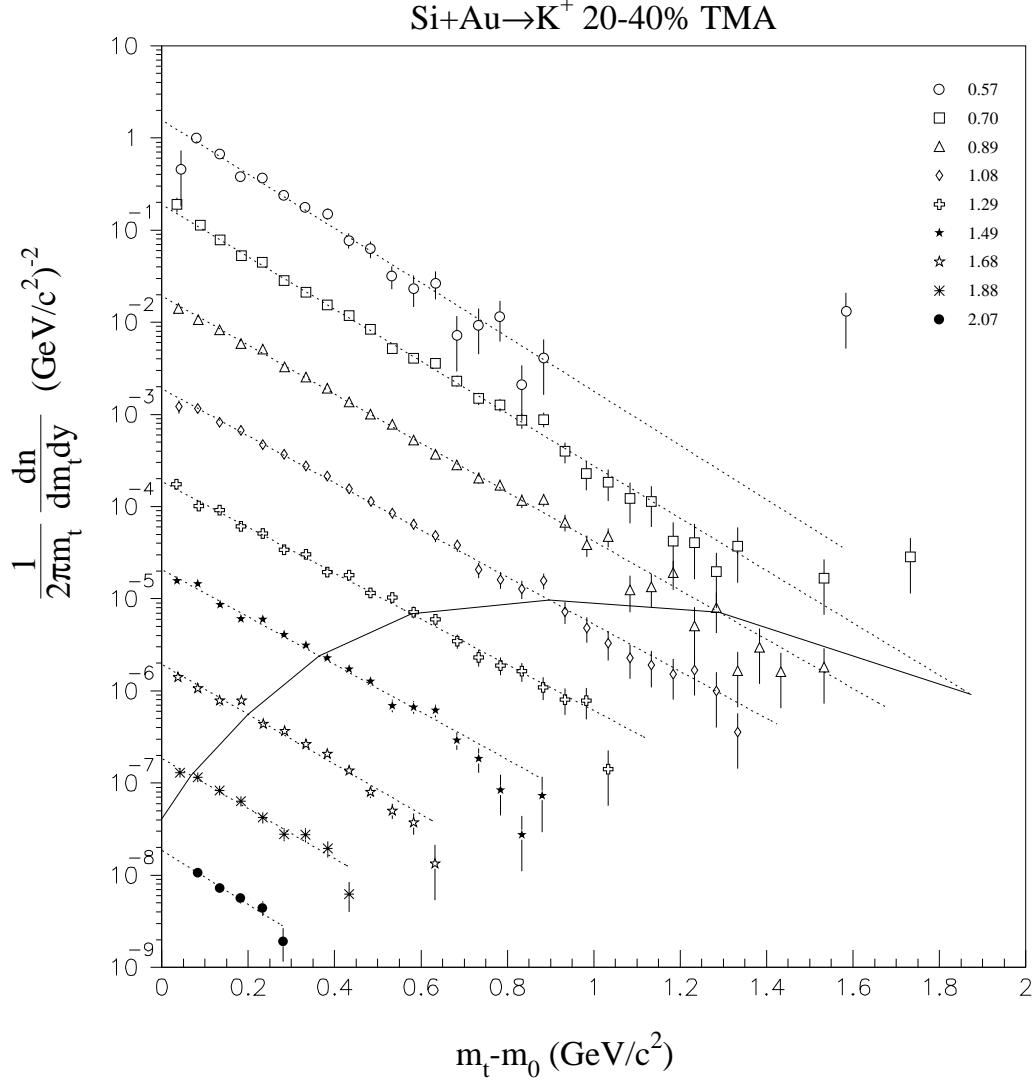


Figure A-17: Si+Au 20–40% TMA K⁺ m_{\perp} Distributions. Data are plotted for slices in rapidity 0.2 units wide. Each slice after the topmost has been divided by successive factors of 10. Data to the right of the solid line in each slice requires GASČ for PID.

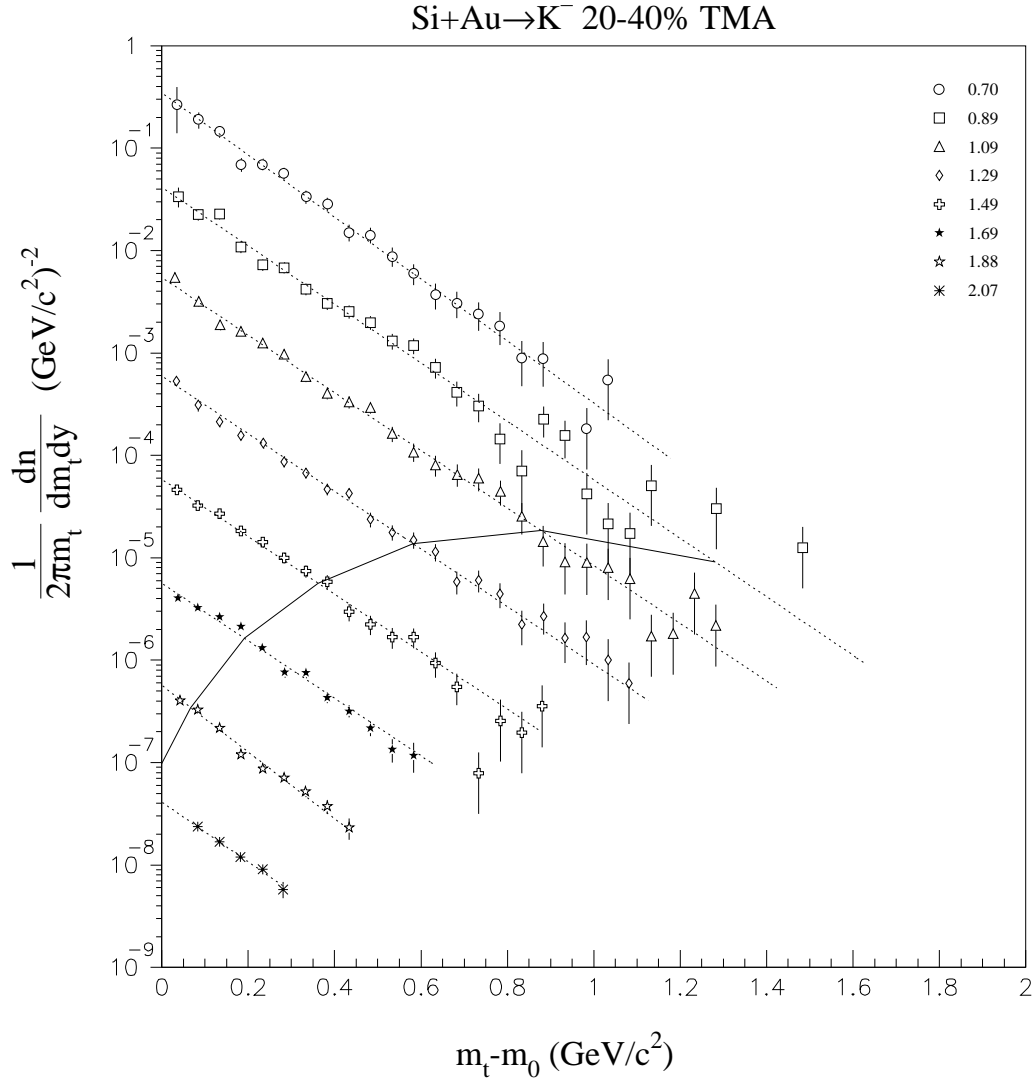


Figure A-18: Si+Au 20–40% TMA K⁻ m_{\perp} Distributions. Data are plotted for slices in rapidity 0.2 units wide. Each slice after the topmost has been divided by successive factors of 10. Data to the right of the solid line in each slice requires GASČ for PID.

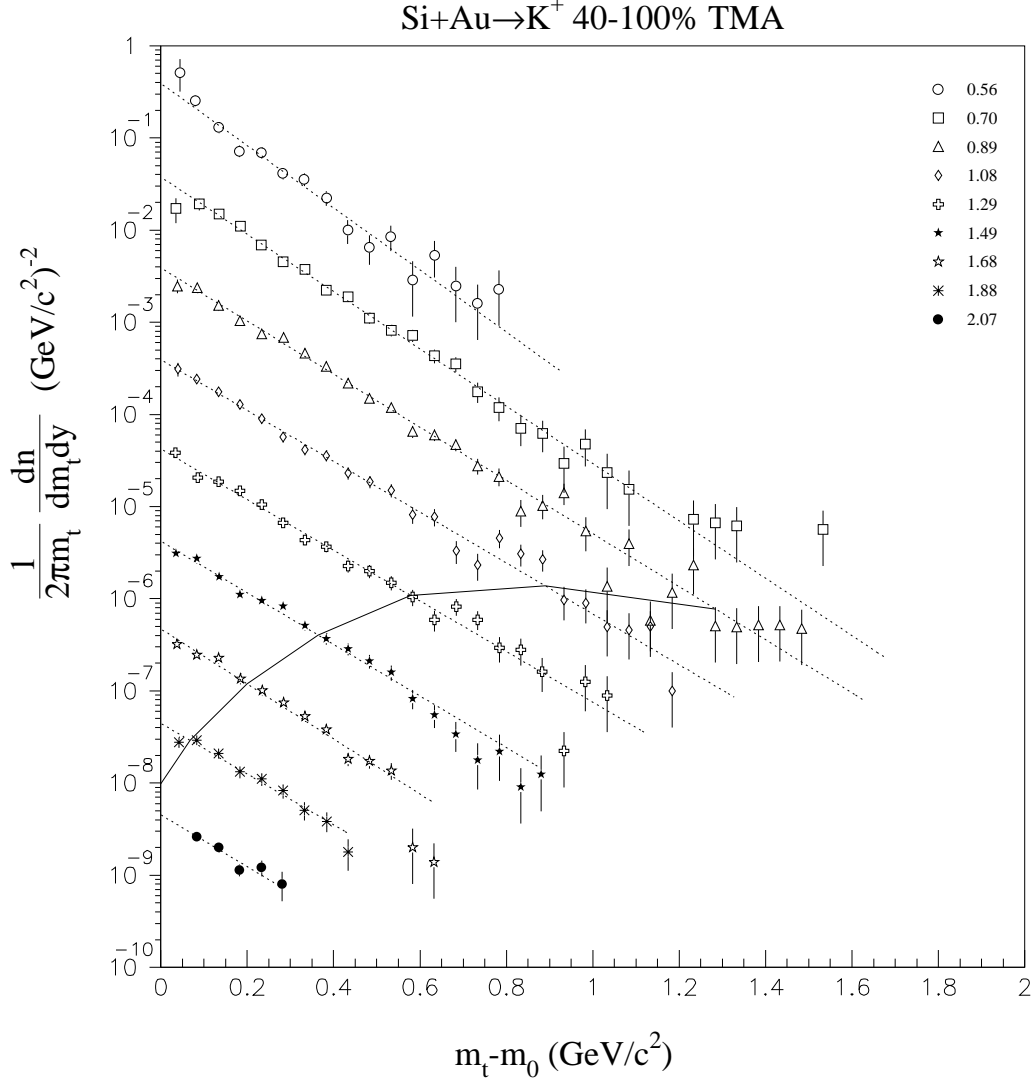


Figure A-19: Si+Au 40–100% TMA K^+ m_{\perp} Distributions. Data are plotted for slices in rapidity 0.2 units wide. Each slice after the topmost has been divided by successive factors of 10. Data to the right of the solid line in each slice requires GASČ for PID.

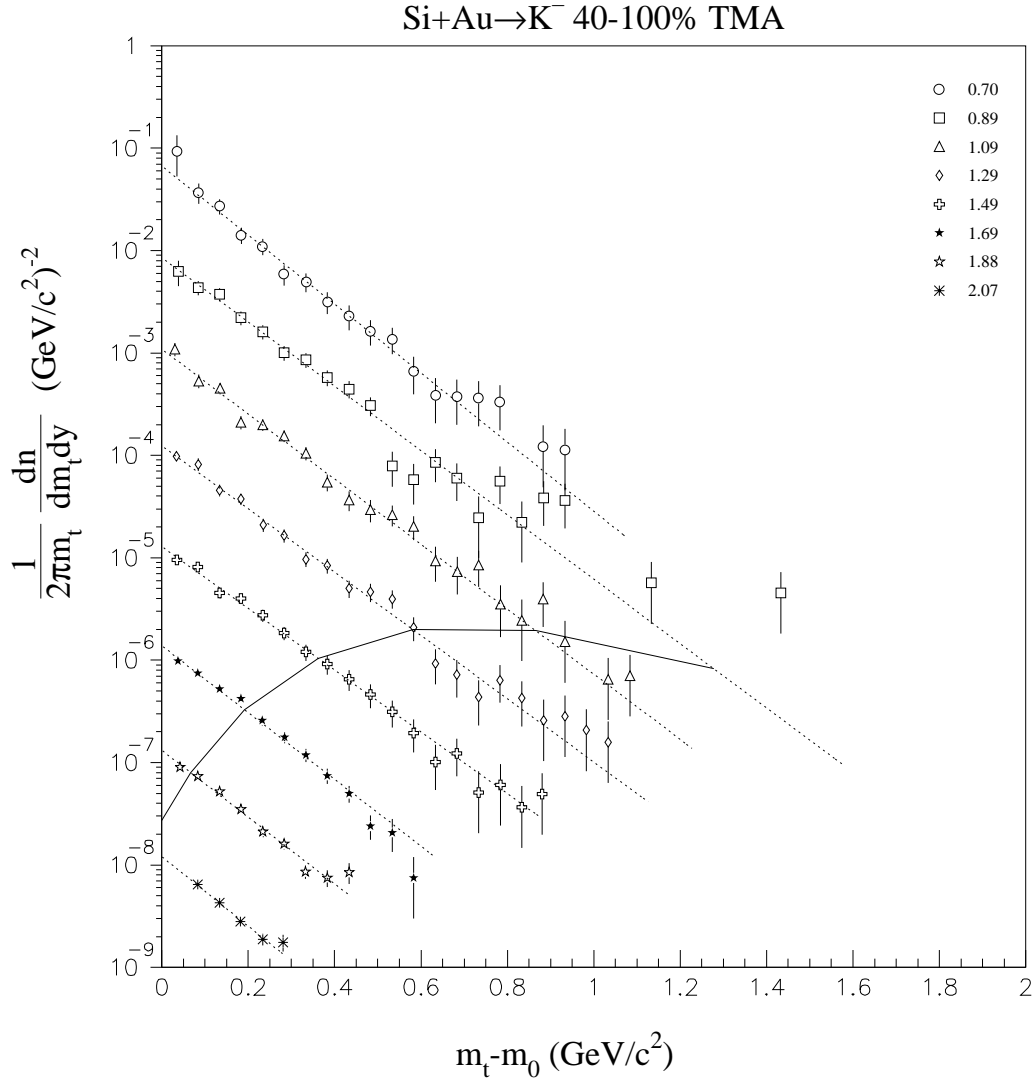


Figure A-20: Si+Au 40-100% TMA K⁻ m_{\perp} Distributions. Data are plotted for slices in rapidity 0.2 units wide. Each slice after the topmost has been divided by successive factors of 10. Data to the right of the solid line in each slice requires GASČ for PID.

APPENDIX A. KAON M_{\perp} DISTRIBUTIONS

Appendix B

E802 Si+A Reference

For convenient reference, the E802 published dn/dy 's as a function of rapidity for pions, kaons and protons for central and peripheral Si+Al, Si+Cu and Si+Au events are presented here. The definition of central and peripheral for this data is based on cuts on the ZCAL forward energy distribution, and is not exactly the same as the definition used in the results presented in Chapter 5. This makes the largest difference in the peripheral cuts, but is not a significant effect for the central data. Both of these figures are taken unchanged from the E802 survey paper [A⁺94].

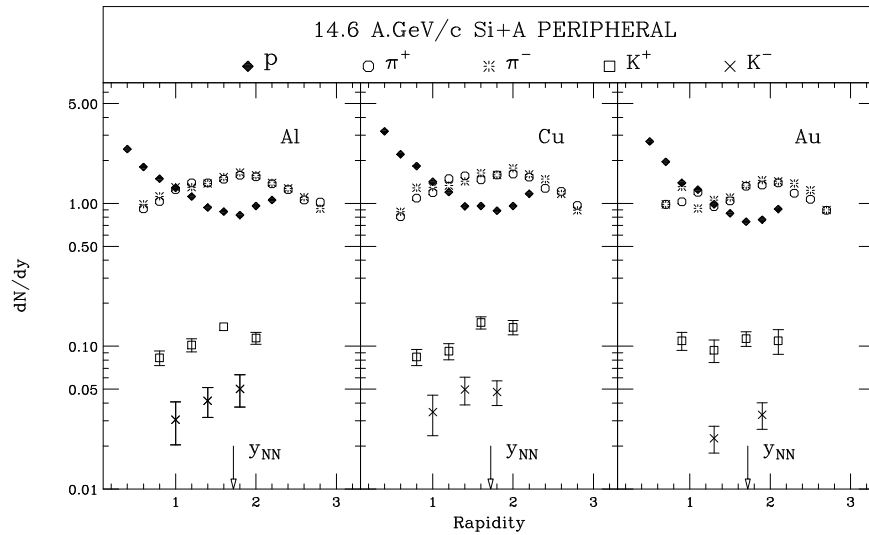


Figure B-1: E802 Peripheral Si+A dn/dy .

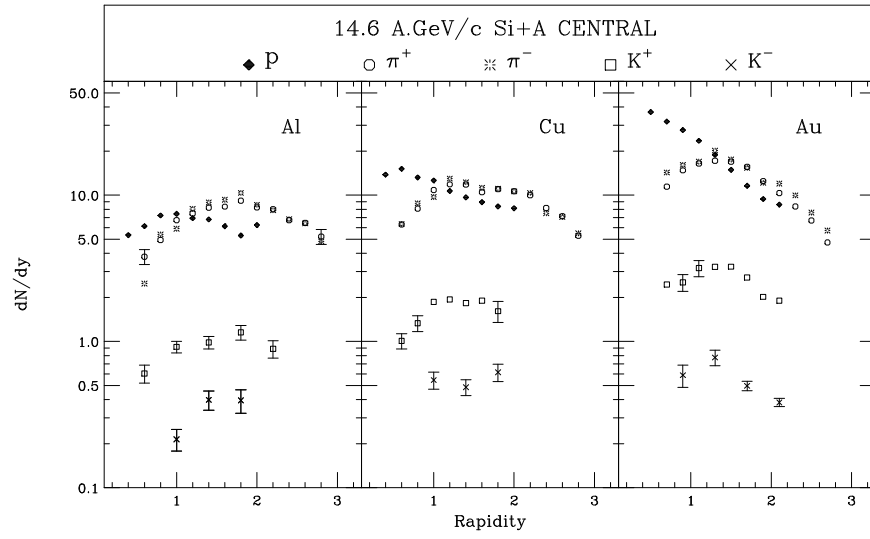


Figure B-2: E802 Central Si+A dn/dy .

Appendix C

LVL2 Trigger Details

In Chapter 3.5, the hardware of the LVL2 trigger was described. However, the LVL2 trigger is also heavily dependent on a large body of software in order to function properly. This appendix will describe the software associated with the LVL2 trigger.

C.1 Calibrations

The proper operation of the LVL2 trigger is dependent on several calibrations. One of these is the determination of allowed straight line tracks behind the magnet. This affects how well the track finding part of the trigger works. The other is the determination of the various constants in the FERET's. This affects how well the particle identification part of the trigger works.

Finding the allowed set of tracks is accomplished using a simple Monte-Carlo simulation of the experiment written by Ju Kang of the University of California, Riverside.

The determination of the FERET calibrations is quite a bit more involved, and was written by Ole Vossnack and Hiroyoshi Sakurai. There are two parts to the procedure: an initial calibration which is done once or twice per running period and requires several runs' worth of data, and a simpler calibration which is done after each run.

The initial calibration of the FERET timing constants is done offline with data taken during 6-10 runs.

One expects there to be drifts in the timing calibration of the FERET's due to effects such as temperature fluctuations. It is important to keep the calibrations current with these drifts, as the

LVL2 trigger depends on them in order to work properly.

C.2 Taking Data Using the LVL2 Trigger

In addition to the the usual setting of scaledowns and trigger bits which must be done for any type of data taking, there are several things which must be done specifically to prepare for taking data with the LVL2 trigger. For example, CAMAC modules need to be initialized, lookup tables need to be downloaded to the MLU's, values need to be sent to the FERA's so that they can perform pedestal subtraction, the PCOS III system need to be readied and the the whole trigger needs to be put in a mode in which it is controlled by the trigger supervisor rather than BNL859. It adds up to quite a list of things that need to be taken care of before the trigger can be used. Of course, these initializations have been automated, but there are complications. The LVL2 trigger can be configured only from the VAX node BNL859 since the CAMAC interface to the LVL2 trigger resides there. However, the normal run initialization is performed from the node BNL802, a different computer with which the operator interacts directly via the operator console. Next, I will describe what is done to get the LVL2 trigger ready for data taking, and how those actions are handled remotely from the main data acquisition computer.

Normally, to start a run, one uses the DCL command procedure, BEGIN.COM. This was not changed when the LVL2 trigger was added. Instead, several LVL2 specific hooks have been added to that command procedure, each of which invokes a different command procedure to handle each of the several initialization tasks. Table C.1 lists those commands procedures and the task for which each is primarily responsible.

Function	Procedure
Configuration selection	LVL2.REMOTE_1
Begin run synchronization	LVL2.REMOTE_2
Configuration recording	LVL2.REMOTE_3
LVL2 verification	LVL2.REMOTE_4

Table C.1: LVL2 initialization procedures

During configuration selection, the user is presented with an ASCII menu of available LVL2

C.2. TAKING DATA USING THE LVL2 TRIGGER

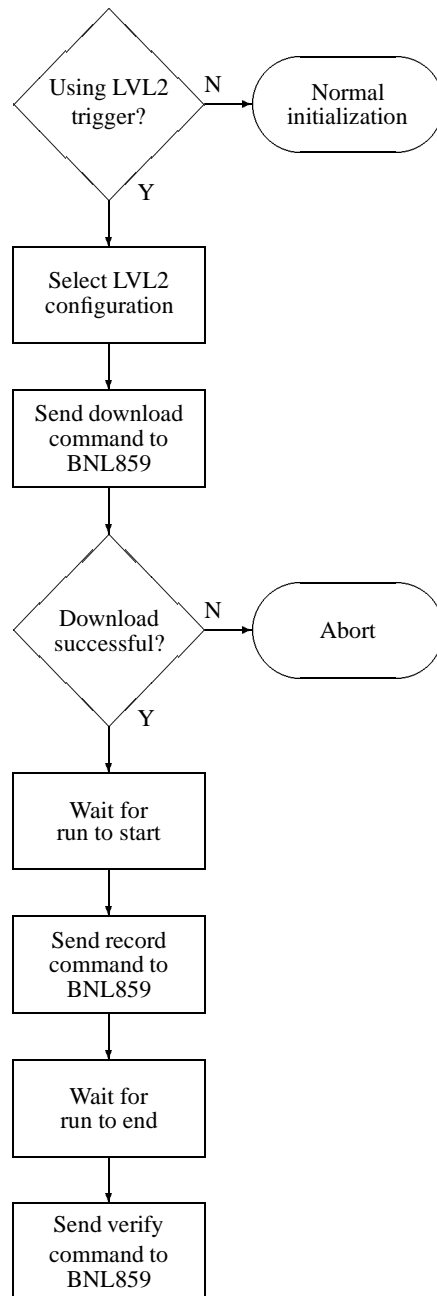


Figure C-1: Flowchart of trigger initialization of LVL2 trigger for data taking

trigger configurations. This menu shows only a handful of the dozens of configurations that are actually stored in the LVL2 database. The selection list is stored directly in the command file LVL2_REMOTE_1, and is edited by an expert as necessary to reflect the upcoming plans for the trigger. One nice feature is that the name of the configuration that is displayed need not be the same as the nearly indecipherable string used internally by the LVL2 database to refer very specifically to a particular configuration. Instead, a short descriptive name may be used. For example, the menu might show “4 kG K^+ / K^- trigger” instead of “B4025050N8801201N025NEGBBT1T2”.¹

When the user tells BEGIN.COM that the LVL2 trigger is going to be used for the upcoming run, a remote task is started on BNL859 which communicates with BEGIN.COM over a DECNET connection. Remote tasks are procedures initiated on a local machine which actually execute on a different machine. It was by using these that the difficulty in having the LVL2 trigger connected only to BNL859 was handled. The thing which is actually started as a remote task on BNL859 is the DCL command procedure LVL2.COM. Once the remote task has been started, it remains running during the entire run. It reads commands sent from BNL802, invokes INTER as needed to interact with the LVL2 trigger and database, and sends back to BNL802 the status of each action it carries out.

C.3 Software Control of the LVL2 Trigger

As shown in the previous section, the LVL2 trigger is made up of many pieces, most of which are software controllable and configurable. While this allows for a great deal of flexibility in running the trigger, it also make for quite a headache, too.

The LVL2 Database

Once the LVL2 trigger has been properly wired together, its functioning is wholly determined by the contents of its lookup tables. The contents of a complete set of trigger lookup tables is said to constitute a *configuration* of the trigger. Therefore it is essential to record accurately which configuration was used for each run during data collection. The contents of these tables have the final say on what the trigger was set up to do during a given run, regardless of what may or may not have

¹Actual name of LVL2 configuration used for run 10766.

C.3. SOFTWARE CONTROL OF THE LVL2 TRIGGER

been recorded in the log book. Since the trigger was a new addition to the experiment, procedures for recording the configuration of the trigger were not well worked out and as a consequence, the hand-recording of the state of the trigger varied considerably.

In addition to recording the configuration of the trigger, these tables need to be retrievable offline so that studies of the LVL2 trigger performance may be made (Section 4.6).

To satisfy this requirement, I designed and implemented a database for storing constants for the trigger. An overview of the functioning of the database in one of its incarnations is given in E859 Internal Memo 2 [Mor91]. The database had to meet several criteria. It had to be relatively small, robust and quick.

An early decision was made not to use the VAX/VMS native RdB database, because it was felt that it was too slow to be used online. It was also felt that as more and more offline analysis moved from the VAX/VMS systems and onto UNIX systems, it would be a good idea to have a database that was portable. At the same time, Brian Cole had written a subroutine library of database utilities based on ZEBRA, proving that a simple, flat database could be written in a reasonable amount of time. For these reasons, it was decided that the LVL2 database would be based on ZEBRA.

INTER

Manipulation of the LVL2 trigger is accomplished through a program named INTER, which is an interactive, command line program based on the KUIP user interface package from CERN. INTER provides an environment in which one may generate new MLU tables, build new configurations for the trigger, download them to the CAMAC hardware, run tests on the trigger, and record entries in the LVL2 database. In addition, all of the functionality of PAW is available inside INTER, so one may also create histograms and display them from the command line. It was thought that this would aid in developing tables for the trigger.

APPENDIX C. LVL2 TRIGGER DETAILS

Appendix D

Spectrometer Acceptance Details

Determining the geometrical acceptance of the spectrometer is essential for calculating cross sections. It is convenient to have an analytic approximation to this acceptance, both because it makes the acceptance calculation quite fast, and because it makes it a little easier to see how the acceptance is determined by the geometry of the spectrometer. Charles Parsons put a lot of work into devising such an analytic method for describing the spectrometer acceptance, and he came up with a reasonable way of describing the acceptance with a few parameters that were closely related to the geometry of the spectrometer [Par92]. However, the final values of those parameters were always adjusted by hand. I have extended some of his work so that this final tweaking is no longer necessary—the parameters describing the acceptance are determined directly from the YBOS geometry constants.

A track in the spectrometer is completely described by the following five parameters:

- p —the track momentum
- ϑ, ϕ —the angles of the initial track direction
- x_0, y_0 —the track origin ($z = 0$ is assumed)

These five parameters can be thought of as the coordinates of a point in a 5-dimensional space. Checking if a track is in the acceptance is then equivalent to determining if this point lies inside some prescribed 5-dimensional region—all points inside the region represent tracks inside the acceptance, all points outside the region represent tracks outside the acceptance. The width of the x_0 and y_0 distributions for a single run are fairly narrow (typically 1-2 mm), so we will treat the x_0 and y_0

APPENDIX D. SPECTROMETER ACCEPTANCE DETAILS

dependence in an average way and not track-by-track. First determine the average value of x_0 and y_0 for a run (or a block of runs, if the values remain relatively constant), then determine the acceptance for that run as though all tracks came exactly from (x_0, y_0) . That leaves just 3 other coordinates to check.

The checking of p , ϑ and ϕ is done in two stages. First, the projection of the track onto the xz -plane is checked to make sure that the track remains within the horizontal confines of the spectrometer. Then, the projection of the track onto the yz -plane is checked to see if the track leaves the acceptance through the top or bottom of the spectrometer. This might seem like a bit of an oversimplification, but because the aperture of the spectrometer is rectangular, the problem can actually be treated this way fairly well.

First consider tracks restricted to $\phi = 0$ only—that is, those tracks that move only in the xz -plane. For tracks inside the spectrometer acceptance, plot ϑ versus $\alpha = qB dl/p$ (α is the angle of the bend that the track makes in the magnet); you'll get a region like that shown in Figure D-1.

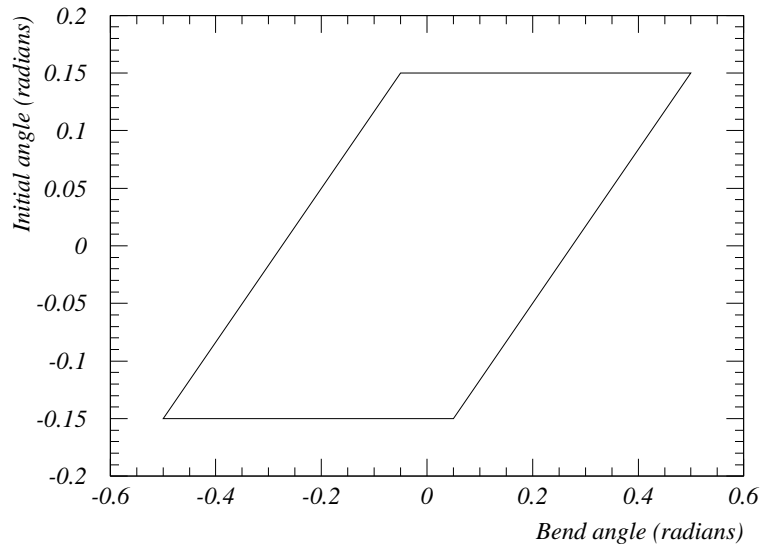


Figure D-1: ϑ versus $qB dl/p$ for good tracks

If you imagine a track that just skims inside the beam side edge of T1 (or T2—they both bound

the acceptance at about the same place), that track will lie along the lower horizontal edge of the polygon. It will hit the same edge of T1, independent of momentum over a quite a wide range of momentum. This is easy to see if you picture the track pinned against the edge of T1—as you vary the momentum, the part of the track after the magnet whips around, but as long as it continues to pass through T3 and T4 it will be inside the acceptance. The same picture holds for the upper horizontal edge of the acceptance. Here, the non-beam side of T1 (or T2) bounds the acceptance, independent of momentum.

So, start with a track, whose sign causes it to bend back toward the beam, and whose (ϑ, α) coordinates place it along the lower edge of the acceptance boundary. If you lower the momentum, at some point it'll careen into TR1. Now there is a relation between the initial direction of the track in the xz -plane and the bend angle in the magnet that will keep the track skimming along the inside edge of TR1. You can increase the initial angle of the track, so that it points farther away from the beam pipe, if you also increase the bend angle in the magnet. This relation determines the rightmost diagonal edge of the acceptance.

Once the initial angle gets large enough, the track will crash into the non-beam side of T1. This is the upper horizontal part of the acceptance. Now you're free to raise the momentum (and change the sign of the track) until the part of the track behind the magnet bumps into the non-beam side of T3 (or T4). Again, a relation between the initial angle and the bend angle holds, and this determines the leftmost diagonal edge of the acceptance. Decreasing the initial angle brings us counterclockwise round the acceptance to where we began.

Since the beam and non-beam edges of the acceptance are due to the vertical edges of the chambers, the above discussion for tracks in the plane holds for tracks out of the plane, as long as we only consider the projection of the track into the xz -plane. This remains true as long as the track doesn't have a ϕ so large that it hits the top of the chambers. That condition will be checked for separately.

My contribution to the problem of calculating the acceptance is code which automatically determines the acceptance polygon using standard geometry files as input. Figure D-2 shows the quantities necessary to calculate the spectrometer acceptance. The horizontal axis in the diagram represents the mid-line of the spectrometer, and the heavy line is the trajectory of a particle, with ϑ the initial angle the particle's path makes with respect to the spectrometer axis. We can represent the

APPENDIX D. SPECTROMETER ACCEPTANCE DETAILS

bending of the trajectory in the magnet as a kink at the midpoint of the magnet. This is equivalent to the overall effect on the particle's trajectory that the actual magnet has, with the exception of vertical focussing. The trajectory is supposed to just hit the side of one of the chambers (or TOF wall) behind the magnet, and so this trajectory lies along one edge of the acceptance.

What we're looking for is the relationship between α and ϑ that puts a track right at the edge of the acceptance. We can then draw curves (one for each edge of each detector) in α - ϑ space representing the locus of all points just hitting the edge of the detector. The region around the origin bounded by these lines represents the acceptance. For ease of calculation, it would be preferable if the curves we draw for each detector in this space were lines, so we will linearize the equations relating α to ϑ .

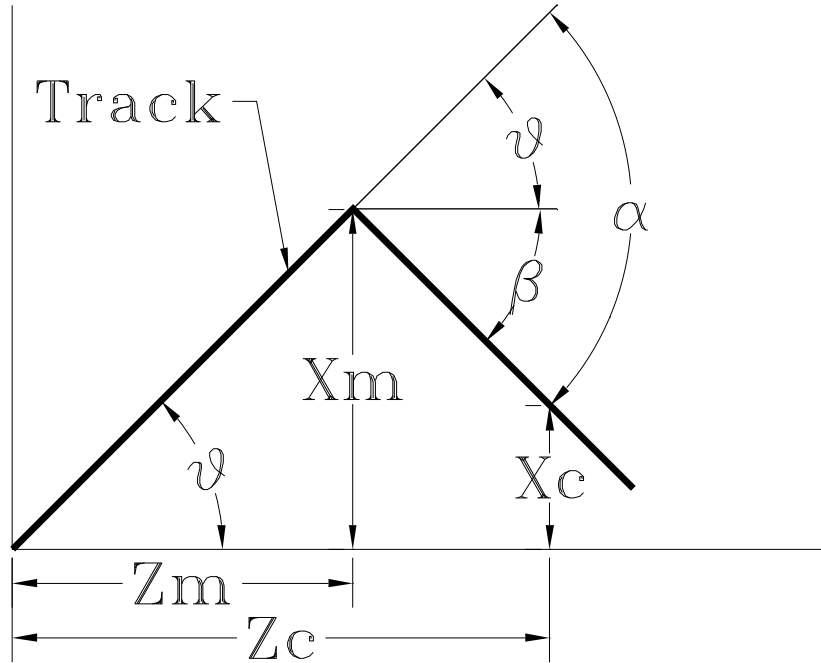


Figure D-2: Schematic of a track in the spectrometer

From Figure D-2 the following relationships can be drawn

$$\tan \vartheta = \frac{X_m}{Z_m} \quad (\text{D.1})$$

$$\tan \beta = \frac{X m - X c}{Z c - Z m} \quad (\text{D.2})$$

$$\beta = \alpha - \vartheta \quad (\text{D.3})$$

Equations D.2 and D.3 can be use to eliminate β , and the result can be combined with Equation D.1 to give

$$\tan(\alpha - \vartheta) = \frac{Z m \tan \vartheta - X c}{Z c - Z m} \quad (\text{D.4})$$

All of the current acceptance code requires ϑ as a function of α . However, since ϑ appears in the argument of the tangent on both sides of the Equation D.4, it is difficult to rearrange the equation to give $\vartheta = g(\alpha)$. Instead, we settle for obtaining $\alpha = f(\vartheta)$. Then this form will be linearized and inverted to obtain a approximation to $g(\alpha)$.

Equation D.4 can be rearranged to yield

$$\alpha = f(\vartheta) = \arctan \left(\frac{Z m \tan \vartheta - X c}{Z c - Z m} \right) + \vartheta \quad (\text{D.5})$$

which can then be expanded in a Taylor series around $\vartheta = \vartheta_0$. This is a useful place to use *Mathematica* or *Maple*.

$$\begin{aligned} \alpha &\approx f(\vartheta_0) + (\vartheta - \vartheta_0) f'(\vartheta)|_{\vartheta=\vartheta_0} \\ &= \arctan \left(\frac{Z m \tan \vartheta_0 - X c}{Z c - Z m} \right) + \vartheta_0 + 1 \\ &\quad + \frac{Z m (Z c - Z m)^2 \sec^2 \vartheta_0}{Z c - Z m - X c + Z m \tan^2 \vartheta_0} (\vartheta - \vartheta_0) \end{aligned} \quad (\text{D.6})$$

Here, ϑ_0 is some value for ϑ chosen through trial and error to minimize the average deviation between the true function and the series representation in the region of interest. This equation can be rearranged into a slightly more convenient form

$$\begin{aligned} \alpha &= 1 + \arctan \left(\frac{Z m \tan \vartheta_0 - X c}{Z c - Z m} \right) + \left\{ 1 - \frac{Z m (Z c - Z m)^2 \sec^2 \vartheta_0}{Z c - Z m - X c + Z m \tan^2 \vartheta_0} \right\} \vartheta_0 \\ &\quad + \frac{Z m (Z c - Z m)^2 \sec^2 \vartheta_0}{Z c - Z m - X c + Z m \tan^2 \vartheta_0} \vartheta \end{aligned} \quad (\text{D.7})$$

APPENDIX D. SPECTROMETER ACCEPTANCE DETAILS

and then inverted to give ϑ as a function of α

$$\begin{aligned} \vartheta = & \left[\alpha - 1 - \arctan \left(\frac{Zm \tan \vartheta_0 - Xc}{Zc - Zm} \right) - \left\{ 1 - \frac{Zm(Zc - Zm)^2 \sec^2 \vartheta_0}{Zc - Zm - Xc + Zm \tan^2 \vartheta_0} \right\} \vartheta_0 \right] \\ & \times \left[\frac{Zm(Zc - Zm)^2 \sec^2 \vartheta_0}{Zc - Zm - Xc + Zm \tan^2 \vartheta_0} \right]^{-1}. \end{aligned} \quad (\text{D.8})$$

Checking the acceptance in the vertical dimension is done by checking the y intersection of the track with a plane at $z = 1$ m. This plane is in front of the magnet, so the momentum plays no role in determining the location of the intersection. It is odd that the y location in front of the magnet suffices to determine whether a track remains inside the vertical confines of the spectrometer for the rest of its trajectory. For example, consider two tracks, both with the same (ϑ, ϕ) , but with different momenta; the lower momentum track will bend more in the magnet. While the slope along the trajectory, dy/ds for both tracks is unchanged by the magnet, because of the large change in direction of the low momentum track, its slope along the beam direction, dy/dz , will be much different after the magnet than the dy/dz of the high momentum track. It turns out that this is a small effect, and to a good approximation, the y acceptance is momentum independent. The maximum and minimum allowed values for the y height of the track are determined directly from data. For more details about how the ϕ range accessible to a particle is determined, see Dan Zachary's CSPAW memo [ZP92].

Appendix E

Time of Flight Wall Calibration

Having the time of flight properly calibrated is essential for identifying particles, and this is especially true for kaons. Because kaons are rare, any timing miscalibration that causes even a small percentage of the pions or protons to be misidentified as kaons can add up to a large effect on the kaon yields. This appendix discusses the procedure used to calibrate the TOF wall and shows an example of the diagnostics used during the particle identification pass, PASS3, to verify the quality of the calibrations.

E.1 Calibration Procedure

The time of flight for a particle hitting the TOF wall is calculated from several raw inputs. The BTOF beam counter scintillator and each of the TOF wall slats are instrumented with two phototubes for which a TDC and an ADC value are recorded. The TDC's record a channel count which is converted to a time using the *clock gain*, which is nominally 50 ps/channel, but is treated as a calibration parameter in the present procedure. The pedestal-subtracted ADC values represent the strength of the signal in the phototube, which is used to adjust the time calculated from the TDC's. This *slewing correction* is made because a large amplitude signal tends to exceed a given discriminator threshold sooner than a low amplitude one. The coefficient of the slewing correction is also a calibrated parameter. In addition, there is a timing offset between the beam counter and TOF wall TDC's that is meaningless and arises because of delays in signal propagation and DAQ overhead. This T0 is another calibration parameter. The calibrations were run in a separate pass over a subset of the

APPENDIX E. TIME OF FLIGHT WALL CALIBRATION

E859 data before the particle identification pass, PASS3, was run.

Rough calibrations for the TOF wall can be obtained by histogramming the TDC value multiplied by a nominal clock gain for each slat. The steep leading edge of the resulting distribution for each slat marks the arrival time of speed-of-light velocity particles. The standard calibration procedure used for the E802 analysis begins with a set of reconstructed tracks with short flight times, assumes that all the particles are pions, assigning the pion mass to each track. Using this mass hypothesis, all of the necessary parameters can be determined. This is the basic procedure that has been used throughout E802 [A⁺92a]. However, since the calibrations are based only on short flight times, the determination of longer flight times are necessarily based on extrapolations outside of the calibration domain. An improved procedure was developed for the E859 analysis, authored principally by Ole Vossnack. It is a procedure that is used to refine the calibrations, as it requires that fairly reasonable timing calibrations already exist. Instead of assuming that all fast particles are pions, the new procedure uses conservative mass and momentum cuts to select pions, kaons, protons and deuterons. The addition of these more massive particles greatly extends the range of flight times that are directly part of the calibration procedure. The procedure is also an improvement because it simultaneously fits all the parameters of the calibration, instead of determining them serially, resulting in a better overall calibration solution.

Given the raw inputs above and a trial set of calibration parameters, the difference, δTOF , between the expected time of flight for a particle, given its mass and momentum, and the measured time of flight may be calculated as

$$\delta\text{TOF} = \frac{L\sqrt{p^2 + m^2}}{cp} - (t_{\text{TOF}} - t_{\text{BTOF}} - t_0). \quad (\text{E.1})$$

A χ^2 statistic for the distribution of δTOF is minimized using MINUIT to vary the calibration parameters.

E.2 TOF Wall Intrinsic Timing Resolution

The timing calibrations were determined in an analysis pass over a selected subset of the whole data set. One of the most important numbers is the intrinsic timing resolution of the TOF wall, as this determines the maximum momentum up to which pions can be separated from kaons using time

E.3. MONITORING OF CALIBRATIONS DURING PASS3

of flight alone. Figure E-1 shows the calculated timing resolution for each of the slats in the TOF wall. For the purposes of the PICD code, a single timing resolution had to be chosen—there is no provision for a slat by slat resolution. We settled on 120 ps as the number to use. There are certainly several slats with worse resolution than this, but it encompasses most of the slats, and quite a few of them actually have resolutions closer to 100 ps.

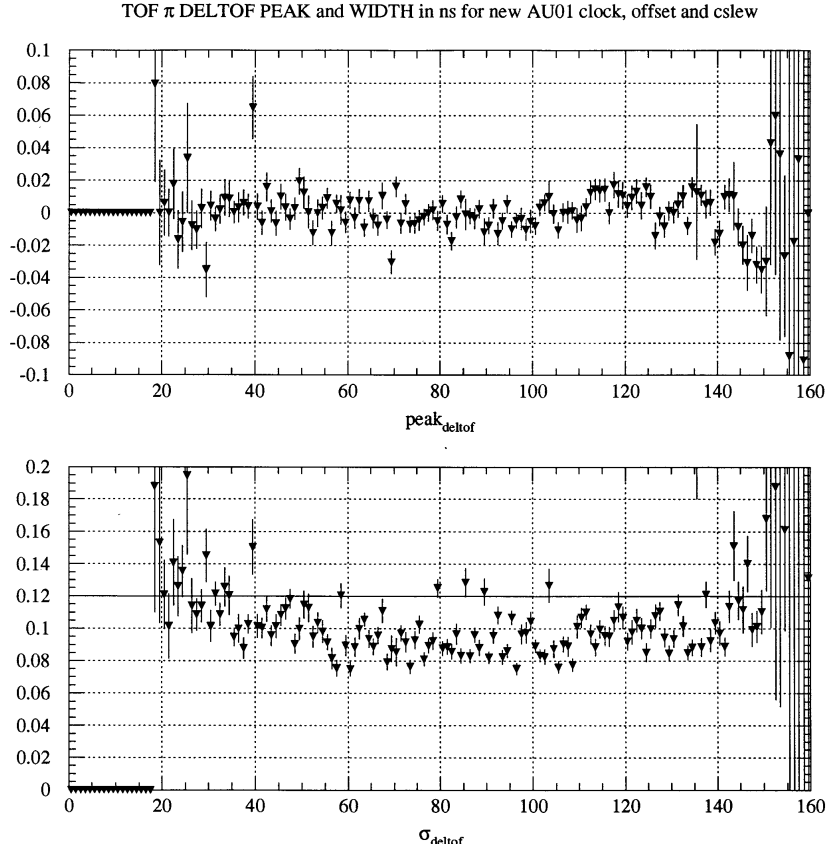


Figure E-1: Intrinsic TOF wall timing resolution

E.3 Monitoring of Calibrations During PASS3

During the PASS3 analysis pass several diagnostic histograms were filled that allowed a close check on the quality of the timing calibrations. Since the calibrations were not actually performed on every run, we wanted to have a way to make sure that the calibrations remained valid as the particle identification pass proceeded. In this thesis, of course, the quality of the calibrations for the kaons is

APPENDIX E. TIME OF FLIGHT WALL CALIBRATION

very important. Since there are relatively few kaons in any run, it is difficult to examine a histogram filled exclusively for kaons and have enough statistics to know whether the procedure is working properly. To circumvent this, identical histograms were simultaneously filled for pions, kaons and protons. By observing that the pion and proton histograms look acceptable, one gains confidence that the calibration for the kaons are in good shape. Figure E-2 shows an example of the type of diagnostic histogram examined during the running of PASS3.

E.3. MONITORING OF CALIBRATIONS DURING PASS3

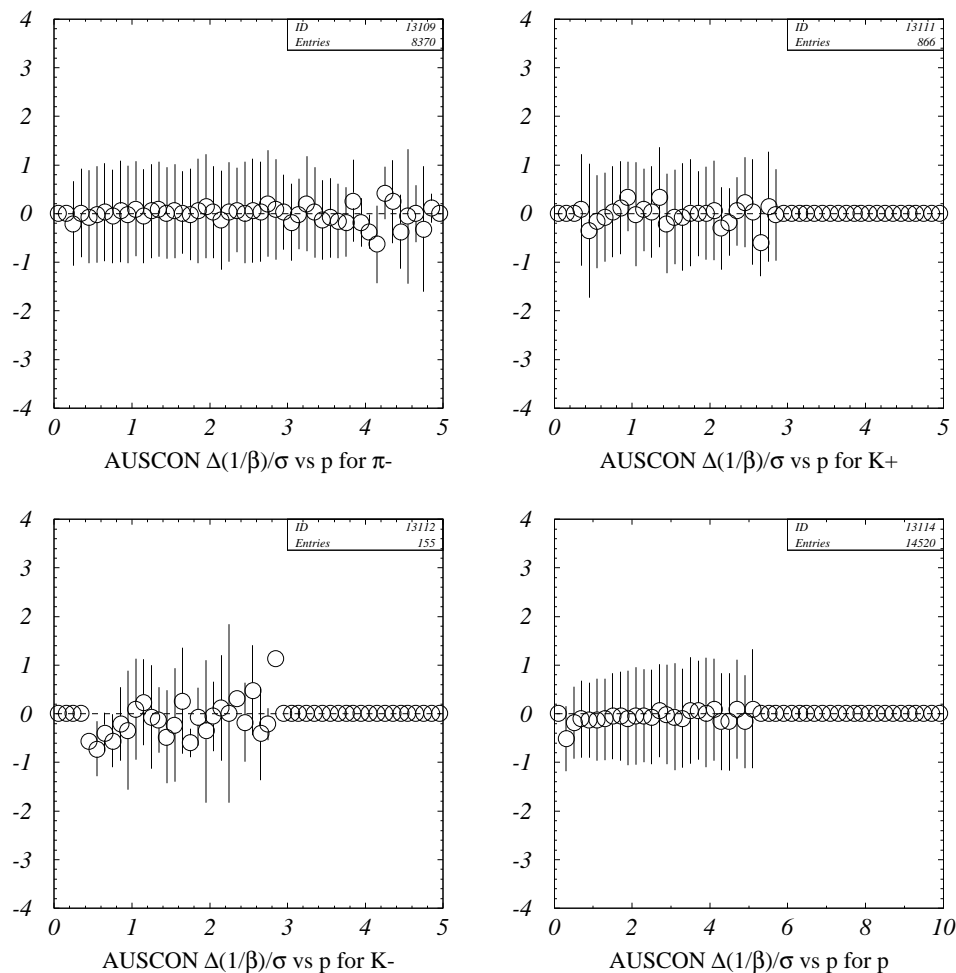


Figure E-2: Comparison of TOF calibrations for different species. This is taken from the PASS3 monitor output for run 10455, a NOPID Au 1% run at 14° . What is plotted is the difference between the measured and expected $1/\beta$, divided by the expected resolution in $1/\beta$, as a function of momentum. The error bars represent the rms width of the distribution at each momentum value. If the calibrations are properly done, this should result in a series of points centered at zero, with error bars reaching to ± 1 . The fact that the pions and protons appear to be properly distributed, gives some confidence that the kaons are being correctly identified.

APPENDIX E. TIME OF FLIGHT WALL CALIBRATION

Appendix F

Cross Section Fitting Procedure

The basis of the procedure used in fitting the E859 single particle spectra is described in a paper by Baker and Cousins [BC84], in which they describe how to fit a model to histogrammed data where the uncertainty associated with each bin arises from a Poisson distribution whose mean is given by the model. In fitting models to spectra we are essentially trying to do the same thing, but we have the complication that we are not fitting directly to binned counts, but rather to a quantity calculated from those counts, the invariant yield. I will briefly describe the method and some of the subtle points, and then show how to apply it to the E859 data.

F.1 Log Likelihood Fits to Histograms

Consider a histogram with n_i counts in bin i and a model depending on some set of parameters $\{\alpha\}$ which predicts a mean of c_i counts in bin i . Then, given the mean c_i , the probability of measuring n_i is given by the Poisson distribution

$$p_{c_i}(n_i) = \frac{e^{-c_i}}{n_i!} c_i^{n_i}, \quad (\text{F.1})$$

where the c_i are implicitly a function of the parameters $\{\alpha\}$. The probability that the observed set $\{n_i\}$ could be sampled from the set $\{c_i\}$ predicted by the model is the product of the probabilities given by Equation F.1 for each of the bins in the histogram. This total probability is the likelihood

APPENDIX F. CROSS SECTION FITTING PROCEDURE

function

$$L(\mathbf{c}, \mathbf{n}) = \prod_i \frac{e^{-c_i}}{n_i!} c_i^{n_i}. \quad (\text{F.2})$$

Maximizing this probability is the goal of the fitting procedure.

Instead of directly maximizing $L(\mathbf{c}; \mathbf{n})$, an associated function

$$\chi^2 = -2 \log \lambda \quad (\text{F.3})$$

is minimized instead. The likelihood ratio, λ , is given by

$$\lambda = \frac{L(\mathbf{c}; \mathbf{n})}{L(\mathbf{n}; \mathbf{n})}. \quad (\text{F.4})$$

This normalized likelihood function asymptotically then approaches a true χ^2 distribution as c_i and n_i become large. The minimization condition of χ^2 is

$$\frac{d\chi^2}{d\alpha} = 0. \quad (\text{F.5})$$

In fitting a histogram, there are two distributions to keep in mind. First is the the number of counts in each bin predicted by the model. Second is the probability distribution of measuring a particular number of counts given the model prediction. In the case of discrete counts in bins, this second distribution is the Poisson distribution, and is always the Poisson distribution, regardless of which model you use to predict the counts in each bin. The only thing that you can change is the number of counts you predict in each bin.

We are often imprecise when we use the term *log likelihood* fitting. Really, there are two parts to this method. The first is determining the probability of getting the observed result given the model prediction, and the second is minimizing the χ^2 statistic formed from the likelihood function. The first part depends on the details of what you're measuring, the second does not. If one is accumulating counts, Poisson probability distributions are the appropriate probability distribution to use for the first part. If, as in the case of the HBT analysis, one is measuring a ratio of two Poisson-distributed numbers, some other probability distribution will be appropriate.

F.2 Log Likelihood Fits to Invariant Yields

The calculated quantity being fit in the single particle analysis is the differential yield (see Section 4.9),

$$\begin{aligned} \frac{d^2n}{2\pi m_{\perp} dm_{\perp} dy} &= \frac{N^*(y, m_{\perp})}{N_{int}} \\ &= \frac{N(y, m_{\perp}) \textit{accept} \times \textit{decay}}{2\pi N_{int} m_{\perp} dm_{\perp} dy} \\ &\equiv w(y, m_{\perp}) N(y, m_{\perp}) \end{aligned} \quad (\text{F.6})$$

where N_{int} is the number of events, $N^*(y, m_{\perp})$ is the corrected number of counts, $N(y, m_{\perp})$ is the raw number of counts detected in the bin centered at (y, m_{\perp}) , *accept* is the geometric acceptance correction and *decay* is the decay correction for those particles which do decay. In all of this, the variable that we expect to have Poisson fluctuations is $N(y, m_{\perp})$.

The basic idea is to make a prediction of the differential invariant yield in a given bin, then use the various factors in Equation F.6 to convert this to a predicted number of counts. The probability of measuring the observed number of counts is given by the value of a Poisson distribution with a mean equal to the predicted number of counts.

Explicitly, the functional form of the m_{\perp} model is

$$\frac{d^2n}{2\pi m_{\perp} dm_{\perp} dy} = A e^{-B(m_{\perp} - m_0)}. \quad (\text{F.7})$$

Suppose that we also have the following

- n_i the raw number of counts in bin i
- w_i the average, over all particles in bin i , of the coefficient in Equation F.6 which relates counts to invariant yield.

In the case that there are no counts in bin i , an approximate value for w_i is calculated using the midpoint of the bin instead of an average over particles. For a given choice of A and B , the predicted differential invariant yield in each bin i is the integral of Equation F.7 over the width of the bin, and for small bins this may be approximated as the function value at the bin center multiplied by the bin width. This is converted to a predicted number of counts, c_i , by further multiplying by the weight

APPENDIX F. CROSS SECTION FITTING PROCEDURE

w_i . The contribution to the χ^2 from each bin is calculated as in the Baker and Cousins paper

$$\chi_i^2 = \begin{cases} 2c_i & \text{if } n_i = 0 \\ 2(c_i - n_i + n_i \ln(n_i/c_i)) & \text{otherwise} \end{cases} \quad (\text{F.8})$$

The contribution from each bin is then summed over the whole histogram, and this is the value which we attempt to minimize by varying the parameters of the model.

The task of minimizing a function is best left to a well designed, robust minimizer. The CERN Library package MINUIT is used for this job [JG92]. You need to provide a subroutine that calculates χ^2 and some starting values for the parameters—MINUIT does the rest. In addition to minimizing the function, MINUIT can also estimate the errors on the parameters and produce plots of the confidence contours.

The χ^2 function can be straightforwardly constructed using Equations F.8. The choice of reasonable starting values for the parameters A and B is done using an analytic form of a linear least squares fit to the natural log of the calculated invariant yield. The variance assigned to each bin is just the square root of the number of counts in that bin. Of course, this gives zero variance to bins with zero counts. However, this procedure is meant only for determining initial values for parameters to be used in the log-likelihood procedure. The fact that unrealistic importance will be given to bins without any counts will be rectified by the log-likelihood minimization. Typical starting values for a K^+ spectrum near mid-rapidity for central Si+Au are $A = 3.5$, $B = 5.0$. The final values of the parameters usually differ by no more than a few percent from the rough initial values.

The above ideas for fitting the invariant yield using log likelihood point estimation are implemented for E859 in a routine called CSFIT. This routine supersedes the routine MTPTFIT, written by Charles Parsons, which also uses log likelihood minimization for point estimation, but which can occasionally under-report errors on the fitted parameters. MTPTFIT determines the parameter errors by sampling the goodness of fit function over a grid of values in parameter space, tracing out a contour across which the value of the goodness of fit function increases by one unit above its minimum value. If parts of the contour lie outside the bounds of the grid that MTPTFIT has chosen, the error is reported as equal to the size of the grid, not the size of the contour. This is a

F.2. LOG LIKELIHOOD FITS TO INVARIANT YIELDS

situation that should only show up in exceptional circumstances, but it is best avoided altogether. As stated above, CSFIT uses MINUIT to calculate the best parameter values and to determine the errors on the fitted values of these parameters. MINUIT determines the parameter errors properly when the fit actually converges, so the routine CSFIT should be used instead of MTPTFIT in all circumstances.

APPENDIX F. CROSS SECTION FITTING PROCEDURE

Appendix G

TMA Groups

This appendix lists the run ranges for each of the TMA groups used in the analysis. By using these groups one should reproduce the TMA cuts.

Group	Runs	Group	Runs	Group	Runs
1	09910–09915	11	10170–10171	21	10736–10743
2	10108–10109	12	10174–10179	22	10744–10749
3	10110–10111	13	10536–10538	23	10889–10891
4	10112–10113	14	10539–10540		
5	10114–10114	15	10541–10541		
6	10119–10123	16	10542–10547		
7	10143–10143	17	10549–10550		
8	10146–10152	18	10598–10604		
9	10162–10163	19	10605–10611		
10	10168–10169	20	10614–10620		

Table G.1: Si+Al 3% TMA Groups

APPENDIX G. TMA GROUPS

Group	Runs
1	10554–10558
2	10560–10572
3	11097–11098
4	11104–11104
5	11105–11105

Table G.2: Si+Al 6% TMA Groups

Group	Runs	Group	Runs	Group	Runs
1	10577–10587	16	10703–10709	31	10882–10888
2	10588–10597	17	10710–10713		
3	10623–10629	18	10714–10716		
4	10630–10637	19	10717–10720		
5	10638–10640	20	10721–10723		
6	10641–10644	21	10724–10727		
7	10645–10649	22	10728–10730		
8	10650–10652	23	10731–10733		
9	10657–10660	24	10751–10755		
10	10662–10672	25	10756–10760		
11	10675–10680	26	10761–10764		
12	10682–10687	27	10765–10769		
13	10688–10691	28	10770–10772		
14	10692–10695	29	10775–10777		
15	10696–10698	30	10778–10784		

Table G.3: Si+Au 1% TMA Groups

Group	Runs
1	09880–09886
2	09887–09908
3	10095–10100
4	10101–10125
5	10126–10156
6	10159–10190
7	10510–10529
8	10563–10568
9	10881–10881
10	11092–11096
11	11101–11109

Table G.4: Si+Au 3% TMA Groups

APPENDIX G. TMA GROUPS

Appendix H

Preliminary ARC 1.9.5 Results

ARC (A Relativistic Cascade) is an event generator based on a hadronic cascade and designed primarily for simulating nucleus-nucleus collisions at AGS energies [PSK92]. Shortly before the time of this writing, version 1.9.5 of the code was made publicly available. As with earlier versions, this version has a parameterization of the rapidity distribution of primary kaon production at odds with experimental data. Perhaps because of the large number of collisions in nucleus-nucleus collisions, this does not seem to have had disastrous effects on the rapidity distribution in Si+A collisions. In fact, ARC reproduces many features of the experimental data quite well. In this appendix, we present a very brief comparison between ARC simulations and E859 data for central Si+Au \rightarrow K.

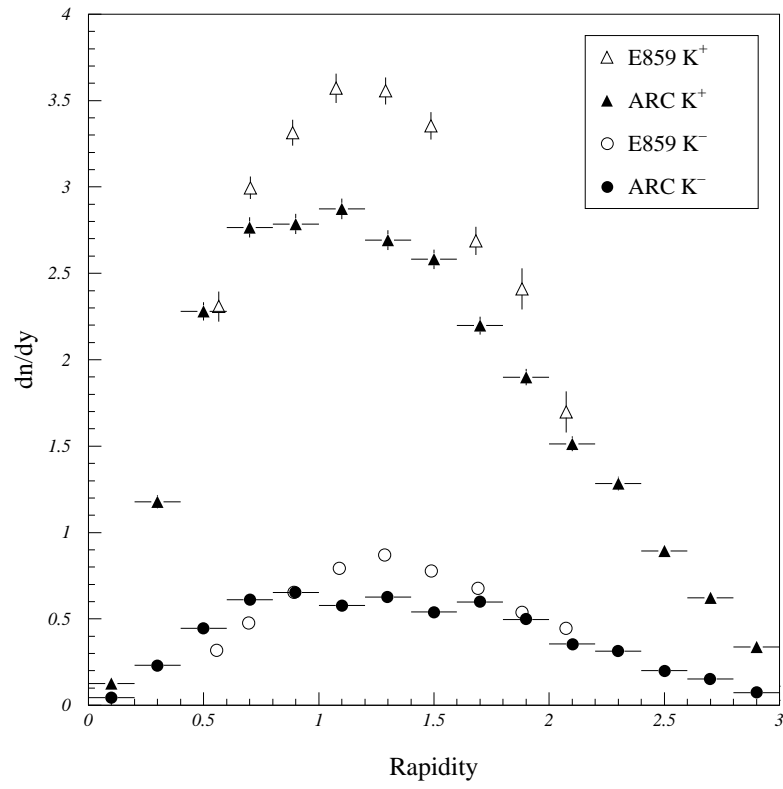


Figure H-1: Comparison of central Si+Au ARC and E859 kaon dn/dy

Appendix I

E859 Collaboration List

E-802 Collaboration, Brookhaven National Laboratory, Upton, NY 11973 USA

ANL-BNL-UCBerkeley-UCRiverside-Columbia-INS(Tokyo)-Kyoto-Kyushu-

LLNL-MIT-NYU-Tokyo-Tsukuba

Y. AKIBA⁶, D. BEAVIS², P. BEERY⁴, H.C. BRITT⁹, B. BUDICK¹¹, C. CHASMAN², Z. CHEN²,
C.Y. CHI⁵, Y.Y. CHU², V. CIANCIOLO¹⁰, B.A. COLE¹⁰, J.B. COSTALES⁹, H.J. CRAWFORD³,
J.B. CUMMING², R. DEBBE², J. ENGELAGE³, S.Y. FUNG⁴, M. GONIN², S. GUSHUE²,
H. HAMAGAKI⁶, O. HANSEN², R.S. HAYANO¹², S. HAYASHI², S. HOMMA⁶, H. KANEKO⁷,
J. KANG⁴, S. KAUFMAN¹, W.L. KEHOE¹⁰, K. KURITA¹³, *R.J. LEDOUX*¹⁰, M.J. LEVINE²,
Y. MIAKE¹³, D.P. MORRISON¹⁰, R.J. MORSE¹⁰, B. MOSKOWITZ², S. NAGAMIYA⁵,
M.N. NAMBOODIRI⁹, T.K. NAYAK⁵, J. OLNESS², C.G. PARSONS¹⁰, *L.P. REMSBERG*²,
D. ROEHRICH², P. ROTHSCHILD¹⁰, H. SAKURAI¹², T.C. SANGSTER⁹, R. SETO⁴,
R. SOLTZ¹⁰, P. STANKUS⁵, S.G. STEADMAN¹⁰, G.S.F. STEPHANS¹⁰, T. SUNG¹⁰,
Y. TANAKA⁸, M.J. TANNENBAUM², J. THOMAS⁹, S. TONSE⁹, J.H. VAN DIJK²,
F. VIDEBAEK², O. VOSSNACK⁵, V. VUTSADAKIS¹⁰, F.Q. WANG⁵, Y. WANG⁵,
H.E. WEGNER², D.S. WOODRUFF¹⁰, Y.D. WU⁵, X. YANG⁵, D. ZACHARY¹⁰ AND
*W.A. ZAJC*⁵

¹ Argonne National Laboratory, Argonne, IL 60439-4843

² Brookhaven National Laboratory, Upton, NY 11973

³ University of California, Space Sciences Laboratory, Berkeley, CA 94720

APPENDIX I. E859 COLLABORATION LIST

- ⁴ University of California, Riverside, CA 92507
- ⁵ Columbia University, New York, NY 10027 and Nevis Laboratories, Irvington, NY 10533
- ⁶ Institute for Nuclear Study, University of Tokyo, Tokyo 188, Japan
- ⁷ Kyoto University, Sakyo-Ku, Kyoto 606, Japan
- ⁸ Kyushu University, Fukuoka 812, Japan
- ⁹ Lawrence Livermore National Laboratory, Livermore, CA 94550
- ¹⁰ Massachusetts Institute of Technology, Cambridge, MA 02139
- ¹¹ New York University, New York, NY
- ¹² Department of Physics, University of Tokyo, Tokyo 113, Japan
- ¹³ University of Tsukuba, Tsukuba, Ibaraki 305, Japan

Bibliography

- [A⁺89] Y. AKIBA *et al.* Studies of high-density baryon matter from extended measurements of particle momentum distributions and from high-precision two-particle correlations. Proposal submitted to the AGS program committee, 1989.
- [A⁺90] T. ABBOTT *et al.* Kaon and pion production in central Si+Au collisions at 14.6 A·GeV/c. *Physical Review Letters*, **64** (1990) 847–850.
- [A⁺92a] T. ABBOTT *et al.* Measurement of particle production in proton induced reactions at 14.6 GeV/c. *Physical Review*, **D45** (1992) 3906.
- [A⁺92b] L. AHRENS *et al.* The operational status of the booster injector for the AGS accelerator complex and BNL. Technical Report 47119, BNL, 1992.
- [A⁺92c] R. ALBRECHT *et al.* Multiplicity and pseudorapidity distributions of charged particles from ³²S induced heavy ion interactions at 200 A GeV. *Zeitschrift fur Physik*, **C55** (1992) 539–548.
- [A⁺94] T. ABBOTT *et al.* Charged hadron distributions in central and peripheral Si+A collisions at 14.6 A·GeV/c. *Physical Review*, (1994).
- [Abb90] T. ABBOTT. *Search for Intermittency in Central Collisions of ¹⁶O+Cu at 14.6 GeV/c*. PhD thesis, University of California, Riverside, 1990.
- [Aic93] J. AICHELIN. Scattering and rescattering in relativistic heavy ion collisions. In *Proceedings of Heavy Ion Physics at the AGS*, 1993.
- [B⁺89] D. BEAVIS *et al.* A calorimeter for relativistic heavy-ion experiments. *Nuclear Instruments and Methods*, **A281** (1989) 367–372.

BIBLIOGRAPHY

- [Bak] M. BAKER. private communication.
- [BC84] S. BAKER and R. COUSINS. Clarification of the use of chi-square and likelihood functions in fits to histograms. *Nuclear Instruments and Methods*, **A221** (1984) 437–442.
- [Bjo83] J. BJORKEN. Highly relativistic nucleus-nucleus collisions in the central rapidity region. *Physical Review*, **D27** (1983) 140.
- [Blo90] M. BLOOMER. *Energy and Baryon Densities in $^{28}\text{Si} + \text{A}$ Collisions at 14.6 A GeV/c*. PhD thesis, Massachusetts Institute of Technology, 1990.
- [Che93] Z. CHEN. Hadron production in $p + \text{A}$ reactions at AGS energies: A review. *International Journal of Modern Physics*, **E2** (1993) 285–331.
- [Cia94] V. CIANCIOLO. *Bose-Einstein Correlations in $\text{Si}+\text{Au} \rightarrow 2K^+ + X$ Central Collisions*. PhD thesis, Massachusetts Institute of Technology, 1994.
- [Col92] B. COLE. *Particle Production at High Transverse Momentum in Nucleus-Nucleus Collisions at the AGS*. PhD thesis, Massachusetts Institute of Technology, 1992.
- [CTDL77] C. COHEN-TANNOUDJI *et al.* *Quantum Mechanics*. John Wiley & Sons, 1977.
- [EK80] A. ETKIN and M. KRAMER. The Brookhaven National Laboratory’s multiparticle spectrometer drift chamber system. *IEEE Transactions on Nuclear Science*, **NS-27** (1980) 139–144.
- [Etk79] A. ETKIN. A drift chamber system for use in a high rate environment. *IEEE Transactions on Nuclear Science*, **NS-26** (1979) 54–58.
- [F⁺79] H. FESEFELDT *et al.* Strangeness-transfer distributions in proton-proton collisions at 12 and 24 GeV/c. *Nuclear Physics*, **B147** (1979) 317.
- [FKBK93] X. FANG *et al.* Medium effects of kaon and antikaon spectra in heavy-ion collisions. *Physical Review*, **C47** (1993) 1678.
- [Gon92] C. GONG. Nuclear medium effect on the kaon dispersion relation. *Journal of Physics*, **G18** (1992) L123–L126.

BIBLIOGRAPHY

- [GR80] I. GRADSHTEYN and I. RYZHIK. *Table of Integrals, Series and Products*. Academic Press, Inc., 1980.
- [Gro90] PARTICLE DATA GROUP. Review of particle properties. *Physics Letters*, **B239** (1990) III.78.
- [H⁺93] S. HAYASHI *et al.* PID859 user's manual. Technical report, Brookhaven National Laboratory, 1993. Internal Memo # 11 to the E859 Collaboration.
- [Han90] O. HANSEN. Nucleus-nucleus collisions at very high energies. In *Mikolajki 1990, Proceedings, Nuclear and atomic physics with the accelerators of the nineties*, pp. 1–18, 1990.
- [Hig75] V. HIGHLAND. Some practical remarks on multiple scattering. *Nuclear Instruments and Methods*, **129** (1975) 497–499.
- [Hua90] H. HUANG. *Semi-inclusive and Inclusive Spectra of Charged Pions, Kaons and Protons from Proton-Nucleus and Silicon-Nucleus Collisions at AGS Energy*. PhD thesis, Massachusetts Institute of Technology, 1990.
- [JG92] F. JAMES and M. GOOSSENS. MINUIT—function minimization and error analysis. Technical Report D506, CERN, 1992.
- [K⁺93] S. KAHANA *et al.* Physics at the AGS with a relativistic cascade. In *Proceedings of Heavy Ion Physics at the AGS*, p. 263, 1993.
- [KD89] P. KOCH and C. DOVER. K^{\pm} , p, and Ω^{-} production in relativistic heavy ion collisions,. *Physical Review*, **C40** (1989) 145–155.
- [Keh91] W. KEHOE. E859 beam counter status. Presented at the E859 Fall 1991 Collaboration Meeting, 1991.
- [Ko83] C. KO. Subthreshold K^{-} production in high energy heavy ion collisions. *Physics Letters*, **B120** (1983) 294–296.
- [Koc90] P. KOCH. Strangeness in nuclear matter under extreme conditions. *Progress in Particle and Nuclear Physics*, **26** (1990) 253–314.

BIBLIOGRAPHY

- [KWXB91] C. KO *et al.* Effect of chiral restoration on kaon production in relativistic heavy-ion collisions. *Physical Review Letters*, **66** (1991) 2577–2580.
- [Lag91] J. LAGET. Strangeness production in nucleon-nucleon collisions. *Physics Letters*, **B259** (1991) 28–28.
- [LeC] Lecroy product catalog.
- [Mor91] D. MORRISON. The LVL2 database and INTER. Technical report, Brookhaven National Laboratory, 1991. Internal Memo #2 to the E859 Collaboration.
- [Nag91] S. NAGAMIYA. Experimental overview. 1991.
- [Par88] S. PARKER, editor. *Nuclear and particle physics source book*. McGraw-Hill Book Company, 1988.
- [Par92] C. PARSONS. *Strange Particle Production in 14.6 GeV/A Nucleus-Nucleus Collisions*. PhD thesis, Massachusetts Institute of Technology, 1992.
- [PSK92] Y. PANG *et al.* Cascade for relativistic nucleus collisions. *Physical Review Letters*, **68** (1992) 2743–2746.
- [RM82] J. RAFELSKI and B. MÜLLER. Strangeness production in the quark-gluon plasma. *Physical Review Letters*, **48** (1982) 1066–1069.
- [Rot93] P. ROTHCHILD. *Rapidity Dependence of Anti-Proton Production in Relativistic Heavy Ion Collisions at 14.6 A GeV/c*. PhD thesis, Massachusetts Institute of Technology, 1993.
- [S⁺86] T. SUGITATE *et al.* 100 cm long time-of-flight scintillation counters with RMS resolution of 50 ps. *Nuclear Instruments and Methods*, **A249** (1986).
- [Sak92] H. SAKURAI. *Study of Antiproton Production in ²⁸Si+A Collisions at 14.6 A GeV/c*. PhD thesis, University of Tokyo, 1992.
- [Sar89] M. SARABURA. *Cluster Production in Relativistic Heavy-ion Collisions*. PhD thesis, Massachusetts Institute of Technology, 1989.

BIBLIOGRAPHY

- [Sau77] F. SAULI. Principles of operation of multiwire proportional and drift chambers. Technical Report 77-09, CERN, 1977.
- [SGOO93] E. STENDLUND *et al.*, editors. *Proceedings of the Third International Conference on Ultra Relativistic Nucleus-Nucleus Collisions*, 1993.
- [Sol94] R. SOLTZ. *Two Pion Correlation Measurement for Si+X at 14.6 A-GeV/c and Au+Au at 11.6 A-GeV/c*. PhD thesis, Massachusetts Institute of Technology, 1994.
- [Sor] H. SORGE. Private communication.
- [Sor93] H. SORGE. Energy dependence of strangeness production in ultrarelativistic pA and AA collisions. In *Proceedings of Heavy Ion Physics at the AGS*, pp. 283–303, 1993.
- [SSG89] H. SORGE *et al.* Poincare invariant Hamiltonian dynamics: Modelling multi-hadronic interactions in a phase space approach. *Annals of Physics*, **192** (1989) 266–306.
- [SSS87] H. SATZ *et al.*, editors. *Proceedings of the Sixth International Conference on Ultra Relativistic Nucleus-Nucleus Collisions*, 1987.
- [Sun94] T. SUNG. *Kaon production in Si+Al and Si+Au collisions at 14.6 A-GeV/c*. PhD thesis, Massachusetts Institute of Technology, 1994.
- [T⁺88] P. THIEBERGER *et al.* BNL setup. *Nuclear Instruments and Methods*, **A268** (1988) 513.
- [Wer89] K. WERNER. Analysis of energy flow in ¹⁶O nucleus collisions at 200-GeV by the multistring model VENUS. *Zeitschrift fur Physik*, **C42** (1989) 85.
- [WLem] W. WATSON and M. LEVINE. The Front End, BNL Report BNL-39806. Technical report, Brookhaven National Laboratory, BNL memo on E802 data acquisition system.
- [Xu94] N. XU. Pion interferometry in ²⁸Si+Pb central collisions. *Nuclear Physics*, **A566** (1994) 585c–588c.
- [Zac93] D. ZACHARY. *Scaling of Energy and Baryon Densities in Relativistic Heavy Ion Collisions*. PhD thesis, Massachusetts Institute of Technology, 1993.

BIBLIOGRAPHY

- [Zaj93] W. ZAJC. Two particle correlations: The next generation. LNS Colloquium at MIT, 1993.
- [ZJ88] W. ZAJC and I. JURICIC. Single track momentum resolution in the E802 spectrometer. E-802-MEM-21, 1988.
- [ZP92] D. ZACHARY and C. PARSONS. CSPAW user's manual. E859 memo 5, 1992.

Acknowledgments

During Ron Soltz's thesis defense, Wit Busza asked him what it was that had interested him in relativistic heavy-ion physics. I don't remember what Ron said, but we all agreed afterward that the proper answer should have been, "Bob Ledoux". Bob's infectious (and barely legal) enthusiasm for physics and people is the real reason I joined this group.

A lot of the reason that I'm enjoyed working and learning here has to be credited to George Stephans. Whenever I doubt my ability to make good decisions, I just remind myself that I chose George as a thesis supervisor. He's great to work with, fun to talk to, and just plain one of the best scientists I've ever met.

The spokesmen of E859, Bill Zajc and Lou Remsberg, deserve an enormous amount of the credit for the success of the experiment. One of these days, I'll think of an idea before Lou and prove it more elegantly than Bill. I'd also like to acknowledge the hard, expert work of the rest of the E802 collaboration, the BNL-AGS staff and the workers of LILCO.

In addition to having them all as good friends, I have learned a great deal of the physics I know (and not just heavy-ion physics, either) from the previous generation of E802 students. Also, Martin Sarabura taught me the tight correlation between Diet Coke consumption and good computer programming, Richard Morse taught me how to wear black properly, Chuck Parsons has rekindled my burning interest in pyromania, Brian Cole taught me how to **express** my ideas, and Walter Kehoe has taught me *style*.

Of course, working with Ron Soltz and Vince Cianciolo has been fantastic. Vince and I have been friends since our very first day here at MIT, and we have watched each other grow from inexperienced dweebs into geeks with almost six years of research experience. Ron has been a very *valuable* friend, and has taught me the high art of the non sequitur. Ole Vossnack, honorary MIT

BIBLIOGRAPHY

graduate student, has shown me that it really is possible to balance physics with a *multitude* of other interests.

Though Ted Sung, Pete Rothschild, Dan Zachary have been with the group for over four years, somehow I still think of them as newcomers. They've been a lot of fun to work with. It's also been great sharing an office with Eleanor Judd. The future of the group is in good hands, especially since it looks like Larry Ahle will be staying on.

Mike Yoo, my roommate for the last two years, and who I've known since before I came to MIT, is one of my best friends here. Mike is a condensed matter physicist, but probably has a better grasp of relativistic heavy-ion physics than I do. I have adopted "Mike Yoo" as a personal mantra.

My mom, my dad and my sister have also been great during this time. I think they're amused by what I do, and I think that's a very healthy attitude for us all to adopt.

You should always save the best for last, so I'd like to thank Kunya for her support and companionship for the years we've been together. Physicists and psychologists seem to make a nice match—don't ask me to explain it.

Biographical Note

The author was born August 15, 1966 in Redondo Beach, California (only because Manhattan Beach did not have a hospital). At the age of four, he moved first to Woomera and then Glenelg, South Australia before returning to Manhattan Beach at the age of seven. The following years were spent learning and perfecting the necessary fundamentals: volleyball, skateboarding, bodysurfing. A stint at Mira Costa High School (home of the Mustangs!), was followed by an undergraduate education in physics at the University of California, Berkeley (home of “Oskie” bear!). Thinking that solid-state physics looked like a promising opportunity, he came to MIT and joined the relativistic heavy-ion research group.